Organic-inorganic hybrids for green photonics : solid state lighting applications

Vânia Patricia Castro Teixeira Freitas

Universidade de Aveiro Departamento de Física
2016

Vânia Patrícia Castro Teixeira Freitas

Híbridos orgânicos-inorgânicos para fotónica sustentável

Organic-inorganic hybrids for green photonics

Universidade de Aveiro Departamento de Física
2016

Vânia Patrícia Castro Teixeira Freitas

Híbridos orgânicos-inorgânicos para fotónica sustentável

Organic-inorganic hybrids for green photonics

Tese apresentada à Universidade de Aveiro para cumprimento dos requisitos necessários à obtenção do grau de Doutor em Física, realizada sob a orientação científica do Doutor Luís António Ferreira Martins Dias Carlos, Professor Catedrático do Departamento de Física da Universidade de Aveiro, Doutora Maria Rute de Amorim e Sá Ferreira André, Professora Associada com Agregação do Departamento de Física da Universidade de Aveiro, Doutor Jean-Louis Bantignies, Professor da Université de Montpellier e Doutora Rozenn Le Parc, Maître de Conférences da Université de Montpellier.

Este trabalho foi desenvolvido no âmbito do projeto COMPETE 2020 (Ref. POCI-01-0145-FEDER-007679), projeto CICECO- Instituto de Materiais de Aveiro (Ref. UID/CTM/50011/2013), projeto PICS 2015: “"White Emission Tuning Through Self Assembling Process", bolsa de doutoramento FCT (Ref. SFRH/BD/87403/2012), financiada por fundos nacionais através de FCT/MEC e cofinanciado por FEDER sobre o acordo de parceria PT2020.

Aos meus pais e ao meu irmão

o júri

presidente

Doutor João Manuel da Costa e Araújo Pereira Coutinho
Professor Catedrático, Universidade de Aveiro

Doutora Verónica de Zea Bermudez
Professora Catedrática, Universidade de Trás-os-Montes e Alto Douro

Doutor Luís António Ferreira Martins Dias Carlos
Professor Catedrático, Universidade de Aveiro

Doutor Senentxu Lanceros-Méndez
Professor Associado, Universidade do Minho

Doutor Pedro Alberto da Silva Jorge
Professor Auxiliar, Faculdade de Ciências, Universidade do Porto

Doutor Stephane Parola
Professor, Ecole Normale Supérieure de Lyon, Université Lyon, França

Doutora Rozenn Le Parc
Maître de Conférences, Laboratoire Charles Coulomb, Université de Montpellier, França

agradecimentos

O trabalho apresentado resulta da colaboração de várias pessoas e instituições, que tornaram possível a realização desta tese.
Agradeço em primeiro lugar aos meus orientadores, Professor Doutor Luís António Ferreira Martins Dias Carlos, Professora Doutora Maria Rute de Amorim e Sá Ferreira André, Professor Doutor Jean-Louis Bantignies e Professora Doutora Rozenn Le Parc pela oportunidade, incentivo, orientação, disponibilidade na partilha de conhecimento e apoio constante.
À Doutora Patrícia Pereira Lima pela sua amizade, disponibilidade, e ensinamentos.
Ao Doutor Michel Wong Chi Man pelas discussões nas diversas etapas do trabalho, pelo incentivo, acompanhamento, disponibilidade, apoio e colaboração constante.
À Professora Doutora Verónica de Zea Bermudez pela ajuda nas diferentes etapas do trabalho e pela sua disponibilidade constante.
Ao Doutor Xavier Catöen, Doutor Sidney Ribeiro, Doutor Édison Pecoraro e Doutor Lianshe Fu pela disponibilidade e colaboração.
À Fundação para a Ciência e Tecnologia pela Bolsa de Doutoramento.
Ao Campus France pela atribuição da bolsa Eiffel.
Ao Departamento de Física e CICECO Aveiro Institute of Materials da Universidade de Aveiro e Laboratoire Charles Coulomb da Université de Montpellier pelas condições de trabalho proporcionadas.
Aos técnicos da Universidade de Aveiro: Ivo Mateus, Miguel Rocha, Francisco Reis, Júlio Gonçalves, Celeste Azevedo, Paula Santos, Rosário Soares, Marta Ferro e Bruno Almeida.
Aos técnicos da Universidade de Montpellier: David Maurin, Philippe Dieudonné, Said Tahir.
Aos técnicos da ENSCM- Ecole Nationale Supérieure de Chimie de Montpellier: Cédric Totee, Pascale Guiffrey e Joris Vezzani.
Aos meus colegas Alexandre Botas, Carlos Brites, Cintya Barbosa, João Amaral, Mengistie Debasu, Molíria Vieira dos Santos, Mariela Nolasco, João Ramalho, Carlos Amorim, Pedro Prezas e António Almeida pelo bom ambiente.
Às minhas amigas Sara Carneiro, Sandra Gonçalves, Eliana Silva, Fábia Reboredo, Lara Carramate, Sandra Correia, Liliana Bastos, Raquel Rondão, Sangeetha Balabhadra e Rita Frias pelo carinho, pelos momentos de boa disposição e descontração, por tornarem tudo mais fácil!
Ao Vitor Pereira pelo apoio.
Um especial agradecimento aos meus pais, ao meu irmão e à Andreia pelo apoio e amor constante.

palavras-chave

Híbridos orgânicos-inorgânicos, método sol-gel, auto-organização, fotoluminescência, espectroscopia de absorção no infravermelho, iluminação de estado sólido, concentradores solares luminescentes.

resumo

O presente trabalho propõe sintetizar novos materiais híbridos orgânicos-inorgânicos do tipo silsesquioxanos em ponte e caracterizar a sua estrutura e propriedades de fotoluminescência com vista a potenciais aplicações na área da fotónica sustentável, nomeadamente, iluminação de estado sólido e concentradores solares luminescentes.

Neste âmbito, foram sintetizadas três famílias distintas de materiais baseados em seis precursores que diferem na sua organização estrutural, ou seja, precursores com estrutura: 1) linear onde a componente orgânica é baseada no grupo malonamida, **P2-m** e **P4-m**; 2) linear onde foi adicionado um anel aromático cuja componente orgânica é baseada em amida e/ou thioamida, **P(UU)**, **P(UT)** e **P(TT)**, e 3) tri-ramificada onde a componente orgânica é baseada no grupo amida, **t-UPTES(5000)**.

Dois híbridos orgânicos-inorgânicos (**M2-m** e **M4-m**) que resultam da hidrólise e condensação dos precursores **P2-m** e **P4-m** foram sintetizados. O papel da presença de um ou dois grupos malonamida foi estudado em termos de estrutura local e propriedades de fotoluminescência.

Três híbridos orgânicos-inorganicos, **H(UU)**, **H(UT)** e **H(TT)**, baseados, respetivamente, em **P(UU)**, **P(UT)** e **P(TT)**, foram sintetizados e caracterizados estruturalmente com o objetivo de estudar o papel das ligações de hidrogénio na auto-organização destes materiais. A presença de diferentes tipos de ligações de hidrogénio (bifurcada, linear e cíclica) induz diferentes tipos de configurações que têm influência nas propriedades físicas (mecânicas e óticas) dos materiais.

Híbridos baseados no precursor **t-UPTES(5000)** foram sintetizados tendo em conta diferentes estratégias de síntese. A variação da concentração de HCl e quantidade de água bem como a síntese em ambiente controlado permitiram melhorar as propriedades óticas deste sistema nomeadamente, o rendimento quântico absoluto e o coeficiente de absorção. Foram também discutidos, os mecanismos de recombinação responsáveis pela emissão através da comparação das propriedades de fotoluminescência observadas nos correspondentes modelos orgânicos e inorgânicos.

Finalmente, devido à simplicidade estrutural os precursores **P2-m** e **P4-m**, estes foram dopados com Eu^{3+}. A estrutura local dos correspondentes híbridos mostra coordenação local entre o ião e a matriz. Materiais eficientes do ponto de vista de rendimento quântico absoluto motivaram o desenvolvimento de concentradores solares luminescentes que apresentam rendimento quântico absoluto máximo de 0.60 ± 0.06 e eficiência ótica de conversão na região espetral de absorção (300-380 nm) de 12.3 %.

keywords

Organic-inorganic hybrids, sol-gel method, self-assembly, photoluminescence, infrared spectroscopy, solid-state lighting, luminescent solar concentrators.

abstract

The presente work aims to synthesize new bridge silsesquioxanes organic-inorganic hybrid materials, and characterize the local structure and photoluminescence properties overlooking potential applications in the area of green photonics, namely, in solid-state lighting and luminescent solar concentrators.

In this context, three distinct families of materials based on six precursors which differ in their structural organization were synthesized, *i.e.* precursors with structure: 1) linear where the organic component is based on malonamide group, **P2-m** and **P4-m**; 2) linear which has been added an aromatic ring whose organic part is based on amide and/or thioamida, **P(UU)**, **P(UT)** and **P(TT)** and 3) branched which the organic component is based on amide group, **t-UPTES (5000)**.

Two organic-inorganic hybrids (**M2-m** e **M4-m**) which results from hydrolysis and condensation of the precursors **P2-m** e **P4-m** were synthetized. The role of the presence of one or two malonamide groups was studied in terms of local structure and photoluminescence properties.

Three organic-inorganic hybrids **H(UU)**, **H(UT)** and **H(TT)** based on **P(UU)**, **P(UT)** and **P(TT)** were synthesized and structurally characterized aiming to study the role of the hydrogen bond in the self-assembling of these materials. The presence of different types of hydrogen bonds (bifurcated, linear and cyclic) induces different conformations which affect the physical properties (mechanical and optical) of the materials.

Hybrids based on **t-UPTES(5000)** precursor were synthesized based on different synthesis strategies. Changing the concentration of HCl and water content as well as the synthesis in a controlled environment allowed the improvement of the optical properties of this system, in particular, the absolute emission quantum yield and the absorption coefficient. In addition, it were studied the recombination mechanisms responsible for the emission through the comparison between the corresponding photoluminescence properties of the organic and inorganic models.

Finally, due to the structural simplicity of the precursors **P2-m** and **P4-m,** these were doped with Eu^{3+}. The local structure of the corresponding hybrids shows local coordination between the ion and the host. Efficient materials concerning the absolute emission quantum yield values motivated the development of luminescent solar concentrators with a maximum absolute emission quantum yield of 0.60 ± 0.06 and optical conversion efficiency in the absorption spectral region (300-380 nm) of 12.3%.

Index

List of abbreviations and symbols

ϕ	Absolute emission quantum yield	**ICP-OES**	Inductively coupled plasma optical emission spectroscopy
Ac	Actinide	**Ln**	Lanthanide
AM 1.5G	Air Mass 1.5 Global	τ	Lifetime
APTES	3-aminopropyltriethoxysilane	**LED**	Light-Emitting Diode
d_{ip}	Average interparticle distance	L	Luminance
BS	Bridged silsesquioxane	**LSC**	Luminescent solar concentrators
cd	Candela	η_E	Luminous efficacy
L_c	Coherence length	**MAS**	Magic-Angle Spinning
CCT	Color Correlated Temperature	**MIR**	Mid-infrared
CRI	Color Rendering Index	**NP**	Nanoparticle
CIE	Commission Internationale d'Éclairage	**NIR**	Near-Infrared
c	Condensation degree	A_{nr}	Nonradiative transition probability
CP	Cross-polarization	**NMR**	Nuclear magnetic resonance
CE	Current Efficiency	**N**	Number of valence electrons
DMDPS	Diphenyldimethoxysilane	n_w	Number of water molecules
D-A	Donor-Acceptor	η_{opt}	Optical convertion efficiency
η	Emission quantum efficiency	**OLED**	Organic Light-Emitting Diode
EQE	External quantum efficiency	**PMO**	Periodic mesoporous organosilic
FIR	Far-infrared	**PTES**	Phenyltriethoxysilane
FT-IR	Fourier transform infrared	**PV**	Photovoltaic
fwhm	Full-width-at-half maximum	**PLED**	Polymer Light-Emitting Diode
HBS	Hydrogen-bond strengthning	**POE**	Poly(oxyethylene)
IR	Infrared	**POP**	Poly(oxypropylene)

PE	Pressure effect
QDs	Quantum dots
R	Radiance
A_r	Radiative transition probability
RGB	Red-Blue-Green
SEM	Scanning electronic microscopy
SSL	Solid-state lighting
SD	Starting Delay
sr	Steradian
d	Structural unit distance
TEOS	Tetraethoxysilane
TGA	Thermogravimetric analysis
t	Thickness
UV	Ultra-violet
WLEDs	White Light-Emitting Diodes
XRD	X-ray Diffraction
tta–H	2-thenoyltrifluoroacetone ligand

1. Introduction

1.1 Context and state of the art

Nowadays, one of the most serious issues that raises many questions about the viability of the future and services involves the green–house gas emission and the increase of the energy consumption associated to the growth of the global population [1,2]. Every year 730 billion metric tons of CO_2 are released into the atmosphere [2]. The environment pollution growing causes serious effects, like global warming and climate changing which are not only affecting human beings but also other living species as well as the entire bio–diversity of the earth [2].

The development of economically and sustainable solutions requires the utilization of not toxic, earth-abundant and inexpensive materials to reduce hazardous waste. "Green" photonics as a photonic technology for a cleaner/greener environment emerged in the last few years with particularly relevance in this regard [2].

"Green" photonics describe any device or process that uses photonics in a sustainable way, yielding an environmentally sustainable outcome and improved public health [3-6]. The contribution of photonics is considered "green" because it can generates or conserves energy, reduces pollution, yields an environmentally sustainable outcome or improves public health [6]. Three main areas were selected as targets towards "green" photonics: solid-state lighting (SSL), photovoltaic (PV) and optical communications.

Focusing our attention in SSL, during the last decades the lighting industry has suffered a deep revolution with the emergence of a new class of semiconducting light sources, such as light-emitting diodes (LEDs), organic light-emitting diodes (OLEDs) and polymer light-emitting diodes (PLEDs).

Unlike incandescent and fluorescent lamps, in which light is created with hot filaments and gases encased in a glass bulb, respectively, in SSL charge carriers (electrons and holes) are injected into solid-state semiconductors where they recombine emitting photons [7]. Thus, a new generation of illumination is emerging with considerable impact on energy consumption and environment [8-11]. Moreover, the need for white light emitters overstep the border of public and domestic lighting finding application in the control of sleep disruption-related diseases [12,13] that affects the human circadian rhythm [13].

Nowadays, 20-25 % of worldwide energy consumption is used for lighting, accounting for ~1.7 billion metric tons of CO_2 every year (equivalent to the emissions from 70 % of the world's passenger vehicles) [8,14]. Traditional incandescent light bulbs and compact fluorescent lamps are quite inefficient converting only ~5 % and 20 % respectively, of electricity into visible radiation (the remaining energy is lost non radiatively in the infrared spectral region as heat). In addition, in many developing countries, lighting is produced using oil lamps due to the absence of grid-based electricity. This is responsible for only 1 % of global lighting, but is hugely inefficient and accounts for 20 % of CO_2 emissions due to lighting [15].

The demand for lighting is increasing rapidly worldwide, it is foreseeable that the lighting consumption will treble by 2030 [8], placing an enormous emphasis on the development of high-efficiency sources. The transition to more sustainable devices is currently a reality in many cities worldwide [16] and it is expected that sustainable devices will achieve significant penetration in the market in the next two decades [17]. Indeed, the annual energy savings due to this increased market penetration are estimated to be approximately 300 TWh by 2030, or the equivalent annual electrical output of about 50 000 MW power plants (decrease in total electricity consumption for lighting by roughly 46 % compared with a scenario with no additional penetration of SSL in the market) [17]. To save energy and reduce CO_2 emissions it is required the development of more efficient ways to produce and consume energy [18].

The LED–based lighting offers advantages in what concerns to the energy and resources saving compared to conventional light sources. A comparison between the properties of the LEDs and conventional light sources in particular incandescent bulbs and compact fluorescent lamps are described below [12,19]:

- luminous efficacy[1] (η_E, lm·W^{-1}), for WLEDs a maximum value of 303 lm·W^{-1} was achieved [20], whereas in the case of compact fluorescent lamps and incandescent bulbs a maximum η_E of 70 lm·W^{-1} and 12-18 lm·W^{-1}, respectively, can be observed [21];
- the LEDs lifetime are ~60 000 h, while for compact fluorescent lamp 8000 h and between 1000-2000 h for incandescent bulbs [22];
- response times of typical red indicator LED can achieve full brightness in microseconds [22];
- high mechanical stability. LEDs, being solid state components, are difficult to damage with external shock. Compact and incandescent bulbs are easily broken if subjected to external shock;
- in addition the LEDs provide environmental protection due to the absent of heavy metals. For example, a fluorescent lamp contains 5 mg of Hg.

Figure 1.1 displays the evolution of η_E of different types of common light sources over the last two centuries. Although the typical improvement rate of the η_E in traditional lamps was lower than 1.2 times per decade [23], it is evident the exponential improvement of LEDs based light sources during the last two decades. The first inorganic LED with emission in the red spectral region and η_E of 0.1 lm·W^{-1} was fabricated by Holonyak and Bevacqua in 1962 based on GaAsP layers [24]. In the 1970s and 1980s, LEDs based on GaP:N (green), GaAsP:N (yellow/red), AlGaAs (red) and AlInGaP (orange/red) were discovered with η_E values between 1 lm·W^{-1} and 10 lm·W^{-1} [25,26]. Since bright GaN-based blue LEDs, were invented by Nakamura in 1993 [27], the major breakthrough in lighting technology that received the Nobel prize in Physics in 2014 "for the invention of efficient blue light-emitting diodes which has enabled bright and energy-saving white light sources" there has been considerable interest in improving their output power.

In the state of the art, η_E values of monochromatic commercial inorganic LEDs (individual luminaires and packages) range from 60 lm·W^{-1} to 130 lm·W^{-1} [28,29], which are two orders of magnitude higher than the value of the first $GaAs_{0.6}P_{0.4}$ red LED demonstrated in 1960s [24]. For commercial inorganic WLEDs, CREE Inc. raised recently the luminous

[1] Luminous efficacy is the ratio between the luminous flux (lm) and the electric power (W).

efficacy record to 303 lm W^{-1} (measured at a Correlated Color Temperature[2] (CCT) of 5150 K and a drive current of 350 mA), which is by far the highest value of all white light sources [20].

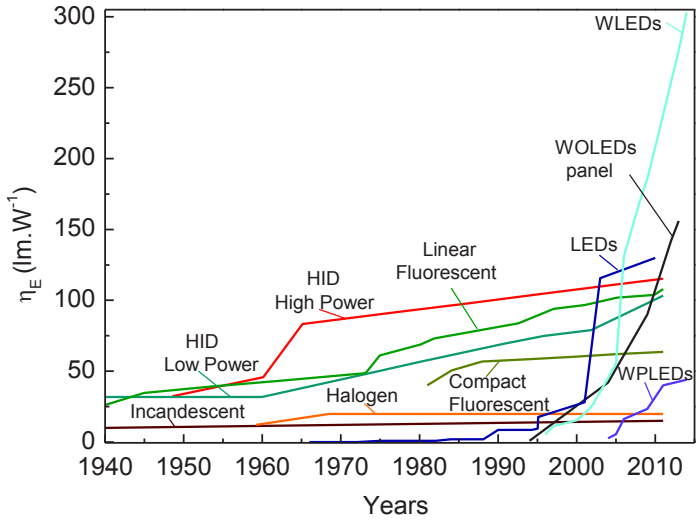

Figure 1.1. Evolution in the luminous efficacy from distinct light sources. The curves of incandescent, halogen, high intensity discharge (HID) (including mercury vapor, metal halide and sodium vapor lamps) and fluorescent lamps are taken from the U.S. Department of Energy Solid-state lighting research and development report [28]. The LEDs and WLEDs curves are taken from Kovac *et al* [30], updated with data from Farinola *et al.* [29] and taken from Narukawa *et al.* [23], updated with data from CREE catalog [20], respectively. The WOLEDs curve built based on data: Chang *et al.* [31] and NEC lighting catalog [32] and the WPLED one is based on data Reineke *et al.* [7], Wu *et al.* [21], Tang *et al.* [33], and Li *et al.* [34].

Although the performance of commercially available OLED panels has not yet met luminous output or cost targets, considerable progress was made in the last decade [28]. OLED panels with η_E >60 lm·W^{-1}, a value higher than those characteristic of incandescent and halogen lighting, are shipping as of spring 2012 [35], and a commercial device, 2.5×10^{-2} $\times2.5\times10^{-2}$ m^2, with η_E =156 lm·W^{-1} and a brightness of 1000 cd·m^{-2} has recently been demonstrated by NEC Corporation [32]. Despite the considerable progress that has been made since 2010, PLEDs is the newest and least mature technology. The efficacy of the state of the art devices has already exceeded that of incandescent light bulb (12–18 lm·W^{-1}) approaching the typical values of compact fluorescent lamps (40–70 lm·W^{-1}) [21]. An interesting example is the white PLED reported by Li *et al.* [34] with η_E of 44 lm·W^{-1} involving a flexible polymer nanocomposite electrode comprising a layer of single-walled

[2] CCT is the temperature of a blackbody radiator that emits the same color of the light source.

carbon nanotubes and a layer of silver nanowires embedded in the surface of a barium strontium titanate nanoparticle-polymer nanocomposite. However, even the most efficient PLEDs are far from practical lighting applications and there are many challenges that persist to be addressed. Examples are the stability of the devices at high electrical current densities that limit their light output per unit area, a crucial point for lighting applications, and operation lifetimes, that have almost not been tested and reported nowadays [21].

The first generation of commercially available WLEDs was based on InGaN chips, emitting in the blue region (~460 nm), combined with a $Y_3Al_5O_{12}:Ce^{3+}$ (YAG:Ce) phosphor layer that absorbs part of the emitted photons converting them into low energy ones in the yellow spectral region [36]. The fraction of the LED emitted blue photons (not absorbed by the active layer) will combine with the phosphor yellow emission giving the white light. The second generation of WLEDs is still based on a blue emitting InGaN LED but combined with a mix of orange and green inorganic phosphors (*e.g.* nitridosilicates, $M_2Si_5N_8$ and $MSi_2O_2N_2$, with M=alkaline earth) [37].

Currently, there are three main methods for generating white light based on LEDs, described below and represented in Figure 1.2 [38-40]:

- blue LED chip covered with a yellow downshifting phosphor (*e.g.* $Ca_{1-x-y},Sr_x,Eu_y)_7(SiO_3)_6Cl_2$ [41]) that allows some of the exciting blue radiation to bleed through;
- $In_xGa_{1-x}N$-based (380 nm to 410 nm) UV-LED chip jointed with red, green and blue (RGB) downshifting phosphors (*e.g.* organoboron dyes [42] or dye-bridged organic-inorganic hybrids [43]);
- individual RGB chips assembled in a single device.

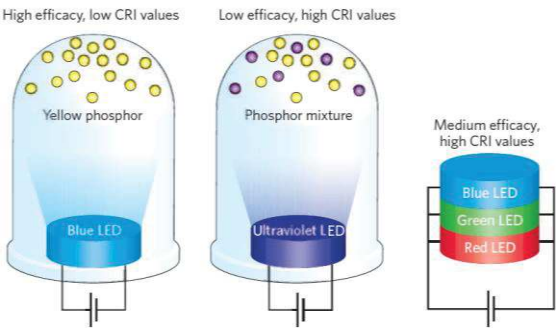

Figure 1.2. Different methods to produce white light based on LEDs. Taken from Pimputkar *et al.* [9].

The RGB approach requires distinct LEDs that must be individually adjusted to balance the emission intensity of each color to generate homogeneous white light, which is a very difficult task because each illuminance distribution is different from the other [38,39]. Furthermore, the differential aging of the LEDs and the poor color rendering index[3] (CRI), lower than 70 [40] of the generated white light (due to narrow emission wavelength gamut) are also drawbacks. Mixing phosphors results in efficiency losses due to self-absorption and the different degradation rates of the individual phosphors lead to changes in emission color over time [44]. The single-phosphor-converted blue LED device is currently the most common WLED produced today, due to the high efficiency of blue LEDs and the yellow-emitting YAG:Ce phosphor. Despite the limitation of relatively poor CRI value (lower than 70), due to the lack of green and red components, strong temperature and current dependence of chromaticity and CCT higher than 4000 K are presented [40].

One of the major targets in SSL research to circumvent these problems is the development of new broadband white light-emitting phosphors. Ideally, such phosphors will have to be excited in the blue or/and emit broadly in the green-to-red spectral regions to create a broad spectrum white light similar to blackbody radiation [45]. Some specific targets are required [46-48]:

- high absolute emission quantum yield (ϕ, higher than 0.5), and Luminance (L) higher than 100–150 cd m^{-2};
- stability over time and under irradiation with UV or blue commercial GaN-based LEDs;
- thermal stability, as the temperature inside a LED can reach ~100 °C;
- composition based on sustainable elements, avoiding large amounts of lanthanide ions (Ln^{3+}) and other critical metals.

The majority of the newly reported compounds are Ln^{3+}-doped oxides [49] and nitrides [37,50], Eu^{2+}-doped sulfides [51], borophosphates [52] and organic electroluminescent materials [7,53]. An intermediate approach is the development of new materials and systems that must aim toward higher levels of sophistication and miniaturisation, be recyclable and respect the environment, be reliable and consume less energy or help save energy. Organic-inorganic hybrid materials appear as a promising solution to develop phosphors with cost

[3] CRI is the quantitative measure of the ability of a light source to faithfully reproduces the color of an object, in comparison with a blackbody (or Planckian) light source.

effective and large scale processable emitters in the visible spectral region under excitation with UV (380–410 nm) and blue (460-490 nm) emitting LEDs. The designation of hybrid originates from the Latin "*hybrida*" that means mixed-breed. A hybrid material is composed of, at least, two different components (an organic and an inorganic one), where the properties of the final material are not just the sum of the individual contributions due to the role of their inner interfaces [54,55].

Organic-inorganic hybrids present several advantages concerning photonic' application' as listed below [56]:

- flexible, relative facile chemistry and highly controlled purity, since they are synthesized from pure precursors;
- versatile shaping and patterning depending on the foreseen application;
- good mechanical integrity, excellent optical quality and easy simple control of the refractive index by changing the relative proportion of the different precursors;
- encapsulation of large amounts of emitting centers (*e.g.*, organic dyes, quantum dots and Ln^{3+} introduced as complexes or salts);
- as they are chemically produced at mild temperature, the dopants can be introduced in the original sol and thus be easily entrapped into the forming matrix and preserved without destruction (particularly relevant for organic dyes);
- they allow interaction of dopants with external liquids or gases, sintering is unnecessary in various systems, since the incorporated optically active molecules are not leached out of the matrix cages by solvents;
- possibility of having energy transfer between the host and the emitting centers, which, in turn, undergo the corresponding radiative emitting process.

Bridged silsesquioxanes (BSs) are a class of organic-inorganic hybrids that deserve particular attention in this thesis. Since 1989, this class of materials has been the subject of intense studies [57-69]. Synthesized by sol-gel process (detailed in Chapter 2), they contain an organic bridging group linked to two or more Si atoms by Si-C bonds [70-78]. For instance, in dye-doped hybrids, the inorganic skeleton circumvents the clustering of the dye molecules inducing the concomitant long term thermal and photostability and less temperature-dependent photoluminescence, while exposing a hydrophilic and easily functionalized surface to the environment [43,79-81]. The sol-gel of BS organic-inorganic hybrids are commonly

used as encapsulating material in the LED housing to improve the light extraction efficiency and protect the device from dust and moisture [82-84]. A recent example involves the combination of a commercial UV-emitting LED chip (InGaAsN, 390 nm) and boehmite-derived hybrid nanoparticles (NPs) that efficiently (ϕ=0.60) convert the UV radiation into white light with (x,y) Commission Internationale de l' Eclairage (CIE) color coordinates of (0.32, 0.33), CRI of 85.5 and CCT of 6111 K [85].

The first examples of the use of hybrid materials comprise layered crystalline organic-inorganic perovskites with η_E =0.2 lmW^{-1} were reviewed by Mitzi *et al.* in 2001 [86]. The interest in these hybrid perovskites as single-phase white light emitters persist, as illustrated by Dohner *et al.* [44]. Recently, organic-inorganic hybrid perovskite based on $MaPbBr_3$ with current efficiency (CE) of 42.9 cd A^{-1} and external quantum efficiency[4] (EQE) [87] of 8.53 % was reported. This study represents a big step toward the development of efficient next-generation emitters with high color purity and low fabrication cost based on perovskites [88].

In addition to the inexpensive and scalable synthesis route and binder-free film deposition methods, crystalline hybrid perovskites display cool white light with CIE (x,y) coordinates of (0.31, 0.36), CRI>85 and CCT=6502 K with a sustained activity under continuous illumination [44]. After those initial works, the research field has been driven by the development of diverse organic-inorganic hybrids with potential for SSL technologies, including dye- and quantum dot-doped hybrids, BS hybrids, and metal organic frameworks.

The next section summarizes the work reported in the literature over the last decades on the generation of white light based on these distinct hybrid matrices. Examples will address siloxane-based hybrids embedding organic dyes, with the formation of covalent or non-covalent, dye-matrix interactions, and functionalized with amine or amide groups, without any chromophore fragment. In this chapter the revision of siloxane-based hybrid embedding organic dyes does not intend to be exhaustive, rather demonstrating the progress of the field towards the fabrication of monochromatic emitting LED and WLEDs. The few examples of quantum dots-doped hybrids and metal organic frameworks that can be found in the literature will not be discussed here.

[4] EQE is the ratio free charge carriers to incident photons.

1.1.1 Dye-bridged hybrids

The interest in organic electroluminescence increases after the pioneering work of Tang and VanSlyke in 1987 on the development of dye-based thin film multilayer OLEDs operating at low driving voltages in the Eastman Kodak research laboratories [89]. Embedding of organic dyes into polymers and organic-inorganic hybrid hosts, with the formation of covalent or non-covalent dye-matrix interactions, improves the thermal stability, mechanical resistance, aging and environmental stability of the dye molecules [81,90] (and of the corresponding electroluminescence devices). Moreover, the structural versatility of the inorganic counterpart allows the minimization of the inter-chromophoric interactions improving the ϕ values and preventing the dye degradation [80,91,92].

The first reports of dye-doped hybrid materials describe dye-modified silanes incorporating hole- or electron-transporting units and light-emitting species in the orange (Si-DCM and Si-PBD, Figure 1.3) [93] and green (Si-NABUP, Figure 1.3 and Table 1.1) [94] spectral regions, paving the way for the production of efficient WLEDs based in organic-inorganic hybrids.

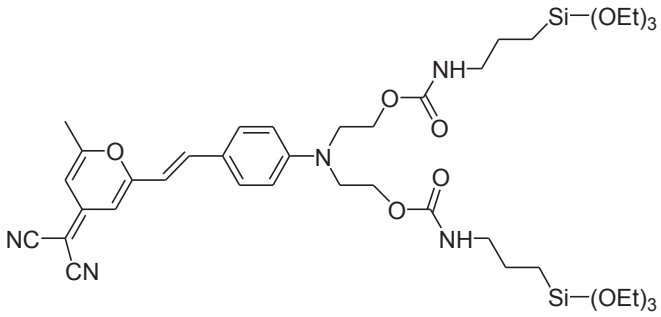

Si-DCM [93]

Figure 1.3. Molecular structures of siloxane hybrid precursors. DCM=4-dicyanomethylene-2-methyl-6-[p-(dimethylamino)styryl]-4H-pyran; PBD=2-(4-biphenylyl)-5-(4-tert-butylphenyl)-1,3,4-oxadiazole; NABUP=N-(4-butyl-phenyl)-4-[(N-2-hydroxyethyl)(methyl)amino]naphthalimide; TPPy=1,3,6,8-tetraphenylpyrene; PHEMA=poly(2-hydroxyethylmethacrylate); DCM-OH=2-(2,6-bis(E)-4-(diethylamino)-2-((6-hydroxyhexyl)oxy)styryl)-4H-pyran-4-ylidene)malononitrile; DADCP=2,5-diamino-3,6-dicyanopyrazine; APTMS=3-(anilinepropyl)trimethoxysilane; XDA=m-xylylenediamine; BSA=4,40-[1,3-phenylenebis(1-methylethylidene)]bis(aniline).

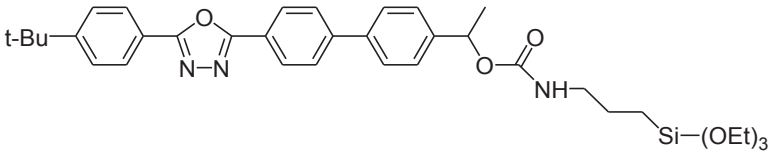

Si-PBD [93]

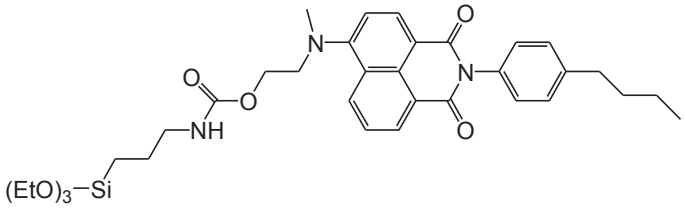

Si-NABUP [94]

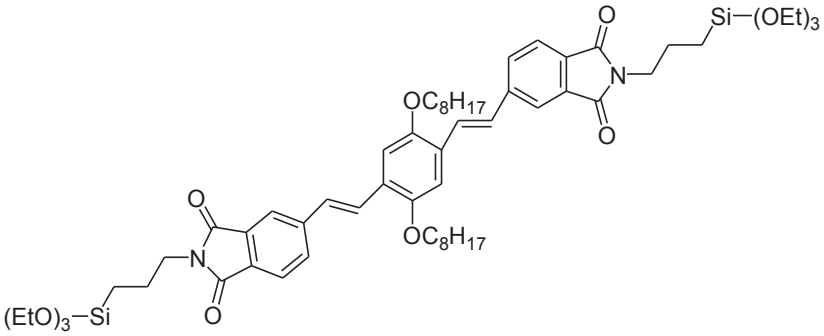

Si-phenylenevinylenediimide [73]

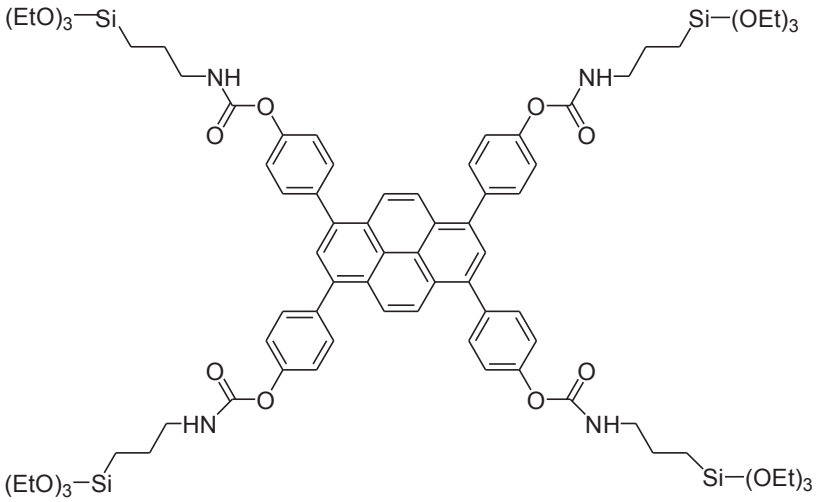

Si-TPPy [95]

Figure 1.3 (Continued)

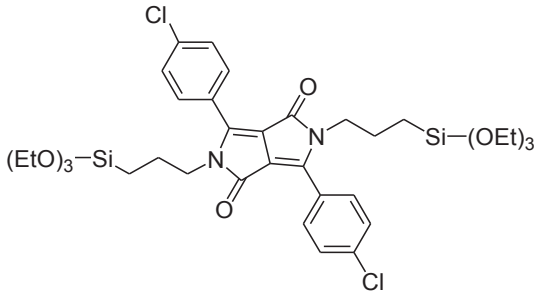

Si-PR254 [79]

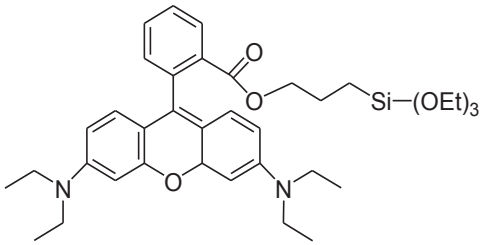

Si-RhB [79]

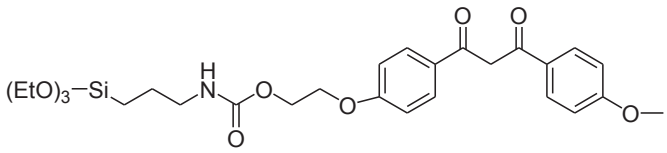

Si-PHEMA [42]

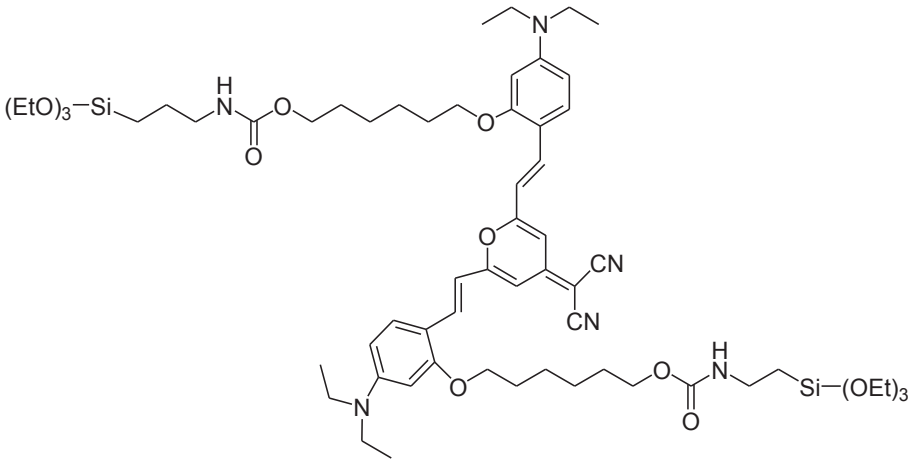

Si-DCM-OH [43]

Figure 1.3 (Continued)

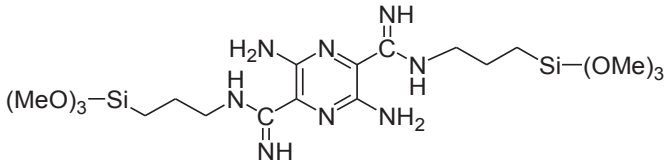

Si-DADCP [43]

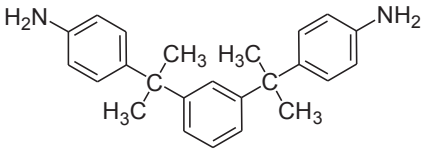

Si-BCA [96]

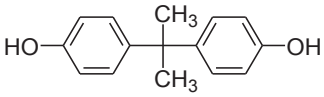

Si-BPA [96]

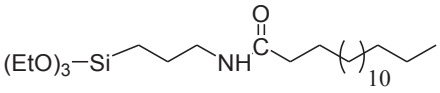

Monoamidosil [67]

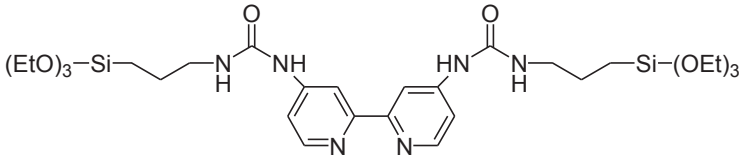

M4 [61]

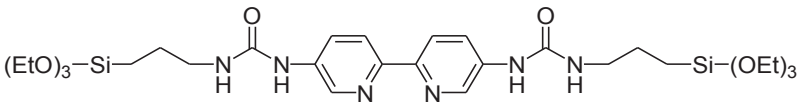

M5 [61]

Figure 1.3 (Continued)

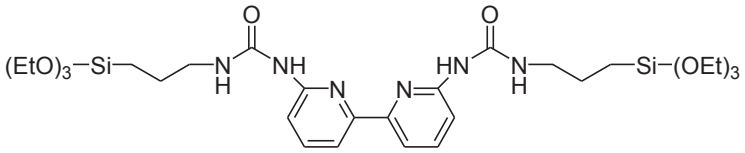

M6 [61]

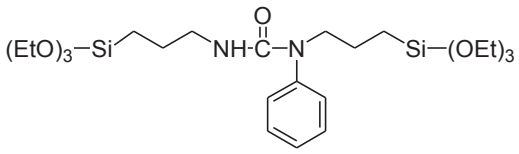

Si-APTMS [97]

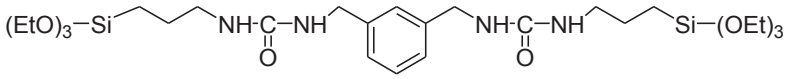

Si-XDA [98]

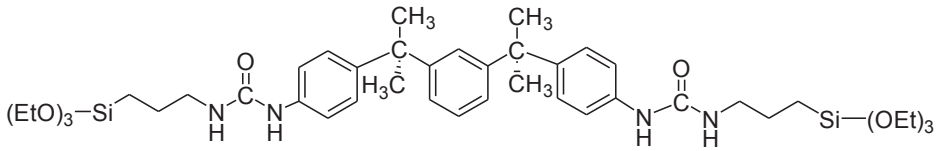

Si-BSA [99]

Figure 1.3 (Continued)

Few years later, inorganic fragments of hydrolysable Tetraethoxysilane (TEOS, $Si(OC_2H_5)_4$) were used to control the molecular aggregation of chromophores in the solid state, in particular the formation of J-aggregates (fluorescent) avoiding the presence of H–aggregates (non-fluorescent) [73]. The silsesquioxane hybrids resulting from the hydrolysis and condensation of the phenylenevinylenediimide silsesquioxane precursor (Si–phenylenevinylenediimide, Figure 1.3) were used to produce WLEDs with *L* values of 10 $cd \cdot m^{-2}$ for voltages lower than 30 V, see Table 1.1 [73].

WLEDs were also fabricated using dye-doped periodic mesoporous organosilica films. The films with blue fluorescence and high ϕ=0.70 were synthesized by surfactant-templated sol-gel polycondensation using a 1,3,6,8-tetraphenylpyrene (TPPy)–containing organosilane precursor (Si-TPPy, Figure 1.3) [95]. Two dyes emitting in the green (Bodipy, ϕ= 0.89) and in the yellow (Rhodamine 6G, ϕ=0.95) spectral regions were doped in mesostructured films. The blue emission of the periodic mesoporous organosilic (PMO) host overlaps the absorption spectra of the dyes and efficient energy transfer occurred. The PMO containing Rhodamine

6G enabled the WLED production, Table 1.1, by coating a commercial UV LED (390 nm) [95].

More recently, luminescent polyhedral oligomeric silsesquioxane bearing in the structure a dye molecule (belonging to the cyanine family) and a functional amino group suitable for intercalation in cationic layered solids was used to produce a WLED [100]. The hybrid LEDs were patterned by photolithography onto glass substrates. White light emission was observed at 4 V and a significant improvement of the electroluminescent intensity was obtained by increasing the voltage up to 9 V [100].

Monochromatic LEDs were also fabricated based on dye-bridged hybrids [42,43,79,101]. An illustrative example is the functionalization of silsesquioxane cores with pyrene and 4-heptylbenzene that produced green emitting LEDs [101]. The resulting materials offer numerous advantages for OLEDs including amorphous properties, high glass transition temperatures, low polydispersity, solubility in common solvents and high purity via column chromatography. The OLEDs performance was characterized, revealing the high EQE of 3.64 % and CE of 9.56 $cd \cdot A^{-1}$, see Table 1.1. These values represent the highest efficiencies reported up to now for fluorescent silsesquioxane based OLEDs [101].

Table 1.1. Emission CIE (x,y) coordinates, CCT (K), CRI and other relevant parameters used to characterize the quality of a light source (described in Chapter 2) based on dye-bridged organic-inorganic hybrids.

Hybrid precursor	CIE (x,y)	Colour	Other parameters
Si-NABUP [94]	(0.31,0.63)[a)]	yellowish-green light[b)]	L=4000 $cd \cdot m^{-2}$ EQE=1 %
Si-phenylenevinylenediimide [73]	(0.33,0.62)[a)]	yellowish-green light[b)]	L=10 $cd \cdot m^{-2}$
Si-TPPy [95]	(0.32,0.34)	white light[c)]	CCT= 6073 K [a]
Si-Vinylsilsesquioxanes [101]	(0.21,0.45)	green light[b)]	L=367 $cd \cdot m^{-2}$ EQE=3.64 % CE=9.56 $cd \cdot A^{-1}$
Si-PR254/Si-Rh6B [79]	(0.3334,0.3360)	white light[b]	CCT= 5452 K CRI=86.7
Si-PHEMA [42]	(0.31,0.34)	white light[a)]	CCT= 6567 K[a)]
Si-DCM-OH/Si-DADCP [43]	(0.348,0.334)	white light[b)]	CCT=4810 K[a)] CRI=85[a)] η_E=23.7 $lm \cdot W^{-1}$
M4 [102]	(0.22, 0.42)	green light[c)]	L=63 $cd \cdot m^{-2}$
M6 [61]	(0.20,0.37)	bluish-green light[c)]	L=14000 $cd \cdot m^{-2}$
CS-SRG-AC [103]	(0.33,0.32)	white light[c)]	CCT=5622 K[a)]

a) Calculated from the reported emission spectrum.
b) Electroluminescence.
c) UV down-shifting luminescence.
d) Luminescence under microwave irradiation

Other example comprises dye molecules containing trialkoxysilyl terminal groups (Si–PR254 and Si–RhB, Figure 1.3) embedded into silica NPs, yielding fluorescent silica NPs emitting in the red and yellowish-green spectral regions [79].

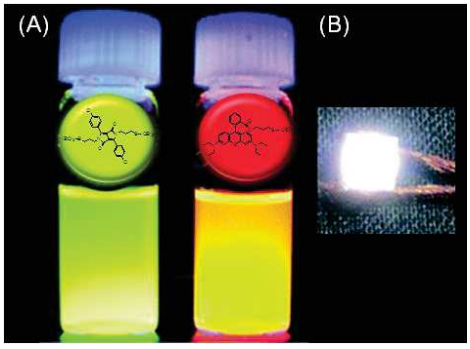

Figure 1.4. Photographs of A) yellowish-green and red fluorescent silica NPs under UV excitation at 365 nm and B) as-prepared fluorescent silica NPs - based WLED (460 nm InGaN blue LED chip encapsulated with fluorescent silica NPs (547 nm and 601 nm)/silicone polymer composite) and the fluorescent silica NPs-based WLED operated at 80 mA. Taken from Jung *et al.* [79].

Combining fluorescent hybrid NPs, Figure 1.4 A, with a commercial blue InGaN LED, leads to the developmet of the WLED, presented in Figure 1.4 B. The resulting three-color RGB LED exhibited a good CRI of 86.7, CCT of 5452.6 K and CIE (x,y) coordinates of (0.3334, 0.3360) [79].

Efficient multi-color light-emitting hybrids were also produced by doping poly(2-hydroxyethyl methacylate-silica hybrids (Si-PHEMA, Figure 1.3) with organoboron dyes emitting in the blue, green and red spectral regions [42]. Pure white light was also attained by controlling the amount of dyes incorporated into the Si-PHEMA hybrids, yielding emission CIE (x,y) coordinates of (0.31, 0.34) and ϕ of 0.47, see Table 1.1 [42].

A third example was reported by Kwak *et al.* [43] involving dye-bridged epoxy functional oligosiloxanes (Si-DCM-OH and Si-DADCP, Figure 1.3) emitting in the green and red spectral regions with ϕ of 0.85 and 0.41, respectively. By controlling the dyes concentration and the ratio between the red and green emitting species, several WLED were produced, using a commercial blue LED as excitation source, Figure 1.5. The best performance of WLED is characterized by a CCT of 4810 K, CRI of 85 and η_E of 23.7 $lm \cdot W^{-1}$, see Table 1.1, being thermal stable, with the CIE (x,y) coordinates remaining unchanged upon heating at 120°C for 1200 h [43].

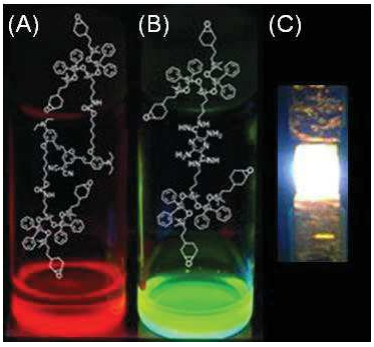

Figure 1.5. Photographs of the dye-bridged oligosiloxanes emitting in the A) red and B) green spectral ranges under UV excitation at 365 nm. C) Photograph of dye-bridged nanohybrid-based WLED. Taken from Kwak *et al.* [43].

Despite the fact that no devices were yet produce, white light emission was recently reported for BSs containing urea or urethane groups modified with [1,3-phenylenebis(1-methylethylidene)]bis(aniline) (BSA) and 4,4´-isopropylidenediphenol (BPA), see Figure 1.3 [96].

The self-assembly of the BSs containing urea or urethane groups matrix was tuned by controlling the rate of the inorganic polycondensation that produces a significant effect on the photoluminescence spectra, the more ordered hybrids display lower emission intensity [96]. In addition monoamidosils (amide cross-linked alkylene–siloxane hybrid materials, Figure 1.3, was doped with variable concentrations of monomethinecyanines, Figure 1.6 [67].

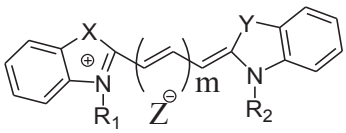

Figure 1.6. Schematic representation of monomethinecyanines where m=0, 1, 3, 5; R_1 and R_2 =H, alkyl, benzyl groups; X and Y= N, O, P, S; Z = I, ClO_4, Cl [67].

The monomethinecyanines were efficiently encapsulated into the hybrid host due to the coordination of the S atoms of the monomethinecyanines to the carbonyl oxygen atoms of the cross-links. The more diluted hybrid materials display white light emission arising from the convolution of the hybrid host intrinsic emission (blue spectral region) with that of the dye (green and red spectral regions). The excitation spectra reveal the occurrence of host-to-monomethinecyanine energy transfer [67].

Another example is the case of different regioisomers of silylated precursors in which the position of the urea functions on the bipyridine moieties was altered (M4, M5 and M6,

Figure 1.3) were used to produce bipyridine-based BS [61,102]. Despite the fact that the emission color for all the hybrids is easily tunable from the blue to the green spectral regions, the distinct nature of the precursor isomers determines the ϕ values of 0.22±0.02 (M4) [102], 0.04±0.01 (M5) and 0.43±0.04 (M6) [61]. These BS hybrids are excited in the UV and near-UV/blue regions, enabling the easy excitation of this material by commercial blue LEDs, inset in Figure 1.7. Under continuous LED illumination (410 nm) the *L* values of 14000 $cd \cdot m^{-2}$, Table 1.1, decrease by a factor of 2 in the first hour of irradiation, see Figure 1.7. After that period, and during approximately 3 h, the *L* values stabilizes [61].

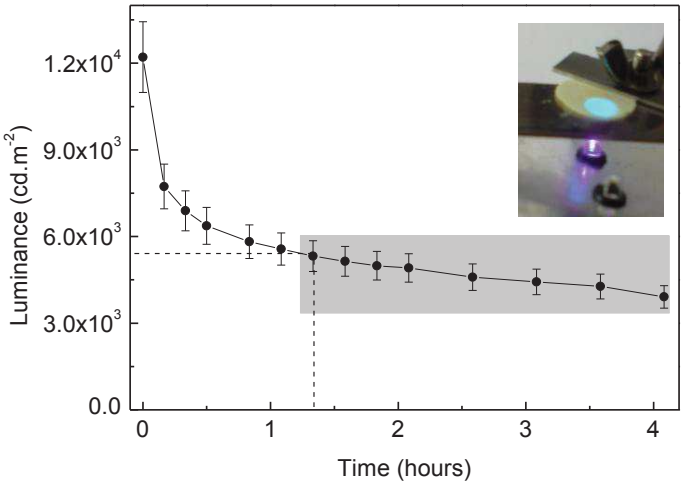

Figure 1.7. Temporal dependence of the luminance values for M6-derived BS under LED irradiation (LED405-33V, operating at 405 nm, 3.9 V and 5.1 mA). The shadowed area identifies the luminance values stable regime under continuous irradiation. The inset shows a photograph of the hybrid excited with the LED405-33V, operating at 405 nm, 3.9 V and 5.1 mA. Taken from Graffion *et al.* [61].

Self-assembly silsesquioxanes containing urea groups were also produced by the polycondensation of a precursor synthesized by the reaction of 3-(anilinepropyl)-trimethoxysilane with 3-(isocyanatopropyl)triethoxysilane (Si-APTMS, Figure 1.3) [97].

Films exhibiting a tunable emission excited from the blue to the red spectral regions were synthesized employing conditions favoring the generation of a broad distribution of cluster sizes [97]. Blue emitters were also attained using BS precursors with m−xylylenediamine (Si-XDA, Figure 1.3) [98].

Another interesting example consists of an organotrialkoxysilane containing an urea group and a dodecyl chain in the organic moiety. The resulting BS was self-assembled

(through strong H–bonds among urea groups and tail-to-tail associations of organic groups) into NPs formed by an agglomeration of crystalline nanorods connected to an amorphous matrix. A colloidal solution of the BS in methanol was used to produce coffee ring structures on the surface of carbon films [104]. The hybrids are blue emitters due to the presence of the silsesquioxanes skeleton with urea groups.

BS hybrid materials were also used to produce pure color emission, as the next examples illustrate in Figure 1.3. Red emission was produced by doping urea-based polysilsesquioxanes (Si-BSA) with Safranine-O [99]. The absence of the blue-green intrinsic emission of the hybrid host indicates efficient hybrid-to-dye energy transfer [99].

A note of caution should be pointed while correlating the performance parameters of the LEDs listed in Table 1.1. In particular, a direct comparison of *L* values arising from electroluminecent devices and UV-LED pumped down–converting phosphors cannot be done because the light generation arises from single electrical excitation and a cascade process involving electrical pumping followed by optical excitation, respectively. Also in the case of light emission generated by the last process the *L* output depends on the LED power used as excitation source.

1.1.2 Dye-doped hybrids

The incorporation of the dyes into the hybrid host also represents an interesting strategy to produce light emitting materials. The incorporaction of the dye molecules (Rhodamine B and Alexa Fluor) into silane precursors, such as tetramethoxysilane, methyltrimethoxysilane, and phenyltrimethoxysilane allowed the production of light emitters, as shown in Figure 1.8. Optical waveguides were produced by lithography and their optical performance was measured revealing absorption and emission features typical of the incorporated dyes. Those hybrids can be used as SSL emitters for low-cost photonic lab-on-chip systems [92].

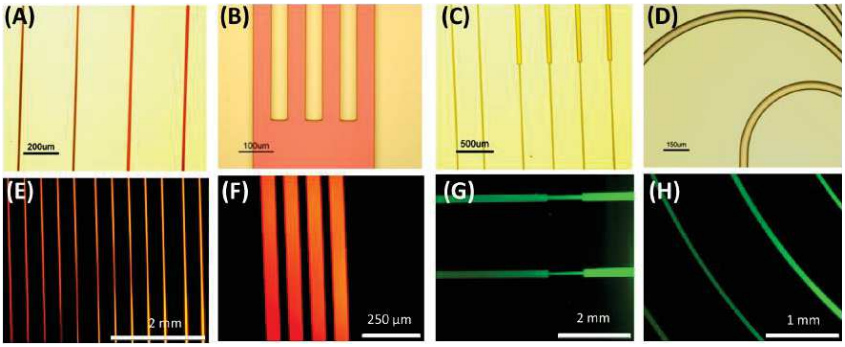

Figure 1.8. (A−D) Bright-field optical and (E−H) fluorescence images of microstructures fabricated using the Rhodamine B doped (panels A, B, E, F) and Alexa Fluor-doped (panels C, D, G, H) xerogel materials. The brighter areas in images G and H come from the residual light emitted by the thick layers of the material created at the sides of the microstructures during the fabrication process. Taken from Carregal-Romero *et al.* [92].

A novel class of white light-emitting hybrids was proposed by the supramolecular co-assembly of organoclays and ionic chromophores [103]. Layered magnesium phyllo(organo)silicate with aminopropyl pendants (AC in Figure 1.9 A) were used as the inorganic counterpart.

The hybrids were co-assembly in solution with organic chromophores (CS and SRG in Figure 1.9 A and B, respectively) yielding gels painted on glass and flexible substrates, Figure 1.9 C. Despite that the hybrid material exhibits pure blue emission centered at 435 nm, white light emission (CS-SRG-AC, Table 1.1) was attained via partial excitation energy transfer to the co-assembled acceptor dye molecules. The hybrid gel retains the blue emission of the free CS molecules, as the fencing of chromophores by the inorganic scaffold minimizes the intermolecular interactions [103,105].

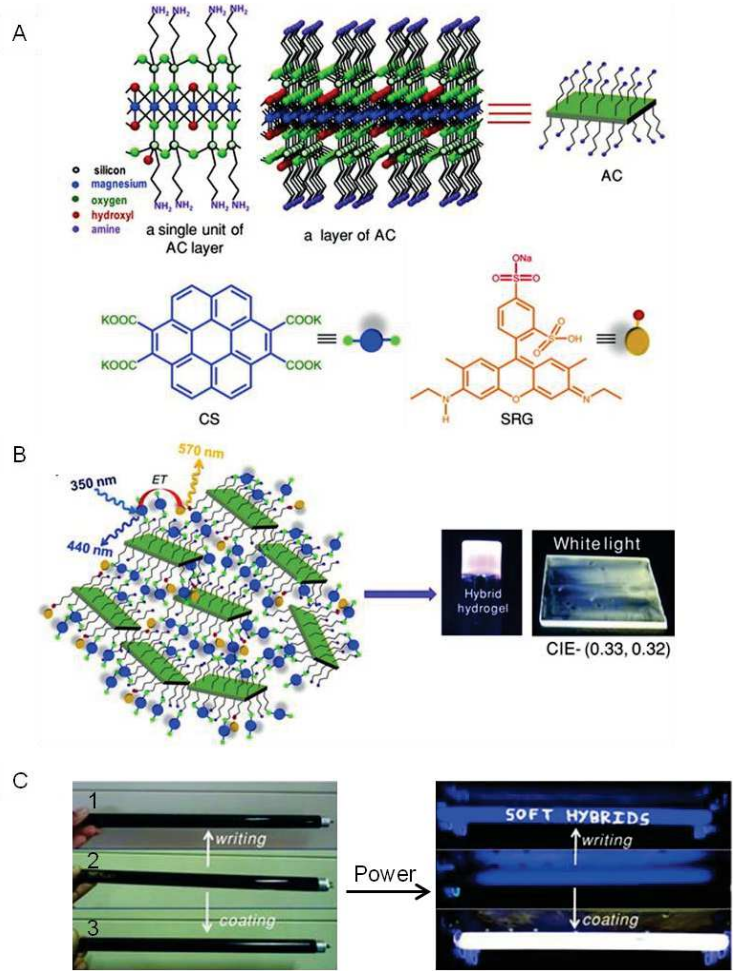

Figure 1.9. A) Molecular structures and schematic representation of the organic and inorganic components (aminoclay (AC), donor (CS) and acceptor (SRG)). B) Schematic representation of the co-assembled clay-chromophore hybrids and of the energy-transfer process. Photographs of the white-light-emitting hybrids in gel and film phases are also shown. C) Hybrids were used to paint and write on commercial UV-lamps (365 nm) 1) written as 'SOFT HYBRIDS' on the surface of the lamp 2) uncoated lamp and 3) lamp fully coated with the soft-hybrids. Taken from Rao *et al.* [103].

The examples presented above describe emission properties governed by the emitting features of the embedded optically active species (dyes). Nevertheless, siloxane-based hybrids lacking the inclusion of external activator centers are able to emit white light, as described next.

1.1.3 Amine- and amide-based hybrids

During the last two decades, a family of amine- and amide-based hybrids, Figure 1.10 of the structure of the respectively hybrid precursors, lacking the incorporation of optically active centers with white light emission visible to the naked eyes, Figure 1.11, have been reported [65,68,106-109].

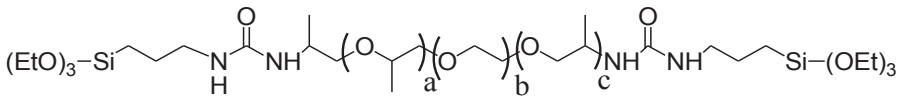

d-UPTES (a+c=2.5, b=40.5, 15.5 or 8.5, are the numbers of OCH_2CH_2 repeats units) [107]

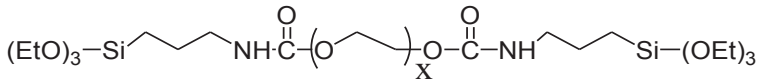

d-UtPTES (x=6 or 45 are the numbers of OCH_2CH_2 repeats units) [68]

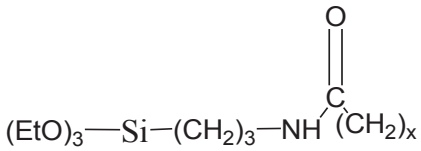

m-ADPTES (x=CH_2 repeats units) [110,111]

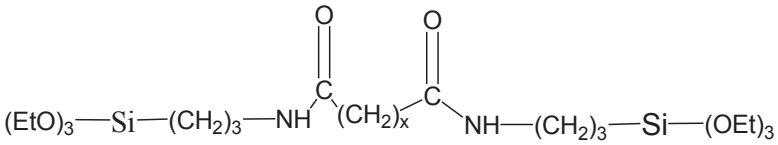

d-ADPTES (x=8, 12, 14 represent the number of methylene groups of the alkylene chain) [65]

Figure 1.10. Molecular structures of siloxane hybrid precursors: d–UPTES=di–ureapropyltriethoxysilane; d–UtPTES=di–urethanepropyltriethoxysilane; m–ADPTES=mono–amidepropyltriethoxysilane; d–ADPTES=di–amidepropyltriethoxysilane.

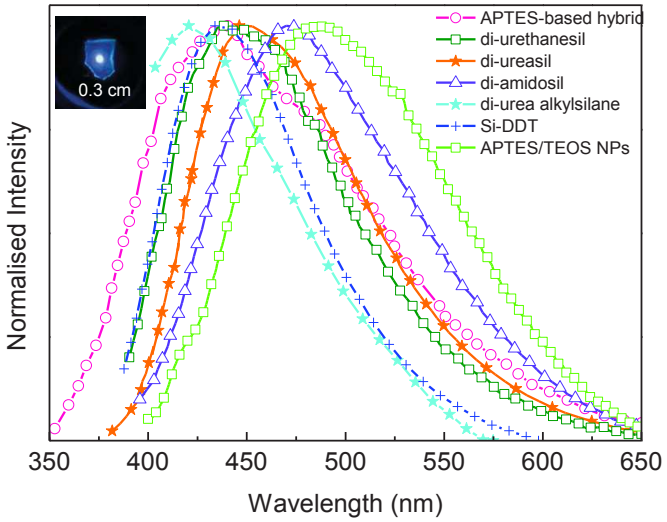

Figure 1.11. Photographs under UV-illumination (365 nm) of di-ureasil. Emission spectra of APTES-based hybrid, di-urethanesil, di-ureasil, di-amidosil, di-urea alkylsilane, silsesquioxane with pendant dodecyl chains and APTES/TEOS NPs. The excitation wavelengths are within 360-375 nm. Adapted from: Green *et al.* [106], Carlos *et al.* [107], Fu *et al.* [68], Nunes *et al.* [65], William *et al.* [109] and Brites *et al.* [108].

Whilst, no reports concerning lighting devices were produced yet, this family of hybrids holds particular interest as distinct synthetic routes based on several precursors have been pursued aiming at enhancing the ϕ values, which is a fundamental parameter concerning new materials for lighting.

The pioneering work of Green *et al.* [106] described the synthesis of organic-inorganic hybrids based on 3-aminopropyltriethoxysilane (APTES) by solvolysis route with a variety of organic carboxylic acids. All the hybrids display similar white light emission, whose ϕ values depend on the carboxylic acid, yielding a maximum ϕ of 0.35±0.10 [106]. Following the same strategy, Bekiari and Lianos reported the formation of hybrid materials through the interaction of APTES with acetic acid [112], whose emission spectra are dependent on the excitation wavelength. Two main emission components were discern in the blue (420-460 nm) and yellow (560 nm) spectral regions with ϕ of 0.21 and 0.12, respectively [112].

Another examples of amide-functionalized hybrids extensively studied in the literature are related with di-ureasil hybrids in which the siliceous skeleton is grafted to polyethylene [68,107,113-115], polypropylene [116] or ethylene chains [98] of different lengths. A squematic representation of the di-ureasil hybrid precursor (d-UPTES) is represented in Figure 1.10.

The di-ureasils were prepared in the absence [113-115] and in the presence of acid (hydrochloric acid, HCl) or basic (ammonium fluoride, NH_4F) catalysts [116] and through

carboxylic acid solvolysis [68,117]. Similarly to that found for APTES derived hybrids [106] the emission spectra are almost independent of the synthesis route [113-115] being, however, observed significant changes in ϕ values. The ϕ values of the hybrids prepared through carboxylic acid solvolysis are, in average, 27-35 % higher than those of the samples synthesized in the absence of a catalyst [107].

The increase in the ϕ values observed for the hybrids prepared through carboxylic acid solvolysis or in the presence of a catalyst with respect to those prepared in the absence of a catalyst was evident in di-ureasils, di-urethanesils [68,107,118], mono-amidosil [110,111] and di-amidosil [65]. A schematic representation of the respectively hybrid precursors (d-UtPTES), (m-ADPTES) and (d-ADPTES) are presented in Figure 1.10.

In the case of the di-urea crosslinked alkylsilane precursor including a dodecyl chain the use of HCl and a large excess of water induced the formation of a crystalline lamellar structure. In contrast, when NH_4F catalyst was employed in ethanol medium under stoichiometric conditions an amorphous material was obtained. The morphology shows a significative impact in the optical proprerties of the materials. The maximum ϕ values achieved at 290 nm was reported to be 0.24±0.02 and 0.14±0.01 for the hybrids prepared in basic and acid catalyst, respectively [69,119].

Silsesquioxane with pendant dodecyl chains (Si-DDT) were produced as flexible films exhibiting a broad visible with a maximum at 422 nm, in which the contribution of at least two different species to the photoluminescence was pointed out [109].

A distinct strategy towards the development of white light emitters lacking metal activator centers, relied on the Ströber method for the processing of siloxane-based organic-inorganic hybrids as NPs [108,120-122]. Luminescent silica spheres functionalized with distinct concentrations of APTES (0-70 mol %) and calcined at 673 K [120,122] and 673−973 K [121] were thus prepared. More recently, it was highlighted that no heat treatment was necessary to produce efficient organosilica based NPs [108].

Recently the synthesis and the luminescence properties of siliceous materials doped with the silicon analogs (Ge, Ti, Zr and Sn) were studied. The nano- and micro-level morphology of the siliceous particles was controlled by the action of polymeric amines (Poly (vinyl amine) (PVA), co(1-vinylimidazole - acrylic acid) (VI-AA) and N-methyl-N,N-bis[3-(methylamino)propyl]amine [tri(1-methylazetane) (N3)). Bright luminescent organo-silica

composites, with lifetimes (τ) values, in the nanosecond time scale, were achieved, see Figure 1.12 [123].

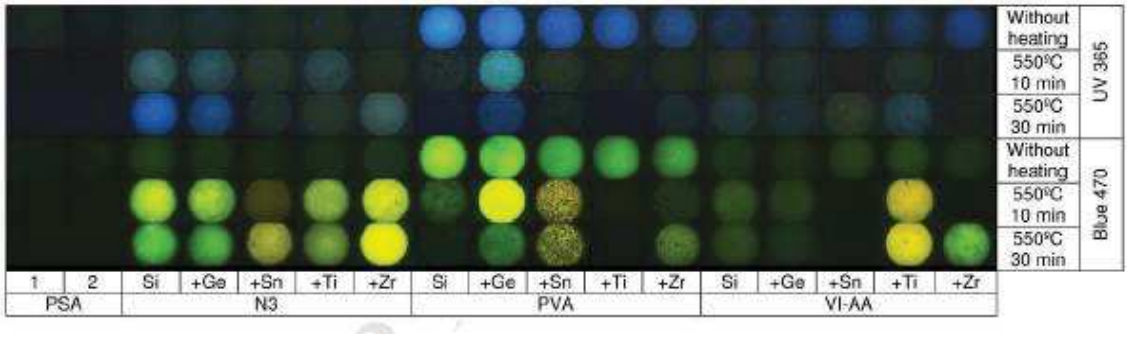

Figure 1.12. Luminescent images of the composite precipitates placed into 96-well array plates. Excitation – 365 nm and 470 nm. PSA: 1 – silica gel for flash chromatography (PSA-1); 2 – silica precipitated from 100 mM sodium silicate with 1 M HCl at pH 5.5 (PSA-2). The conditions of microphotography (power of the lamp, diaphragm, and exposure) were identical in all cases. Taken from Annenkov *et. al.* [123]

Table 1.2 shows a summary of the different synthesis strategies used to prepare selected BS organic-inorganic hybrids and the respective ϕ values.

Table 1.2. Synthesis details: method, catalyst, molar ratio H_2O:ethanol:catalyst, exciation wavelength (λ_{exc}, nm) and ϕ values of representative BS organic-inorganic hybrids.

Materials	Method	Catalyst	Molar Ratio (H_2O:ethanol:catalyst)	λ_{exc}	ϕ	Reference
APTES-based hybrid	Acid catalysis	CH_2O_2	Not reported	365	0.35±0.01	[106]
		$C_2H_4O_2$		360	0.21±0.02	[112]
di-ureasil	Conventional		1.5:4.0:0.0	400	0.07±0.01	[115]
	Acid Solvolysis	CH_3CO_2H	0.0:1.3:1.0	375	0.10±0.01	[68]
		$C_5H_{10}O_2$	0.0:2.4:1.0			
di-urethanesil	Conventional		1.5:4:0.0	400	0.12±0.01	[124]
	Acid Solvolysis	CH_3CO_2H	0.0:1.3:1.0		0.20±0.01	[68]
		$C_5H_{10}O_2$	0.0:2.4:1.0			
mono-amidosil	Conventional		2.0:4.0:0.0	360-380	0.10±0.01	[110]
	Acid catalysis	HCl	600.0:0.0:0.2		0.15±0.01	
			300.0:0.0:0.2		Not reported	
			100.0:0.0:0.1			
di-amidosil	Conventional		2.0:4.0:0.0		0.05±0.01	[65]
di-urea crosslinked alkylsilane	Basic catalysis	NH_4F	6.00:60.00:0.01	290	0.24±0.02	[119]
	Acid catalysis	HCl	600.0:0.0:0.2		0.14±0.01	
Si-DDT	Acid Solvolysis	CH_2O_2	-	-	-	[109]
APTES/TEOS NPs	Basic catalysis	NH_3	3.2:0.0:1.0	300-385	0.12	[120]
			3.6:24.8:1		0.05	[121]
			3.4:16.0:1.0		0.09	[122]
			0.0:10.0:1.0		0.15±0.02	[108]

$C_2H_4O_2$=Acetic acid; CH_2O_2=Formic acid; $C_5H_{10}O_2$=Valeric acid APTES=3-aminopropyltriethoxysilane; d-UPTES=di-ureapropyltriethoxysilane; d-UtPTES=di-urethanepropyltriethoxysilane; m-ADPTES=mono-amide-propyltriethoxysilanes; d-ADPTES=di-amidepropyltriethoxysilanes; DDT=dodecane thiolate.

.

1.2 Objectives and organization of the thesis

The major objective of this thesis aims the development of BS organic-inorganic hybrids with potential applications in "green" photonics, such as white light emitters and luminescent solar concentrators (LSC).

During the last years it has been highlighted the potential contribution of BS organic-inorganic hybrids, without metal activator centers, in "green" photonics [65,66,68,97,102,106-108,115,117,120,125-131], due to high ϕ values, stability over time under irradiation and the ability to be excited with economic light sources [8].

In the framework of the above contextualization, the first chapter summarizes the state of the art of BS organic-inorganic hybrids which present intriguing white light emission properties. The revision of the state of the art was focus in BS organic-inorganic hybrids embedding organic dyes, with the formation of covalent or non-covalent, dye-matrix interactions, and functionalized with amine or amide groups, without any chromophore fragment.

Chapter 2 deals with the background concepts used along the thesis. Three different aspects were focused:

- fundaments of sol-gel methodology (used to prepare the materials developed in this thesis);
- light emission quantification parameters used to evaluate the performance of the materials: (CCT, CRI, CIE (x,y) coordinates, Radiance (R), *L* and ϕ);
- electronic structure and energy levels of Eu^{3+} (used to generate monochromatic emission in this thesis).

The following chapters are dedicated to the synthesis description and structural/photoluminescence characterization of BS organic-inorganic hybrids, in order to get more information about the local structure and optical properties of these materials.

Figure 1.13 shows a schematic representation of the six different BS hybrid precursors studied here.

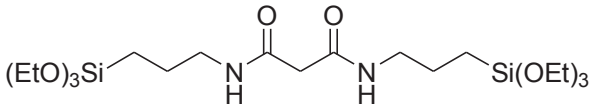

P2-m

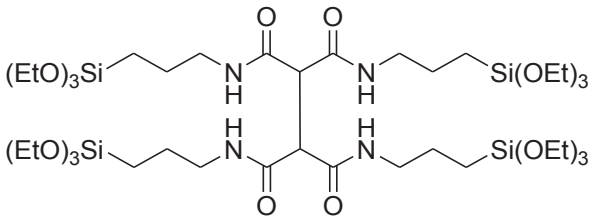

P4-m

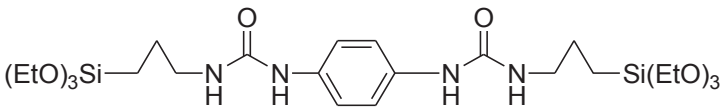

P(UU)

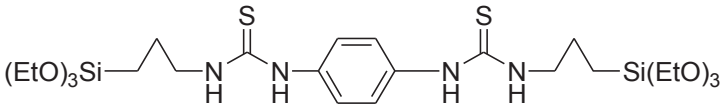

P(TT)

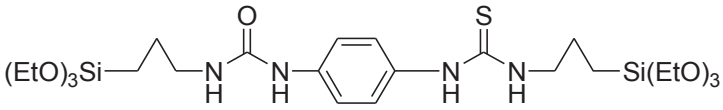

P(UT)

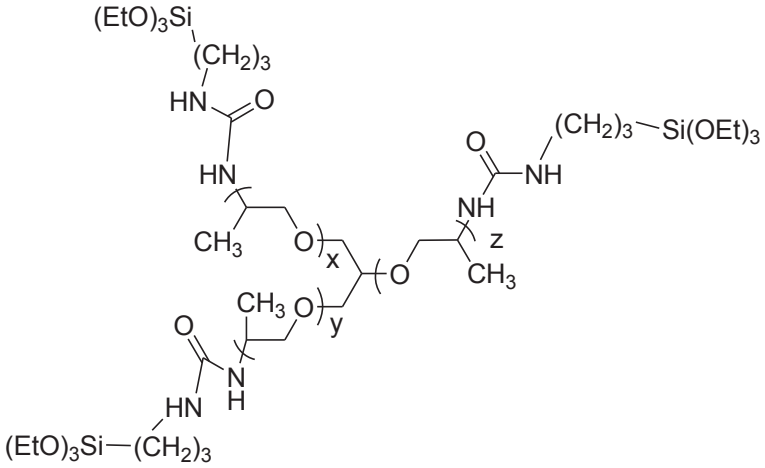

t-UPTES (5000), (x+y+z)=85

Figure 1.13. Molecular structures of BS hybrid precursors developed in this thesis.

In Chapter 3, two families of BS organic-inorganic hybrid based on malonamide group are presented: the **malonamide BS** and **di-malonamide BS** materials were obtained from hybrid precursors **P2-m** and **P4-m**, respectively see Figure 1.13. The linear geometry of these systems is based on malonamide group linked to the siliceous skeleton through a propyl group. While a single malonamide group is present in **malonamide BS**, the **di-malonamide BS** is formed through H−bond interactions linking the two malonamide groups.

In Chapter 4, BS organic-inorganic hybrids based on amide and thioamide groups originating three distinct systems: **di-amide cyclohexane BS**, **di-thioamide cyclohexane BS** and **amide-thioamide cyclohexane BS,** which were obtained from linear hybrid precursors **P(UU)**, **P(TT)** and **P(UT)**, respectively, represented in Figure 1.13. The replacement of the urea by thiourea group should induces great modifications in the H−bonds interactions, which are the main responsible for the self-assembling of the materials. The impact of the H−bonds interactions, on the local structure and physical properties of the materials are evaluated. In crystalline organic model compounds self-structures via H−bonds and their corresponding organic-inorganic hybrids resulting from both H−bonding and siloxane condensation. A transcription between local structure and optical/mechanical properties observed in organic model compounds and hybrid materials are performed.

In Chapter 5, **tri-ureasil BSs** with branched geometry, based on urea group are presented. The tri-ureasil prepared under acidic conditions (pH=2) reported in a previous work presents low ϕ values (0.01±0.001). Aiming to enhance the ϕ values, we decided to modify the synthesis procedure using two different synthesis strategies, (1) variation of the concentration of HCl and water content and (2) control of the atmosphere conditions during the sol-gel reactions. The local structure and optical properties of the resulting materials were studied. The chemical/physical mechanisms responsible for the intrinsic emission in **t-U(5000)** was also evaluated. Knowing the origin of the emission we are more able to improve the emission properties and then develop materials with tuneable optical properties. The presence of a new emission component (peaking at 300 nm) that appears under UV-excitation (no reported before for amine- amide- functionalized hybrids) was studied throught comparison between emission properties of organic and inorganic model compounds. In addition, the origin of the recombination mechanisms responsible for the emission in the tri-ureasils was also studied.

The final goal of this thesis, discussed in Chapter 6, foresees the incorporation of Eu^{3+} and of the organic molecule 2-thenoyltrifluoroacetone ligand (tta–H) into BS organic-inorganic hybrids based on malonamide and di-malonamide. The local structure was evaluated in order to study the coordination between Eu^{3+}-local coordination in the hybrid host. The Eu^{3+}-based di-malonamide materials were used as optical active layer in LSCs whose performance was evaluated.

Finally, in chapter 7 the general conclusions and future perspectives are presented.

2. Background

2.1 Sol-Gel Process

The development of new materials combining different components in one system is one of the most expanding fields in materials chemistry [72,132]. In particular, the mild and polyvalent synthetic conditions offered by the sol–gel process, such as, low temperature processing and shaping, availability of numerous metallo-organic precursors, high sample homogeneity and purity of the precursors and the processing versatility of the method, allow the synthesis of multifunctional organic–inorganic hybrid structures [56,72,132-142].

The combination of the appropriate processing conditions with the adequate choice of the organic and inorganic components dictates the morphology, molecular structure, and the properties of the final hybrid materials [141]. In this thesis all the samples were prepared by the sol-gel process. Therefore, fundamental aspects of this process are described in the next subsection.

2.1.1 Fundamental aspects

The sol-gel process is based on the formation of a colloidal suspension (sol) and on the gelation of the suspension to form a three dimensional network (gel) [139]. The preparation of the materials can be summarized in the following steps [143]:

- synthesis of the material from hydrolysis and partial condensation of alkoxides;
- formation of the gel via polycondensation to form metal-oxo-metal or metal-hydroxy-metal bonds;
- aging, where condensation continues within the gel network, often shrinking it and resulting in expulsion of the solvent;

- drying the gel either to form a dense 'xerogel' via collapse of the porous network or an aerogel for example through supercritical drying.

While the above steps are common to most of the sol-gel processes, the nature of the specific reactions involved in hydrolysis and condensation reactions differ substantially between the various types of precursors [144]. Because of their high reactivity with water, metal alkoxides $Si(OR)_n$, where R represent the alkyl group and *n* the number of alkoxy group linked to Si, in particular TEOS, are the most widely used precursors in the sol–gel process [141].

The final product of the sol–gel process depends on several aspects such as:

- the electronegativity between the oxygen and the metal atoms, affecting the ionic character of the metal-oxygen bond;
- the electron donating/withdrawing ability of the alkyl/aryl chain, that has reflection on the stability of the alkoxy groups.

Both of these factors influence the relative rates of hydrolysis and condensation and the degree of oligomerization or polymerization [143].

The hydrolysis reactions, during which alkoxy groups (-OR) are replaced by hydroxy groups (-OH) with a pentacoordinate transition state, occur in both the acidic (Scheme 2.1) and basic (Scheme 2.2) catalyzed systems [143]. In the acidic catalysis, the alkoxy groups are easily protonated. As electron density is withdrawn from silicon, it gets more electrophilic, thus more prone to react with water molecules. In addition, the alkoxy becomes a better leaving group upon protonation.

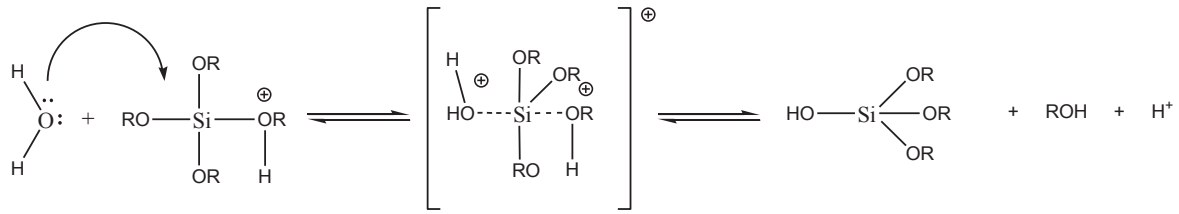

Scheme 2.1. Acidic catalyzed hydrolysis of silicon alkoxy. Taken from Danks *et al.* [143].

Under basic conditions, the hydroxy ions replace water as nucleophilic agent, due to their higher nucleophilicity, (Scheme 2.2).

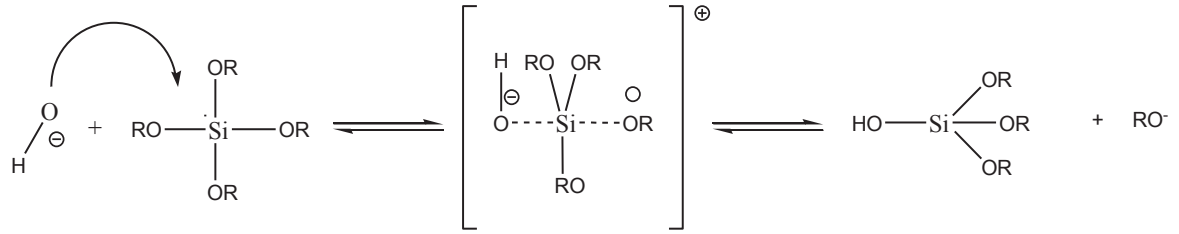

Scheme 2.2. Basic catalyzed hydrolysis of silicon alkoxy. Taken from Danks *et al.* [143]

Through a condensation reaction, the silanol groups react to produce siloxane bonds (Si-O-Si) and alcohol (ROH) or water. Also the condensation can be catalysed by either acidic (Scheme 2.3) or basic (Scheme 2.4) catalysis [143]. The progression of the condensation depends on the degree of hydrolysis. If hydrolysis is complete before the first condensation step, the resulting product is $(OH)_3Si\text{-}O\text{-}Si(OH)_3$ with 6 sites for subsequent condensation steps. Multiple condensation steps result in small, highly branched agglomerates in the "sol" which eventually crosslink to form a colloidal gel. In acidic conditions, where the first hydrolysis step is typically the fastest, condensation begins before hydrolysis is complete.

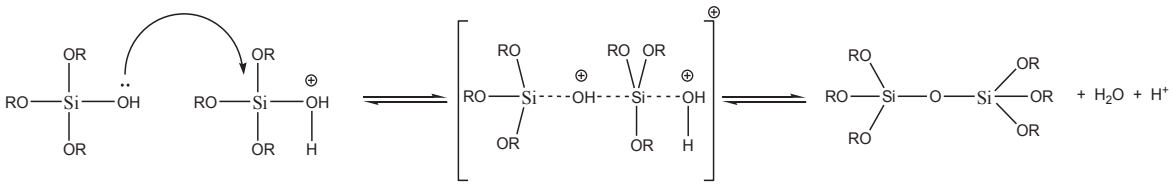

Scheme 2.3. Acidic catalysed condensation of silicon alkoxy. Taken from Danks *et al.* [143].

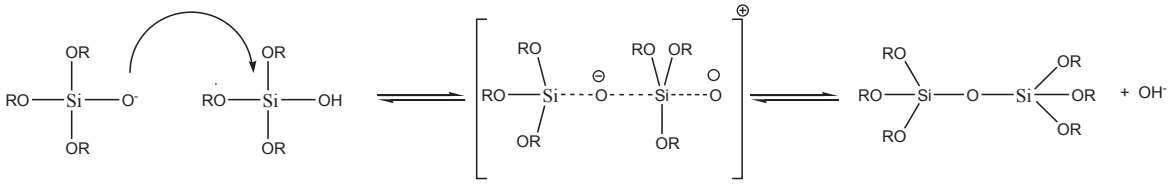

Scheme 2.4. Basic catalysed condensation of silicon alkoxy. Taken from [143].

The differences between acidic and basic catalyzed reactions and the consequences for particle morphology are conceptually represented in Figure 2.1. In a basic solution, particles grow in size with decrease in number; in acidic solution particles tend to aggregate into three-dimensional networks and form gels.

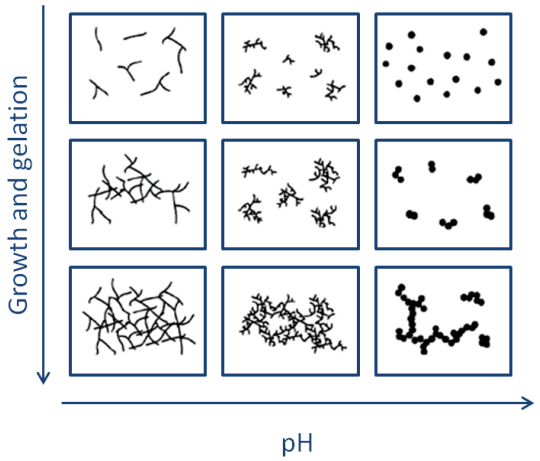

Figure 2.1. Diagram showing how pH affects the growth and structure of a gel. Adapted from Danks *et al.* [143].

The pH value is a very important factor in the rates of hydrolysis and condensation rates, Figure 2.2. While hydrolysis is accelerated by acidic catalysts, condensation is faster in

the presence of basic catalysts. In contrast with the situation found with acidic catalysts, basic catalyst promotes condensation at a relatively early stage.

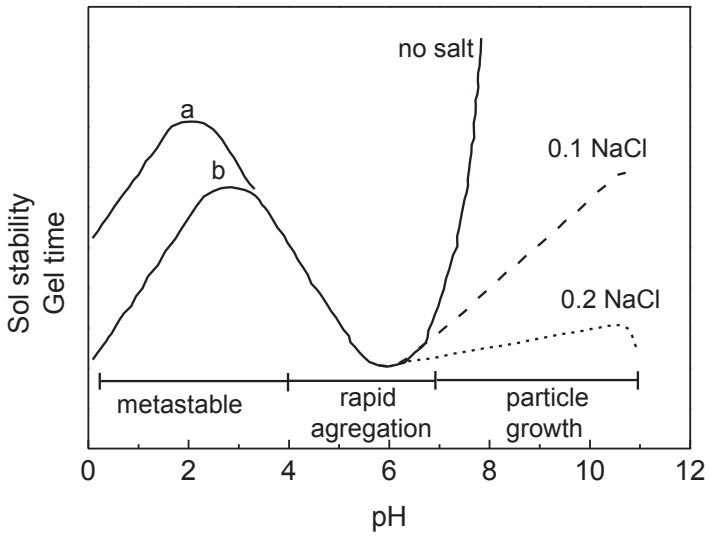

Figure 2.2. Scheme illustrating the effect of the pH in a colloidal silica-water system, where *a* and *b* represent low (0.1 parts-per million) and high (10 parts-per million) amount of hydrofluoric acid, respectively. Adapted from Brinker *et al.* [139].

The rate of an acidic catalysed hydrolysis is governed by the concentration of H^+ in the solution. The faster hydrolysis promotes the formation of short linear chains and induces a rather weak polymer network. In the case of basic catalyzed hydrolysis, the reaction rate is function of the hydroxyl concentration in solution. The hydrolysis reaction is slow and is a rate-determining step, whereas the condensation is relatively fast. This type of condensation favours the formation of highly cross-linked polymers or colloidal particles. The mechanisms described so far are applicable only when dealing with HCl *vs* NH_4OH-catalyzed reactions.

Gelation may occur after the sol (or colloidal suspension of solid particles in a liquid) is cast into a mold, allowing objects of a required shape to be made. Bond formation does not stop at the gel point.

Aging is the process of change in structure and properties that take place after gelation. Aging may involve further condensation, dissolution, and reprecipitation of monomers and oligomers, or phase transformations within the solid and liquid phases [141]. Drying under normal conditions is accompanied by shrinkage of the gel network. The resulting dried gel, usually called xerogel, is reduced in volume by a factor of 5–10 compared to the original wet

gel [141]. If the wet gel is dried under supercritical conditions, the shrinkage will be minimum and the resulting product will be called aerogel. When the smallest dimension of the gel is greater than a few millimeters the material is usually classified as a monolith. If, however, gelation occurs through rapid evaporation of the solvent, films and fibers are obtained.

2.1.2 Classification of organic-inorganic hybrids and design strategies

It is well known that the structure, degree of order, and general features of these nanosized systems depend not only on the chemical features of the organic and inorganic components, but also on the interactions which are established between them. Based on the type of interactions occurring between organic and inorganic components we can divide the large class of hybrids into two distinct subclasses, usually designated as Class I and Class II. **Class I** includes the hybrid materials where both components are linked through weak interactions, such as van der Waals contacts, hydrogen bonds (H−bonds) or electrostatic forces. In **Class II**, at least a proportion of the organic and inorganic components of the hybrids are linked through strong chemical bonds (covalent and ion-covalent), which is the case of the hybrid materials developed within the framework of this thesis.

The inherent flexibility of the sol-gel method, allows the implementation of several design strategies, commonly designated by route A (the one that will be followed in this thesis), route B, route C and route D [56,72,132,136].

Route A: soft chemistry-based approaches including the conventional sol-gel chemistry from specific bridged and polyfunctional precursors and hydrothermal processes. Amorphous hybrid networks are obtained by conventional sol-gel pathways through hydrolysis-condensation of various metal species (alkoxydes/halide derivatives) which can be organically modified. This route is simple, low cost and yield amorphous materials. The materials are cheap, versatile, transparent and contain interesting properties that give rise to commercial products that can be process as monoliths, powders or films. However, they are polydispersed in size and locally heterogeneous in chemical composition. Thus, an important task is the improvement on the control of the local structure and their degree of organization. Two main approaches are used to achieve such control:

- The use of bridge precursors (such as silsesquioxanes - $X_3Si\text{-}R'\text{-}SiX_3$, where R' represent the organic spacer and X=Cl, Br, -OR), where the organic bridge allows the improvement of the interaction and yield materials with better degree of organization. This strategy can be complemented by using functional groups like urea type [69,145,146], allowing better self-assembly through the ability of the organic moieties to establish both strong H–bond networks and efficient packing via π–π or hydrophobic interactions [69,145,146].
- Hydrothermal synthesis performed at moderate temperatures (20–200 °C) in polar solvents (water, formamide, toluene, alcohol, dimetilformamida…) of metal organic frameworks. Metal organic frameworks constitute a very interesting class of hybrid materials with high and tunable porosity and crystalline architecture. Applications of these materials [147] in the fields of gas absorption [148], separation or purification, luminescence [149], catalysis or nanomedicine [150] are being developed.

Route B: assembling or dispersion of well-defined nanobuilding blocks that consist of perfectly calibrated preformed objects that keep their integrity in the final material. Examples of materials obtained using this route are: clusters [151], organically pre- or post-functionalized NPs, nano-core shells or layered compounds able to intercalate organic compounds [72]. These materials have commercial applications, such as nanofillers in the *Green Tyres* developed by Michelin company through a collaboration with Rhodia [72].

Route C: well known self-assembly process [152], which consists in the organization of growing inorganic or hybrid networks through the use of an external templates, such as micelles. These inorganic or hybrid phases can be generated from precursors previously described in route A or B [55], high control and tuning of the hybrids interfaces, and leads to a whole continuous range of nanocomposites, from ordered dispersions of inorganic bricks in a hybrid matrix to highly controlled organic polymers within inorganic matrices.

Route D: so-called integrative synthesis [55,72] and offers the controlled design and assembling of hybrid materials in the 1 Å to 500 Å range. Micromolding methods have been developed, in which the use of controlled phase separation phenomena, emulsion droplets, latex beads, bacterial threads, colloidal templates or organogelators enable control of the shape of complex objects at the microscale [55,72]. This strategy, when combined with routes A, B and C, allows the building of hierarchically organized materials in terms of construction and function.

2.2 Quantification of light emission

To characterize the physical properties of the light and color sensation by the human eye, radiometric/photometric units are required. The η_E, R, L, and ϕ values allows an accurate comparison between different materials [140].

The luminous intensity is a photometric quantity, which represents the light intensity of an optical source, as perceived by the human eye. The luminous intensity is defined as a monochromatic light source emitting an optical power of (1/683) Watt at 555 nm into the solid angle of 1 steradian (sr) has a luminous intensity of 1 candela (cd). The luminous flux, which is also a photometric quantity, represents the light power of a source as perceived by the human eye. The unit of luminous flux is the lumen (lm) and it is defined as a monochromatic light source emitting an optical power of (1/683) Watt at 555 nm has a luminous flux of 1 lumen (lm).

The luminous efficacy (lm W^{-1}) of a light source is a measure of how well a light source produces visible light and is given by the ratio between the luminous flux (lm) and the electric power (W). In the lighting community, luminous efficiency is often referred to as luminous efficacy of the source. For light sources with a perfect electrical power to optical power conversion, the luminous efficiency is equal to the luminous efficacy.

The Radiance ($W \cdot m^{-2} \cdot sr^{-1}$) measures the quantity of radiation that passes through or is emitted from a surface and falls within a given solid angle in a specified direction. When radiance is weighted by the human eyes sensitivity, *L* values ($cd \cdot m^{-2}$) are reported.

The absolute emission quantum yield is an experimental evaluated quantity given by the ratio of the number of emitted photons over the number of absorbed ones [54]. The experimental measurement of emitting and absorbing photons is accurately performed with an integrating sphere and a calibrated detector setup.

Besides luminous efficacy, Radiance, Luminance and absolute emission quantum yield, three others parameters are used to characterize the quality of a light source are the following: CIE (x, y) coordinates, CRI and CCT values.

The CIE (x,y) coordinates are usually calculated using the system proposed in 1931. This procedure is based on the human eye response to the visible light, where there are three cone cells responsible for the color distinction. Each cone cell presents a different sensibility, designated as $\bar{x}_\lambda$, $\bar{y}_\lambda$ and $\bar{z}_\lambda$ with maximum values at ~ 419 nm, 531 nm and 558 nm,

respectively. The sum of the three cone sensitivity functions is called the photonic response and displays a maximum sensibility centered at 555 nm, in the green spectral region. The $\bar{x}_\lambda$, $\bar{y}_\lambda$ and $\bar{z}_\lambda$ are called the CIE color-matching functions. In addition, the CIE defined three new primary colors X, Y and Z, needed to match any specific colors. These quantities, X, Y and Z, are known as tristimulus values. These primary colors established by the CIE have a great advantage when compared with other color systems, since the color-matching functions do not display negative parts. The emission is weighted by the $\bar{x}_\lambda$, $\bar{y}_\lambda$ and $\bar{z}_\lambda$ functions in order to determine the X, Y and Z primary color though the following equations set:

$$\begin{cases} X = \int_i \bar{x}_i . E_i d\lambda \\ Y = \int_i \bar{y}_i . E_i d\lambda \\ Z = \int_i \bar{z}_i . E_i d\lambda \end{cases} \qquad 2.1$$

where E stands for the emission spectra intensity and i represents the emission wavelengths. To simplify the calculus, the spectra can be divided in small wavelength intervals, (usually = 5 nm or 10 nm), that can be rewritten as:

$$\begin{cases} X = \sum_{\lambda=380}^{720} \bar{x}_\lambda . E_\lambda \Delta\lambda \\ Y = \sum_{\lambda=380}^{720} \bar{y}_\lambda . E_\lambda \Delta\lambda \\ Z = \sum_{\lambda=380}^{720} \bar{z}_\lambda . E_\lambda \Delta\lambda \end{cases} \qquad 2.2$$

To make the color perception easier, the tristimulus are converted into a two dimensional system, through a linear transformation. The tristimulus are transformed into chromaticity coordinates, (x,y), that are plotted in a two dimensional chromaticity diagram, see Figure 2.3.

The color coordinates are related to X, Y and Z by:

$$\begin{cases} x = \dfrac{X}{X+Y+Z} \\ y = \dfrac{Y}{X+Y+Z} \end{cases} \qquad 2.3$$

The (x,y) chromaticity diagram has particular characteristics:

- center of the diagram is taken as the white point (0.33,0.33);
- curve that is made of pure colors from the blue to the red, covering the entire spectral visible range (380-730 nm), is designated as spectral locus;
- straight line that connects the two extremes of the spectral locus is denominated as purple boundary. The colors represented by the purple boundary are not pure colors, as they include a mixture of pure red and blue.
- area circumscribed by the diagram, spectral locus and purple boundary, encloses the domain of all colors. The CIE tristimulus X, Y and Z do not belong to the spectral locus, and therefore they do not represent real colors. This is a direct consequence of the postulate that states that any visible color can be obtained by adding only positive quantities of X, Y and Z.

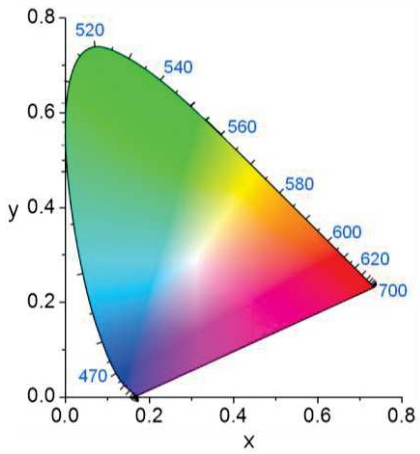

Figure 2.3. The CIE (x,y)-chromaticity diagram 1931.

CRI is a number ranging from 0 to 100 that is the quantitative measure of the ability of a light source to faithfully reproduce the color of an object, in comparison with a blackbody (or Planckian) light source [29]. The CRI of a typical incandescent lamp is 100, whereas the

typical values of fluorescent tubes and inorganic WLEDs are around 75, values lower than 70 are unacceptable for indoor lighting applications [31]. CRI values over 80 can be readily obtained using OLEDs, illustrating one of the advantages of using OLEDs as high quality broad-band light sources [29]. CRI is calculated using eight illuminated object in CIE 1995 color space when illuminated by a given light source [153]. As greater the difference in the appearance of the color of the illuminated object relative to the lower standard will be the CRI.

CCT is the temperature of a blackbody radiator emitting the same color of the light source [29]. In general, CCT values ranging from 2500 to 6500 K are required for lighting, incandescent lamps have CCT values of ~2700 K (warm white) and fluorescent lamps between 3000–4000 K (cool white) [43]. Suppose the epicenter of convergence is at the point on the chromaticity diagram (x_e, y_e) with x_e= 0.3320 and y_e = 0.1858. If we draw a line from this point to a point (x, y) on the Planckian locus, we obtain the CCT value. The tangent of the angle (t) between the y axis and this line is the reciprocal of the slope and given by the following equation [154]:

$$t = \frac{(x - x_e)}{(y - y_e)} \qquad 2.4$$

The CCT values can be calculated through the following polynomial function [154]:

$$CCT = at^3 + bt^2 + ct + d \qquad 2.5$$

where a= 449, b= 3525, c=6823.3 and d= 5520.33.

2.3 Electronic structure and energy levels of lanthanide ions

In recent years, a significant amount of research has been focused on the possibility of using hybrid frameworks incorporating Ln^{3+} as matrices in optical active devices. In this thesis, the materials studied in Chapter 6 have been synthetized through sol-gel process incorporating Ln^{3+} for their specific luminescence properties. In the following we will describe the electronic structure of lanthanide.

The rare earth elements are characterized by the progressive fulfillment of the 4*f* and 5*f* atomic orbitals and are divided in two groups: Ln and actinides (Ac). The Ln^{3+} have a base electronic structure common to that of Xenon, $1s^2 2s^2 2p^6 3s^2 3p^6 3d^{10} 4s^2 4p^6 4d^{10} 5s^2 5p^6$ with two or three valence electrons ($6s^2$ or $5d^1 6s^2$) and the progressive fulfilment (with the increase of the atomic number) of the 4*f* orbitals.

This group consists of 15 elements with atomic numbers 57 through 71, from lanthanum to lutetium. In the solid state, these elements originate, in general, ions triply ionized, which involves the variation of the number of valence electrons (N) between N=1 and N=14 (N=6 in the case of Europium, Eu^{3+}). The first ionization state of Ln^{3+} results from the removal of one electron 6*s*, lutetium is the only exception. The second state of ionization corresponds to the removal of another 6*s* electron. Finally, the third ionization state, which is the general state usually observed for these elements, occurs with the removal of 6*s* and 5*d* electrons and, frequently, also, one 4*f* electron. This electronic structure is responsible for the transitions between states of the $4f^N$ configuration [155].

The first emission and excitation spectra of compounds based on Ln^{3+} were observed by Becquerel in 1908 [156]. At low temperature, the emission and absorption spectra are, in general, characterized by sharp and well defined lines. These lines, comparable to the spectral lines of atoms and free molecules, result from the splitting of the energy levels of the $4f^N$ configuration, by action of the electrostatic field generated by the surrounding ligands. The quasi-atomic nature of the spectra suggests that the interaction between the ion and the ligands is small compared, for instance, to observe in the transition metals. This fact is consistent with the delocalization of the $4f^N$ orbital inside the $5s^2$ and $5p^6$ orbitals, the $4f^N$ electrons being shielded by those external orbitals. This shielding effect allows treating the local-field interaction as a perturbation to the atomic levels energy of the 4*f* orbital. These elements have, accordingly, a small ability to participate in the formation of chemical bonding. The delocalization of the 4*f* shell is known as Ln^{3+} contraction [157].

Table 2.1 presents, as an example, the energy terms (multiplets) of the $4f^6$ configuration for Eu^{3+} expressed in the Russel-Saunders coupling scheme.

Table 2.1. Multiplets of the configuration $4f^6$.

Configuration	Multiplets	Total number of multiplets
	^{1}S P D F G H I K L M N ^{3}P D F G H I K L M N O	
	4 64 84 7 34 2 2 6 59 7 9 663 3	
f^6	^{5}P D F G H I K L ^{7}F	119
	3 23 22	

In this notation, the orbital angular momentum of the individual electrons add to form a resultant orbital angular momentum *L*. Likewise, the individual spin angular momenta are coupled to produce a resultant spin angular momentum *S*. Then *L* and *S* combine to form the total angular momentum *J*, with J_Z being its z component:

$$J = \begin{cases} |S+L|, \dots S-L \Leftarrow S > L \\ L+S, \dots L-S \Leftarrow S \leq L \end{cases} \quad 2.6$$

In the Russel-Saunders coupling scheme, the terms *L* and *S* define one of the (2S+1)(2L+1) terms (or multiplets) of the configuration, generic represented by $^{(2S+1)}L_J$, in which (2S+1) indicates the spin multiplicity.

The numbers (bold) under the different terms in Table 2.1 indicate the number of multiplets described by the same values of *L* and *S*, showing that these numbers are not sufficient to individually classify each energy term.

Each of these energy levels can be represented by a barycenter corresponding to the average of the energy. This average energy level is represented by the Hamiltonian of the free ion H_{FI}, which describes the interactions between the N electrons of the 4*f* shell, as the other shells are completely filled. To a first approximation the effect of the filled electronic shells (or subshells), which are spherically symmetric, is the same for all the terms of the $4f^N$ configuration. The H_{FI} is composed by one part due to the central field, H_0, that shift all the possible *f* configurations with N electrons as a whole, and by several other interactions, which are generally treated as perturbation:

$$H_{FI} = H_0 + H_c + H_{SO} \quad 2.7$$

Among these interactions the interelectronic repulsion, H_c and the spin-orbit interaction, H_{SO}, are the most relevants [158]. The relative magnitude of the different interactions follows the order: $H_0 > H_c > H_{SO}$. Being so, in a first approximation, H_{FI} can be written as the sum of the term corresponding to the interaction between the N electrons and the term relative to spin-orbit interaction.

Even though the interaction between the 4*f* electrons and the chemical environment is small it is responsible for the optical properties of the Ln^{3+}. On placing a Ln^{3+} in a given chemical environment (crystal, glass, solution), the spherical symmetry of the free ion is destroyed and each spectroscopic level splits under the influence of the asymmetric electric field produced by the environment. This is termed the crystal, or ligand, field effect. The interaction between the ions and the environment is written in terms of a local field Hamiltonian, H_{LF}, which translates the breaking of the symmetry levels of the free ion. This symmetry breaking gives rise to the field degeneracy removal, in maximum of $(2J+1)$ components for integer values of *J*. Each component of the local field is characterized by the quantum number J_Z. The breaking of degeneracy by a field generated by the ligands around the ion is called Stark effect, which is dependent on the local symmetry group around the ion in the host, as shown in Table 2.2.

Table 2.2. Splitting observed in each of the *J* level (integer) for the 32 groups of symmetry.

Crystallographic system	***J***						
	0	**1**	**2**	**3**	**4**	**5**	**6**
Cubic	1	1	2	3	4	4	6
Hexagonal and Trigonal	1	2	3	5	6	7	9
Tetragonal	1	2	4	5	7	8	10
Triclinic, monoclinic and orthorhombic	1	3	5	7	9	11	13

* **Cubic**: O_h, O, T_d, T_h, T; **Hexagonal**: D_{6h}, D_6, C_{6h}, C_6, D_{3h}, C_{3h}; **Tetragonal**: D_{4h}, D_4, C_{4v}, C_{4h}, C_6, D_{2d}, S_4;**Trigonal**: D_{3d}, D_3, C_{3v}, C_3, S_6; **Orthorhombic**: D_{2h}, D_2, C_{2v}; **Tetragonal**: C_{2h}, C_2, C_s (or C_{1h}); **Triclinic**: S_2 (or C_i), C_1.

The number of splitted components increases with the decreasing symmetry of the ion surroundings. This happens because the decrease of the symmetry corresponds to a decrease of the number of equivalent directions, or, in other words, the charge distribution around the ion becomes less spherical (characteristic of the free ion). Consequently, the interaction

between the ion and the charge distribution around will provoke a splitting of the free ion levels.

The ligand field interaction is also of fundamental importance in the case of 4*f*-4*f* transition intensities. Since we are concerned with optical transitions, two operators can perform the transition: the electric dipole operator and the magnetic dipole operator. The 4*f*-4*f* transitions are in principle electric dipole forbidden by Laporte's rule which states that electronic transitions conserving either symmetry or asymmetry with respect to an inversion center are forbidden [158]. However, the interaction with the ligand field parameters of odd parity or with vibrational states of the host also of odd parity mixes electronic states of different parity into the 4*f* wave function. Moreover, the ligand field tensor parameters of even parity mixe electronic states with different *J* but same *S* and *L*. This is the so-called *J*-mixing.

The Particular case of the Eu^{3+} ion

Figure 2.4 displays a schematic representation and order of magnitude of the effects of the intra-atomic and ligand field interactions acting on the $4f^N$ configuration, in particular of the Eu^{3+} ($4f^6$).

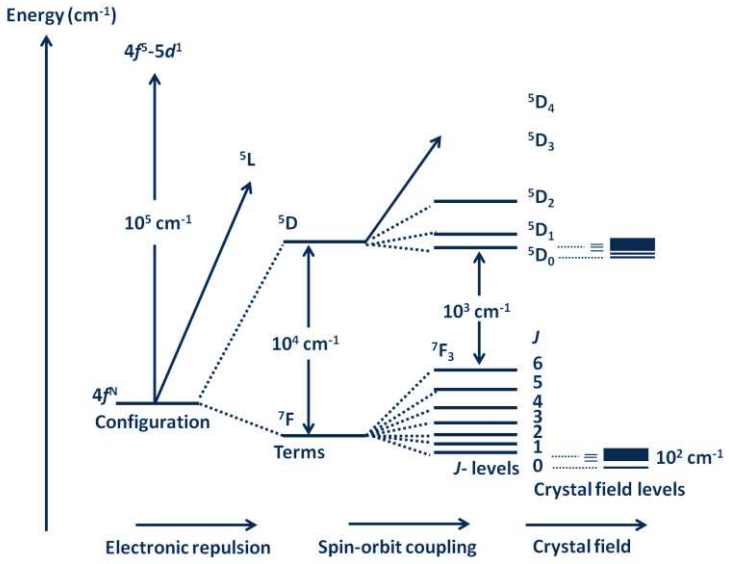

Figure 2.4. Schematic representation and order of magnitude of the effects of the intra-atomic and ligand field interactions acting on the $4f^N$ configuration of the Eu^{3+} [158].

The optical properties of Eu^{3+}-containing materials are directly related to the *f-f* transitions in a $4f^6$ electronic configuration [54]. In the Eu^{3+} the intra-$4f^6$ transitions occur, generally, between the $^5D_0$ and ^7F_J (J=0,1,2,3,4,5,6) levels. All these transitions are essentially of induced electric dipole type, except for the $^5D_0 \rightarrow {}^7F_1$ transition (magnetic). For Eu^{3+} the intensity parameters are difficult to obtain from experimental absorption measurements. In fact few absorption bands are observed with enough intensity in the visible range. However, the pure magnetic-dipole character of the $^5D_0 \rightarrow {}^7F_1$ transition enables the determination of such intensity parameters from the emission spectrum. The emission intensity (*I*) taken as the integrated intensity *S* of the emission curves, for the $^5D_0 \rightarrow {}^7F_{0\text{-}4}$ transitions, is expressed by:

$$I_{i\rightarrow j} = \hbar w_{i\rightarrow j}\, A_{i\rightarrow j}\, N_i \equiv S_{i\rightarrow j} \qquad 2.8$$

where *i* and *j* represent the initial ($^5D_0$) and final ($^7F_{0\text{-}6}$) levels, respectively, $\hbar w_{i\rightarrow j}$ is the transition energy, $A_{i\rightarrow j}$ corresponds to Einstein's coefficient of spontaneous emission and N_i is the population of the $^5D_0$ emitting level [124]. Since this transition does not depend on the local ligand field felt by Eu^{3+}, it may be used as reference for the entire emission spectrum, in vacuum $A_{0\text{–}1}$=0.01465 ms^{-1}, between the $^5D_0$ and the $^7F_1$ Stark levels [159].

Besides the interest in Eu^{3+}-containing materials due to their light-emission properties, the sensitivity of the $4f^6$ transitions can also be used to obtain further information about the local environment around the metal ions [155]. This is another important feature particularly evident for Eu^{3+}, which is a powerful local ion probe due to some peculiar spectroscopic characteristics, such as:

- large energy difference between the $^5D_0$ first excited state and the high-energy $^7F_6$ level of the fundamental state (~12300 cm^{-1}). The smaller this gap, the easier is its closing by non-radiative deactivation (e.g., O–H vibrations);
- non-degenerated first excited state that allows a simpler Stark-effect analysis, with the subsequent correspondence between the observed *J*-splitting degeneracy and the Eu^{3+} local-site symmetry;
- presence of the ligand-field-independent $^5D_0 \rightarrow {}^7F_1$ magnetic-dipole transition, already discussed;

- presence of a single $^5D_0 \rightarrow {}^7F_0$ line allowed for C_s,$C_{1,2,3,4,6,}$ and $C_{2v,4v,6v}$ point symmetry groups with a predominantly electric-dipole nature. The energy of this non-degenerated transition may be directly related to the covalency of the chemical bonds of the first coordination shell in Eu^{3+} (nephelauxetic effect) [160-162];
- observation of vibronic lines in a relatively large spectral region of the $^5D_0 \rightarrow {}^7F_2$ excitation transition (24400 – 21550 cm^{-1}), allowing, in a unique way, the identification of vibration modes up to ~3000 cm^{-1}, related to the Ln^{3+} local environment;
- presence of ligand to metal charge transfer in the UV-Visible region of the excitation spectra, ascribed to particular ligand groups.

Changes in the number of Stark components of each intra-4*f* manifold, variations in the relative intensity between them, differences observed in the energy of particular lines, and the analysis of the excited-state decay curves furnish important information about the metal-ion local coordination, such as the existence of more than one Eu^{3+} local symmetry group, the number of coordinated water molecules, the magnitude of the ligand field, and the importance of the covalency of the Eu^{3+}-ligands bonds [54].

Generally, in Eu^{3+}-contaning hybrids the large values usually found for the *fwhm* of the non-degenerated $^5D_0 \rightarrow {}^7F_0$ line, ranging typically from ~20 cm^{-1} to 30 cm^{-1}, point out that in the Eu^{3+} ions are accommodated in a continuous distribution of closely similar local sites. In general, the number of Stark components observed for the $^7F_{1-4}$ levels corresponds to the $(2J+1)$ maximum local-field splitting (1, 3, 5, 7, and 9, respectively), indicating a low-symmetry local environment (belonging to the orthorhombic, triclinic, or monoclinic crystallographic classes) [163]. If the Eu^{3+} local symmetry group does not present a centre of inversion, the Laporte's rule is relaxed due to odd parity terms in the ligand field Hamiltonian, and the emission spectrum is dominated by the $^5D_0 \rightarrow {}^7F_2$ transition.

High-energy vibrational modes from the hybrid host can deactivate the $^5D_0$ excited state, leading to quenching of emission by nonradiative paths. As already mentioned, in particular OH oscillators are very effective in that deactivation, in such a way that the evolution of the $^5D_0$ excited-state lifetime can be easily connected to the number of water molecules, (η_w), in

the Eu^{3+} first coordination sphere, which can be estimated using the empirical formula of Supkowski and Horrocks (equation 2.9) [164]

$$\eta_w = 1.11 \times [A_{exp} - A_r - 0.31] \quad 2.9$$

where $A_{exp}=(\tau)^{-1}$, with τ representing the $^5D_0$ experimental lifetime in ms.

The emission features of the hybrids were quantified and compared through the estimation of the $^5D_0$ radiative transition probabilities (Ar) and nonradiative transition probabilities (A_{nr}) and of the quantum efficiency (η). Assuming that only nonradiative and radiative processes are involved in the depopulation of the $^5D_0$ state, η may be defined as:

$$\eta = \frac{A_r}{A_r + A_{nr}} \quad 2.10$$

3. Malonamide and di-malonamide bridged silsesquioxanes

3.1 Introduction

The development of eco-friendly system is a challenging and sustainable concept in order to develop materials with potential applications as white light emitters. However, to be considered truly "green", the materials used to generate light emission must be eco-friendly. The presence of sustainable elements (carbon, hydrogen, oxygen, and nitrogen) into the materials makes them completely incinerable; no generate incombustible waste and consequently more environmentally friendly to be used in the proposal of "green" photonics.

Malonamide (NH-C=O-CH_2-C=O-NH) is a good exemple of a friendly material. Despite the fact that malonamide have been used in the area of clean technology [165-169], there are no studies related to the emission of these materials, lacking metal activator centers.

In this chapter, the development of light emitting BS organic-inorganic hybrids based on malonamide and di-malonamide were prepared by the sol-gel process. BS hybrid precursors consist of a malonamide chelating group formed through the formation of amide bons between diethyl malonate or tetraethyl ethanetetracarboxylate and APTES molecule. The linear geometry of these systems is based on malonamide group linked to the siliceous skeleton through a propyl group. While a single malonamide group is present in **malonamide BS**, the **di-malonamide BS** is formed through H–bond interactions that link two malonamide groups. The impact of one or two malonamide groups in the morphology, local structure and potential application as light emitting will be evaluated next.

3.2 Synthesis

The synthesis of **malonamide** and **di-malonamide** hybrid materials, named as **M2-m** and **M4-m** are obtained from hydrolysis and condensation of the hybrid precursors named as **P2-m** and **P4-m**, where M stands the hybrid materials and P the hybrid precursor, m is related with the presence of malonamide group and the numbers 2 and 4 indicate the number of ethyl groups present in the organic precursor.

Malonamide BS

The synthesis of the hybrid precursor (**P2-m**) is based on a mixture of APTES (10 mL, 43.0 mmol) and diethyl malonate (2.8 mL, 17.5 mmol) placed under Ar in a sealed flask heated to 150 °C for 24 h under vigorous stirring. Upon cooling, a solid was formed which was filtered and washed with anhydrous Ethanol (EtOH, 3×10 mL) and then dried under vacuum. The precursor **P2-m** was obtained as a yellow and transparent liquid. ^{1}H NMR ($CDCl_3$, 400 MHz): δ (ppm): 0.61 (CH_2Si, 4H, t), 1.21 (CH_3, 18H, t), 1.62 (CH_2, 4H, m), 3.13 (CH_2CO, 2H, s), 3.21 (NCH_2, 4H, q), 3.78 (OCH_2, 12H, q), 7.26 (NH). ^{13}C NMR ($CDCl_3$, 100 MHz): δ (ppm): 7.7, 18.3, 22.7, 40.8, 42.0, 58.4, and 167.4.

To obtain the hybrid material (**M2-m**), a mixture of dimethylformamide (DMF, 0.74 mL) and methanol (MeOH, 2.2 mL) was added to **P2-m** (300 mg, 0.587 mmol), (DMF/MeOH=1/3 v/v, 1.0:5.7 molar ratio). The mixture was heated at 50 °C until a clear solution was obtained. Then, distilled H_2O (129.4 μL) was added and the mixture was stirred for 5 min at 50 °C. Finally, 0.1 M of NH_4F (29.4 μL, 0.00294 mmol) was added and stirred during 15 min at 50 °C. The molar ratio used was P2-m:H_2O:NH_4F=1:15:0.005. A schematic representation of the synthesis is shown in Scheme 3.1.

The suspension was cast into a polystyrene mould and left to gel covered with Parafilm® and kept at 50 °C overnight. Gelation occurred overnight yielding a free standing film, shown in Figure 3.1. The hybrid was dried at 50 °C for about six days.

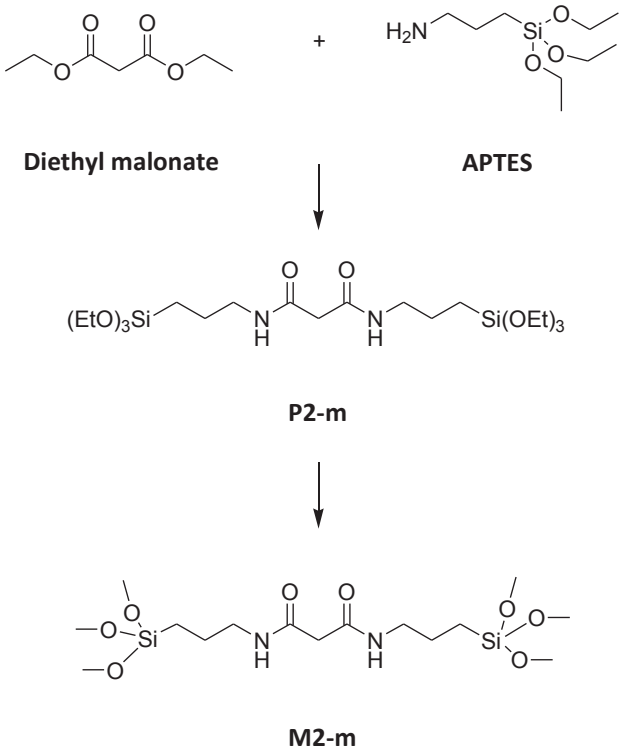

Scheme 3.1. Schematic representation of the synthesis of **M2-m**.

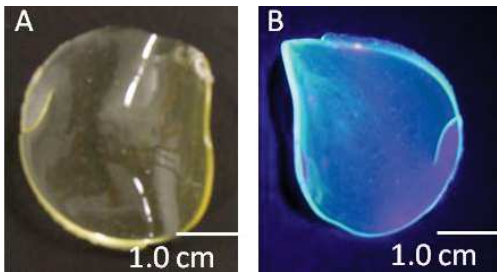

Figure 3.1. Photographs of **M2-m** under A) daylight illumination and B) excited at 365 nm.

Di- Malonamide BS

The synthesis of the hybrid precursor (**P4-m**) is based on a mixture of APTES (10 mL, 43.0 mmol) and tetraethyl ethanetetracarboxylate (3.0 g, 9.4 mmol) placed under Ar in a sealed flask heated to 100 °C for 18 h under vigorous stirring. Upon cooling, a solid was formed which was filtered and washed with anhydrous EtOH (3 × 10 mL) and then dried under vacuum. The precursor **P4-m** was obtained as a white powder. ^{1}H NMR ($CDCl_3$, 400 MHz): δ (ppm): 0.58 (m, 8 H), 1.19 (t, J = 7.0 Hz, 36 H), 1.57 (m, 8 H), 3.16 (m, 8 H), 3.78 (q, J = 7.0 Hz, 24 H), 4.05 (s, 2H), 7.41 (br, 4 H). ^{13}C NMR ($CDCl_3$, 100 MHz): δ (ppm): 7.7, 18.3, 22.6, 42.5, 53.7, 58.3 and 168.1.

To obtain the hybrid material (**M4-m**), a mixture of DMF (0.74 mL) and MeOH (2.2 mL) was added to **P4-m** (300 mg, 0.294 mmol), (DMF/MeOH=1/3 v/v, 1.0:5.7 molar ratio). The mixture was heated at 60 °C until a clear solution was obtained. Then, distilled H_2O (129.4 μL) was added and the mixture was stirred for 20 min at 60 °C. Finally, 0.1 M NH_4F (29.4 μL, 0.00294 mmol) was added. The molar ratio was P4-m:H_2O:NH_4F=1:30:0.01. A schematic representation of the synthesis is shown in Scheme 3.2.

The suspension was cast into a polystyrene mould and left to gel covered with Parafilm® and kept at room temperature for two days. Gelation occurred within 20 min yielding a white powder, shown in Figure 3.2. The hybrid was dried at 50 °C for about one week.

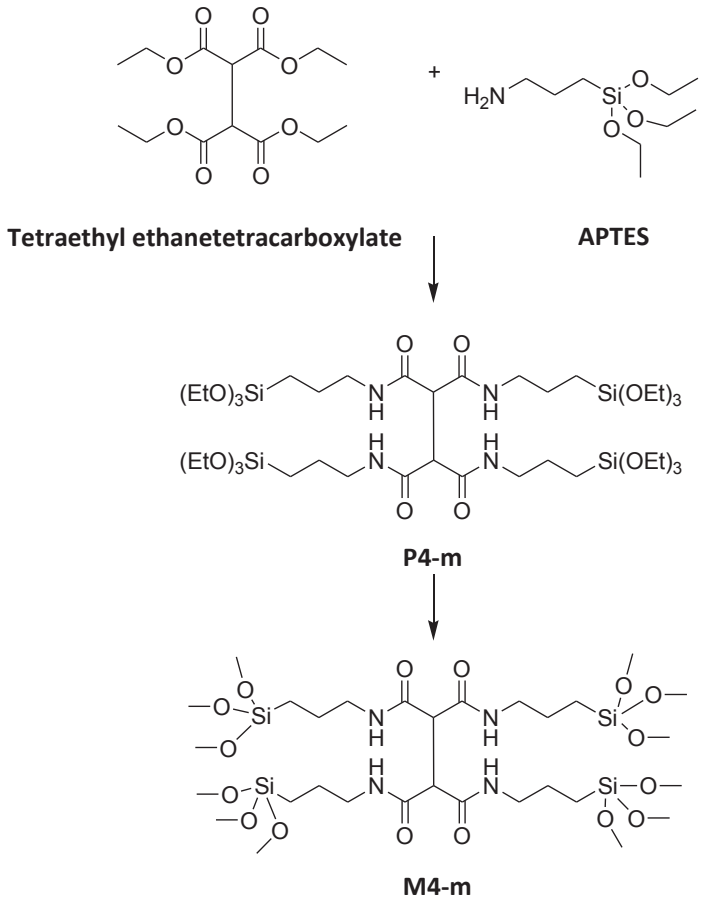

Scheme 3.2. Schematic representation of the synthesis of **M4-m**.

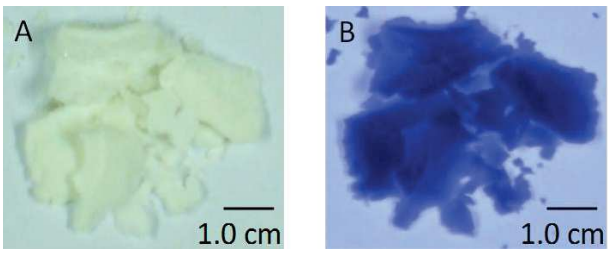

Figure 3.2. Photographs of **M4-m** under A) daylight illumination and B) excited at 365 nm.

3.3 Morphology and local structure

Different morphologies were obtained either in the presence of one or two malonamide groups. The SEM images of **M2-m** depicted in Figure 3.3 shows the presence of dense and amorphous materials with irregular morphology and size.

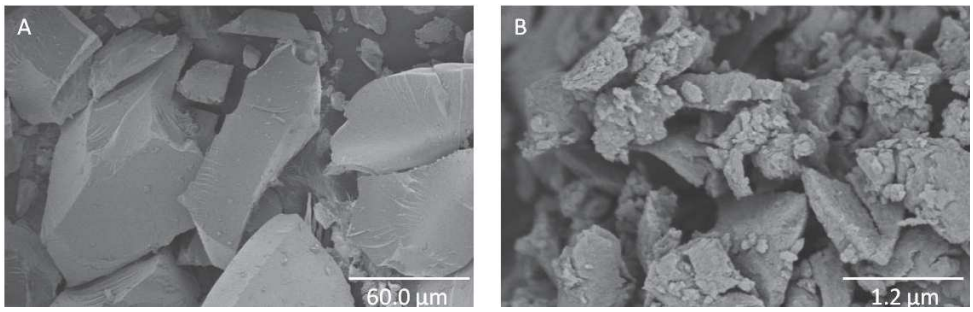

Figure 3.3. SEM image of **M2-m** at A) 60.0 µm and B) 1.2 µm.

The SEM image of **M4-m**, see Figure 3.4, reveals the presence of nanospheres with different size.

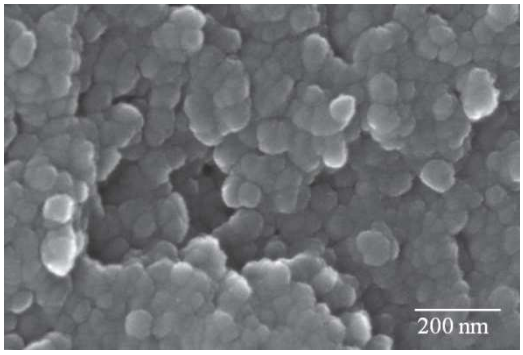

Figure 3.4. SEM image of **M4-m**.

The thermal stability of **M2-m** and **M4-m** was studied based on TGA, see Figure 3.5. Similar TGA spectra were obtained for **M2-m** and **M4-m**. For temperatures below 100 °C, the TGA curves show a weight loss of ~5 % (**M2-m**) and 7 % (**M4-m**) ascribed to desorption of physically absorbed water and residual solvents [170,171]. The weight loss of ~5 %, observed between 100 °C and 350 °C, could be related with removal of the entrapped water or solvents. Between 350 °C and 550 °C a weight loss of ~30 % is related with the

decomposition of the organic part of the hybrids. Above 550 °C a weight loss of ~6 % (**M2-m**) and 10 % (**M4-m**) was ascribed to the release of water formed from the further self-condensation of silanol groups [170,171].

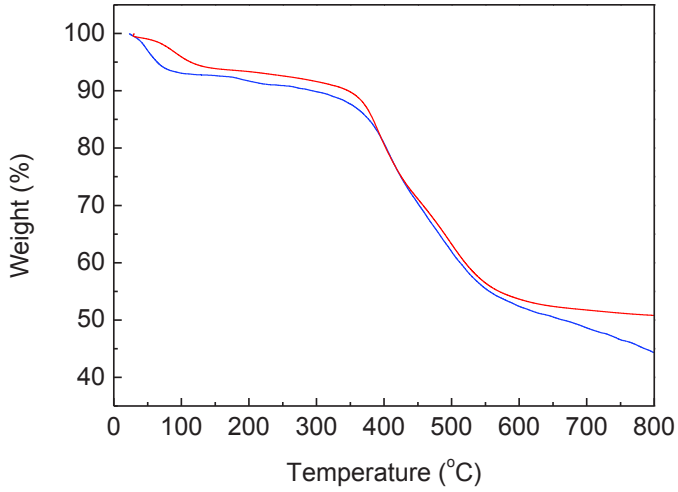

Figure 3.5. TGA curve of **M2-m** (red line) and **M4-m** (blue line).

The ^{29}Si MAS NMR spectra of **M2-m** and **M4-m** are shown in Figure 3.6 A and B, respectively. The ^{29}Si MAS NMR spectra of **M2-m** exhibit two peaks centred at ~–58.8 ppm and ~–67.4 ppm characteristic of T_2 [CH_2-Si$(OSi)_2(OH)$] and T_3 [CH_2-Si$(OSi)_3$] silicon environments, respectively. The condensation degree (*c*) was calculated from the following expression:

$$c = \frac{1}{3} \times (\%\, T_1 + 2 \times \%T_2 + 3 \times \%T_3), \qquad 3.1$$

yielding *c* value of 91 %. The ^{29}Si MAS NMR spectra of **M4-m** exhibit three peaks centred at ~–48.4 ppm, ~–59.7 ppm and ~–68.4 ppm characteristic of T_1 CH_2-Si$(OSi)_1(OH)_2$, T_2 and T_3 silicon environments, respectively with a *c* value of 80 %. Also the Q-type environments (SiO_4) emerge at ~–109.0 ppm for **M4-m**, evidencing partial cleavage of the Si-C bonds during the synthesis. However, as each of the ethane-tetracarboxamide moieties is bound through four positions, this should not significantly affect the overall properties.

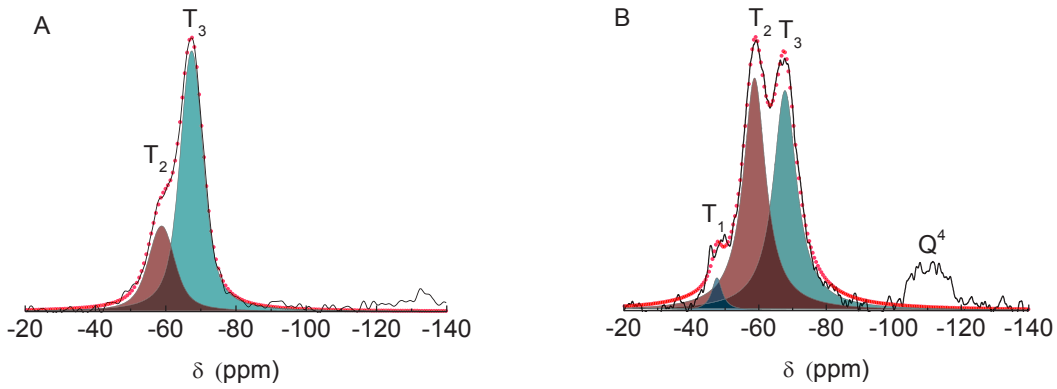

Figure 3.6. ^{29}Si MAS NMR spectra of A) **M2-m** and B) **M4-m**. The fit using a sum of Voigt functions (shadowed areas) ascribed to T_1, T_2 and T_3 silicon environments, and the overall fit (red circles) are also shown.

The ^{13}C CP/MAS NMR spectra of **M2-m** and **M4-m** are depicted in Figure 3.7. The covalent bonding of the organic fragment with the siloxane network is proved by the presence of the resonances corresponding to C^1, C^2 and C^3 assigned to the propyl carbon atoms directly bonded to the silicon atoms. The resonances corresponding to C^5 and C^4 were ascribed to CH and C=O, respectively. The absence of C^5 resonance in **M2-m** could be related to the *fwhm* of the C^3 resonance. In case of **M2-m** we observed *fwhm* of (0.0521±0.0009 ppm) for C^3 resonance that is broader than in case of **M4-m** (0.0411±0.0004 ppm). Thus, we suggest that the C^5 resonance in case of **M2-m** is hidden under C^3 resonance. Overall the ^{13}C CP/MAS NMR spectra of **M2-m** and **M4-m** are very similar to those of **P2-m** and **P4-m**, respectively with the exception of the two signals peaking at 18.0 ppm and 58.0 ppm assignable to $(EtO)_3$–Si groups that disappear after the sol-gel reaction.

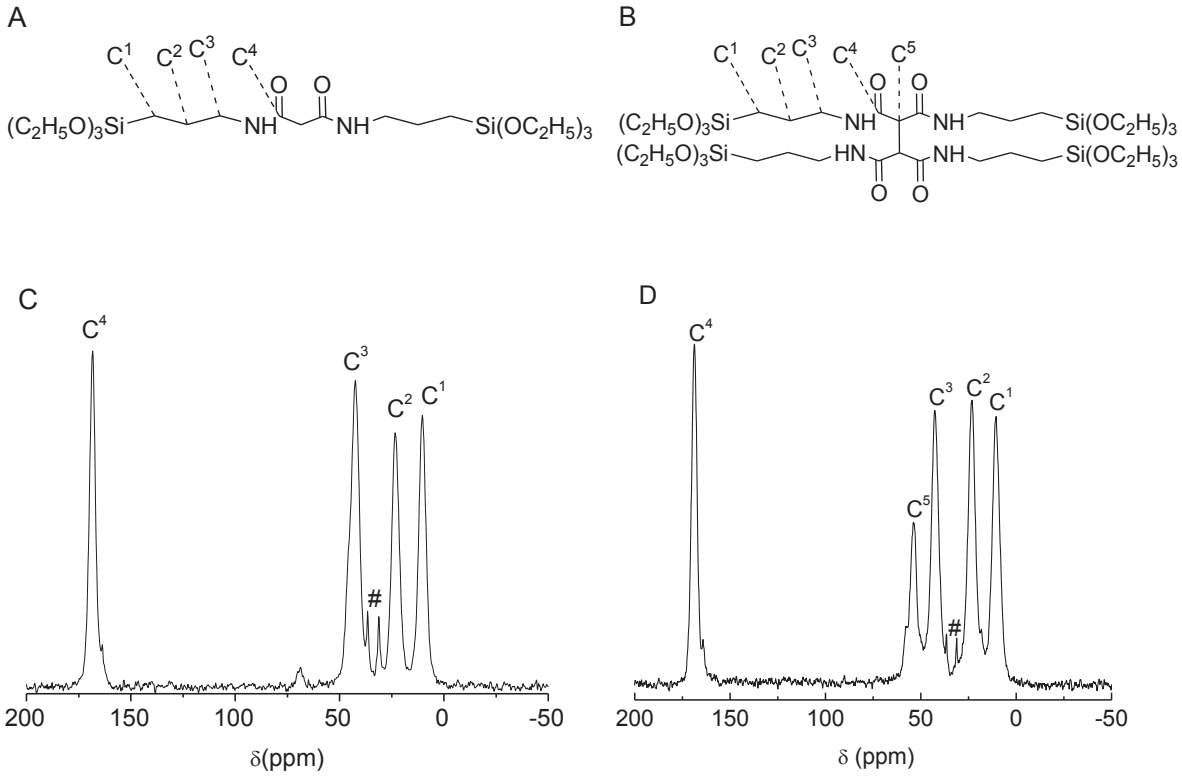

Figure 3.7. (Up) Schematic representation of the structure of A) **P2-m** and B) **P4-m** and (Down) ^{13}C CP/MAS NMR spectra of C) **M2-m** and D) **M4-m**. The C^1, C^2, C^3, C^5 and C^4 resonances appear at 10.8 ppm, 23.7 ppm, 42.9 ppm, 54.0 ppm and 168.6 ppm, respectively. The symbol (#) correspond to DMF solvent.

The diffractograms of **M2-m** and **M4-m,** depicted in Figure 3.8, are characteristic of amorphous materials. The diffractogram of **M2-m** and **M4-m** show at lower q values (where q represents the magnitude of the scattering vector) a broad component at 5.4 nm^{-1} for **M2-m** and a sharp peak at 3.72 nm^{-1} for **M4-m**, with characteristic spacing (d) calculated using the equation 3.2, of 1.16 ± 0.01 nm and 1.69 ± 0.01 nm, respectively. These components are related with the distance between siliceous domains [69,111,119,172].

$$d = \frac{2\pi}{q} \qquad 3.2$$

Also a broad component with maximum intensity at ~8.5 nm^{-1} can be identified in X−ray diffraction pattern of **M2-m**. A similar component (at 8.5 nm^{-1}) appears as a shoulder for **M4-m**, with d values of 0.74 ± 0.01 nm. This component could be related with the

NH–NH distance. In addition, other component peaking at ~9.7 nm^{-1} appears for **M4-m**, with *d* value of 0.66 ± 0.01 nm, which may result from three distinct contributions:

- separation between two neighboring malonamide group [69,111,119,172,173];
- ordering within the siloxane domains [111,173];
- chain-chain spacing [69,111,119,173].

At higher *q* values a broad band at ~15 nm^{-1} appears for **M2-m** and **M4-m**, which was ascribed to the presence of amorphous siliceous domains with *d* value of 0.42 ± 0.01 nm.

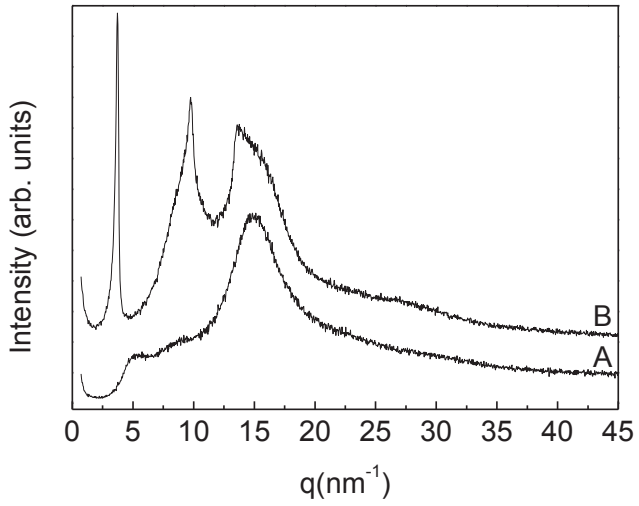

Figure 3.8. X-ray diffraction patterns of A) **M2-m** and B) **M4-m**.

In order to study the vibrational properties of the organic and inorganic components of **M2-m** and **M4-m**, the FT-IR spectra are recorded, see Figure 3.9. The FT-IR spectra for both materials exhibit a broad band between 930 cm^{-1} and 1170 cm^{-1} attributed to the condensed siloxane groups from symmetric and asymmetric elongation vibration ((ν_s(Si-O-Si) and ν_{as}(Si-O-Si)), respectivel. Non-covalent H–bonding interactions involving "Amide" groups and in particular H–bonding [174], are probed in the intramolecular frequency range from 1400–1800 cm^{-1} related with "Amide I" and "Amide II" vibrations and 3000–3700 cm^{-1} in the "Amide A" vibrations. The infrared active "Amide I" band profile, dominated by carbonyl stretching vibrations ν(CO) appears at 1673 cm^{-1}. "Amide II", arising mainly from NH

bending, appear ~1555 cm^{-1}. The "Amide A", associated to ν(NH) appears at 2933 cm^{-1} and at 3300 cm^{-1}, are ascribed to more and less engaged NH, respectively.

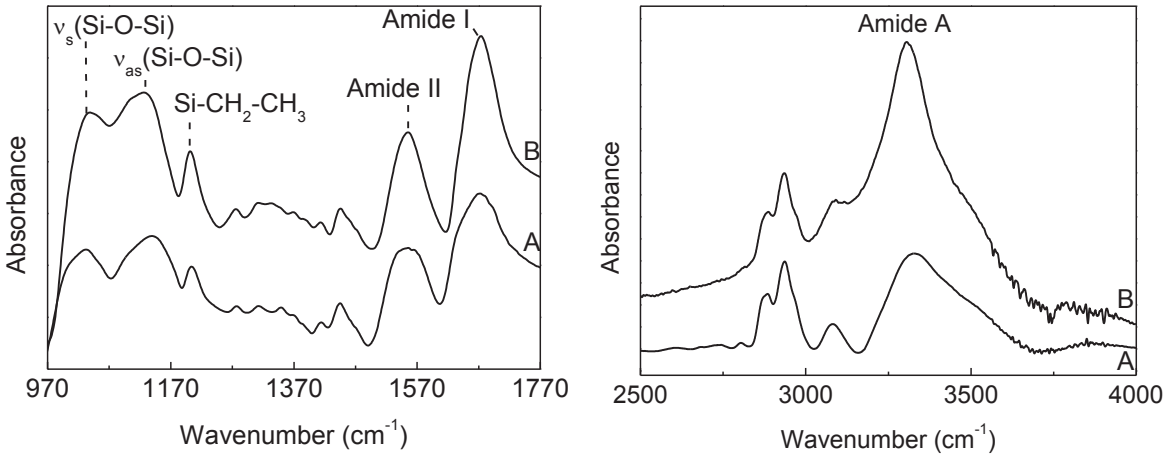

Figure 3.9. FT-IR spectra in the regions of Left) siloxane groups, "Amide I" and "Amide II" regions and Right) "Amide A" region of A) **M2-m** and B) **M4-m**.

In order to evaluate the optical properties of malonamide and di-malonamide BS in the next section photoluminescence properties were studied (emission and excitation spectra, CIE (x,y) coordinates and absolute emission quantum yield).

3.4 Photoluminescence

Figure 3.10 A shows the room temperature emission of **M2-m** and **M4-m** under different excitation wavelengths. The emission spectra are composed of a broad band between 320 nm and 590 nm, whose maximum intensity deviates to the red as the excitation wavelength increases. This behavior was already observed for amine- amide- hybrid materials in particular di-ureasil [68,106,107,113,115-117,175], di-urethanesils [68], mono-amidosils [111] and di-amidosils [65]. The origin of this emission, has been ascribed to the overlap of two distinct emissions mediated by donor-acceptor (D-A) pair transitions that occur within the urea, urethane or amide and cross-linkages and within the siliceous skeleton, due to the presence of oxygen related defects (•O-O-Si≡(CO_2)) [107]. In addition, it was also observed a red shift of ~30 cm^{-1} in the emission spectra of **M4-m** comparatively to **M2-m**.

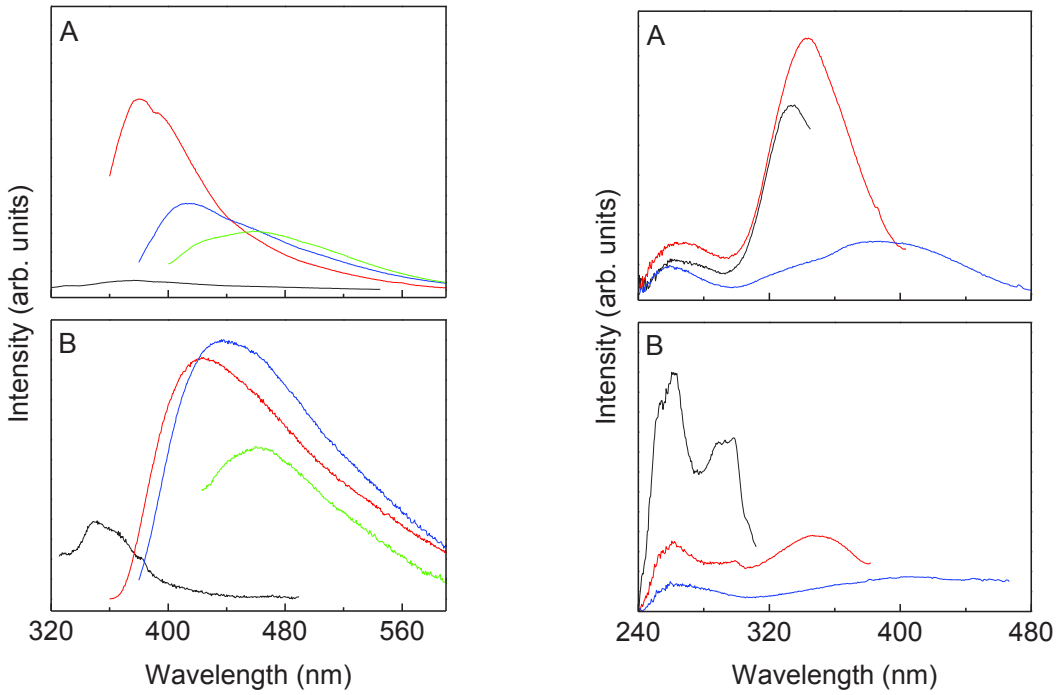

Figure 3.10. Left) Emission spectra excited at 280 nm (black line), 340 nm (red line), 360 nm (blue line) and 380 nm (green line). Right) Excitation spectra monitored at 360 nm (black line), 420 nm (red line) and 520 nm (blue line) of A) **M2-m** and B) **M4-m**.

Figure 3.10 B shows the excitation spectra of **M2–m** and **M4–m** with two main components between 240 nm and 440 nm. In agreement with the emission spectra, the high- and low-wavelengths can be ascribed to the preferential excitation of the urea- and siliceous-related emission, respectively. Comparing the excitation spectra of **M2-m** and **M4–m**, we can observe an increase of the relativel intensity of the higher wavelength component (related to urea group) for **M2-m**.

The above mentioned light emission of hybrid materials based on malonamide was also characterized throught CIE (x,y) coordinates. The dependence on the excitation wavelength enables the emission colour coordinates tuning within the blue spectral region of the CIE (x,y) chromaticity diagram. The emission colour coordinates of **M2-m** and **M4-m** are depicted in Figure 3.11 and vary from the purple-blue region (0.17, 0.07) for **M2-m** and (0.19, 0.24) for **M4-m** excited at 340 nm to the cyan spectral region (0.16, 0.27) for **M2-m** and (0.15, 0.31) for **M4-m** excited at 380 nm.

A B

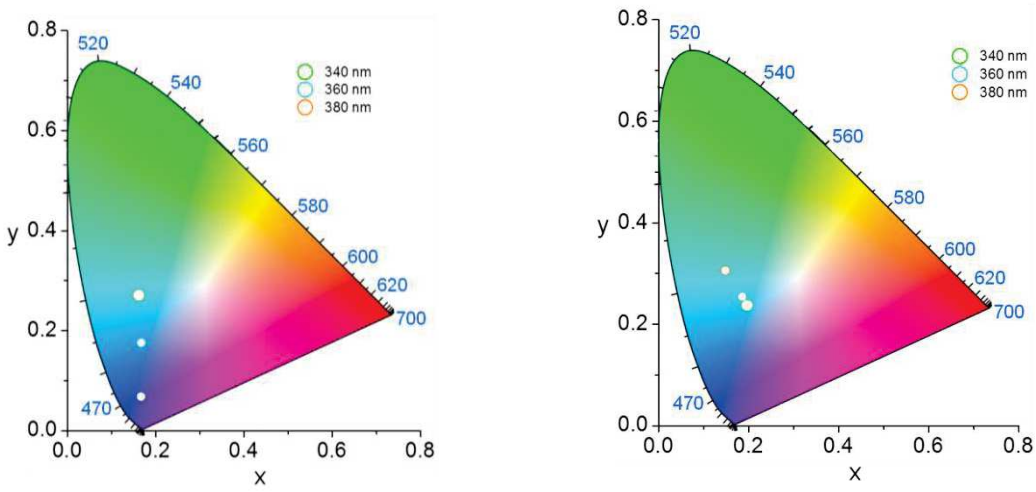

Figure 3.11. CIE (x,y) coordinates at 300 K, excited at 340 nm, 360 nm, and 380 nm of A) **M2-m** and B) **M4-m**.

In order to quantify the emission properties of **M2-m** and **M4-m**, ϕ values were measured, yielding a maximum ϕ value of 0.22±0.02 for **M2-m** and 0.10±0.01 for **M4-m** under 360 nm of excitation.

3.5 Conclusions

In this chapter, amouphous BS organic-inorganic hybrids based on the malonamide were synthetised by sol-gel process as free standing films and powder. The presence of the one or two malonamide groups induces materials with different morphologies, distinct *c* values and photoluminescence properties.

While the ^{29}Si MAS NMR spectrum of **M4-m** show the presence of T_1, T_2 and T_3 silicon environments, the ^{29}Si MAS NMR spectrum of **M2-m** is absent of T_1 silicon environment, which result in an increase of the *c* value for **M2-m**.

Concerning the photoluminescence properties, **M2-m** and **M4-m** presents blue emission under UV-excitation, with a red shift in the emission spectra for **M4-m** comparatively to **M2-m**. In addition, the maximum ϕ value of **M2-m** (0.22±0.02) is higher than in case of **M4-m** (0.10±0.01) under 360 nm of excitation.

4. Amide- Thioamide- bridged silsesquioxanes

4.1 Introduction

In this Chapter we are interested in self–assembled hybrid silicas which do not require any use of an external agent. Our general objective is:

1) to understand how the modulation of the interactions though H–bonds affects the local structure of the hybrid silicas, see Figure 4.1;

2) to study the relation between the structure of these hybrid silicas and their the mechanical and optical properties.

With this aim, our approach is the following one: we aim at modulating H–bond strength through playing with the organic sub-structures in which thiourea groups are substituted to urea groups. As a matter of fact the σ and π components of the C=S bonds are weaker that the one in C=O, thus the electronegativity of sulfur (2.41-2.55) is lower that in case of oxygen (3.17-3.50) [176]. Therefore intermolecular H–bonds between thiourea groups are expected to be weaker than H–bonds between urea goups [176,177].

A

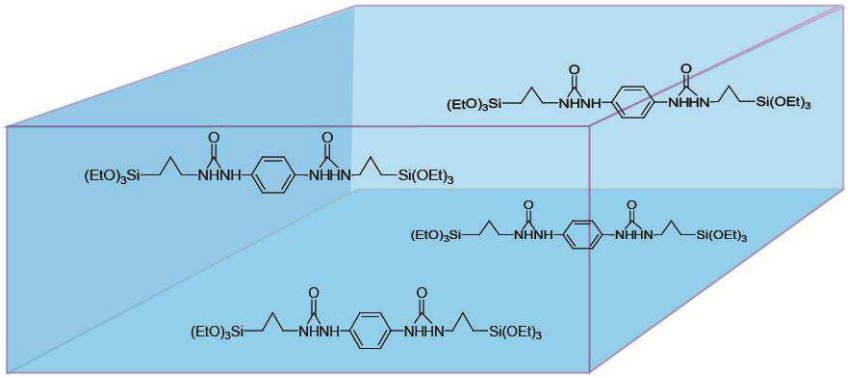

B

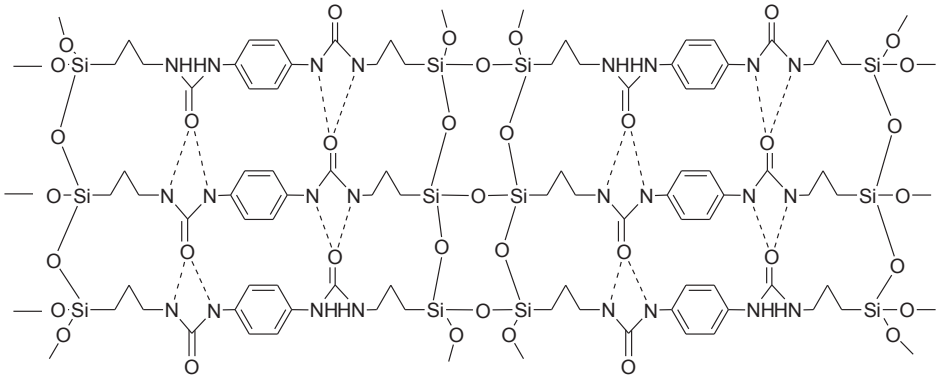

Figure 4.1. Schematic representation during bottom-up structuring of organic-inorganic hybrid silica through self–assembling process of precursors. A) **P(UU)** in solution and B) self–assembling of **H(UU)** through hydrogen and covalent bond interactions.

Three distinct BS organic-inorganic hybrids precursor (**P**) based on bis-urea **(UU)**, bis-thiourea **(TT)** and a mixture of urea and thiourea **(UT)** were prepared allowing a potential modulation of intermolecular H–bonding interactions from stronger H–bonds (**UU**) to weaker H-bonds (from **UT** to **TT**). Figure 4.2 shows a schematic representation of the structure of hybrid precursors based on amino/thioamino-cyclohexane link to the silane. Hybrids materials (**H**) were prepared by sol-gel process. The synthesis details are shown in Appendix B.

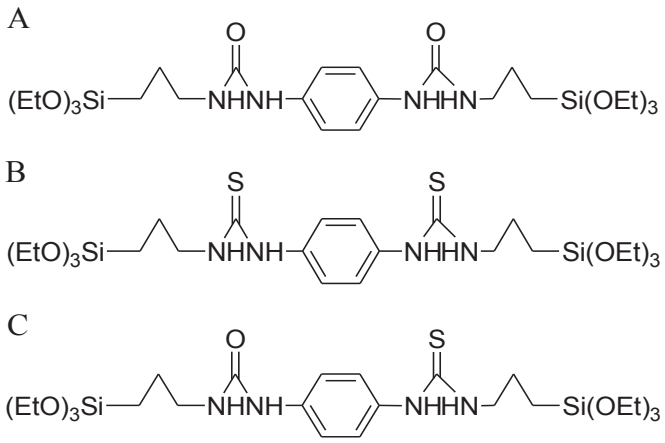

Figure 4.2. Schematic representation of the structure of hybrid precursors A) **P(UU)**, B) **P(TT)** and C) **P(UT)**.

4.2 ^{29}Si MAS NMR and ^{13}C CP/MAS NMR

Hydrolysis and condensation reactions of **H(UU)**, **H(UT)** and **H(TT)** were verified through ^{29}Si MAS NMR and ^{13}C CP/MAS NMR. The ^{29}Si MAS NMR spectra of **H(UU)**, **H(TT)** and **H(UT)** are shown in Figure 4.3. The ^{29}Si MAS NMR spectra of **H(UU)** exhibit four peaks centred at ~36.3 ppm, 48.2 ppm, 57.2 ppm and 66.2 ppm characteristics of T_0 [CH_2-Si-$(OH)_3$] T_1, T_2 and T_3 silicon environment, respectively with *c* value of 50 %. In addition Q-type environment (SiO_4) emerges at −111.0 ppm evidencing partial cleavage of the Si-C bonds during the synthesis. Note that the hybrid freeze dry based on urea-urea previously reported in [178] is absent of T_3 and Q^4 environments. In the ^{29}Si MAS NMR spectra of **H(TT)** we observe resonance at −50.2 ppm, −57.9 ppm and −66.4 ppm and for **H(UT)** −49.6 ppm, −57.8 ppm and −66.4 ppm characteristic of T_1, T_2, and T_3 silicon environments respectively, with *c* values of 88% **H(TT)** and 80% for **H(UT)**.

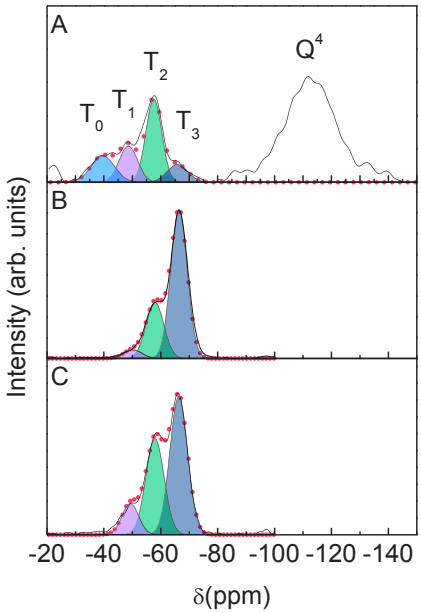

Figure 4.3. ^{29}Si MAS NMR of A) **H(UU)**, B) **H(TT)** and C) **H(UT)**. The fit using a sum of Gaussian functions (shadowed areas) ascribed to T_0, T_1, T_2 and T_3 silicon environments, and the overall fit (closed circles) are also shown.

The ^{13}C CP/MAS NMR spectra of hybrid materials are reproduced in Figure 4.4 (left) the corresponding assignment is indicated in schematic representation of the structure in Figure 4.4 (right). The presence of the resonance assigned to C=O or C=S groups is evidenced by the low field signal at ~ 158 ppm and ~ 179 ppm, respectively. The butyl group can be assigned by the presence of the carbons resonances at ~10.4 ppm, 23.0 ppm, 25.8-32.7 ppm, 38.5-47.5 ppm in the all hybrids. The carbon resonance (C and CH) from the phenyl group was identified at ~ 119.4 ppm and 128.9 ppm and 135.1 ppm. The presence of the peaks at ~18.1 ppm and 58.4 ppm in the **H(TT)** and **H(UT)** was assignable to $(EtO)_3$-Si groups give us indication of the incomplete hydrolysis of the materials.

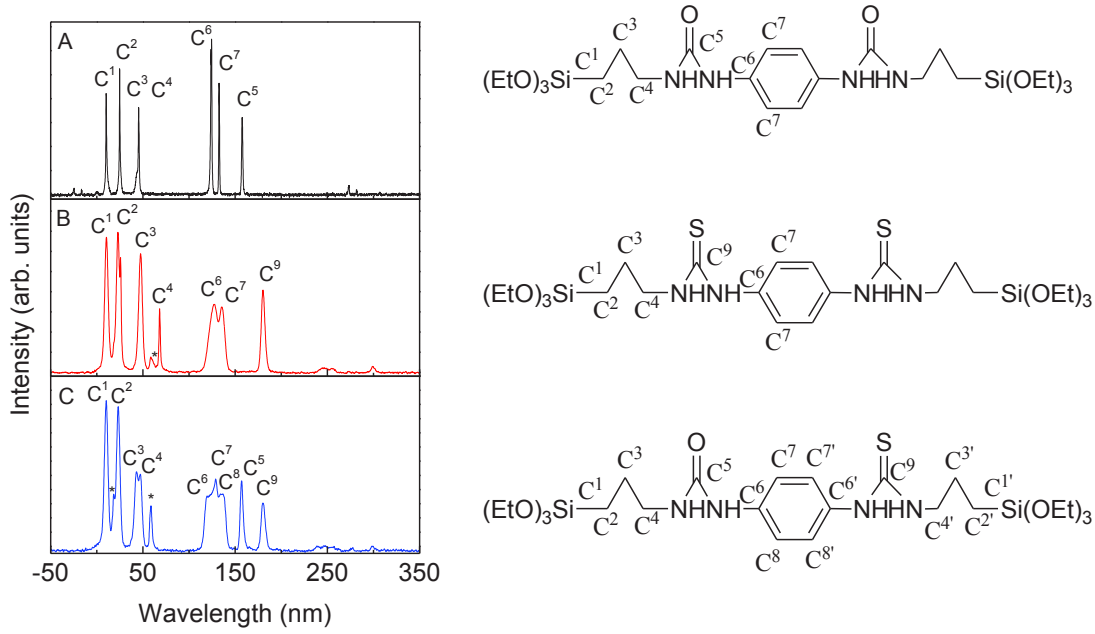

Figure 4.4. (Left) ^{13}C CP/MAS NMR spectra of A) **H(UU)**, B) **H(TT)** and **H(UT)** and (Right) Schematic representation of the chemical structure of hybrid precursors and correspondent assignment of the ^{13}C CP/MAS NMR. The symbol (*) correspond to $(EtO)_3$-Si groups.

As the materials studied present very variable degrees of crystallization, our approach extensively rely on vibrational spectroscopy. Before presenting the spectroscopic studies on the selected systems, it is required to give a brief introduction on infrared spectroscopy related to the interactions by H–bonds between "Amide" and "Thioamide" groups.

4.3 Introduction to IR spectroscopy for the study of H–bonds between "Amides" and "Thioamides" groups

The basic principle of infrared spectroscopy is determined by the absorption of infrared radiation which excites vibrational transitions of molecules/materials. This is generally the case when the frequencies of light are in the mid (MIR) and far (FIR) infrared spectral regions are equal to vibrations frequencies. The molecular dipole moment changes during the vibration are also required for infrared absorption of incident light. Since vibrational frequency

and probability of absorption depend on the strength and polarity of the vibrating bonds, they are influenced by intra- and intermolecular effects. The approximate position of an infrared absorption band is determined by the vibrating masses and the type of bond (single, double, triple), the exact position by electron withdrawing or donating effects of the intra- and intermolecular environment and by coupling with other vibrations. The strength of absorption increases with increasing polarity of the vibrating bonds. The effect of the environment on vibrational frequencies is often a telltale of how hybrid silica is organized.

In this thesis, we will study both MIR and FIR spectral regions. We concentrate our discussion on the vibrational features sensitive to the self-assembling properties of the organic-inorganic precursor, see Figure 4.5, namely, the urea and thiourea vibrations. We detail below the main type of vibrations probed.

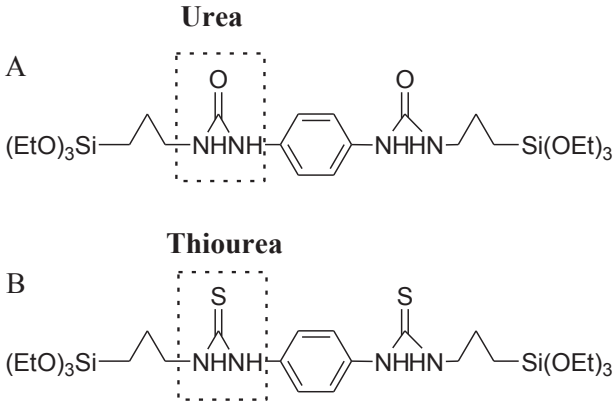

Figure 4.5. Schematic representation of the structure of hybrid precursors A) **P(UU)** and B) **P(TT)**.

In the MIR (4000 – 200 cm^{-1}), on can notice that thermal energy kT at room temperature corresponds to ~ 200 cm^{-1}, it implies that absorption in this range is generally from the vibrational ground state to the first excited vibrational state. In the high frequency domain (4000 – 3000 cm^{-1}), intermediate frequency domain (1800 – 1500 cm^{-1}) and (500 – 800 cm^{-1}) "Amide A and B", "Amides I, II" and "Amide V" vibrations are respectively probed, see Figure 4.6 (Up).

"Amide A" vibrations are dominated by interatomic NH stretching vibrations between roughly 3450 cm^{-1} and 3200 cm^{-1}, see Figure 4.6 (down) A. It is exclusively localized on the NH group and is therefore mainly insensitive to the conformation of the backbone of the

system. The "Amide A" band is usually part of a Fermi resonance doublet with the second component absorbing weakly between 3200 cm^{-1} and 3000 cm^{-1} ("Amide B"). They are a fingerprint of urea and thiourea groups.

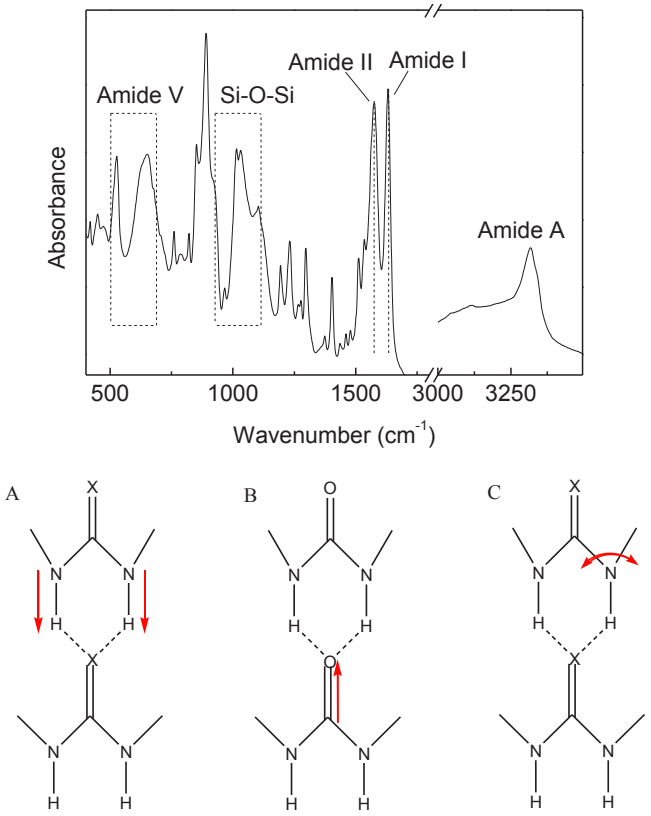

Figure 4.6. (Up) Typical FT-IR spectra of hybrid silica, (Down) Schematic representation of the main vibrational modes study: A) "Amide A", B) "Amide I" and C) "Amide II" vibrations.

The "Amide I" vibration, absorbing between 1700 cm^{-1} and 1620 cm^{-1}, arises mainly from the C=O stretching vibration of urea groups, see Figure 4.6 (down) B. It is classically coupled with other vibrations of the urea group with minor contributions from the out-of-phase CN stretching vibration, the CCN deformation and the NH in-plane bend.

The "Amide II" mode is the out-of-phase combination of the NH in plane bend and the CN stretching vibration with smaller contributions from the CO (CS) in plane bend and the CC and NC stretching vibrations in urea and thiourea groups see Figure 4.6 (down) C.

The "Amide V" vibration, absorbing around 500 cm^{-1} to 700 cm^{-1} contains important contributions from NH out of plane deformation, mixed with CN torsion. It has been shown in amorphous polyamides that "Amide V", identified around 720 cm^{-1}, is very sensitive to H–bond strengthening [179].

For hybrids containing thiourea groups, a vibration equivalent to "Amide I" is expected. Yet one can notice that the position of the vibrations involving mainly C=S stretching of thiourea is still controversial in the literature. Whereas some papers strongly determine the area around 700 cm^{-1} as the region of ν(C=S), others seem to indicate higher frequency (1413 cm^{-1} [179] or 1094 cm^{-1} [180]). The existence of a symmetric (740 cm^{-1}) and anti-symmetric (1417 cm^{-1}) C=S vibration in pure thiourea has also been evoked [181]. Other works seems to indicate that this vibration depends on the type of compounds in which this vibration occurs [182].

The "Amides" vibrations are very sensitive to H–bonds, which stabilize the structure of hybrid silica containing urea and thiourea groups. They are fingerprints of local order around "Amide" group and report on the strength and dispersion of H–bond. They are fingerfprints of local order around "Amide I" group. As a general rule, H–bonding lowers the frequency of stretching vibrations, since it lowers the restoring force, but increases the frequency of bending vibrations since it produces an additional restoring force [183]. As a consequence when temperature dependence of these modes is studied, non harmonic behavior are classically exhibited. The decrease of the temperature increasing the H–bond strength, this phenomenon leads to downshift of the "Amide A" and "Amide I" modes and an upshift of the "Amide II" modes [184]. Temperature studies of the IR spectra of the H–bonded systems are very useful and are systematically performed here.

In hybrid silica, typical strong, intermediating and weak H–bond lead to average "Amide I" vibration position, below 1650 cm^{-1}, between 1650 cm^{-1} and 1675 cm^{-1} and between 1675 cm^{-1} and 1695 cm^{-1}, respectively. For "Amide A" typically position are below 3350 cm^{-1} (strong H–bond), between 3350 cm^{-1} and 3380 cm^{-1} (intermediating H–bond) and between 3380 cm^{-1} and 3430 cm^{-1} (weak H–bond) [184].

When temperature decreases, a strong increase in intensity can be observed in "Amide V" vibration. This behavior is related by an increase in the dipole momentum, associated to the the effective equilibrium charge on hydrogen atom [185].

In the FIR (200 – 10 cm^{-1}), this part of the spectrum for a wide range of organic molecules is dominated by vibrations involving a substantial fraction of the atoms forming the molecules and motion associated with intermolecular H–bond vibrations. Due to their collective nature such modes are highly sensitive to the intra- and intermolecular structure and

thus provide a unique fingerprint of the conformational state of the molecule and effects of its environment. H–bond fingerprints are typically exhibited between 100 cm^{-1} and 200 cm^{-1} in hybrid silica [184]. Temperature dependence of the H–bond vibrations are also classically non harmonic. This anharmonicity is expected to increase with the H–bond strength.

Next section is focus in the vibrational study of the **UU**, **UT** and **TT** systems. A detailed vibrational study using infrared dynamic of the "Amide" groups is used to study the structuring through H–bonding in **UU**, **UT** and **TT** systems.

4.4 Vibrational study of amide-thioamide bridged silsesquioxanes

4.4.1 Vibrational study of UU system

We first introduce bis-urea hybrid material **H(UU)**. The main information about the local structure and vibration modes of this material have formerly been studied in details in the frame of Gaëlle Creff Thesis [178].

M(UU) organic model compound, composed by the same organic sub-structure than **H(UU)** has been synthethized in the frame of this work in order to point out the self–assembling properties of the organic substructure decorelated from the sol-gel condensation of the organic part, see Figure 4.7.

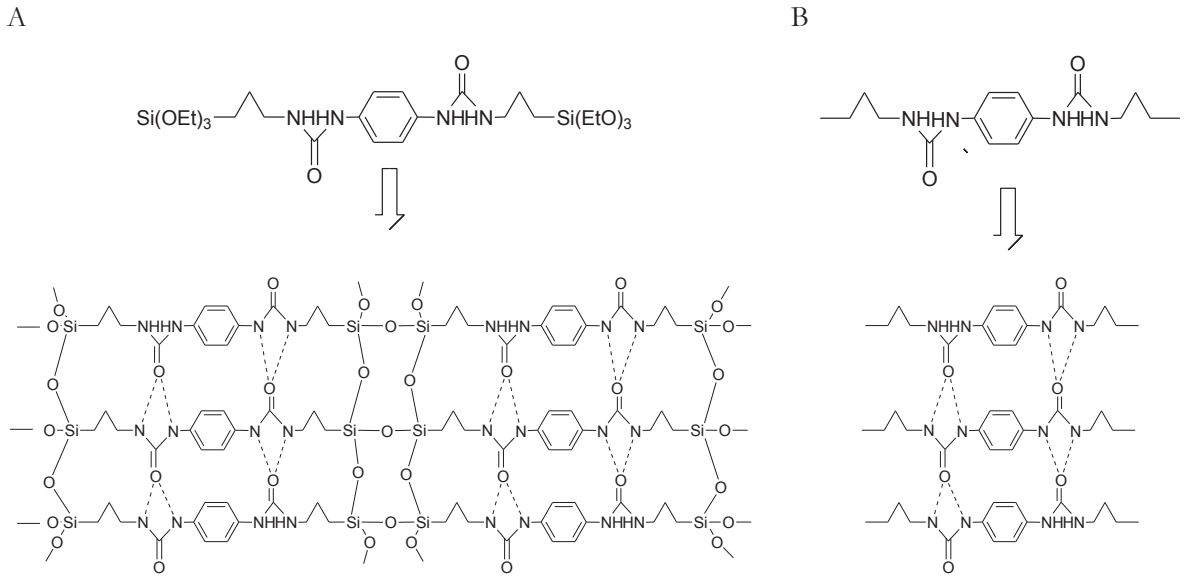

Figure 4.7. Schematic representation of the self–assembling through hydrogen and covalent bond interactions on A) **H(UU)** and on H-bond interaction in B) **M(UU)**.

Hereafter, a comparison between **H(UU)** with the corresponding organic model **M(UU)** in the "Amide" vibrational domains is performed. Figure 4.8 shows the comparison of the FT-IR spectra of the hybrid **H(UU),** precursor **P(UU)** and the model compound **M(UU)** in the "Amide I" and "Amide II" (Figure 4.8 A) and "Amide A" (Figure 4.8 B) spectral regions.

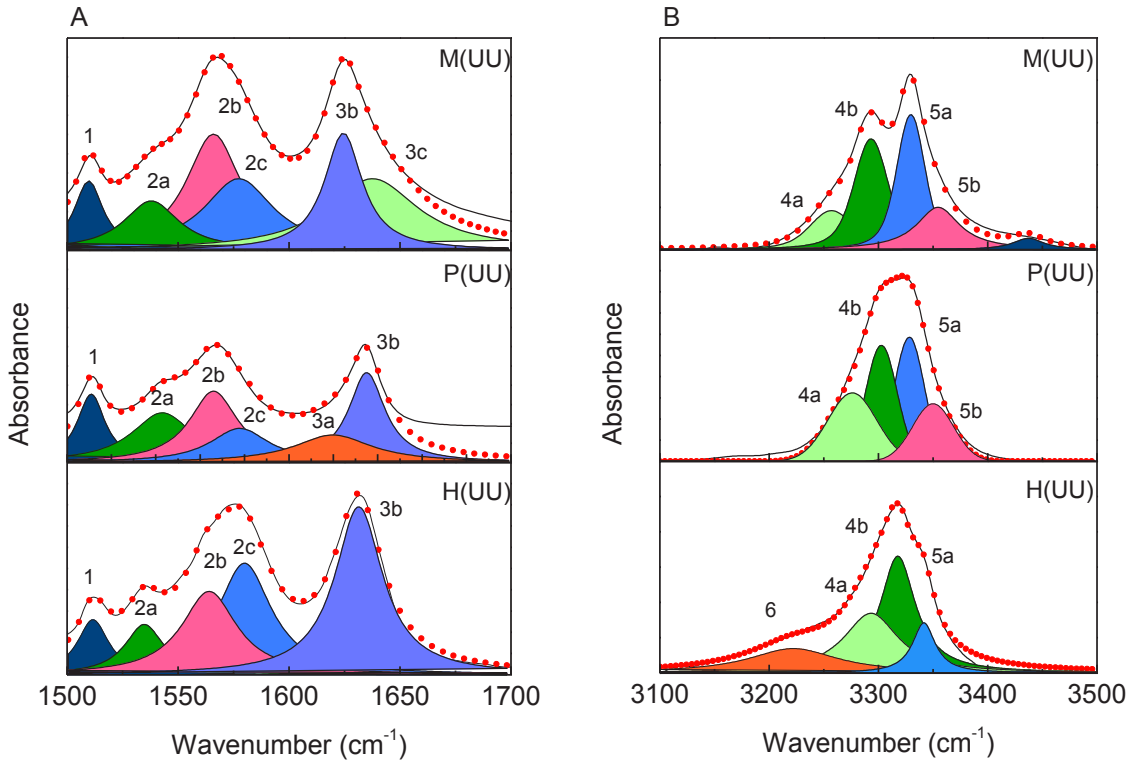

Figure 4.8. FT-IR spectra in A) "Amide I" and "Amide II" regions and B) "Amide A" region of **M(UU)**, **P(UU)** and **H(UU)**. The fitted are represented by red dots and the experimental spectra are given with black lines.

The features observed for **M(UU)**, **P(UU)** and **H(UU)**, are rather similar considering the number of bands. Therefore the assignment of the main vibrational bands of **H(UU)** is given in Table 4.1 and is applied to **P(UU)** and **M(UU)**. It is important to notice that **P(UU)** is crystalline and the NH···O distance in this bifurcated H–bond system is around 2.8 Å [186]. We concentrate in the following on the comparison between **H(UU)** and **M(UU)** as **H(UU)** and **P(UU)** show similar intramolecular IR dynamics.

Table 4.1. FT-IR assignment of the mainly vibrations of **M(UU)** and **H(UU)** in "Amide I", "Amide II" and "Amide A" regions. DFT calculation results are also show based on **H(UU)** [178].

Wavenumber (cm^{-1})			Assignment
M(UU)	**P(UU)**	**H(UU)**	**(based on DFT calculation of H(UU)[178])**
3328	3327	3340	H–bonded "Amide A" *symmetrical ν(NH)
3293	3302	3318	H–bonded "Amide A" *asymmetrical ν(NH)
2958	2973	2938	ν(CH) cycle
2923	2928	2926	$\nu(CH_3)$
2894	2882	2893	$\nu(CH_2)$
2859	-	2873	
1630	-	-	δ(OH) (water)
1625	1634	1632	H–Bonded "Amide I"
1565	1566	1575	H–Bonded "Amide II"
1538	1542	1534	"Amide II" and ν(C=C)
1512	1510	1512	
563	*na*	530	"Amide V"
664		615	

* Symmetries of ν(NH) were calculated by DFT using the structure of a cluster of two organic-inorganic molecules extracted by the hybrid **H(UU)** structure [174]. *na*: information non available.

Despite this great similarities between **H(UU)** and **M(UU)** spectra, some differences are observed in "Amide I", "Amide II" and "Amide A" regions. An upshift of "Amide I" is clearly exhibited for **H(UU)** ($\Delta\nu$= + 7 cm^{-1}, see Table 4.2) indicating small weakening of the H–bond strength and a increase in H–bond dispersion due to the modification of the local order obtained after polycondensation in **H(UU)**. The "Amide A" also indicate a similar behavior ($\Delta\nu$= + 12 cm^{-1} and $\Delta\nu$= + 25 cm^{-1} for symmetric and asymmetric components, respectively), see Table 4.2.

Table 4.2. Shifts (cm^{-1}) observed in the "Amide I", "Amide II" and "Amide A" regions with a decreases of temperature from 290 K to 10 K, of **M(UU)** and **H(UU)**.

Designation	Shift (cm^{-1})				
	"Amide II"	**"Amide I"**	**Δν(10 K)**	**Δν(290K)**	**"Amide A"**
M(UU)	+7	-5	40	53	+15
H(UU)	+8	-3	47	58	+12

A deeper comparison of these two materials involves measurements as function of temperature. As a matter of fact, the anharmonic temperature dependence of "Amide" bonds involved in H–bond is related to H–bond strength.

Figure 4.9 A and B are respectively presenting the thermal dependence of "Amide I", "Amide II" and "Amide A" regions respectively for **H(UU)**, revealing a clear anharmonic behavior of these "Amide" vibrations with temperature. The same type of measurements, performed for **M(UU)** are shown on Figure 4.9 C and D. One can notice small differences as compared with features observed for **H(UU)** shown on Figure 4.8 because the samples correspond to different synthesis batches.

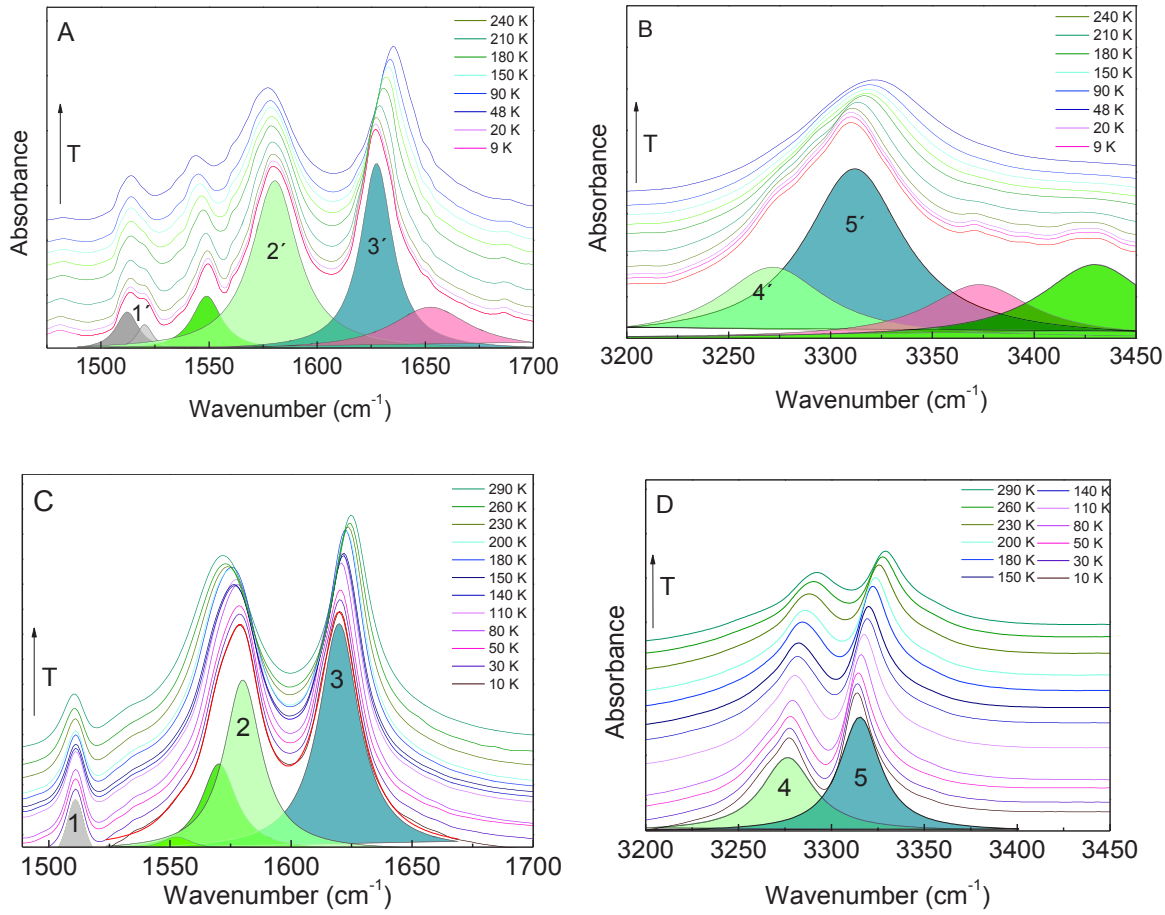

Figure 4.9. FT-IR spectra as function of temperature in A) "Amide I" and "Amide II" regions of **H(UU)**, B) "Amide A" region of **H(UU)**, C) "Amide I" and "Amide II" regions of **M(UU)** and D) "Amide A" region of **M(UU)**. The deconvolution (r^2>0.99) using a sum of Lorentzian functions (shadowed areas) is also shown.

"Amide I" downshifts whereas "Amide II" upshifts, in both **H(UU)** and **M(UU)**, which is typically shown when H–bond strengthen at low temperature. Moreover the smaller Δν measured between "Amide I" and "Amide II", at low temperature, is known as a good indicator of stronger H–bond strength. The downshift exhibited by "Amide A" with decreasing temperature is also consistent with this result, see Figure 4.10. We also notice a broadening of the "Amide" mode for **H(UU)** compared to **M(UU)** indicating an increasing dispersion of H–bond strengths for **H(UU)**.

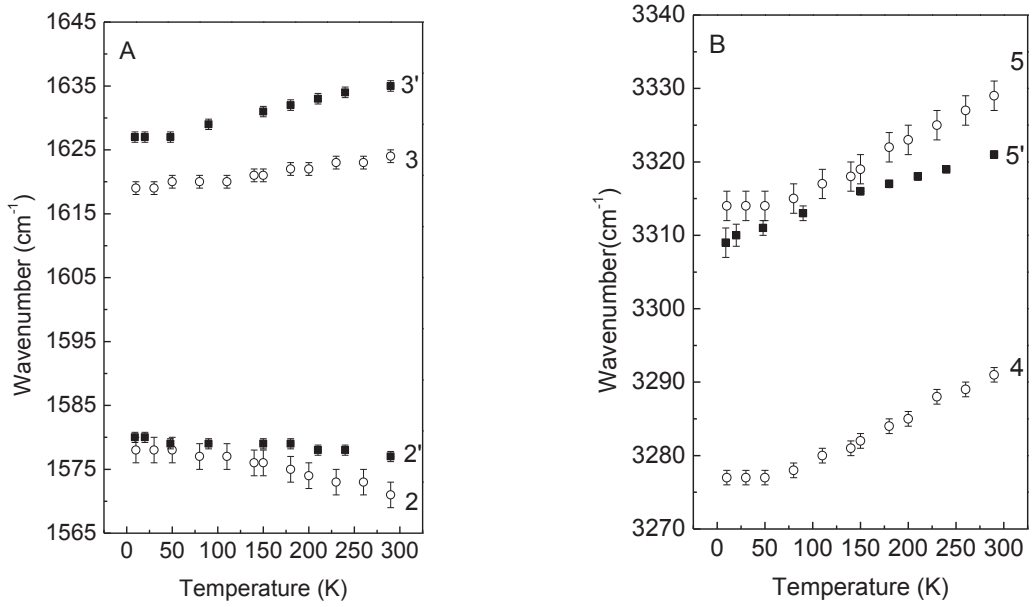

Figure 4.10. Thermal dependence of the components A) 2, 2´ in "Amide II" and 3, 3´ in "Amide I" regions, and B) 4, 5, 5´ in "Amide A" region of **M(UU)** (open circles) and **H(UU)** (closed squares). The error bars are also represented.

A quantitative analysis of the thermal dependence of "Amide I", "Amide II" and "Amide A" depicts a weaker dependence for **H(UU)** than for **M(UU)**, see Table 4.2. As already noticed above, H–bonds in **H(UU)** are shown to be slightly weaker than in **M(UU)**, also resulting to a weaker enhancement in H–bond strength at low temperature. As a result a more anharmonic potential is found when H–bond strength decreases.

Figure 4.11 shows the "Amide V" spectral region related to out of plane δ(NH) vibration for **M(UU)**. Some contributions at 563 cm^{-1} (8) and 664 cm^{-1} (9), intense and well defined at 10 K, appear very strongly damped at 290 K so that the band 8 almost disappears at 290 K. Such a strong modulation in the intensity in "Amide V" has formerly been associated to H–bond strength modulation [185].

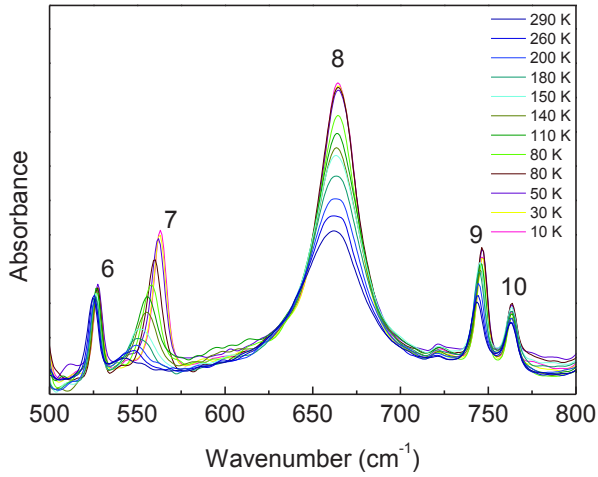

Figure 4.11. FT-IR spectra as function of temperature in "Amide V" region of **M(UU)**.

Unfortunately, for hybrid materials, this region is dominated by Si-O vibrations, therefore "Amide V" vibrations can hardly be observed deconvoluted from Si-O broad contributions. Therfore reliable information in this region is only available for models.

To summarize, from spectroscopic comparison of **M(UU)** and **H(UU)**, the local structure in **UU** system is strongly determined by strong non covalent interactions as it is preserved during sol-gel process even if an increasing dispersion og H–bonds strengths is exhibited after inorganic polycondensation [187]. In **UU** system, this local structure relies on bifurcated H–bonds between urea groups [174,186]. Figure 4.12 illustrates X-ray diffraction pattern of **H(UU)** and the self assembling through bifurcated H–bonds in **H(UU)** lamellar crystal [174].

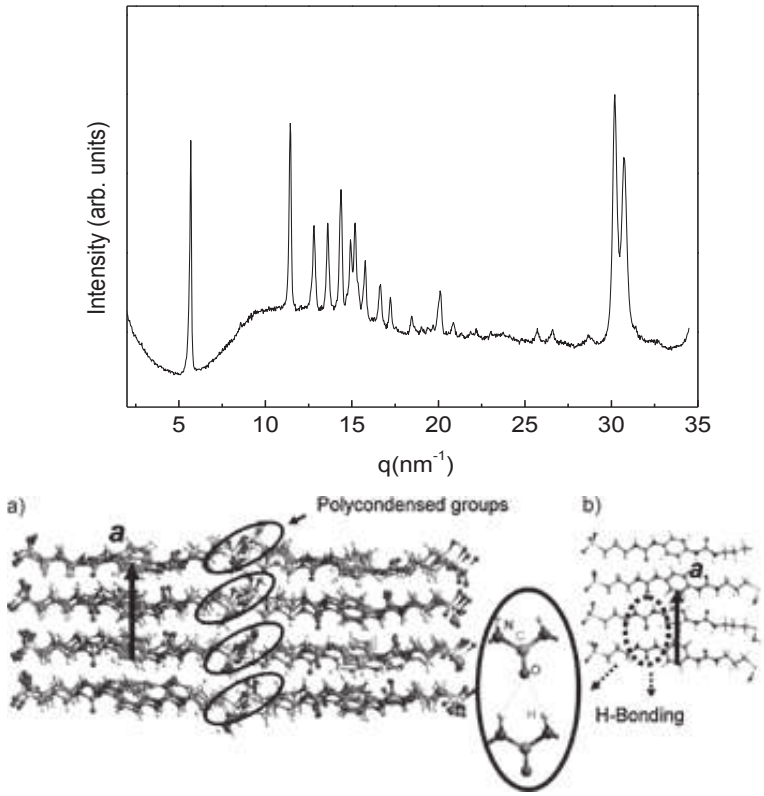

Figure 4.12. (Up) X-ray diffraction patterns of the **H(UU)** structure and (Down) schematic representation of the bifurcated H–bond done throught a) covalent and b) non covalente interactions in **H(UU)** and **P(UU)** [174].

We show that the intramolecular vibrational dynamics of **M(UU)** and **H(UU)** present significant similarities. The results demonstrate a global transcription of the local arrangement around "Amide" modes involved in H–bonds, between the organic sub-structure of the model and the organic-inorganic hybrid material.

Thus, on the basis of the knowledge of the local structure of crystallized **H(UU)**, we demonstrate that the local arrangement of the organic sub-structures in **M(UU)** is also based on connections through bifurcated intermolecular H–bonds.

In the case of the study of **UT** and **TT** systems, hybrids are not crystallized unlike the models (see Figure B. 3 in Appendix B). We use here the structure of the crystallized models to carry out a detailed vibrational study of these compounds by coupling experimental measurements and DFT calculations. This study shall allow to characterize these various types of H–bonds as well as to quantify the modulation of the H–bond strength in the models **M(UT)** and **M(TT)**.

Secondly, the comparison of the vibrational dynamics of model and hybrid shall allow the extraction of information on the local structure related to the organic sub-structure of the hybrid. We will also estimate the degree of transcription between models and hybrids in relation with the various types of H–bonds.

4.4.2 Vibrational study of UT systems

The substitution of an urea by a thiourea in the organic structure of the hybrids **H(UT)** should lead to a decrease of the intermolecular interactions through H–bonds [185,188]. As discussed above, our interest will be first driven on crystallized model **M(UT)**. As for the **UU** systems, the study concentrates on the intramolecular "Amide" vibrations which are very sensitive to H–bond interactions.

The structure of **M(UT)** shown in Figure B. 4 in Appendix B, was determined within the framework of this research project (collaboration with Hubert Wadepohl,' Anorganisch-Chemisches Institut, University of Heidelberg, Germany), more details in Table B. 1 in Appendix B. Once this structure known, it is possible to simulate IR spectra though DFT calculation (collaboration with Patrick Hermet, Institut Charles Gerhardt Montpellier, UMR 5253 CNRS-UM2-ENSCM-UM1, Montpellier, France) and to assign the vibrational modes. At first, this extensive study of **M(UT)** model will be presented, and then, on the base of identified spectral signatures, the infrared spectra of **H(UT)** will be analysed.

IR study of M(UT)

The knowledge of the structure is required to realize the DFT simulations in crystalline phase that allow the understanding of intermolecular interactions. We remind, here below, the local order in **M(UT)** resulting from single crystal diffraction. The molecules **UT** in **M(UT)** crystal have a *trans-trans* configuration. Figure 4.13 shows the packing of molecules in **M(UT)** associated to two types of H–bonds.

In the first type urea H–bonded mode (***DB***), strongly held dimers are formed by the association of two **M(UT)** molecules through two H–bonds between the urea oxygen atoms and the thiourea NH groups.

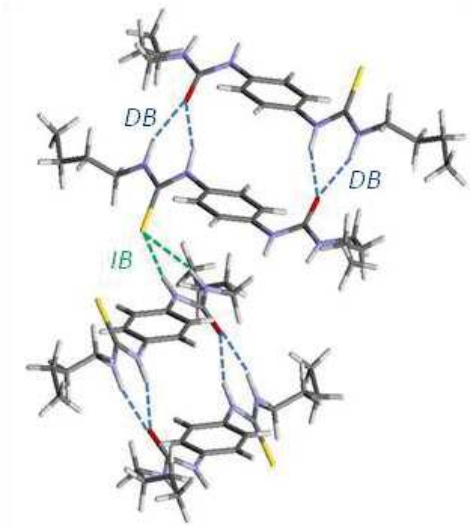

Figure 4.13. H–bond local arrangement of **M(UT)**. See Figure B. 4 in Appendix B for more details of the **M(UT)** structure.

The second type, thiourea H–bond mode (***IB***) implies the sulfur atom of the thiourea functions and the NH groups of the urea function. ***IB*** interaction is strongly asymmetrical (angles *CSH* 101 ° and 128 °) whereas ***DB*** interaction corresponds to almost classical bifurcated H–bond (angles *COH* 139 °) [189]. Table 4.3 shows that ***DB*** distances are significantly smaller (around 15%) than ***IB*** distances. Roughly, this preliminary observation is consistent with the expectation of weaker interaction for H–bonds involving sulfur than for H–bonds involving oxygen [188-190].

Table 4.3. H–bond lengths in **M(UT)** obtained from single crystal X-ray diffraction.

H–bond distances	
IB (C=S····H-N-C=O)	***DB*** (C=O····H-N-C=S)
B-side 3.34Å	B-side 2.85Å
A-side 3.52Å	A-side 2.88Å

Note: B (Butyl side) and A (Aryl side)

The structure solved by single crystal X-ray diffraction has been relaxed by DFT and infrared spectrum was simulated. According to group theory, among 144 vibrationnal modes expected, for **UT** crystal, only *B1u*, *B2u* and *B3u* modes are IR actives, *Ag*, *Bg1*, *Bg2* and *B3*

modes are Raman active, *Au* modes are silents (see Appendix A for details on DFT calculation and Figure B. 6 in Appendix B for Raman active mode assignment).

On Figure 4.14, IR spectra simulated by DFT is compared to experimental spectra measured at 10 K. A very good agreement is observed in the region of "Amide I" and "Amide/Thioamide II".

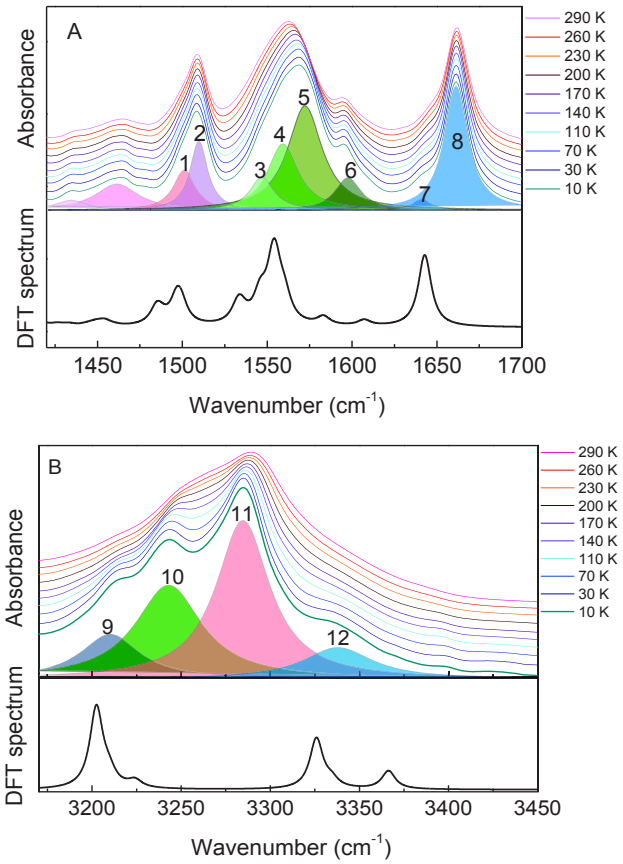

Figure 4.14. FT-IR spectra as function of temperature in A) "Amide I" and "Amide/Thioamide II" regions and B) "Amide/Thioamide A" region of **M(UT)**. The deconvolution (r^2>0.99) using a sum of Lorentzian functions (shadowed areas) is also shown.

The experimental spectra are deconvoluted for an easier comparison with DFT and the assignment of the main vibrational bands in the regions of interest, are given in Table 4.4

Table 4.4. FT-IR assignment of **M(UT)** in "Amide I", "Amide/Thioamide II" and "Amide/Thioamide A" regions based on DFT calculation, (very weak (vw), weak (w), medium (m) and strong (s)) represent the intensity of the interaction B and A correspond to butyl and arly side respectively. The letters **U** and **T** refer to urea and thiourea group.

Components	Experimental Wavenumber	Simulated Wavenumber	Intensity	Assignment
1	1501	1484,75	m	δ(NH) on urea (UB+UA) and slightly on thiourea (TB+TA) dominated by ***IB*** small contribution from aryl
		1487,45	vw	Aryl ring coupled to δ(NH) on urea (UB+UA) dominated by ***IB*** coupled to aryl
		1487,47	w	
2	1509	1496,52	m	In plane vibration of aryl ring coupled to δ(NH) on thiourea (TB+TA) and on urea
		1499,22	m	In plane vibration of aryl ring coupled to δ(NH) on thiourea (TB+TA)
3	1547	1532,45	m	δ(NH) from thiourea on butyl side(TB) and slightly urea
		1534,53	w	
4	1560	1543,86	vw	δ(NH) from thiourea (TA) and urea (UB) dominated by IB
		1544,24	w	
		1545,27	m	δ(NH) and ν(CN) from thiourea (TB, TA) and urea (UA)
5	1572	1553,14	m	δ(NH) and ν(CN) from thiourea (TA) and urea (UB,UA)
		1554,95	s	
		1560,36	m	
6	1595	1583.06	w	ν(CC) vibration of aryl ring (H and C) coupled to "Amide I" (carbon from ν(CO), H from δ(NH))
		1583.21	vw	
		1584.59	vw	
7	1597	1607,01	w	ν(CC) vibration of aryl ring (balanced) coupled to "Amide I" and H from δ(NH) on thiourea (TA)
		1607,10	vw	
8	1661	1641,92	vw	"Amide I" (carbon from ν(CO), H from δ(NH)) coupled to ν(CC) vibration of aryl ring and δ(NH) from thiourea
		1642,79	s	
		1645,01	vw	
9	3210	3202	s	ν(NH) from urea (U) on butyl side (B) and from thiourea (T) on aryl side (A) mixing ***IB*** and ***DB***
		3209	w	ν(NH) from urea un butyl side (UB) dominated by ***IB***
10	3242	3223	w	ν(NH) from urea on butyl side (UB) and from thiourea on aryl side (TA) mixing ***IB*** and ***DB***
		3225	vw	ν(NH) from thiourea on aryl side (TP) dominated by ***DB***

Table 4.4 (Continued)

Components	Experimental Wavenumber	Simulated Wavenumber	Intensity	Assignment
11	3284	3325	w	ν(NH) from thiourea on aryl side (TA) dominated by ***DB***
		3325	vw	ν(NH) from thiourea on butyl side (TB) dominated by ***DB***
		3334	m	ν(NH) from thiourea on butyl side (TB), (TA) small, dominated by ***DB***
12	3338	3364	vw	ν(NH) from urea on aryl side (UA) dominated by ***IB***
		3366	vw	
		3366	w	

The two components (1) and (2) observed in"Amide/Thioamide II" region, in Figure 4.14, are ascribed to ν(CC) vibration of aryl ring coupled to δ(NH) .Vibration (1) only involves "Amide" from urea (1). The broad "Amide/Thioamide II" contribution between 1520 cm^{-1} and 1620 cm^{-1} can be deconvoluted with 4 bands (3, 4, 5 and 6). Whereas component 3 is dominated by δ(NH) in thiourea. Components 4, 5 and 6 involve simultaneously urea and thiourea groups. For component 6 a coupling with aryl vibration is also observed, see Figure 4.15.

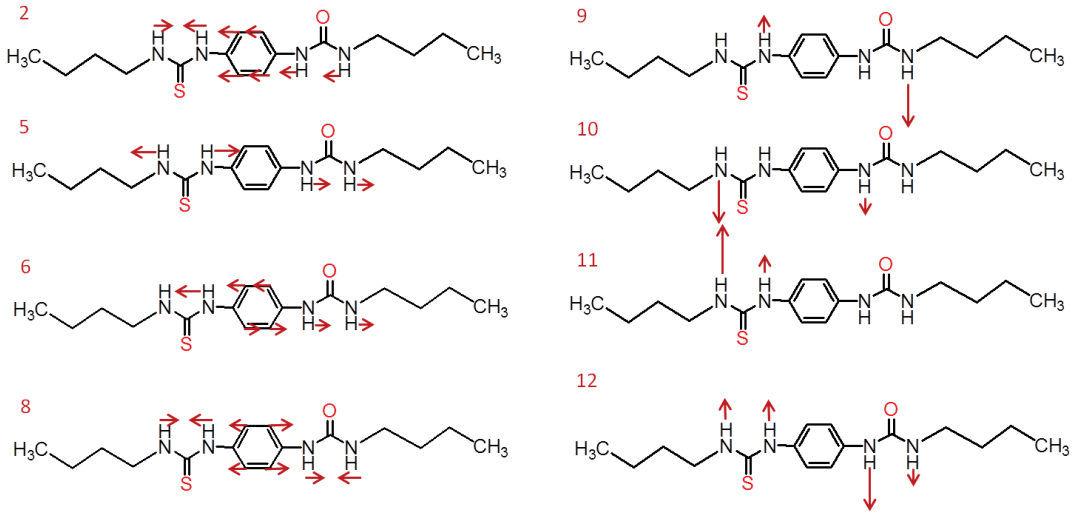

Figure 4.15. Atomic motions of the the most intense bands at 2) 1499 cm^{-1}, 5) 1554 cm^{-1}, 6) 1583 cm^{-1} in "Amide/Thioamide II" region, 8) 1642 cm^{-1} in "Amide I" region and 9) at 3202 cm^{-1}, 10) at 3325 cm^{-1}, 11) at 3334 cm^{-1} and 12) at 3366 cm^{-1} in the"Amide/Thioamide A" region of **M(UT)**.

Figure 4.14 B shows the FT-IR spectra of **M(UT)** between 290 K and 10 K in the "Amide/Thioamide A" region compared with DFT spectrum. Four groups of frequencies are predicted from simulation. A complex FT-IR band is shown for the experimental spectrum at 10 K. The shape is well deconvoluted using 4 contributions labelled 9, 10, 11 and 12 with maximum peak position at 3210 cm^{-1}, 3242 cm^{-1}, 3284 cm^{-1} and 3338 cm^{-1}, respectively. Despite a shift between experimental and simulated spectra (due to anharmonicity), it is possible to assign these experimental features thanks to DFT, see Table 4.4.

"Amide/Thioamide A" vibration dominated by interatomic interaction ν(NH) involving ***DB*** and ***IB*** bonds (components 11 and 12) are identified at high energies (3284 cm^{-1}, 3338 cm^{-1}), respectively, see Figure 4.15. As expected ν(NH) corresponding to ***IB*** bonds appears a higher frequency than ν(NH) associated to ***DB*** bonds in agreement with the higher bond length measured for ***DB***. Lower energy contributions (9 and 10), classically assigned to the most engaged H–bonded, are shown here to be assigned to vibrations involving ν(NH) coupling urea and thiourea groups, see Figure 4.15.

IR spectra have been measured from 10 K to 290 K in "Amide I", "Amide/Thioamide II" and in "Amide/Thioamide A" regions. The classical upshift of "Amide II" with decreasing temperature is only observed for components 3, 4 and 5 corresponding to the most H–bonded "Amide", see Figure 4.16 A. We observe also that when aryl vibrations are coupled to "Amide/Thioamide II" vibrations, harmonic temperature behavior is shown. The most intense "Amide I" component (8) observed at 1642 cm^{-1} show a puzzling harmonic behavior very different from the classical shift observed in **UU** system, see Figure 4.16 A.

Concerning the thermal dependence of "Amide/Thioamide A" presented on Figure 4.16 B, the components (9 and 12) show classical pseudo harmonic behavior while the components (10 and 11) exhibit a typical behavior of H–bonded system with a downshift of the frequencies when the temperature decreases. Considering the assignments of the pure urea (11) or thiourea groups (12), stronger ***DB*** strengthen when temperature decreases and less involved ***LB*** does not show any specific behavior.

Whereas the behavior of components 11 and 12 is well understood through the relative H–bond strength of ***DB*** and ***IB*** bonds, the different behavior between the components 9 and 10, probably related to coupling between urea and thiourea groups is an open question.

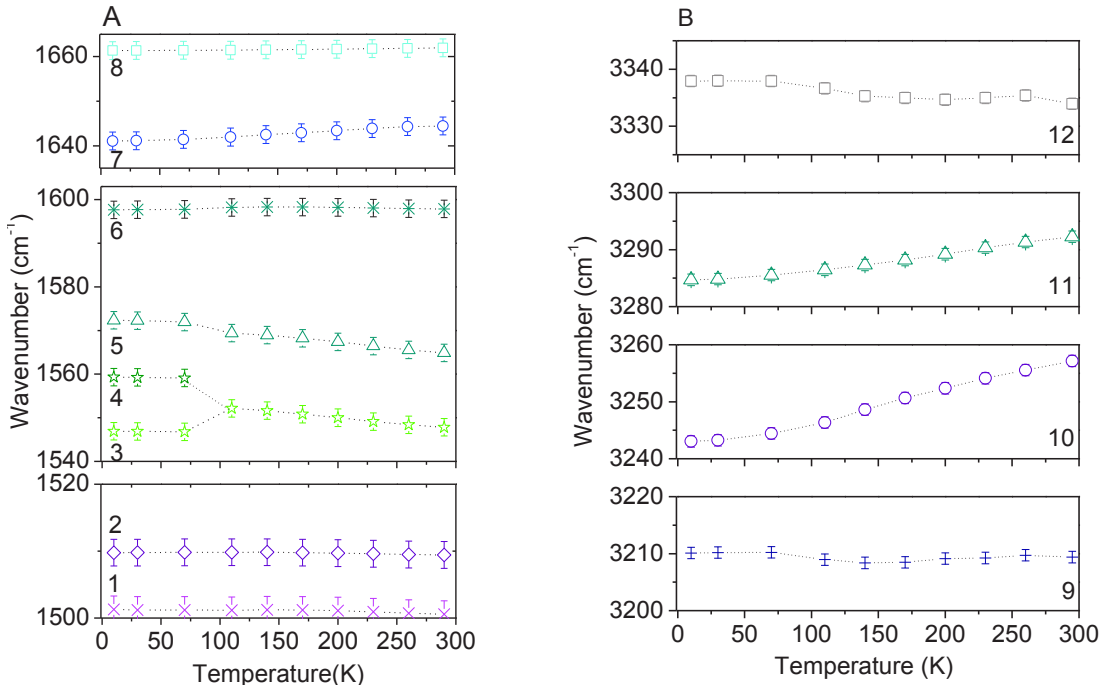

Figure 4.16. Thermal dependence of the different components in A) "Amide/Thioamide II" regions and B) "Amide/Thioamide A" region of **M(UT)**. The lines through the data are a guide to the eye and the error bars are also represented.

M(UT) in the "Amide/Thioamide V" region shows a strong variation of intensity from 10 K to 290 K, see Figure 4.17. The vibrational modes show more intense sensibility to temperature. More are assigned to out of plane δ(NH) thanks to DFT, see Table 4.5. Moreover, vibrations involving modifications of dimer H–bond (***DB***) or interdimer H–bond (***IB***) can be discriminated. Independently from this assignment all "Amide/Thioamide V" modes are strongly damped at high temperature indicating significant H–bonding network.

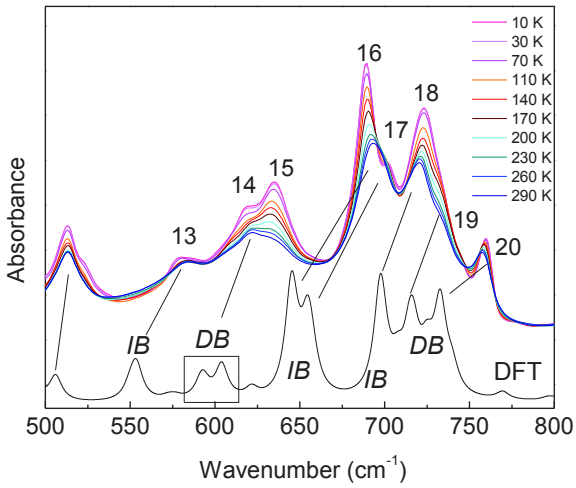

Figure 4.17. FT-IR spectra as function of temperature in "Amide/Thioamide V" region of **M(UT)**. The DFT spectrum is also shown.

Table 4.5. FT-IR assignment in "Amide/Thioamide V" based on DFT calculation of **M(UT)**.

Components	Experimental Wavenumber	Simulated Wavenumber	Assignement
	512	505	CH from cycle
13	579	550	Out of plane δ(NH) in Urea (***IB***)
14	620	592	Out of plane δ(NH) in Thiourea (***DB***)
15	635	603	
16	689	645 654	Out of plane δ(NH) in Urea (***IB***)
17	722	696 697 698	Out of plane δ(NH) in Urea (***IB***)
18,19	734	714 717 718 724 725 726	Out of plane δ(NH) in Thiourea (***DB***) and skeleton
20	760	732 739 740	Out of plane δ(NH) in Thiourea (***DB***) + δ(CH)

To summarize, this preliminary work on **M(UT)** has shown that assignment of vibrations in mixed urea/thiourea system is not straightforwardford. The fine assignement enabled by DFT reveals complex "Amide" vibrations involving both types of H–bonds. Also "Amide/Thioamide II" vibrations can be coupled to aryl vibration and exhibit anharmonic behavior. "Amide I" signs for strongly the bonded ***DB*** interactions, but is strongly harmonic

unlike the classical behavior observed in **M(UU)**. Finally, in "Amide/Thioamide A" and "Amide/Thioamide V", spectroscopic signatures are identified as specific markers for the two specific types of urea-thiourea H–bonds ***DB*** and ***IB*** revealed by diffraction.

Vibrational study of H(UT)

Figure 4.18 A compare the IR spectra of **M(UT)** and **H(UT)** in the "Amide I" and "Amide/Thioamide II" regions. Some of the main "Amides" components (1, 2, 3, 4, 5) assigned in **M(UT)** can be also identified in **H(UT)** after deconvolution and are denominated (1', 2', 3', 4', 5') in the hybrid. Nevertheless, a dramatic broadening of the vibrational features is observed for **H(UT)** compared to **M(UU)/H(UU)** systems. This could be related to inhomogeneous local disorder in **H(UT)** suggesting the constraints due to siloxane condensation affect differently ***DB*** and ***IB*** H–bonds. As expected "Amide/Thioamide II" contribution downshifts and "Amide I" upshifts in the hybrid as compared to the organic substructure. This phenomenon is classically assigned to an average weakening of the intermolecular H–bonds. In details the deconvolution of the spectra shows that "Amide I" exhibits in the **H(UT)** two types of contributions, one remaining engaged by H–bonds at the level of the substructure (alpha (α), 1660 cm^{-1}) and another one (beta (β), 1692 cm^{-1}), clearly poorly engaged in H–bond (see section 4.3).

On Figure 4.18 C we notice that this separation into two "Amide I" groups is also found when the H–bonded network of the organic substructure is disrupted by heating **M(UT)** in $CHCl_3$. As a matter of fact, the high frequency component at 1692 cm^{-1} corresponds to very weakly H–bonded "Amide I" (to be compared to the position in THF 1705 cm^{-1}, see Figure B. 7 in Appendix B) whereas the feature remaining at 1660 cm^{-1} is due to H–bonded species. Therefore from this assignment it is possible to quantify the ratio of alteration of H–bond due to the sol–gel process through the deconvolution see Table 4.6 based on the hypothesis that the extinction coefficients are the same. In the "Amide/Thioamide II" region, one can notice that "Amide I" behavior is consistant with the broadening of "Amide II" features. As for the aryl vibrational contributions (2') it seems almost insensitive to inorganic polymerization.

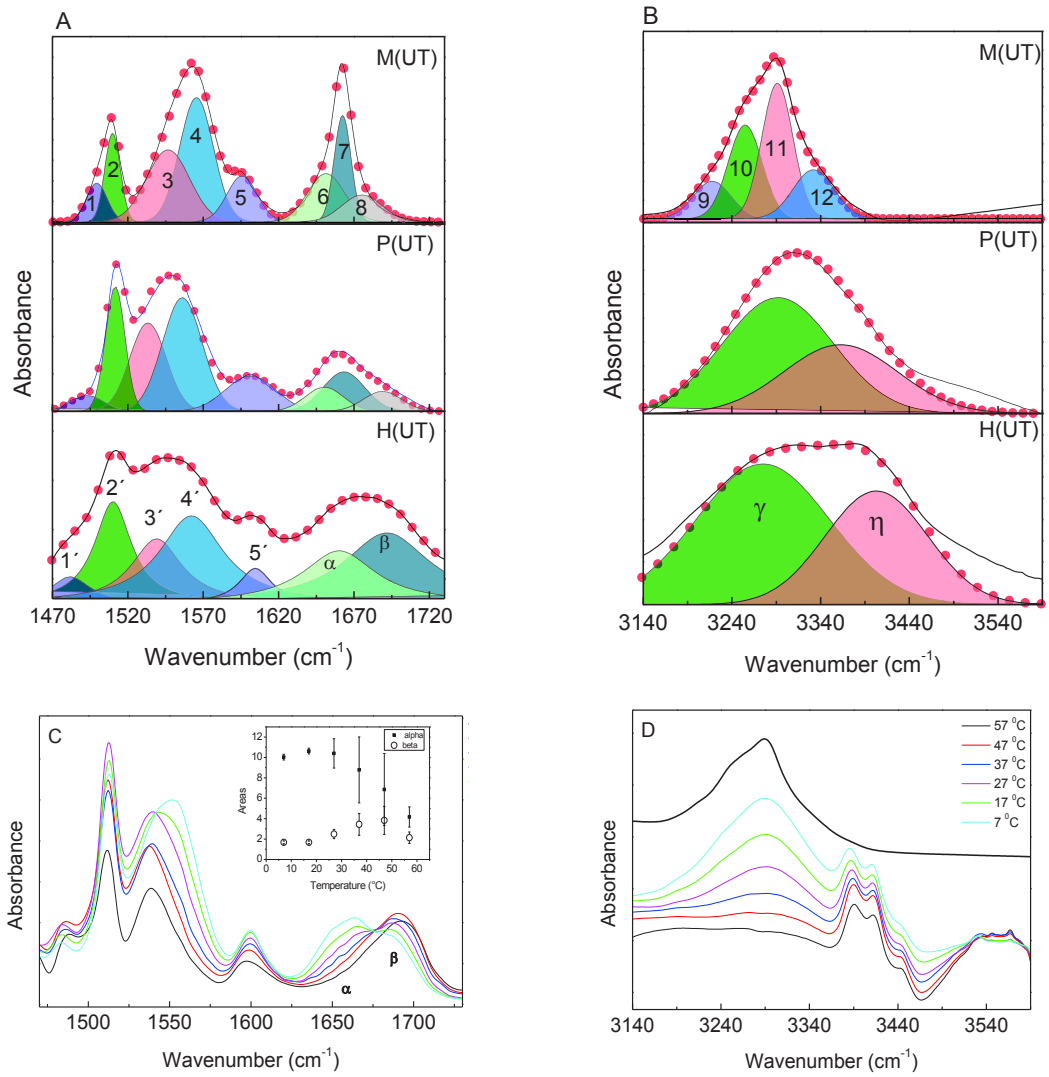

Figure 4.18. FT-IR spectra in A) "Amide I" and "Amide/Thioamide II" regions and B) "Amide/Thioamide A" region of **M(UT), P(UT)** and **H(UT)**. The deconvolution (r^2>0.99) using a sum of Lorentzian functions (shadowed areas) is also shown. FT-IR spectra of **M(UT)** in chloroform as function of temperature in C) "Amide I", "Amide/Thioamide II" regions and D) "Amide/Thioamide A" region. The inset in Figure C show the quantification of weak and intermediately strong bonds of **M(UT)** in chroroform, the error bars are also represented.

Table 4.6. Proportion of the two populations bonded urea and very weakly bonded/free urea as a function of temperature.

Temperature (°C)	Area (%)		$\frac{\alpha}{\alpha+\beta}$	$\frac{\beta}{\alpha+\beta}$
	α	β		
7	68.4	31.6	0.684	0.316
17	72.2	27.7	0.722	0.277
27	59.3	40.6	0.593	0.406
37	52.3	47.7	0.523	0.477
47	48.6	51.4	0.486	0.514
57	45.9	54.1	0.459	0.541

"Amide/Thioamide A" region shown on Figure 4.18 B also shows two broad contributions γ and η respectively corresponding to bonded species (same mean frequency than for **M(UT)** and unbonded species (see free "Amide/Thioamide A" in $CHCl_3$ on Figure 4.18 D around 3400 cm^{-1}).

The structural study of the model **H(UT)** indicates original intermolecular interactions in these systems showing two types of local organization associated with the establishment of H–bonds. The first ones are intra-dimer bonds ***DB*** (between urea C=O and NH from thiourea) and the second are inter-dimer bonds ***IB*** (between thiourea C=S and NH from urea). We note that the substitution of an urea by a thiourea affects significantly the structure of nanomaterials [188-192].

We see here that coupling DFT calculations in crystalline phase and experiments is required to study the urea-thiourea interactions because a high degree of coupling of the "Amide" vibrations observed.

In an expected way, the intermolecular vibrational dynamics is particularly sensitive to this local structure. The "Amide/Thioamide A" vibrations allow to study separately both types of interactions and show that the intra-dimer H–bonds are on average stronger than inter-dimers ones.

The results obtained on hybrid suggest a partial transcription of the model **M(UT)** to the hybrid **H(UT)**. The materials present two types of intramolecular "Amide" vibrations. The first ones correspond to interactions by H–bonds comparable to the model in term of

strength. The seconds indicate the significant presence of weakly bound eventually free-"Amide". In both cases, we note a dispersion of H–bond strength consistent with the amorphous character of the material.

4.4.3 Vibrational study of TT system

As **H(TT)** hybrid material is amorphous (see Figure B. 3 in Appendix B), interactions through H–bonds in **TT** system are studied here, following the same methodology used for **UT** system.

Vibrational study of M(TT)

We present firstly the structure of crystallized **M(TT)** used for the DFT calculations, (see Figure B. 5 and Table B.2 in Appendix B). In **M(TT)** crystal the molecule present *cis-trans*, configuration. Three different types of H intermolecular bonds are identified: (A) In the first type thiourea H–bonding (***CB***), a formation of a ring planar cycles through two H–bonds is shown, (B) thiourea H–bond mode (***LB***) originating from link between sulfur atoms NH group, (C) out-of plane thiourea H–bonds (***TCH$_3$***) originating from the sulfur atom of the thiourea group and the CH_3 of the butyl, see Figure 4.19.

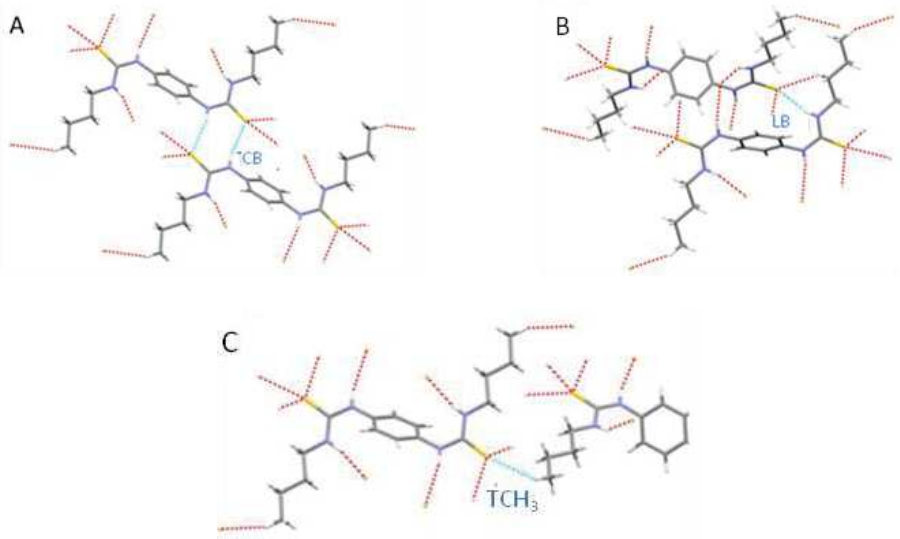

Figure 4.19. H–bonds local arrangement of **M(TT)**. The designation ***CB*** and ***LB*** derived from cyclic bond and linear bond, respectively.

Typical [189,191] H–bond distances are given in Table 4.7. Intermolecular ***CB*** thiourea H–bonds appears in **M(TT)** surprisingly shorter compared to H–bonds in **UU** and **UT** systems. This could be related to the cyclic character of this type of H–bond. ***TCH$_3$*** H–bond gives to very small modifications in the ν(CH) stretching and are not discussed in the following.

Table 4.7. H–bond lengths obtained from X-ray diffraction, between sulfur and nitrogen (***CB*** and ***LB***) and between sulfur and carbon (***TCH$_3$***) in **M(TT)**.

H–bond distances (XRD)		
CB	***LB***	***TCH$_3$***
C=S···H-N: 2.54 Å	C=S···H-N: 2.72 Å	C=S···CH$_3$: 2.99 Å

Based on single crystal structure of **M(TT)**, infrared spectrum was calculated from DFT (according group the DFT, among 72 vibrationnal modes expected, *Au*, *Bu* modes are IR actives and *Ag*, *Bg* are Raman active, the last ones are detailed in Figure B. 5 and Table B.2 in Appendix B). Simulated spectra and experimental spectra at 10 K are compared on Figure 4.20. Appart from a shift, a very good agreement enables an accurate assignment of the experimental modes in both "Thioamide II" and "Thioamide A" regions, see Table 4.8.

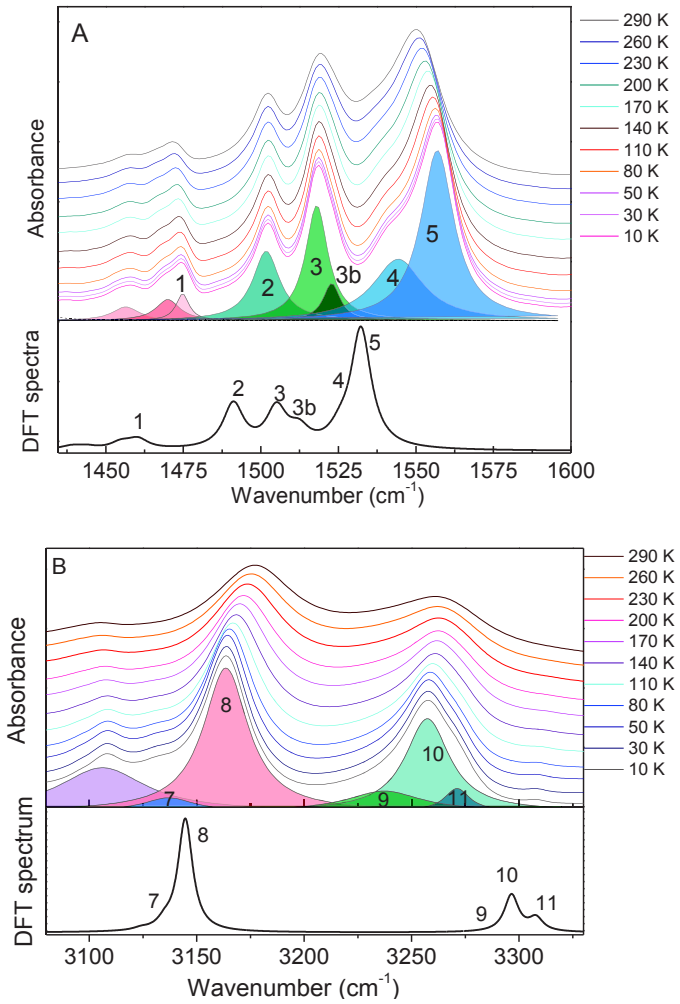

Figure 4.20. FT-IR spectra as function of temperature in A) "Thioamide II" regions and B) "Thioamide A" regions of **M(TT)**. The deconvolution (r^2>0.99) using a sum of Lorentzian functions (shadowed areas) is also shown.

The component 1 is dominated by δ(CH) in plane, component 2 couples δ(CH) in aryl and "Thioamide II" vibration. Components 3, 4 and 5 are directly related to "Thioamide II" vibrations and involve simultaneously δ(NH) associated to both ***CB*** and ***LB*** H–bonds.

In "Thioamide A" region the components identified as 8 and 10 in Figure 4.20 B are dominated by ν(NH) associated respectively to cyclic H–intermolecular bond (***CB***) and by linear H–bond (***LB***), respectively. The position of the component 8 (***CB***) is lower compared to component 10 (***LB***). Furthermore ***CB*** H–bond distance (2.54 Å) is significatively shorter than ***LB*** H–bond distance (2.72 Å). The association of both results indicates that ***CB*** H–bonds are stronger than ***LB*** H–bond in **M(TT)**.

Table 4.8. FT-IR assignment in "Thioamide II" and "Thioamide A" regions based on DFT calculation of **M(TT)**, (medium (m) and strong (s)) represent the intensity of the interaction.

Components	Experimental Wavenumber	Simulated Wavenumber	Intensity	Assignment
1	1475	1454 1457 1460	s	$\delta(CH_2)$, $\delta(CH_3)$
2	1502	1490 1491	s	In plane δ(CH) aryl
3	1519	1505	s	"Thioamide II" involving *LB* and *CB*
3b	1522	1512	s	
4	1544	1525	s	
5	1577	1532	m	
6	3106	3056, 3056, 3030, 3029	s	$\nu(CH_3)$
7	3136	3235	w	ν(CH) aryl
8	3164	3144	s	ν(CH)aryl+weak "Thioamide A" (CB H bond)
9	3239	3145	s	ν(CH)aryl + "Thioamide A" CB H bond)
10	3257	3296	w	"ThioAmide A" (LB H bond)
11	3271	3307		

Figure 4.20 also presents measurements from 10 K to 290 K and the thermal dependence of the most intense features is given in Figure 4.21. Despite a similar assignement, ("Thioamide II") the component 5 exhibits a strong anharmonic behavior as compared with the components 2 and 3. This strong thermal dependence is typical of NH engaged H−bonds. The different "Thioamide II" has different symetries; the ***CB*** and ***LB*** H−bond are moving in anti-phase for the component 5 and in phase for components 3 and 4, see Figure 4.21. This point could be the key for the harmonicity of 3.

In the region of "Thioamide A" (see Figure 4.20 B and Figure 4.21 B), as expected, the thermal dependence of the main components (8 and 10) exhibit different thermal behavior. In particular, the component 8 (cyclic ***CB***, more engaged) exhibits a strong anharmonic shift (+ 14 cm^{-1}) compared with the component 10 (linear ***LB***, less engaged) that slightly shifts (+ 5 cm^{-1}). The different thermal behavior of the two bands follows a classical behavior related with the relative different strength of H−bonds between ***CB*** and ***LB***.

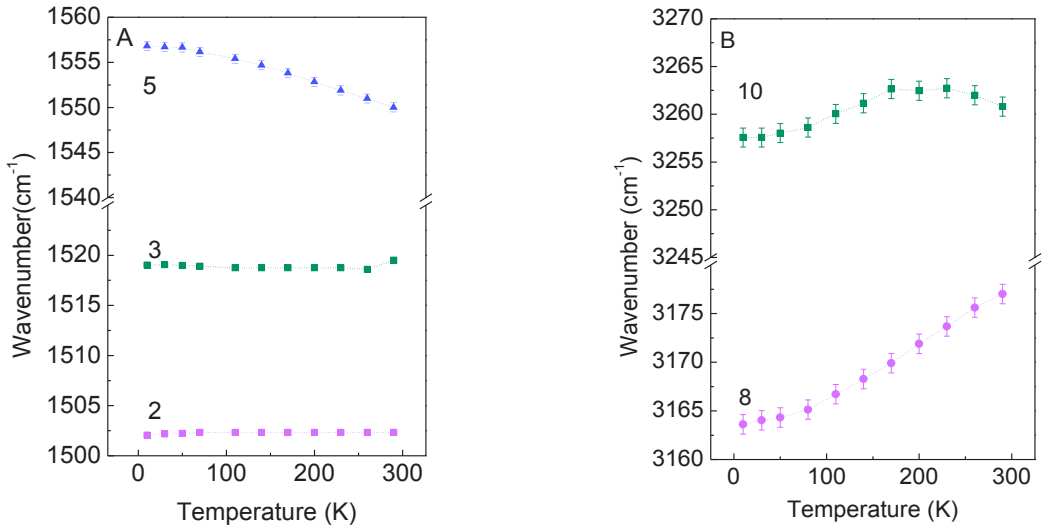

Figure 4.21. Thermal dependence of the components assigned by A) 2, 3 and 5 in "Thioamide II" region and B) 8 and 10 in "Thioamide A" region. The lines through the data are a guide to the eye and the error bars are also represented.

Figure 4.22 shows a squematic representation of the motions of the H–bond interactions related with the components 1, 2, 3, 4, 5, 8 and 10.

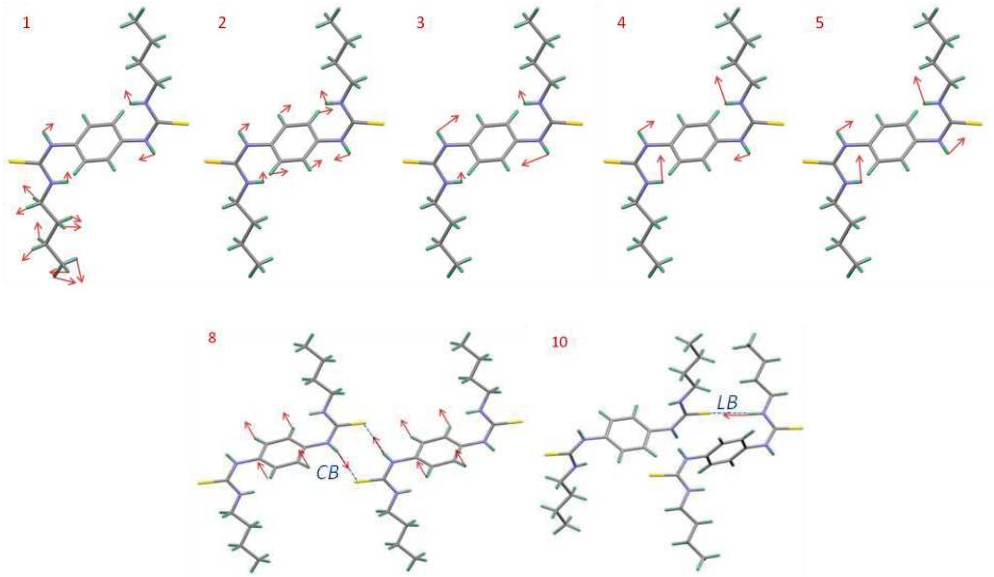

Figure 4.22. Schematic representation of the H–bond interactions related with the components 1, 2, 3, 4, 5, 8 and 10 corresponding to atomic motions (1) at 1457 cm^{-1}, (2) at 1490 cm^{-1}, (3) 1505 cm^{-1}, (4) 1525 cm^{-1}, (5) at 1532 cm^{-1} (8) at 3144 cm^{-1} and (10) at 3296 cm^{-1}.

In "Thioamide V" region shown in Figure 4.23 the infrared spectrum of **M(TT)**, depicts some peaks that are significatively damped when temperature is increased. According to the assignment, most of the components observed in this region are related to out of plane δ(NH), see Table 4.9. The components 12, 13, 14, 15 and 16 are associated to vibration inducing a modification of the linear (***LB***) H–bond whereas components 17 and 18 observed at high frequencies are associated to cyclic (***CB***) H–bond. One can notice that comparison between DFT spectra and experimental one shows a strong shift for components 17 and 18 related to the strong ***CB*** H–bond. Apart from a change in the intensity with a decrease of the temperature, the vibration associated to ***LB*** H–bond does not shift significatively. However, in case ***CB*** H–bond a downshift of - 6 cm^{-1} can be observed.

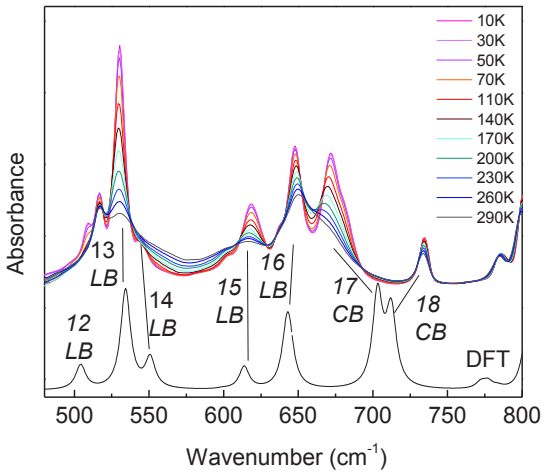

Figure 4.23. FT-IR spectra as function of temperature in "Thioamide V" region of **M(TT)**. The DFT spectrum is also shown.

Table 4.9. FT-IR assignment in "Thioamide V" region of **M(TT)** based on DFT calculation (medium (m), and strong (s)) represent the intensity of the interaction.

Component	Experimental Wavenumber	Simulated Wavenumber	Intensity	Assignement
12	509	502	s	Out of plane δ(NH) relatively to C=S
13	529	534		
14	545	550	s	Out of plane δ(NH) relatively to C=S
15	603	599		
16	619	613	m	Out of plane C relatively to SNN
17	636	642 643	s	Out of plane δ(NH) relatively to C=S
18	673	703		
19	734	708	s	CH_2 rock + Out of plane δ(NH) relatively to SH

Vibrational study of H(TT)

Figure 4.24 shows the comparison between the infrared spectra of the **M(TT)** and **H(TT)** in "Thioamide II" and "Thioamide A" regions. The FT-IR spectra of **H(TT)** in both regions show a much broader shape of "Thioamide II" bands compared with **M(TT)**. The precursor **P(TT)** remains close to **M(TT)** even if some modifications are exhibited in the relative intensities. After inorganic polycondensation, IR spectra is deeply modified (see IR spectrum of **H(TT)**). The two components observed in **H(TT)** infrared spectra in the "Thioamide II" region can be identify reasonably: component (2) at lower frequency (1510 cm^{-1}) is related to δ(CH) aryl in plane as this band appears for all hybrids at the same position and component (3) at higher frequency (1542 cm^{-1}) is associate to "Thioamide II" vibration.

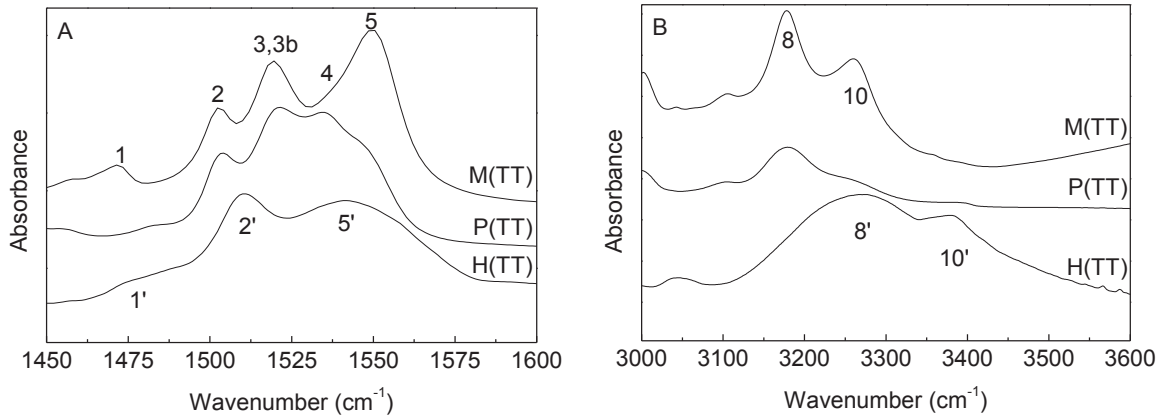

Figure 4.24. FT-IR spectra in A) "Amide I" and "Amide II" regions and B) "Amide A" region"of **M(TT), P(TT)** and **H(TT)**.

In the "Thioamide A" region, at first sight a significant broadening and a global upshift of the "Thioamide A" features is shown in agreement with the "Thioamide II" behaviour. It indicates that intermolecular H–bonding network is very inhomogeneous and weaken in the hybrid. Therefore the spreading of the H–bonding strengths suggests that affiliation of ***CB*** or ***LB*** H–bond is not relevant anymore showing the dramatic impact of the inorganic polycondensation for this compound.

Two types of intermolecular H–bonds (cyclic and linear) are evidenced in **M(TT)**. Infrared spectroscopy enables the differenciation the behavior of these two H–bonds. The integrity of the intermolecular organization of model **M(TT)** is lost in the corresponding

hybrid. A mean weakening and a significative dispersion of H–bonds are observed in hybrid amorphous material.

Summary: on the modulation of the interaction through H–bonds in models and hybrids urea thiourea systems

In the compounds studied here it appears that, intermolecular interaction through H–bonds depends significatively from the substitution of oxygen by sulfur, see Figure 4.25.

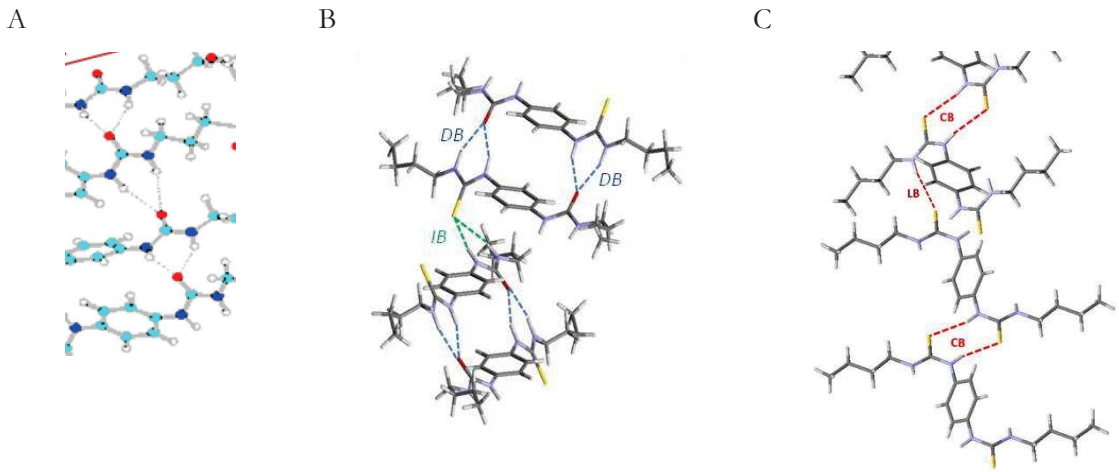

Figure 4.25. Schematic representation of the local environnment throught intermolecular H–bonds in A) **H(UU)**, B) **M(UT)** and C) **M(UU)**.

1) **For model compounds:**
   - Intermolecular (N-H…X) H–bonds are very different according to the system, see Figure 4.25;
   - For **M(UU)** a bifurcated H–bonds with N-H…O distance of 2.8 Å is suggested from comparison with IR dynamic of **P(UU)**;
   - For **M(UT)** an asymetric intra-dimer bifucated H–bonds with N-H…O distance of 2.85 Å and 2.88 Å and asymetric inter-dimer bifucated H–bonds N-H…S of 3.34 Å, 3.52 Å were obtained from single crystal X-ray diffraction;
   - For **M(TT)** a cyclic H–bond with N-H…S distance of 2.54 Å and linear H–bond distance N-H…S of 2.72 Å, were obtained from single crystal X-ray diffraction.

It is thus possible to see that the organization in **M(UU)**, base on stacking of molecules interaction through two bifurcated H–bonds, is also found in **M(UT)** at the scale of a dimer. Assymetric interdimer bifurcated H–bonds with a much longer H–bond distance (>15%) also appear as a consequence of the substitution of one oxygen by a sulfur [189,191]. As for a system based on H–bonds interactions via solely thiourea, **M(TT)**, specific H–bonds interactions appear, in complete disruption with the organization described in **M(UU)** and **M(UT)**. As a matter of fact, cyclic and linear bonds have previously been reported in thiourea based systems [191].

This analysis is based only on structural arguments, it can be noticed that the influence of the chemistry (solvent used during the sol-gel process for example) cannot be studied as the different systems are not soluble in the same solvent.

2) Comparison of the infra-red dynamics in models and hybrids:

- For **UU** system similar local organization are observed between **M(UU)** and **H(UU)** associated to the presence of bifurcated H–bonds network;
- For **UT** system the transcription of the local structure from the model to the hybrid seems to be preserved partialy, at the scale of interactions intradimer H N-H…O bonds. Nevertheless, a significative part of intra-dimer bonds appear as nearly free (approximation 50 %).
- For **TT** system, the local structure via H N-H…S cyclic and lineal bonds observed in the model does not appear as preserved in the hybrid material. The network of H–bonds in **H(TT)** appears as completely disordered and with significatively weaker mean bonds and compared to **M(TT)**. Thus intermolecular interactions through H–bonds between thiourea species don't appear strong enough to face the disorder introduced by inorganic polymerization unlike urea based systems. The cyclic H-bonds cannot, in this case, preserved the local organization.

The comparison of the spectra signatures for **M(UU)**, **M(UT)** and **M(TT)** can be performed based on N-H bounded "Amides", see Figure 4.26.

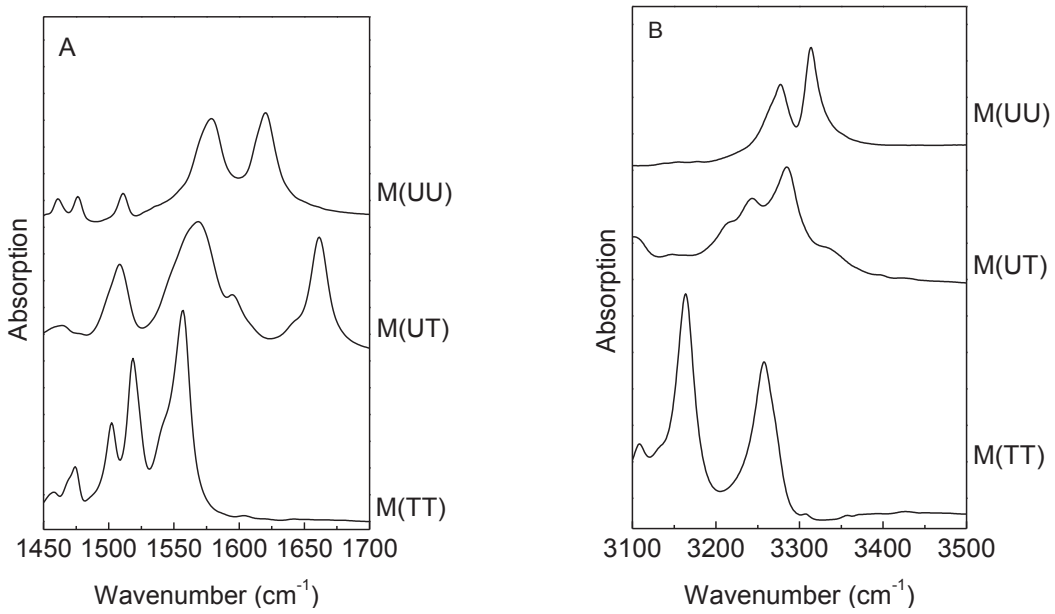

Figure 4.26. FT-IR spectra acquired at 10 K in A) "Amide I", "Amide/Thioamide II" and B) "Amide/Thioamide A" regions of **M(UU)**, **M(UT)** and **M(TT)**.

The vibrations "Amide/Thioamide II" mainly reflect an average environment in the systems because of the coupled character of these vibrations. They globaly decrease in frequency passing though **UU**, **UT** then **TT** when N-H … X, (where X= O or S), distances decrease and also when the diversity of environment also increases. This band is sensitive at the same time to the strength of H–bonds and to the structure. This result can thus be interpreted as a progressive decrease of the intermolecular interactions by H–bond or/and the raising sensitization to the progressive modification of the molecular structure with the increase of the substitutions O > S.

"Amide/Thioamide A" vibrations globaly decrease in frequency when N-H…X distances are reduced. On the basis of the results DFT, a dependence of the frequencies of vibrations with the various environments of links H with the N-H … X distances is proposed in Figure 4.27. Here the advantage lies in the fact that the frequencies are characteristic of the various "Amide/Thioamide A" in H–bonds strengthening of interatomic NH stretching vibrations. On the basis of bond strength inversely proportional to the of internal force constant strength (related to the frequency of "Amide/Thioamide A", the strengths of intra-dimers connections in **UT** are comparable to those of the **UU** systems with comparable distances. The inter-dimer intermolecular H–bond in **UT** involving the sulfur from thiourea

and the NH from urea seems weaker and the distance more important. We can note that the dependence of the "Amide I" between **UU** and **UT** is not consistent with that of the "Amide A". In this latter case the potential of "Amide A" is fully harmonic contrary to **UU** system.

For the system **TT** system, we observe that the frequencies of "Thioamides A" involved in cyclic and linear H–bonds appears at lower frequency than in **UT** and **UU** systems. In a concomitant way the H–bond distances are much smaller for **M(TT)**. These results also show that the inter-thioureas cyclic H–bonds are stronger than linear ones.

Base on this analysis, the results suggest that the inter-molecular thioureas-thiourea H–bonds would be stronger in **M(TT)** than H–bonds observed in **M(UT)** and **M(UU)** systems. These results surprising if we consider that the electronegativity of the sulfur is lower than that of the oxygen.

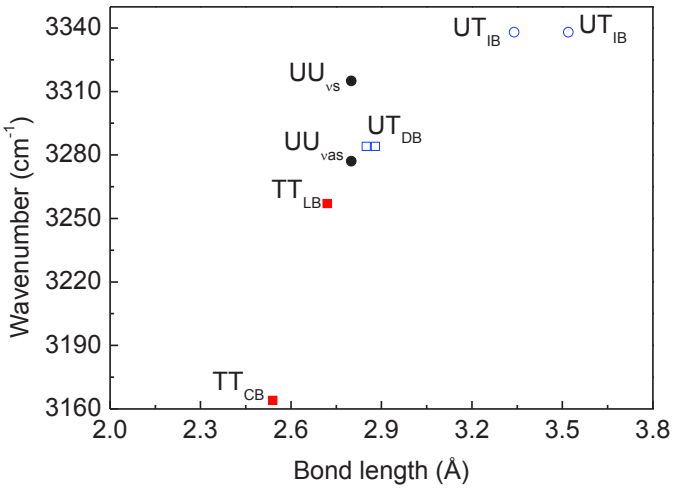

Figure 4.27. Bond length in the "Amide A" vibration observed in **M(UU)**, **M(UT)** and **M(TT)**.

4.5 Influence of modulation of H–bonds on the mechanical behaviour under high pressure

As well as H–bond strength can be modulated by temperature, the effect of pressure on H–bonds can be a very efficient tool to understand this type of interaction.

Pressure studies on H–bonded materials have been reported in literature [193,194], not only to predict the response of a crystal structure to pressure, but also, to solve problems related to polymorphism, crystal engineering and structure-properties correlations.

It is well established that pressure can reduce the distances between molecules and that compressibility of H–bonded crystals is related to the nature, the strength of H–bonds. Under compression molecules tend to achieve close packing, affecting H–bonding interactions. Phase transitions driven by H–bonds can be observed through changes of configuration of molecular fragments, changes in polarization of H–bond, migration of a proton from one atom to other etc. [195,196]. When phase transitions, observed through pressure, mainly involve modifications of intermolecular H-bonds, the changes are observed to be reversible.

Therefore, in the next section, in situ high pressure vibrational spectroscopy experiments are performed on hybrid materials and model organic substructures, in order to study how the modulation of the different bonds encountered in **UU**, **UT** and **TT** systems affect their mechanical properties under pressure. Thus pressure dependence in the "Amide I", "Amide II" and "Amide A" and "Amide V" regions of **UU**, **UT** and **TT** systems are presented.

Under pressure, for most intramolecular bonds, the intermolecular vibrations frequency upshifts, as a result of the force constant increase. We name this upshift hereafter the "*pressure effect*" (PE). We have shown earlier that "Amides I" and "Amide A" are very good markers of intermolecular H–bond strengthening (HBS), leading to a downshift of their frequencies. Therfore the pressure dependence of these "Amide" vibrations will result from the superimposition of the PE and of the H-bond response, see Table 4.10.

Table 4.10. Expected influence of H-bond response to applied pressure and PE on the different "Amide" vibrations.

Vibrational region	PE	HBS
"Amide A"	upshift	downshift
"Amide I"	upshift	downshift
"Amide II"	upshift	upshift

4.5.1 Infrared study of UU system

The first study under pressure will be presented for **UU** system. Figure 4.28 shows the FT-IR spectra as function of pressure in "Amide II" and "Amide I" regions for **M(UU)** and **H(UU)**, respectively. At first glance, most features are shifted under pressure and a broadening is observed for **M(UU)** and **H(UU)**, as pressure increases.

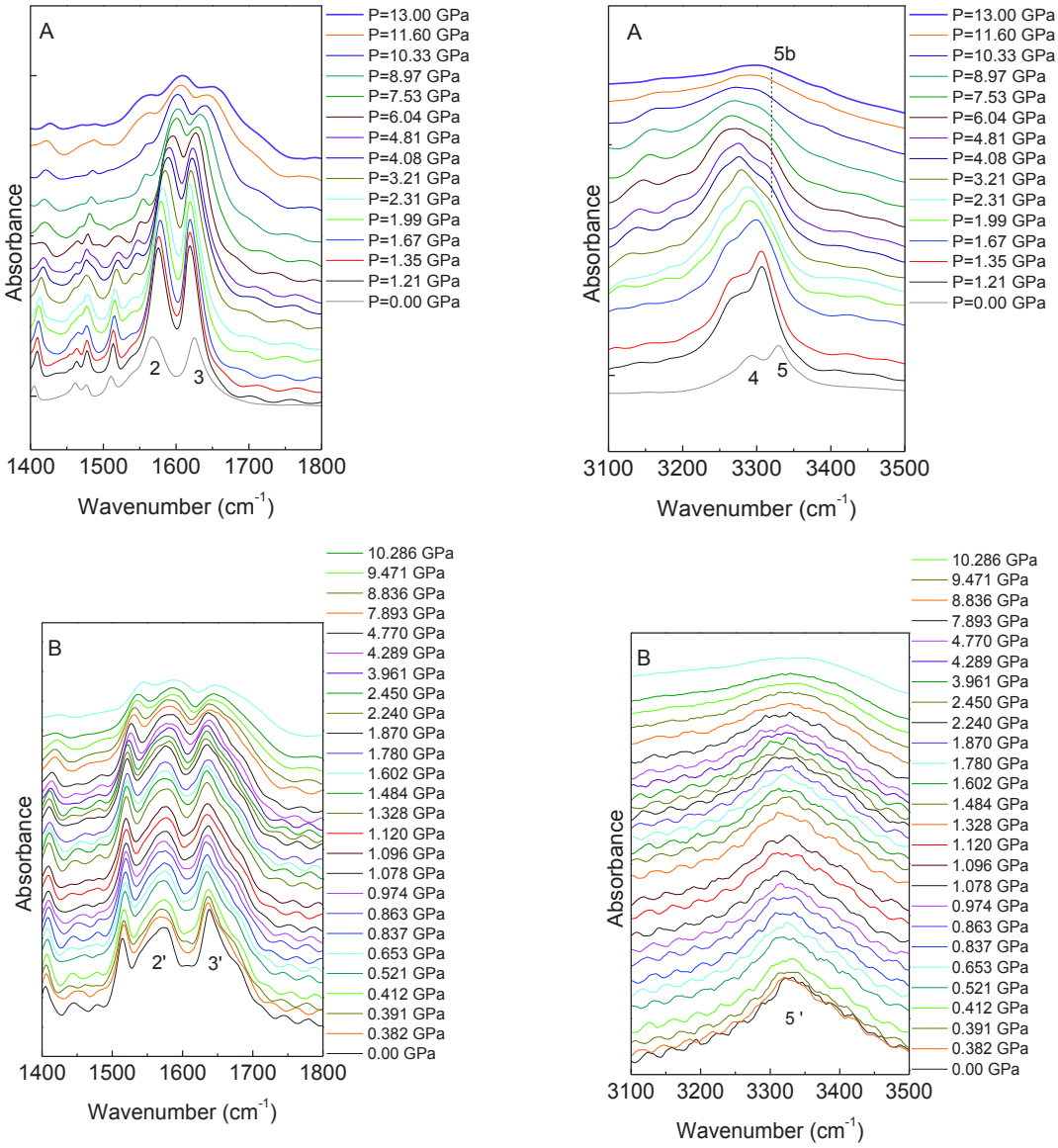

Figure 4.28. FT-IR spectra as function of pressure in the "Amide I" and "Amide II" (left) and "Amide A" (right) regions of A) **M(UU)** and B) **H(UU)**.

In Figure 4.29 the pressure dependence in "Amide I", "Amide II" and "Amide A" regions for **M(UU)** (open circles and crosses) and **H(UU)** (full squares) are superimposed. In the following "Amide" regions are analysed the one after the others. For one region, the results on models **M(UU)** and **H(UU)** are discussed simultaneously.

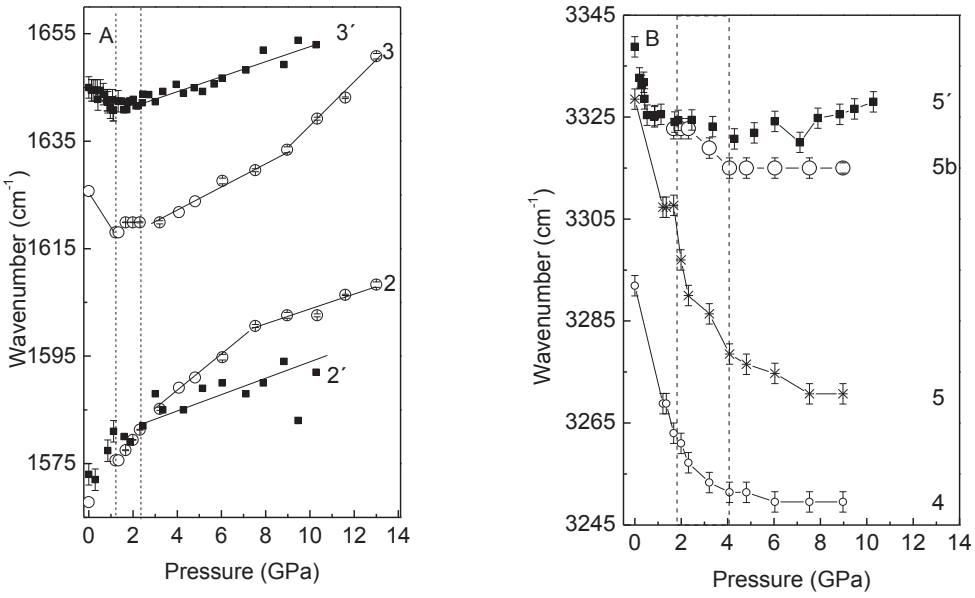

Figure 4.29. Pressure dependence of the components assigned by A) 2 and 3 in "Amide I" and "Amide II" regions and B) 4 and 5 in "Amide A" region of **M(UU)** (open circles) and **H(UU)** (full squares). Assignment is given in Figure 4.28. The lines through the data are a guide to the eye and the error bars are also represented.

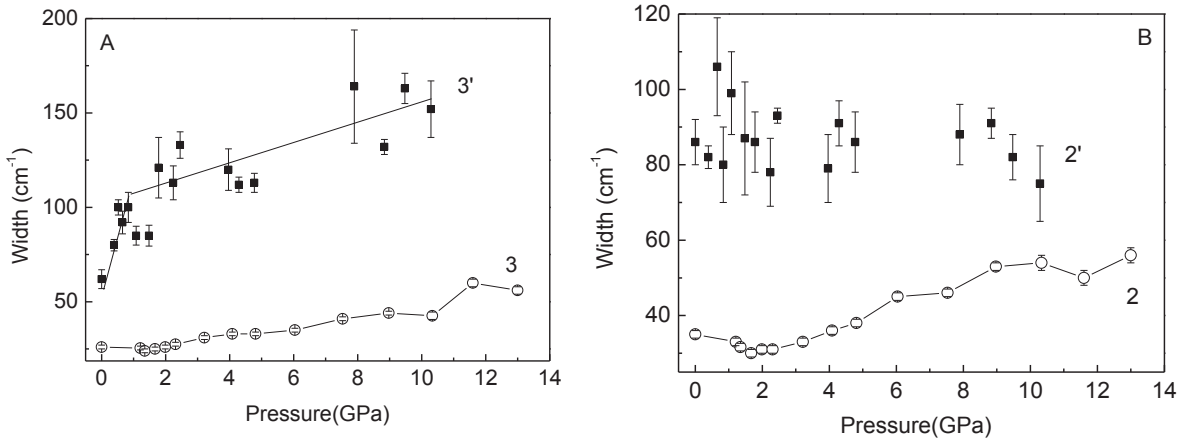

Figure 4.30. Width of the components A) 3 and 3´ in "Amide I", B) 2 ans 2' in "Amide II" as function of pressure of **M(UU)** (open circles) and **H(UU)** (full squares). The lines through the data are a guide to the eye and the error bars are also represented.

In the region of "Amide A" (Figure 4.29 B) two regimes are observed in the temperature dependence of **M(UU)**:

- From 0 GPa to 2-3 Gpa a dramatic decrease of the frequency of component 4 and 5 is observed as a function of pressure;

- Around 1.2 GPa a new component (5b) appears at high frequencies;
- From 3 GPa to 8 GPa, the pressure dependence of components 4 and 5 becomes smaller, and the new component (5b) no longer evolves in this domain (> 4 GPa).

For **M(UU)**, we can interpret this global behavior under pressure as following :

- From 0 to 1.2 GPa a dramatic HBS (-15 cm^{-1}/GPa for "Amide A");
- From 1.2 to 3-4 GPa, a moderate HBS (-8 cm^{-1}/GPa for "Amide A")
- From 4 to 10 GPa, a strong competition between PE and H-bond reenforcement.

For the hybrid **H(UU)**, a similar tendency is observed for the broad "Amide A" band. A drastic decrease of the frequency is observed up to 1 GPa, signing for HBS and the frequency globaly remains constant from 1 GPa to 8 GPa (1.12 cm^{-1}/GPa), suggesting that HBS is compensated by PE. For higher pressures, the frequency of component 5 slighly upshifts by 1.3 cm^{-1}/GPa. All the different regimes are quantitatively summed in Table 4.11.

Table 4.11. Summary of the pressure and slope details obtained from FT-IR pressure behavior of **M(UU)** and **H(UU)**.

Vibrational region		M(UU)				H(UU)		
Amide A	**Pressure (GPa)**	**0-2**	**2-4**		**4-9**	**0-1**	**1-8**	**8-10**
	Slope (cm^{-1}/GPa)	-15±1	-8±1		1-7±0.2	-23±3	0	1.3±0.2
Amide I	**Pressure (GPa)**	**0-1.2**	**1.2-2.5**	**2.5-8**	**8-13**	**0-1.5**	**1.5-2.5**	**2.5-10**
	Slope (cm^{-1}/GPa)	-6±1	0	2.5 ±0.2	4±0.2	3.4±0.48	0	1.4±0.1
Amide II	**Pressure (GPa**	**0-3**	**3-8**		**8-13**	**0-3**		**3-10**
	Slope (cm^{-1}/GPa)	5.4±0.2	3.4±0.2		1.4±0.2	4.7±0.8		0.5±0.3

The pressure behavior of "Amide II" and "Amide I" are in agreement with the behavior observed for "Amide A" in **M(UU)** and **H(UU)**.

For "Amides II", component 2 upshifts following three different regime (0-3 GPa; 3-8 GPa and 8-13 GPa) characterized by an increasing slopes, see Table 4.11, for **M(UU)**. While for **H(UU)** (component 2') two main regimes are found. In the first from 0 GPa to 3 GPa the

PE follows the model behavior and after 3 GPa a weak slope, consequence of PE compensation, is shown and is in agreement with "Amide" dependence.

For "Amides I" behavior are observed as a function of pressure exhibiting a dramatic sensitivity to pressure compared to "Amide A" and "Amide II" vibrations. A clear change of slope is identified around 1.2 GPa.

- Before 1.2 GPa "Amide I" frequency is significatively decreasing for **M(UU)** and for **H(UU)**), indicationg that HBS dominates the pressure behavior;
- Between 1.2 GPa and 2.5 GPa a plateau is observed, showing that *PE* counterbalance the *HBS*. It is worth noting that competition of PE with HBS act differently as a function of pressure on "Amide I" compared to "Amide A";
- Beyond 2.5 Gpa "Amide I" frequency starts to increase with pressure, because PE is the dominant effect;
- Besides, a change of slope, (see Table 4.11) is observed around 8 GPa (for **M(UU)** only).

For **M(UU)** it is interesting to observe that, above 2 GPa, as HBS becomes more moderate, the width of "Amide I" and "Amide II" significantly increases. This behavior indicates H–bonding distorsion leading to increasing disorder in local structure with pressure. The appearance in "Amide A" of 5b component around 1.2 GPa also participates to that dispersion. For **H(UU)**, the width of "Amide I" increases strongly up to 2 GPa and more moderately above, see Figure 4.30 A, indicating that, contrary to **M(UU)**, increasing disorder is observed concomitantly with the strong HBS regime .

Pressure experiments in the region of "Amide V" have only been performed in infrared up to 650 cm^{-1}, because of the cut off of the detector up that region, see Figure 4.31.

Results for **M(UU)** in this region are presented above, the same study is not available for hybrid **H(UU)** as contributions from Si-O bonds dominate the spectra. The component 8 observed at 543 cm^{-1} related to out of plane δ(NH) can be followed while applying pressure. From 0 GPa to 0.91 GPa, a clear increase in the relative intensities of the component 8 as compared to component 7 is shown on Figure 4.31 A and Figure 4.31 B. A simultaneous upshift of the component 8 from 543 cm^{-1} to 578 cm^{-1} is observed. This evolution of the

spectra can be compared to that observed when temperature was decreased to 10 K, see Figure 4.31 C, *i.e.*, HBS is shown when reducing temperature (see previous section).

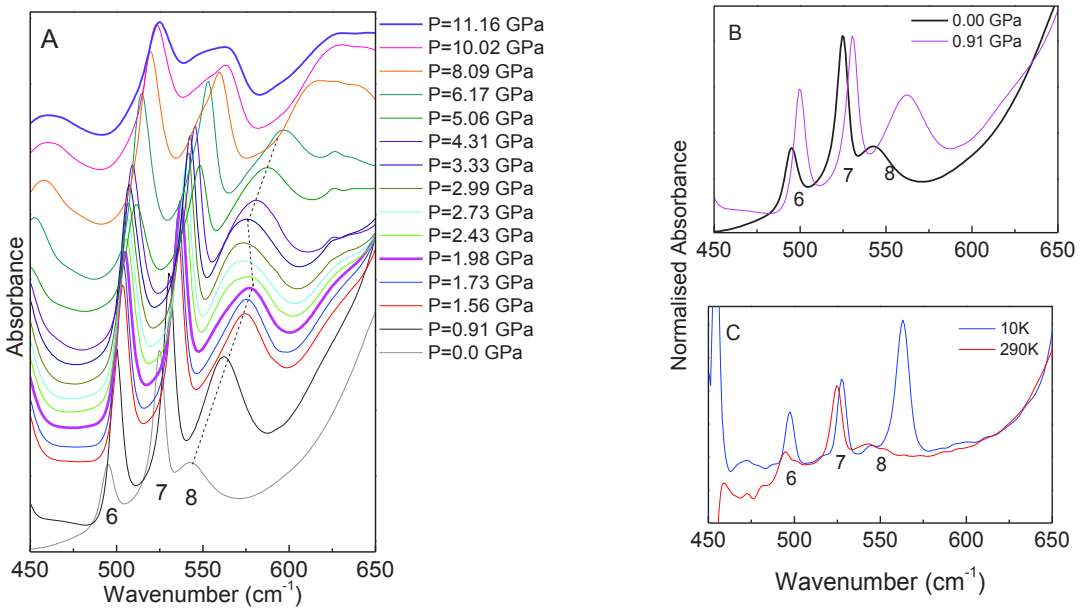

Figure 4.31. A) FT-IR spectra as function of pressure in "Amide V" region. The dashed lines through the data are a guide to the eye. B) FT-IR spectra acquired before apply pressure (0.0 GPa) and after decompression (0.91 GPa) and C) FT-IR spectra acquired at 10 K and 290 K of **M(UU)**. For Figure B and C the spectra have been normalized assuming that the intensity of mode 7 is less affected by pressure and temperature changes. The lines through the data are a guide to the eye.

A change in the behavior is observed from 2 GPa to 3.3 GPa where component 8 appears broader and downshifted. This broadening could be related to a new component at lower frequencies such as the weakly bonded component 5' appearing at 2 GPa in "Amide A". For pressures higher than 3 GPa the band 8 upshifts again continuously up to 11 GPa. Therefore the "Amide V" behavior is consistent with other "Amide" vibrations.

FAR-infrared region gives information on the intermolecular bonds interactions. For **H(UU)**, above 2.5 GPa, a broadening of the peak centered around 138 cm^{-1} is observed and assigned to intermolecular H–bond see Figure 4.32. As a matter of fact, for higher pressure a new component appears around 170 cm^{-1}, signing for an increased dispersion of H–bonds and appearance of a new environment with stronger H–bond. One can notice that this behavior is consistant with "Amide I" and "Amide A" vibrational dependance under pressure

where HBS compete with PE in this pressure range. The two peaks remain with consequent intensity over 12.7 GPa. One can notice that information obtained in this range is more sensitive to structural medium range order compared to intramolecular range.

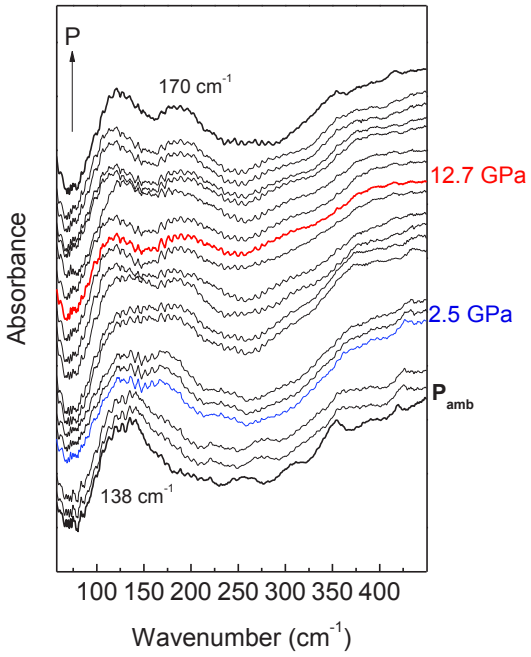

Figure 4.32. FAR infrared as function of pressure and of **H(UU)**.

To summarize, this set of results indicates that in the first regime between 0 GPa and 1.2 GPa a significant strengthening of the H–bond occurs for both **M(UU)** and **H(UU)** as shown by both Amide A and Amide I downshifts. Above 1.2 GPa hybrid and model exhibit different behavior.

- For **M(UU),** between 1.2 GPa and 2.5 GPa a new "Amide A" component (5b) related to weaker H–bond appears for the model **M(UU).** Simultaneously**,** .a plateau is observed for "Amide I" interpreted as the compensation of HBS by PE. Beyond 2.5 GPa, *PE* dominates the pressure dependence of "Amide I" and a progressive increase of structural disorder is exhibited. Around 6-8 GPa the system presents a strongly disordered character.
- For the hybrid **H(UU)**, the changes observed between 1.2 GPa and 8 GPa lead to progressive disorder concomitant with futher HBS and above 8 GPa the PE is dominating "Amide A" and "Amide I" behavior .

The differences observed between **M(UU)** and **H(UU)** (limited pressure of H–bond compression and weaker slopes for "Amide I") can be accounted to the presence of the polycondensed silicate network that induces some constrains on the organic network relaxation. The response of polycondensed silicate network can be observed in the region of Si-O stretch in the range 1000-1100cm^{-1}, see Figure 4.33. It means that silicate network is not significantly affecting the pressure range where different H–bonds behaviors are exhibited. It suggest that relative degrees of freedom are still available for H–bonds to absorb the pressure constrains. The broad band is relatively constant up to 6 GPa. Above this pressure a general broadening is observed.

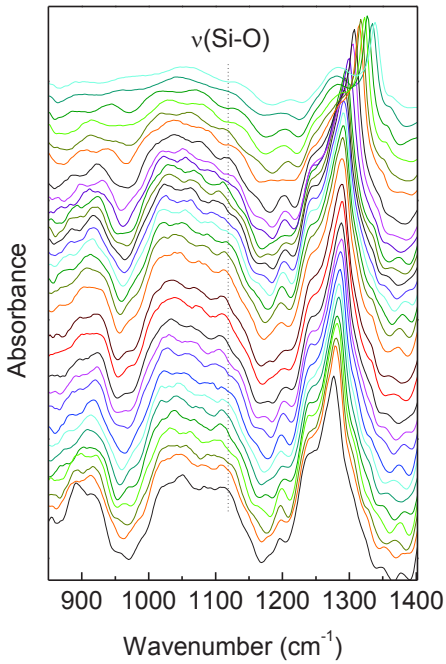

Figure 4.33. FT-IR spectra as function of pressure in ν(Si-O) vibration of **H(UU)**. The lines through the data are a guide to the eye.

In order to estimate the elastity of the compression mechanism involved between 0 GPa and 12 GPa in **H(UU)**, ex situ X-ray diffraction measurements have been performed after densification in Belt Cell for **H(UU).** Three samples have been prepared after permanent densification at 1.8 GPa, 2.5 GPa and 7.7 GPa. The results in Figure 4.34 show that the main Bragg peaks of pristine samples are observed at 1.8 GPa and 2.5 GPa meaning that a global elastic response of the system is obtained. Yet at 7.7 GPa, the remaining feactures

are very broad, signing for a global distorsion of the system in agreement with vibrational siloxane network response, see Figure 4.34.

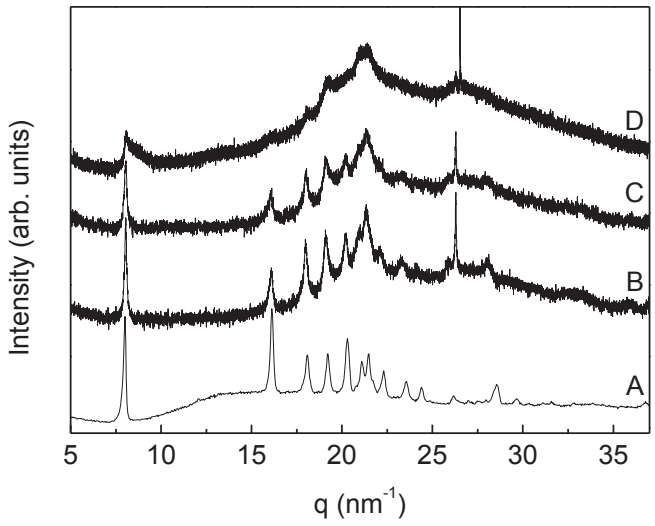

Figure 4.34. X-ray diffraction patterns measurement of **H(UU)** after pressurization at A) 0.0 GPa, B) 1.8 GPa, C) 2.5 GPa and D) 7.7 GPa.

Finally a simple model could be proposed in order to explain the compression mechanism associated to bifurcated urea-urea bonds in **UU** system. Up to 2 GPa the intermolecular H–bonds become much stronger as they are compressed. Broad dispersions of H–bonds strength are observed. One can notice that stronger H–bonds appear. A progressive disorder around H–bonds is exhibited concomitantly to futher HBS as pressure increases. Silica network is not affected by pressure below 6 GPa. Finally, we show that H–bonds act as a constrains relaxor up to 6-7 GPa.

Note that the reversibility of **M(UU)** and **H(UU)** is discussed next. Now that the compression mechanism has been decrypted for urea urea bifurcated H–bonds, it is interesting to compare it with the behaviour of **UT** compound which exhibit also bifurcated bonds but invoving both urea and thiourea groups. We present in the following subsection the behaviour of **UT** systems at high pressure.

4.5.2 Infrared study of UT system

Figure 4.35 shows the spectra at high pressure in the "Amide I", "Amide/Thioamide II" and "Amide/Thioamide A" regions for **M(UT)**, (see Figure 4.35 A) and **H(UT)**, (see Figure 4.35 B), respectively. Some peaks are shifting with pressure increase.

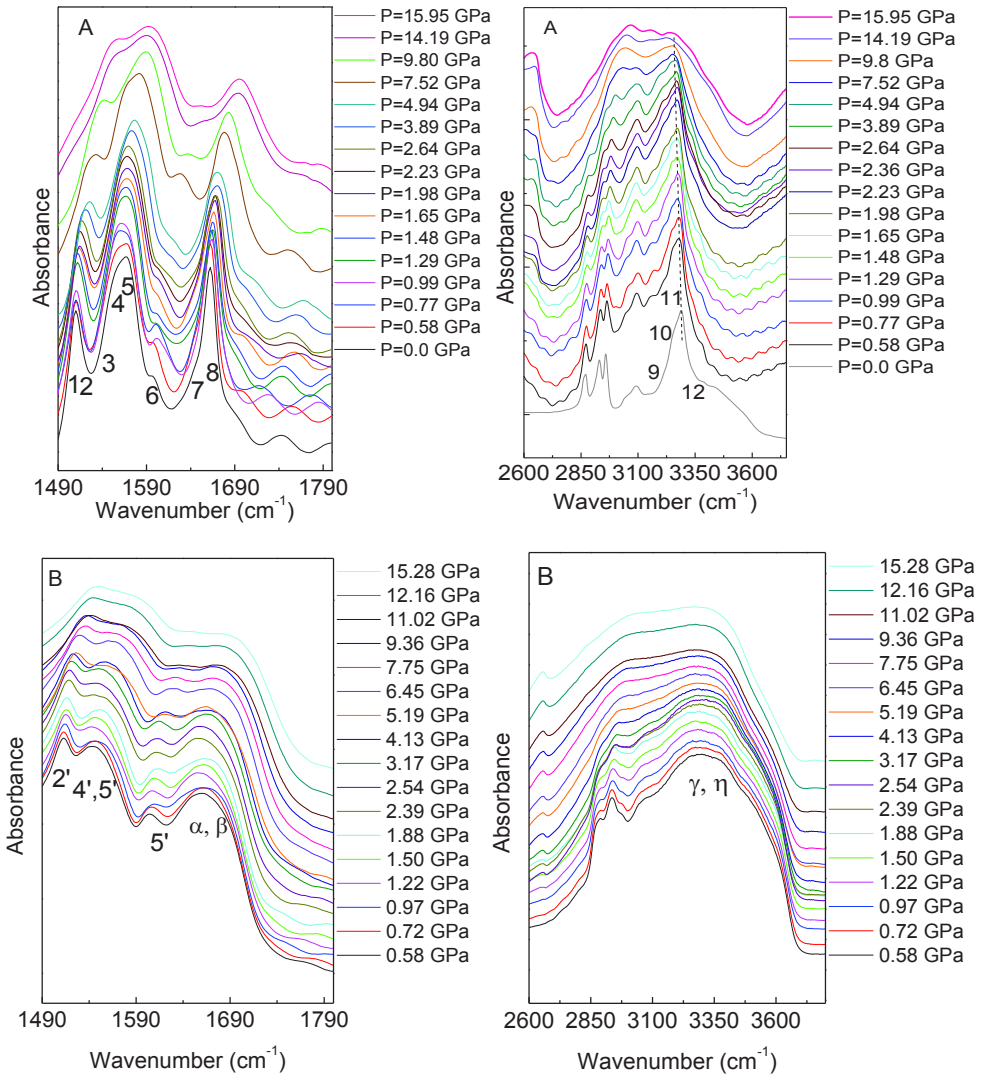

Figure 4.35. FT-IR as function of pressure in "Amide I", "Amide/Thioamide II" and "Amide/Thioamide A" regions for A) **M(UT)** and B) **H(UT)**. The lines through the data are a guide to the eye.

Detailed pressure dependence is shown on Figure 4.36, for both **M(UT)** and **H(UT)**.

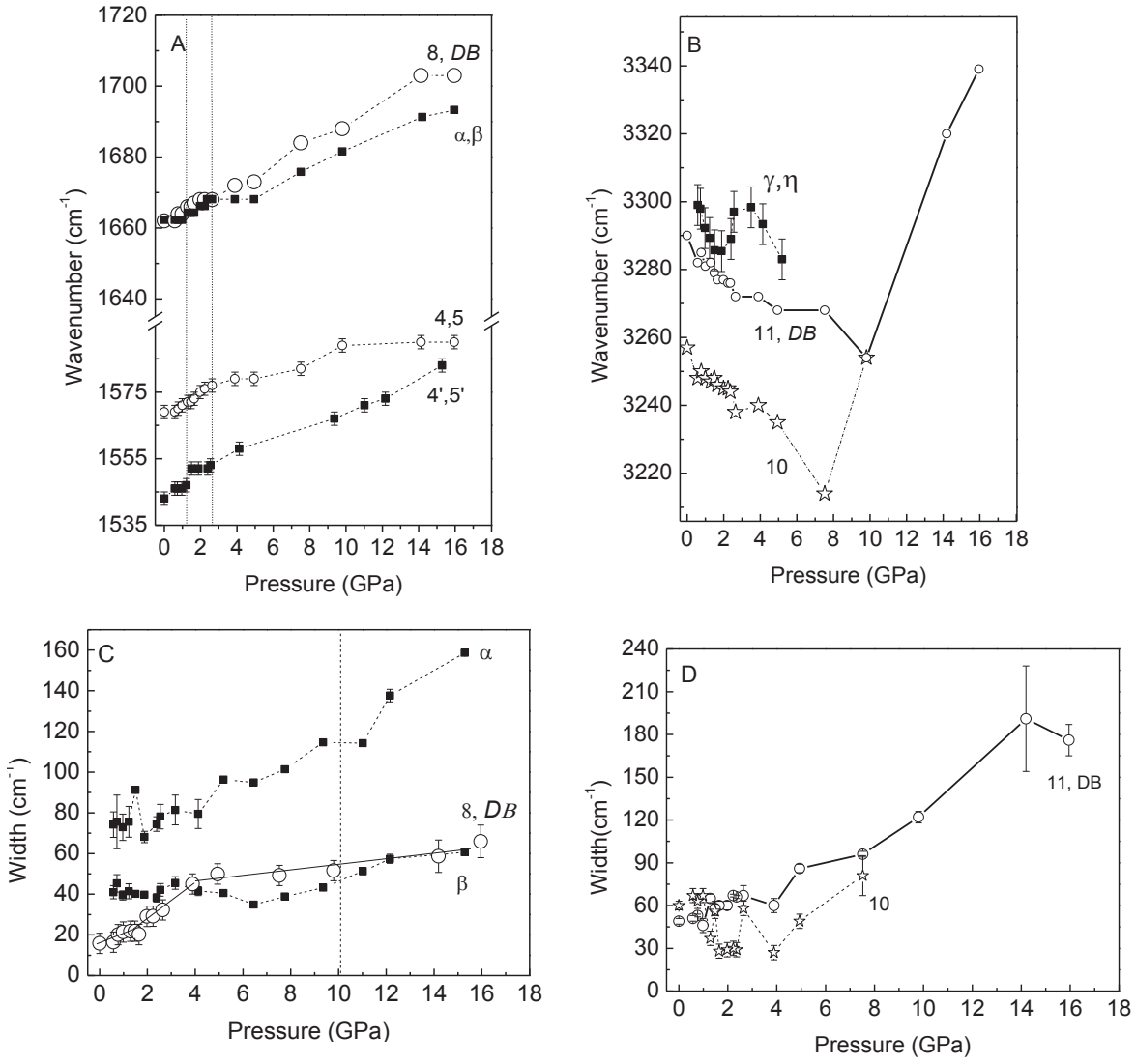

Figure 4.36. A) Pressure dependence in the "Amide I", "Amide/Thioamide II" and Pressure dependence in "Amide/Thioamide A" regions. C) Width as function of pressure in "Amide I" and D) Width as function of pressure in "Amide/Thioamide A" regions of **M(UT)** (open circles) and **H(UT)** (full squares). The lines through the data are a guide to the eye and the error bars are also represented.

For "Amide/Thioamide A" in **M(UT)** the broad band has been deconvoluted into the 4 components defined earlier. Component 9 and 10, both involving ***IB*** and ***DB*** vibrations, component 11, related to ***DB*** and component 12 related to ***IB***. As components 9 and 12 are very weak, we shall focus on the dependence of the component (11) which presents a downshift of ~ 34 cm^{-1} down to 8-10 GPa, signing strong HBS dor ***DB***. This downshift is firstly very strong up to 2 GPa, then the decrease in wavenumber becomes softer, see Table

4.12, reporting slopes in different pressure ranges. Over 10 GPa, the position of the band increases strongly but unfortunately few pressure point could be measured in this range. This increase indicates that PE dominate the pressure dependence and suggests that HBS decreases (or disappears) dramatically. The width of "Amide/Thioamide A" in **M(UT)** increases very strongly from 10 GPa indicating a much higher degree of disorder above this pressure.

"Amide/Thioamide A" in **H(UT)** is very broad and the pressure dependence could be measured up to 6 GPa. A clear downshift is observed up to 1.5 GPa, indicating HBS. From 1.5 GPa to 2.5 GPa an upshift would appear followed by a new downshift. Above 6 GPa, a strong enlargement of the broad band is observed, see Figure 4.35, signing for an increasing disorder.

The behavior of "Amide I" for **M(UT)** mainly reflecting ***DB*** bond behavior with an average constant upshift from 0 GPa to 15GPa, wich results from the competition between ***DB*** HBS (downshift) and PE (upshift). Note that the different regimes observed for "Amide A" are not observed for "Amide I" it is worth recalling that thermal dependence for "Amide I" in **M(UT)** was very harmonic and could sign for a very distinctive energy potential for this strong ***DB*** urea thiourea H–bond.

"Amide/Thioamide II" gives averaged information on both ***IB*** and ***DB*** and their HBS decrease. From 0 GPa to 2.5 GPa the strong slope could be the result of concomitant PE and H–bond reinforcement. Over 2.5 GPa, as the slope decreases, H-bonds are still strengthening but more softly.

Table 4.12. Summary of the pressure and slope details obtained from FT-IR pressure behavior of **M(UT)** and **H(UT)**.

Vibrational region		M(UT)			H(UT)		
Amide A	**Pressure (GPa)**	**0-2.5**	**2.5-10**	**10-16**	**0-1.5**	**1.5-2.5**	
	Slope (cm^{-1}/GPa)	-5.7±0.6	2.3±0.7	14±1	-15±2	0	
Amide I	**Pressure (GPa)**	**0-2.5**	**2.5-14**		**0-1**	**1-2.5**	**2.5-12**
	Slope (cm^{-1}/GPa)	3.2±0.3	**2.9**±0.1	α	0	7.2±0.4	3.1±0.2
				β	0	7±1	2.7±0.2
Amide II	**Pressure (GPa**	0-2.7	2.7-10	10-16	**0-2.7**		**2.7-16**
	Slope (cm^{-1}/GPa)	3.9±0.2	1.5±0.2	0.17±0.05	4.0±0.6		2.2±0.1

High pressure behavior in **M(UT)** has been measure up to 650 cm^{-1} for "Amide/Thioamide V" within FAR infrared domain, see Figure 4.37. An interesting behavior can be observed for the broad contribution 13 cm^{-1} at 580 cm^{-1} assigned to out of plane δ(NH) related with ***IB*** link. A downshift is shown up to 3-4 GPa. Over that pressure, the component upshifts, see Figure 4.37 A and C. Spectra at 10 K and 290 K are also shown on Figure 4.37 B for comparison. Despite a small discrepancy in the shape of the pressure measurement (due the cut off of the detector) the downshift observed concomitanty with an increase in intensity is also observed when temperature goes from 290 K to 10 K as a signature of HBS. Therefore the results indicate HBS for ***IB*** up to 3-4 GPa. ***DB*** also shows HBS in this pressure range (see "Amide/Thioamide A" and "Amide I" pressure dependance). But above this critical pressure only is only ***DB*** demonstates further HBS.

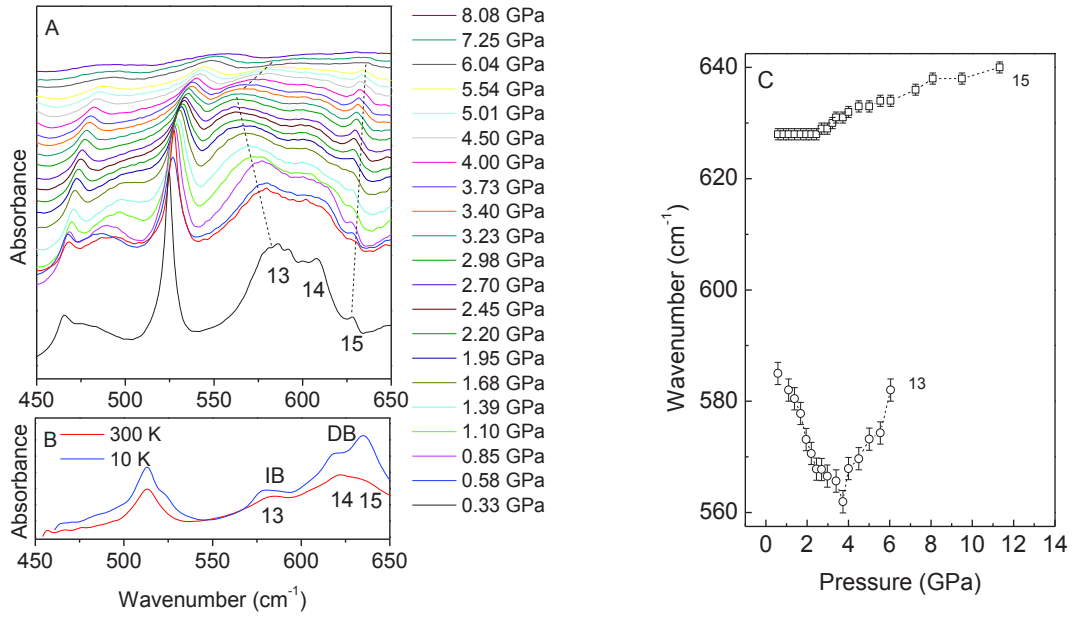

Figure 4.37. A) FT-IR as function of pressure of **M(UT)** in the "Amide/Thioamide V" region. The lines through the data are a guide to the eye. B) FT-IR spectra recorded at C) Pressure dependence of the components peaking at 524 cm^{-1} and 585 cm^{-1}. The lines through the data are a guide to the eye.

To summarise, for **M(UT)**, we can deduce from "Amide/Thioamide A" dependences that dimer bond (***DB***) gets stronger from 0 GPa to 8 GPa with two regimes: a strong HBS up to 2-2.5 GPa and a intermediate HBS between 2.5 GPa and 8 GPa. Interdimer bond, (***IB***), seems to be strengthened up to 3-4 GPa according to "Amide/Thioamide V" behavior.

For the hybrid **H(UT)**, a strong H–bond strengthening is observed from 0 GPa to 1.5 GPa, see "Amide/Thioamide A". From 1.5 GPa to 2.5 GPa, the PE suddenly become dominant giving raise to upshift. Over 2.5 GPa, HBS seems to increase again compensating PE (until 4 GPa). In this range, the organic network associated to stronger H–bond becomes more disordered. Futher disorder appears with increasing pressure above 4 GPa.

Figure 4.38 shows the infra-red spectra in the region of Si-O vibration. The broad band is not much affected by pressure up to 5-6 GPa as for **H(UU)**. Over that pressure the Si-O signature becomes much broader. Siliceous parts of the network don't seem to be reacting to compression before 5-6 GPa.

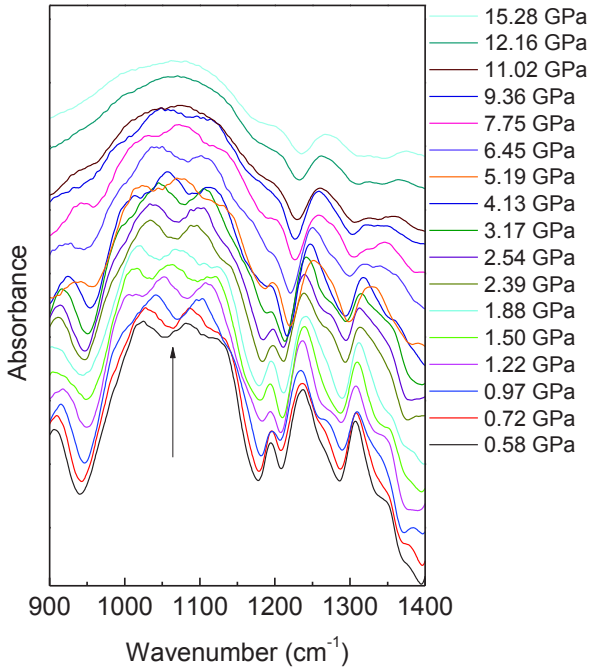

Figure 4.38. FT-IR spectra as function of pressure in Si-O-Si bridge region of **H(UT)**.

Therefore we can conclude that, for **H(UT)** a complex compression mechanism is observed from 0 GPa to 6 GPa involving mainly H–bond environment between organic substructures. This complex mechanism reflects the variety of populations of H–bonds represented in this material: two types of bonds involving C=O from urea (one weakly bonded β and one strongly bonded α) for which "Amide I" gives an average response. Also some H–bonds involving C=S bonds are not excluded, for which we only acess average information through "Amide/Thioamide II" and "Amide/Thioamide A". These different

bonds are characterized by their different strength and are thus expected to exhibit different compressibility

4.5.3 Infrared study of TT system

The pressure experiment of **M(TT)** and **H(TT)** was performed in the "Amide" region. Figure 4.39 shows the FT-IR spectra in the "Thioamide II" and "Thioamide A" regions of **M(TT)** and **H(TT)** as function of pressure. Thermal dependence is depicted in Figure 4.40.

As previously reported, the "Thioamide A" region of **M(TT)** shows two main components (8 and 10) assigned to the ***CB*** (most engaged) and ***LB*** (less engaged) H–bond interactions, respectively. These components react differently as a function of pressure. For ***CB,*** we observed between 0 GPa and 1.1 GPa a decrease in frequencies characteristic of a HBS (see component 8 on Figure 4.40 B). The slopes of the different regimes are detailed in Table 4.13. Between 1.1 GPa and 2.4 GPa frequency of component 8 does not evolve any more, then, it upshifts between 2.4 GPa and 4 GPa until reaching a frequency comparable to that observed at 0 GPa. Therefore, this behavior shows 3 regimes: HBS dominant behaviour; compensation of PE and HBS, and PE dominant behaviour. For the linear bond ***LB***, we observe a very different behavior with a linear decrease of the frequency of "Amide A" between 0 GPa and 4 GPa which indicates a dominant HSB in this pressure range. From 4 GPa the differentiation of both types of H–bonds is not possible any more.

For **H(TT)** hybrid, "Thioamide A" follows the same pressure dependence than linear H–bond of **M(TT)** in the range 0-2 GPa indicating HBS. The plateau observed above 2 GPa and the upshift observed at higher pressures the result of PE/HBS compensation and PE dominating effect at high pressure. Table 4.13 summarizes the different regime observed and the associated pressure dependances.

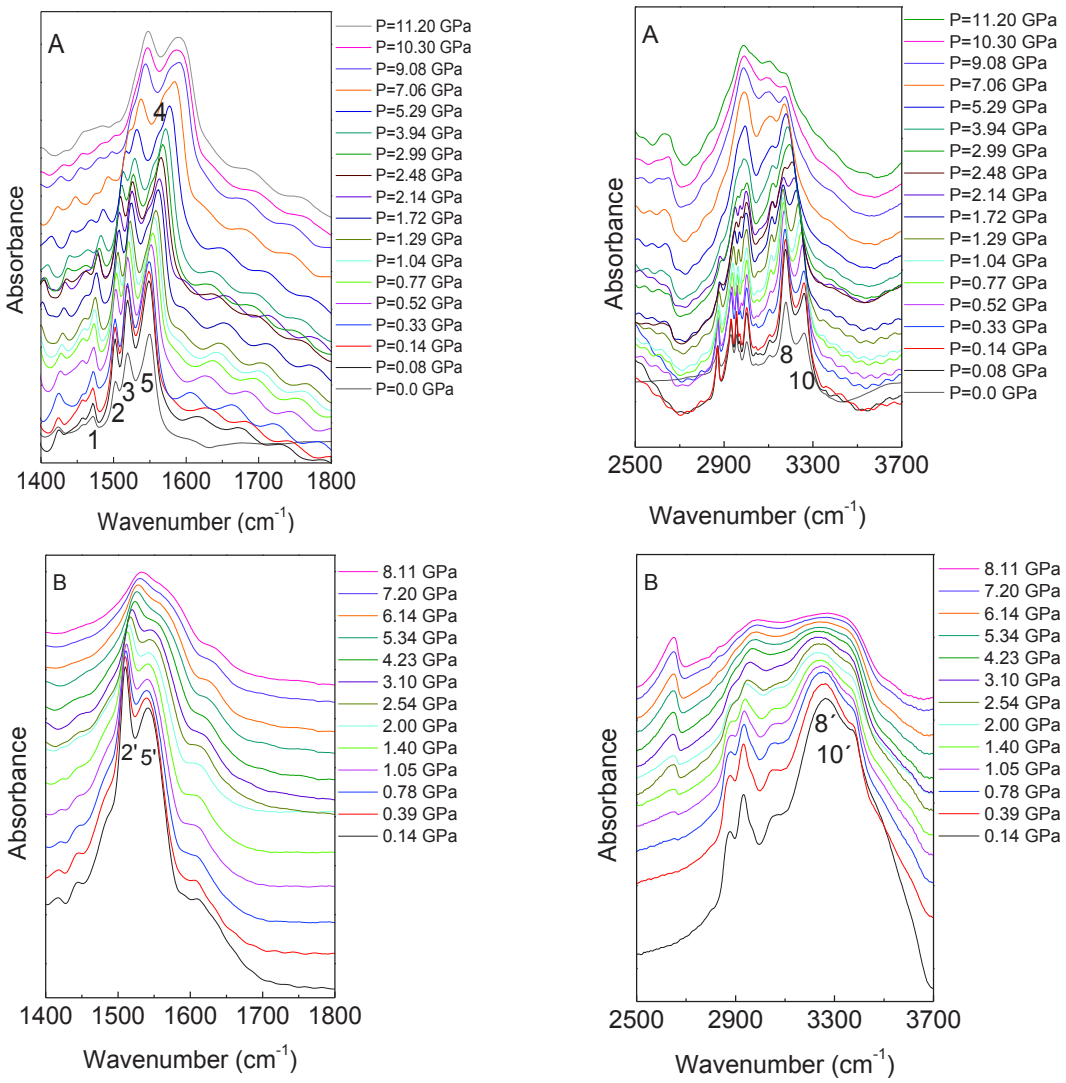

Figure 4.39. FT-IR spectra as function of pressure in the "Thioamide II" and "Thioamide A" regions of A) **M(TT)** and B) **H(TT)**.

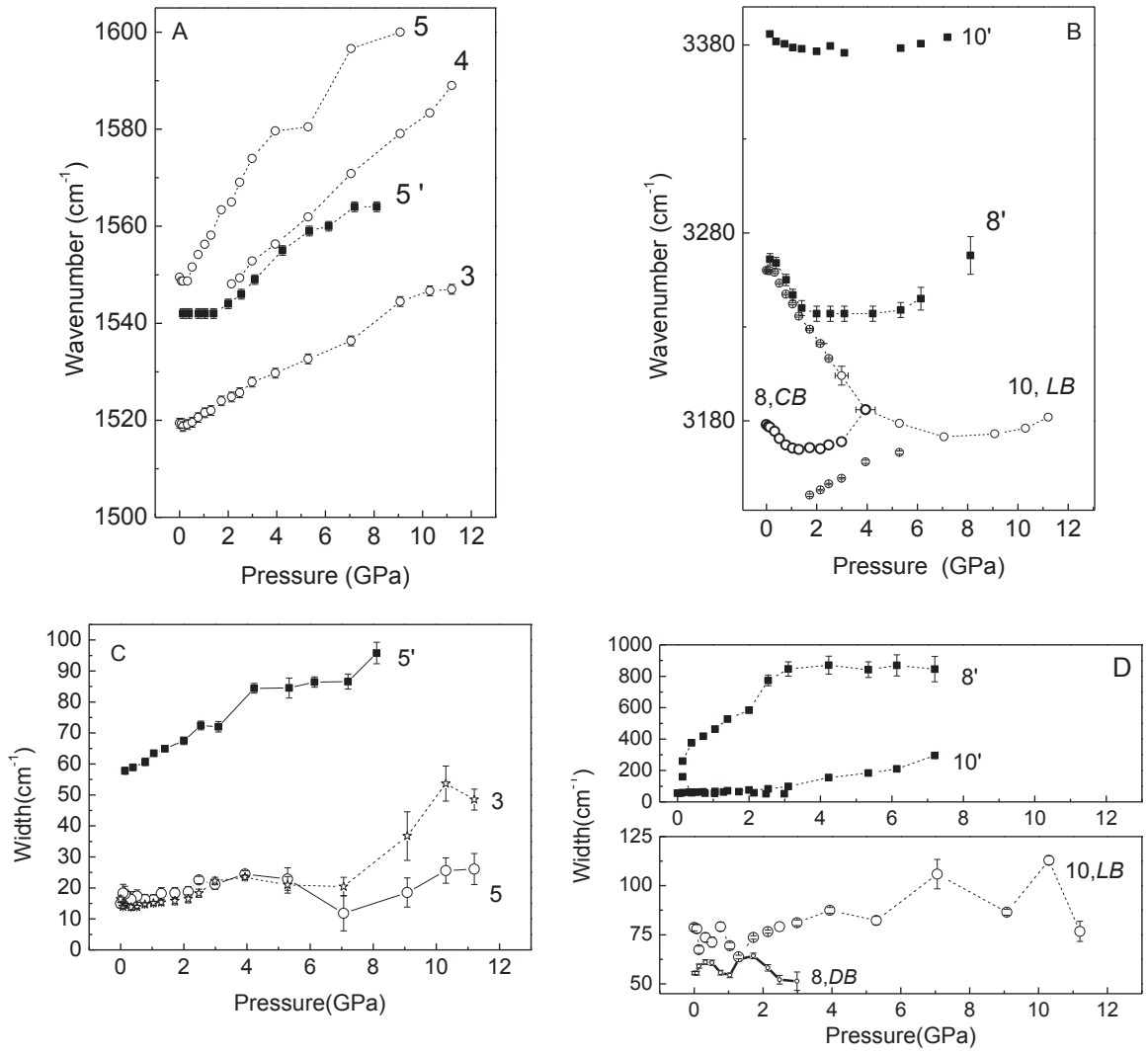

Figure 4.40. Thermal dependence of the components identified in A) "Thioaminde II" and B) "Thioamide A" regions of **M(TT)** (open circles) and **H(TT)** (closed squares). The width of the components C) 3, 5, and D) 8 and 10 are also represented. The lines through the data are a guide to the eye and the error bars are also represented.

Table 4.13. Summary of the pressure and slope details obtained from FT-IR pressure behavior of **M(TT)** and **H(TT)**.

Vibrational region		M(TT)					H(TT)			
	Pressure (GPa)		**0-1.1**	**1.1-2.4**	**2.4-4**	**4-6-12**		**0-1.5**	**1.5-6**	**6-8**
Amide A	Slope (cm^{-1}/GPa)	**8**	-11±1	0	11±3		8'	-4.6±0.4	0	10±1
		10		-19±1		-4.6±0.4 2.3±0.8	10'	-6±1		3.1±0.1
	Pressure (GPa			**0-2**	**2-4**	**4-12**		**0-2**		**4-12**
Amide II	Slope (cm^{-1}/GPa)	3		2.6±0.1						
		4			4.4±0.1			0		3.5±0.2
		5		8.3±0.2		4±1				

Figure 4.40 A shows, for **M(TT)** the pressure dependence of the "Thioamide II" vibrational bands 3, 4 and 5 related to vibrations involving both ***LB*** and ***CB*** bonds simulteously. Linear increases are shown for the 3 components, nevertheless components 4 and 5 exhibit higher slope, see Table 4.13. Therefore "Thioamide II" shows a classic behavior in pressure, what is not very surprising as HBS and PE induce upshift. These vibrations keep linear pressure dependence without any distinction in compression regimes, suggesting averaged answer of this vibration. From 6-7 GPa, we can note a strong increase in disorder for component 3, see Figure 4.40 C.

For **H(TT)**, "Thioamide II" vibration (5') keeps the same position up to 1.4 GPa (PE/HBS compensation). From 1.4 GPa to 8 GPa an upshift with a slope comparable to component 4 for **M(TT)** is shown.

In "Thioamide V" region, high pressure behavior has been measure up to 650 cm^{-1} for **M(TT)**, see Figure 4.41 A. From 0 GPa to 2 GPa the intensity of the contributions observed at 517 cm^{-1}, 534 cm^{-1}, 571 cm^{-1}, 598 cm^{-1} and 515 cm^{-1} are strongly modified. These changes in intensity follow the same trend than the one observed when temperature goes from 290 K down to 10 K (see Figure 4.41 C), signing for HBS. These results mean that HBS is the dominant phenomenon in this pressure domain.

Therefore, the behavior of the "Thioamide V" through the variations of intensity of the modes related to linear H–bonds ***LB*** seems to confirm results obtained from "Thioamide A" where HBS is shown to be dominant compared to PE.

Raman spectra have also been measured up to 7.46 GPa in the region of "Thioamide V" in Figure 4.42 A. Interestingly, it gives some complementary information on the region over 650 cm^{-1}, thus giving some complementary information in the region related to H-bonds. From 0.39 GPa, the shoulder observed at 630 cm^{-1} is geeting more resolved to give rise to a sharp peak. A small peak seems to appear around 612 cm^{-1} from 3.57 GPa. Similar effects were observed going from 290 K to 10 K, see Figure 4.42 B. Note that appart from these two peaks, sharpening effects are not obvious for other components as compared to low temperature behavior. These similarities between the Raman behavior at high pressure in the region between 600 cm^{-1} and 650 cm^{-1} associated to ***LB*** and the behavior observed at low temperature demonstrates a strenghening of ***LB*** H-bond in the range 1.4-7.5 GPa. The very sharp peaks also attest for a very well defined environment related to these bonds. As for features related to ***CB*** bond, only a strong damping is observed above 4-5GPa.

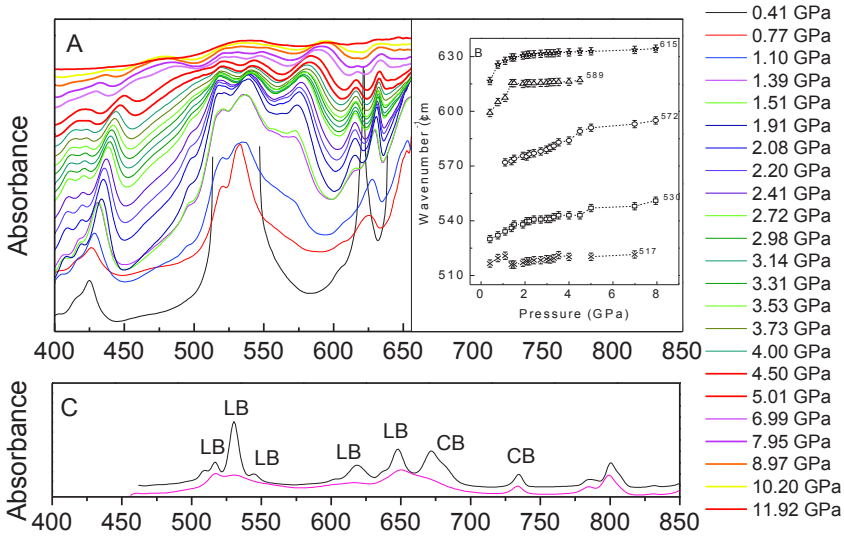

Figure 4.41. A) FT-IR as function of pressure of **M(TT)** in the "Thioamide V" region. B) Pressure dependence of the components peaking at 517 cm^{-1}, 530 cm^{-1}, 572 cm^{-1} and 616 cm^{-1}. The lines through the data are a guide to the eye and the error bars are also represented. C) FT-IR spectra recorded at 290 K (red line) and 10 K (black line).

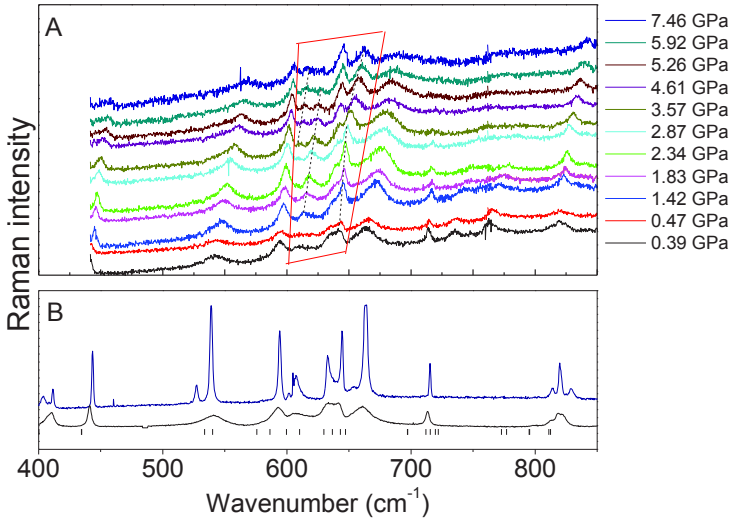

Figure 4.42. Raman spectra A) as function of pressure and B) acquired at 10 K (blue line) and 290 K (black line) in the "Amide V" region of **H(TT)**. The lines through the data are a guide to the eye and the error bars are also represented.

Si-O stretch region is shown on Figure 4.43. From 5-6 GPa, the broad component becomes less defined as already observed for **H(UU)** and **H(UT)**.

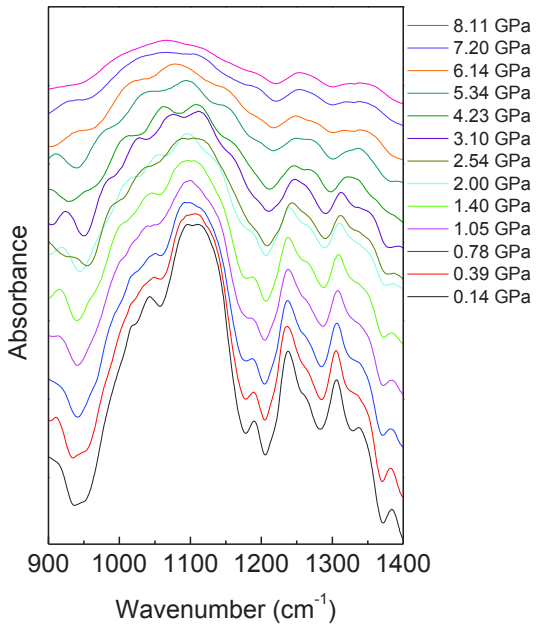

Figure 4.43. FT-IR spectra in the Si-O-Si vibration region for **H(TT)**.

To summarize these results on **TT** system, in the model **M(TT)**, the compression mechanism involves the strengthening of two types of bonds ***CB*** and ***LB***. These two types of bonds respond differently as shown through "Amide A". The strengthening of linear bond ***LB***, can be observed at least until 4-6 GPa whereas strengthening of ***CB*** bond is unambiguous up to 3 GPa. Above 4 GPa ***CB*** and ***LB*** are not dissociable.

For **H(TT)**, for which weaker H–bonds with a broader dispersion are found, a strong compression involving HBS is also observed from 0 GPa to 2 GPa. Above that pressure, and up to 5-6 GPa, the pressure shifts become weaker (see "Amide II") or vanishes (see "Amide A"), as a result of competition between PE and HBS. Above 5-6 Gpa, PE is clearly dominating the pressure dependence, HBS is even smaller or eventually H–bonds start to weaken. As a matter of fact, above this pressure the siliceous network becomes sensitive to pressure and H–bond network is adjusting the changes involved by the reorganization of the siliceous part.

4.5.4 Reversibility of H–bond compression mechanism

Infrared spectra measured during decreasing pressure also give us some insight on the reversibility of the compression mechanisms. We present here the pressure dependence upon decompression for the three models **M(UU)**, **M(UT)** and **M(TT)**, see Figure 4.44. For all models systems, the samples recover their initial form after decompression, and it is confimed by the comparison of the spectra before compression and after release, see Figure 4.45. Only small discrepancies are found as the pressure release is not absolutely complete. Therfore, it appears that, independanly from the type and strength of H–bond and the structure of the model, the compression process is reversible at the level of the organic substructure.

One can notice that decompression path for pressure dependence does not always follow the dependence observed for compression. Some hysteris are exhibited down to 2 GPa in particular in the region of "Amide A" for **M(UU)** and **M(UT)**. From 2 GPa to complete pressure release, the path is found to be the same. However for **M(TT)**, no hysteresis is observed. This later point could be specific of thiourea-thiourea H–bonds.

The hybrids samples after pressure release have also been compared with pristine samples. The results are shown on Figure 4.45 for **H(UU)**, **H(UT)** and **H(TT)**. For hybrids also, reversibility can be observed for the features related to the local structure around H–bonds.

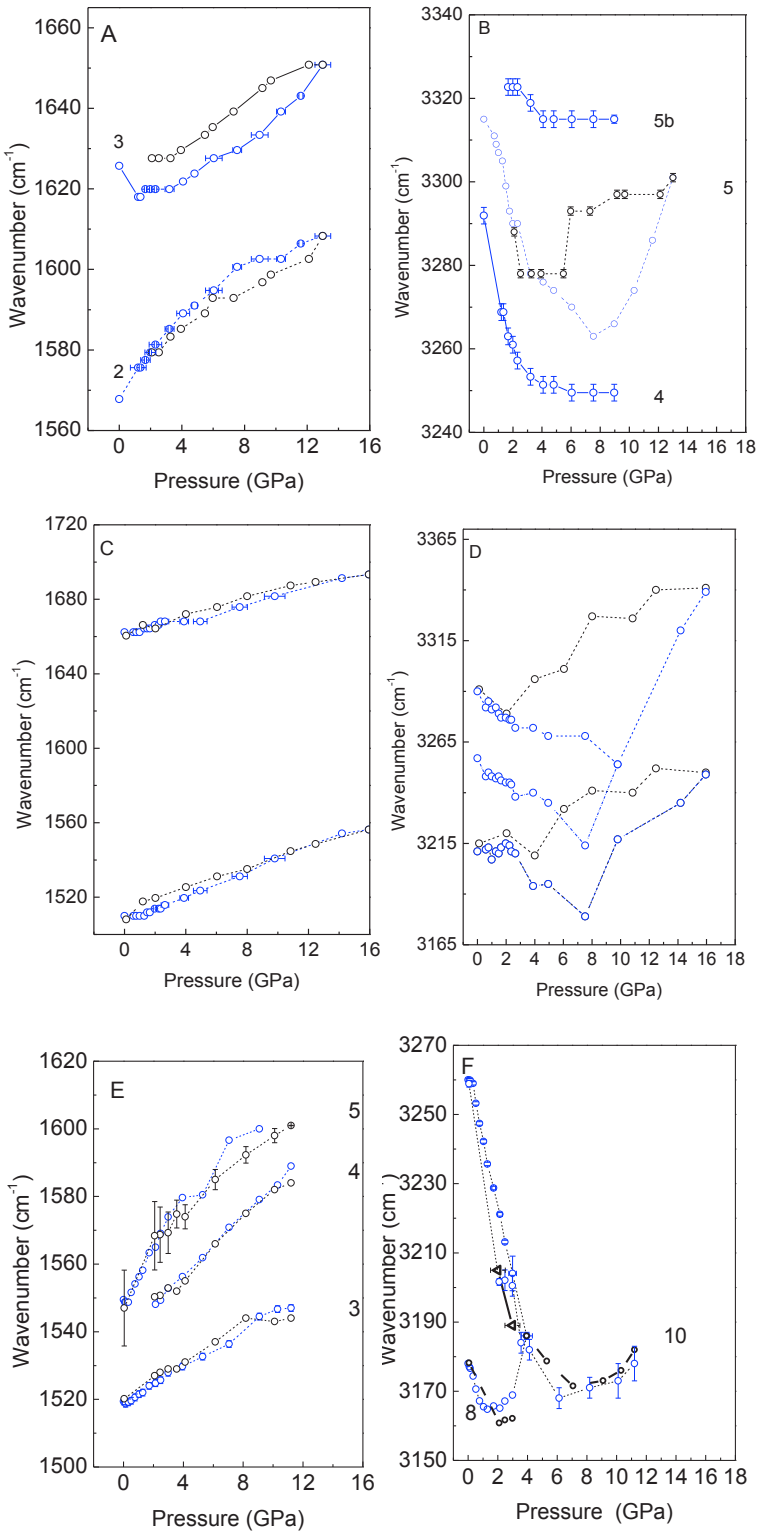

Figure 4.44. Pressure dependence during decompression (black symbol) as compared to compression (blue symbol) in "Amide I and II" region of A) **M(UU)**, C) **M(UT)** and E) **M(TT)** and "Amide A" of B) **M(UU),** D), **M(UT)** and F) **M(TT)**.

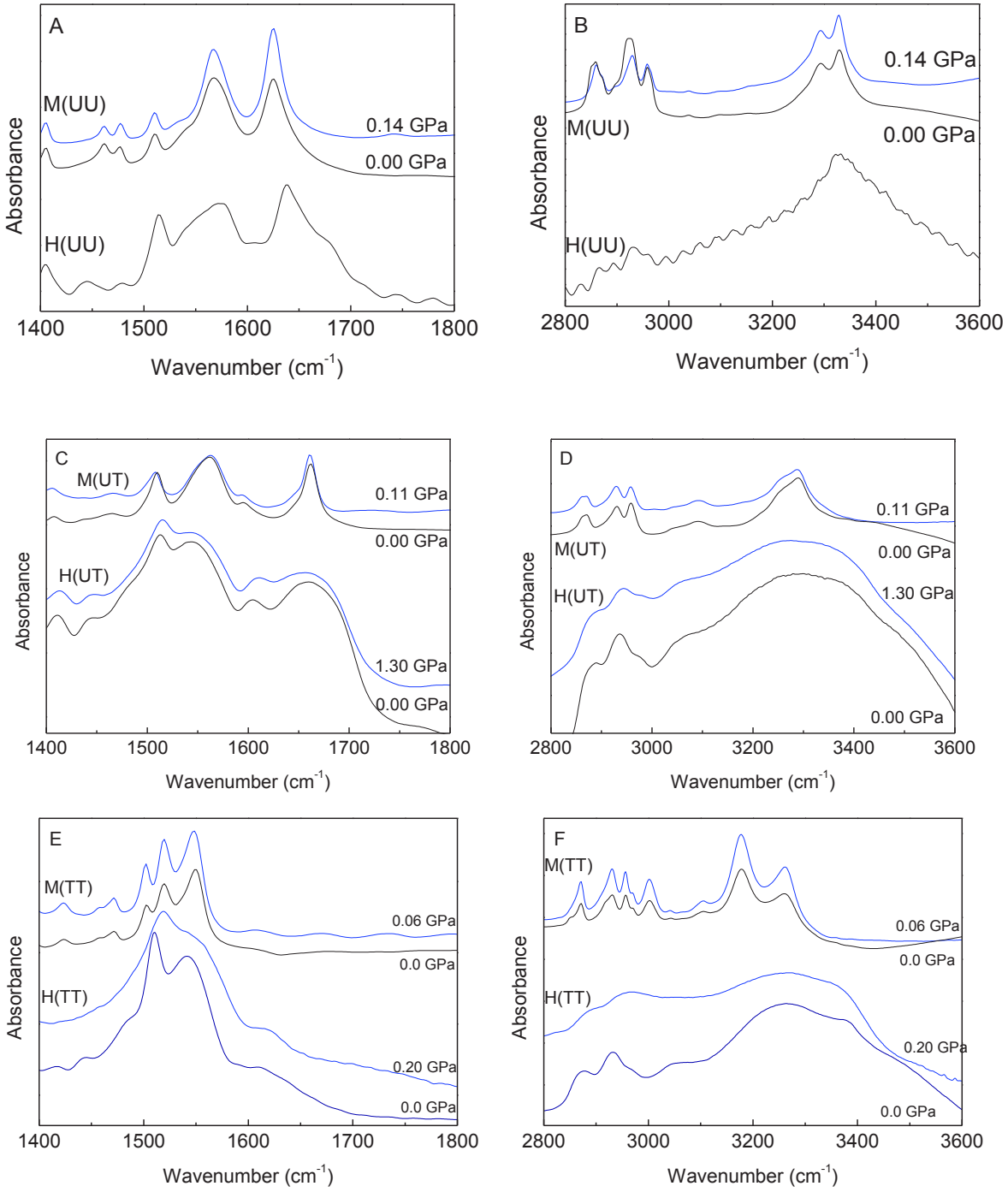

Figure 4.45. FT-IR spectra before compression (black line) and after pressure release (blue line) in the region "Amide II and I" for A) **UU** sytem, C) **UT** system and E) **TT** system and in the "Amide A" for B) **UU** system D) **UT** system and F) **TT** system.

These results reveal that H–bonds, involving either urea, or thiourea or both groups play a key role in the reversible structural compression in the hybrids systems studied here,

they act as a spring that can be compressed or that restore its initial length when pressure is released. One can notice that the hysteresis observed for "Amide A" decompression in **M(UU)** and **M(TT)** seem to indicate that H–bonds involving urea have a longer "pressure memory effect" of their compression and that thiourea-thiourea bonds are restored immediately.

Figure 4.46 also compares the hybrids nanomaterials after decompression in the region of Si-O vibration. It is interesting to note that for **UT** the broad signal after recovery is slightly different, in particular the peak around 1084 cm^{-1} is not visible anymore and instead the feature around 1024 cm^{-1} appears broader and up shifted. The differences are even more obvious for **H(TT)** where Si-O band was very well structured before compression and appears only as a broad band after pressure release. We therefore have an indication that the siliceous network has been modified. As we reported before, these changes seem to appear for pressures above 6 GPa. Nevertheless, this modification does not affect the rearrangement the the organic substructure, which, recovers its pristine H–bonds environnement on average.

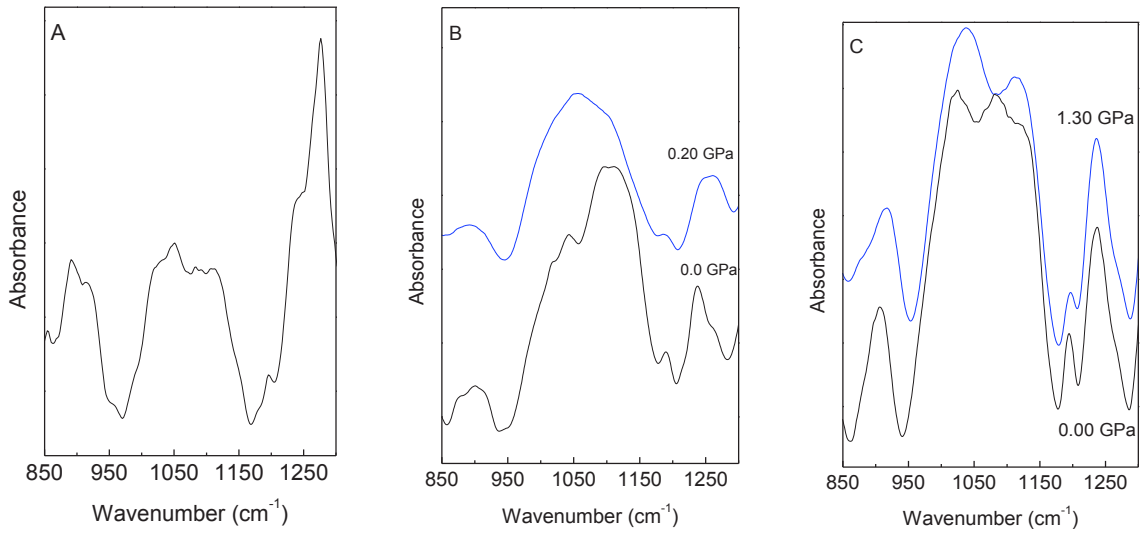

Figure 4.46. FT-IR spectra before compression (black line) and after pressure release (blue line) in the region "Amide V" for A) **H(UU),** B) **H(UT)** C) **H(TT)**.

The "Amide A" pressure dependence measured for the different samples, gives some insight on pressure response of these different H–bonds.

The bifurcated bonds in **M(UU),** the dimer bonds ***DB*** in **M(UT)** and the cyclic bonds ***CB*** in **M(TT)** exhibit a strong HBS mechanism from 0 GPa to a critical pressure (Pc) equal

to 1.5-2.0 GPa. For linear bond ***LB*** in **M(TT),** a strong HBS is observed up to Pc= 4-6 GPa, see Figure 4.47. Above that critical pressure, H–bond moderately strengthens. Above that pressure, HBS competition with PE gives rise to small slopes or plateaus in the pressure dependence.

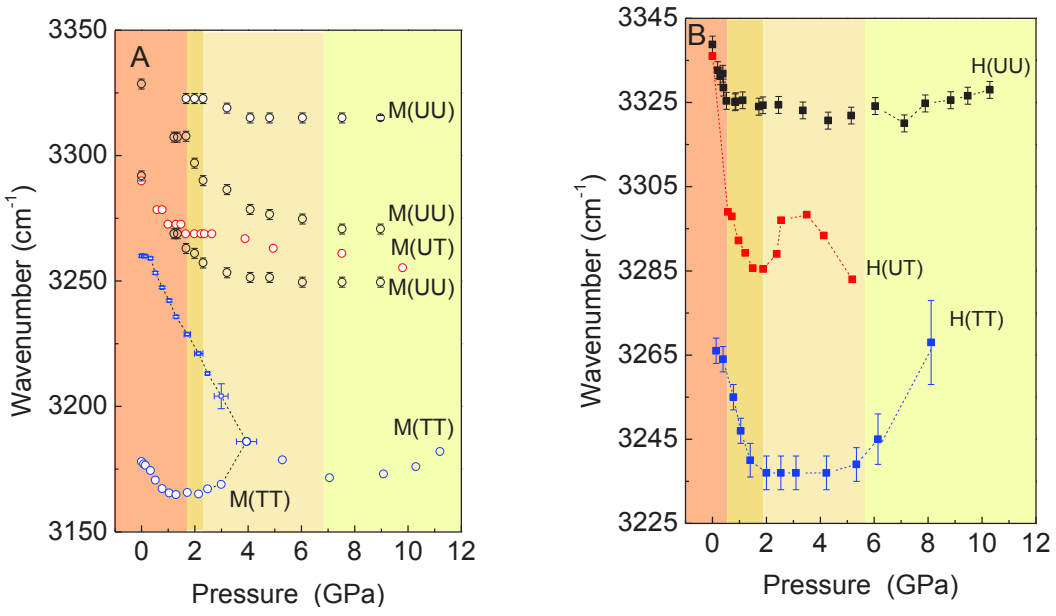

Figure 4.47. Comparison of the pressure dependence in the "Amide/Thioamide A" region of A) **M(UU)** (open black circles), **M(UT)** (open red circles) and **M(TT)** (open blue circles) and B) **H(UU)** (closed black squares), **H(UT)** (closed red squares) and **H(TT)** (closed blue squares). The red lines through the data are a guide to the eye.

For hybrids a strong HBS is observed for **H(UU)** between 0 GPa and 1 GPa. For **H(TT)** and **H(UT)** the strong HBS of H–bonds is observed up to 1.5 GPa. Up to 6 GPa H–bonds signatures for **H(UU)** and **H(TT)** remain at the same frequencies as a result of the competition between HBS and PE, see Figure 4.47 B. Above 6 GPa, PE is clearly dominant. We can note that from this pressure the siliceous network begins to be distorted. Original pressure dependence is shown for **H(UT)** when two specific thiourea and urea environments are present.

Finally whatever the H–bond type is, these bonds act as springs and allows the relaxation of constrains in the materials at the level of the substructure environment involving H–bonds. The substitution of urea by thiourea leads to a modulation of H–bonds and also a modulation of relaxor behavior as shown from reversibility paths.

4.6 Photoluminescence

The photoluminescence properties of organic model compounds and hybrid materials based on the self-assembling of functional groups (urea and/or thiourea) in the temperature range 12 K- 300 K were studied.

It is well know that the extension and the magnitude of the H–bonds between adjacent urea groups might determine the relative intensity of the NH-related emission which induces differences in the emission properties of the materials [197].

In this section, the effect of the H–bond strength in the emission properties of the organic model compounds was discussed in terms of the magnitude of the H–bond between urea-urea, urea-thiourea and thiourea-thiourea.

The mono- di-substitution of the urea for thiourea group induces a modification of the H–bond strength, as previously observed from infrared spectroscopy. Concomitantly with these modifications in H–bonds, optical properties should be modified. The decrease of the H–bond interaction predicts a decrease in energy for the recombination associated with the thiourea *vs* urea groups. Moreover, the arrangement of the structure and the conjugation between the benzene and urea/thiourea groups in our materials should have impact on the emission of the materials.

Organic-model compounds

The emission spectra of **M(UU)**, **M(UT)** and **M(TT)** based on urea and thiourea groups are presented below. The emission of the organic model compounds depend of the excitation wavelength (Figure 4.48) and temperature (Figure 4.49).

Figure 4.48 shows the emission spectra at room temperature of **M(UU)**, **M(TT)** and **M(UT)** as function of excitation wavelength. The emission spectra of **M(UU)**, shows a broad band in the purplish blue spectral region, independently of the excitation wavelength. Similar emission was reported for amorphous organo-bridged silsequioxanes based on bis-urea group [2]. In this work, the effects of the self-assembling of the nanobuild blocks on the emission properties of crystalline lamellar and the amorphous hybrid materials were discussed in terms of the magnitude of the H–bonds between adjacent organic groups. Crystalline lamellar and the amorphous hybrid materials based on bis-urea group present different emission properties

that result of a different nanostructuring of the organic units in these solids. The emission properties of the amorphous hybrid reported in [2] are rather similar to those observed for **M(UU)**.

The mono or di- substitution of oxygen by sulfur induces the appearance of an emission at higher wavelength, observed for **M(UT)** and **M(TT)**, Figure 4.48 B and Figure 4.48 C, respectively. The room temperature emission spectra of mono-substitute organic model compound shows a broad band in the blue-green spectral region, which is dependent on the excitation wavelength, it can be observed that the emission of the di-substitute organic model compound, is not affected by the excitation wavelength. In addition, the component that appears at lower wavelength (325 nm) for **M(UU)** disappears after addition of the thiourea group.

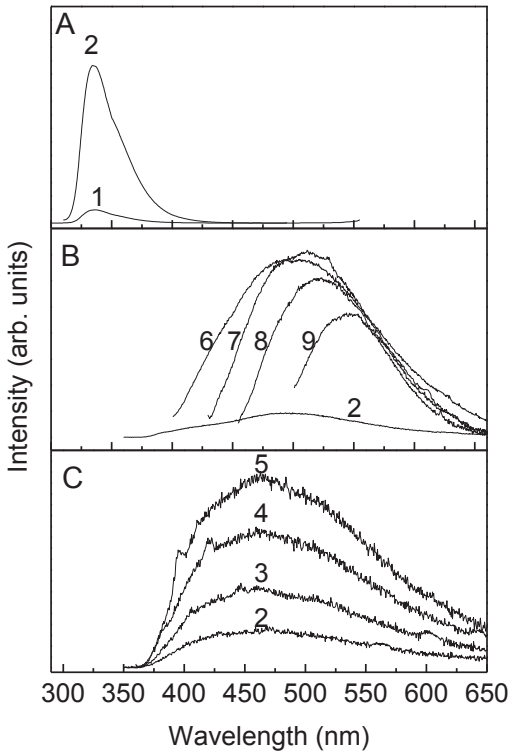

Figure 4.48. Emission spectra (300 K) excited at 1) 250 nm, 2) 280 nm, 3) 300 nm, 4) 320 nm, 5) 340 nm, 6) 360 nm, 7) 380 nm, 8) 400 nm and 9) 440 nm of A) **M(UU)**, B) **M(UT)** and C) **M(TT)**.

Changes in the temperature affect the emission properties of **M(UU)**, **M(UT)** and **M(TT)**, see Figure 4.49. A new component emerges (at ~480 nm and 495 nm) excited between 280 nm and 320 nm for all organic model compounds. The emission shows a vibrational progression spacing (Δ_1= 826 cm^{-1}) with *fwhm* of 470 cm^{-1} independently of the excitation wavelength, see Figure 4.50. The presence of a structural vibration progression independent of the excitation wavelength is characteristics of a triplet state.

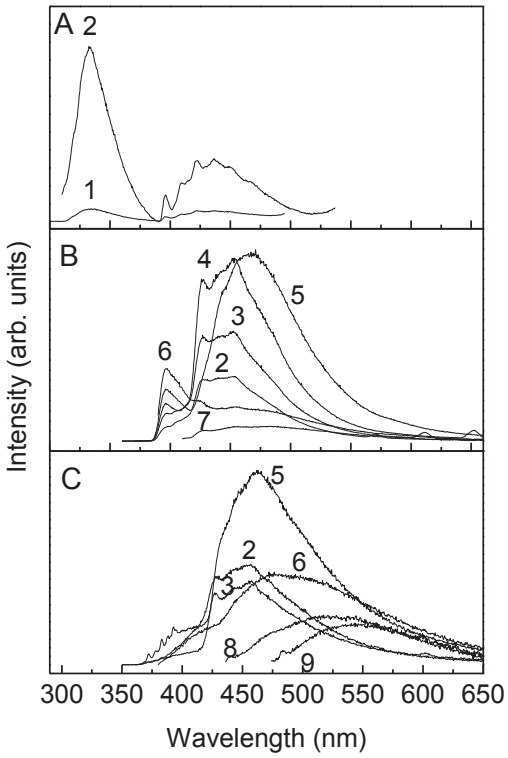

Figure 4.49. Emission spectra (12 K) excited at 1) 250 nm, 2) 280 nm, 3) 300 nm, 4) 320 nm, 5) 340 nm, 6) 360 nm, 7) 380 nm, 8) 400 nm and 9) 440 nm of A) **M(UU)**, B) **M(UT)** and C) **M(TT)**.

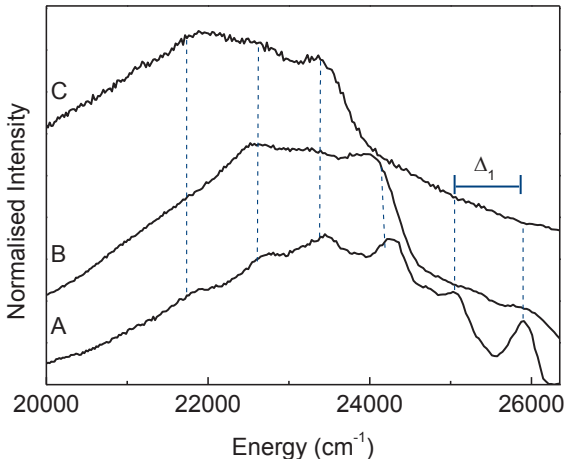

Figure 4.50. Low temperature emission spectra excited at 280 nm of A) **M(UU)**, B) **M(UT)** and C) **M(TT)**. The observed spacing for the vibrational progression of (Δ_1=826 cm^{-1}) between the adjacent peaks are also indicated.

In addition, for organic model compounds based on thiourea **M(UT)** and **M(TT)**, the emission spectra excited between 340 nm and 440 nm show a broad band in the blue-green spectral region dependently of the excitation wavelength.

Figure 4.51 shows the excitation spectra of **M(UU)**, **M(UT)** and **M(TT)** monitored in the maximum of the emission spectra of each component. Two main contributions can be identified at 12 K, one component at ~ 280 nm and other at 340 nm, last one just present for **M(UT)** and **M(TT)**.

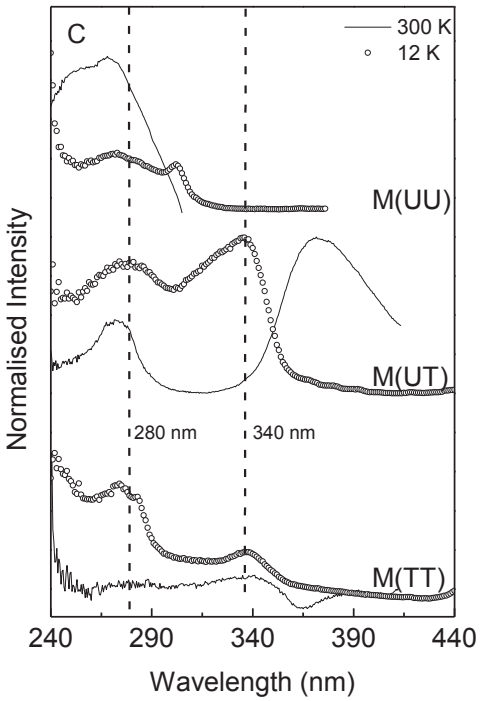

Figure 4.51. Excitation spectra monitored at 325 nm (300 K) and 426 nm (12 K) for **M(UU)** and 460 nm for **M(UT)** and **M(TT)** acquired at 300 K and 12 K.

In summary, two main components were identified in the emission spectra of organic model compounds. In case of **M(UU)**, a component in the purplish blue spectral region excited in UV (250 nm – 300 nm) is observed at 300 K and 12 K. The second component that appears just at low temperature is observed at higher wavelength, present a vibrational progression spacing 826 cm^{-1} for all organic model compounds. In addition for **M(UT)** and **M(TT)** the emission spectra show an emission in the blue/green spectral region, depend of the excitation wavelength.

A comparison at low temperature between the emission and excitation spectra of organic model compounds and corresponding hybrid materials is presented in the following sub-section.

Organic-inorganic hybrid materials

In order to simplify the photoluminescence comparison between organic model compounds and hybrid materials selected excitation and monitored wavelengths have been chosen in this section. The emission spectra of **M(UU)** and **H(UU)**, excited at 280 nm are rather similar, Figure 4.52 A. The component observed in the purplish blue spectral region for

M(UU) blue shifts (5 cm^{-1}) for **H(UU)**. A similar shift was observed in the excitation spectra, Figure 4.52 B.

The stronger H−bond interactions of **H(UU)** comparatively to **M(UU)** (observed from infrared spectroscopy) could be related to the changes in the emission properties.

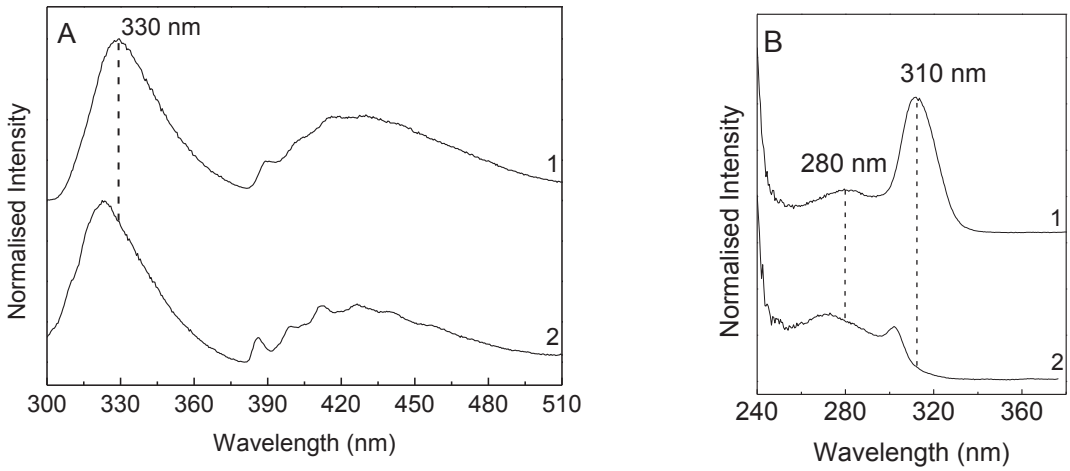

Figure 4.52. Low temperature A) Emission spectra excited at 280 nm and B) excitation spectra monitored at 426 nm of 1) **H(UU)** and 2) **M(UU)**.

Figure 4.53 A shows the comparison between the emission spectra of **M(UT)** and **H(UT)** excited at 280 nm. The component that appears below 400 nm for **M(UT)** was not identified in case of **H(UT)**. In addition the most intense component at higher wavelengths blue shifts for **H(UT)**. Also the excitation spectra of **H(UT)** show modifications relatively to the **M(UT),** Figure 4.53 B. The relatively intensity of the component at lower wavelengths is less intense in the case of **H(UT)** and the component at higher wavelength blue shifts comparatively to **M(UT)**.

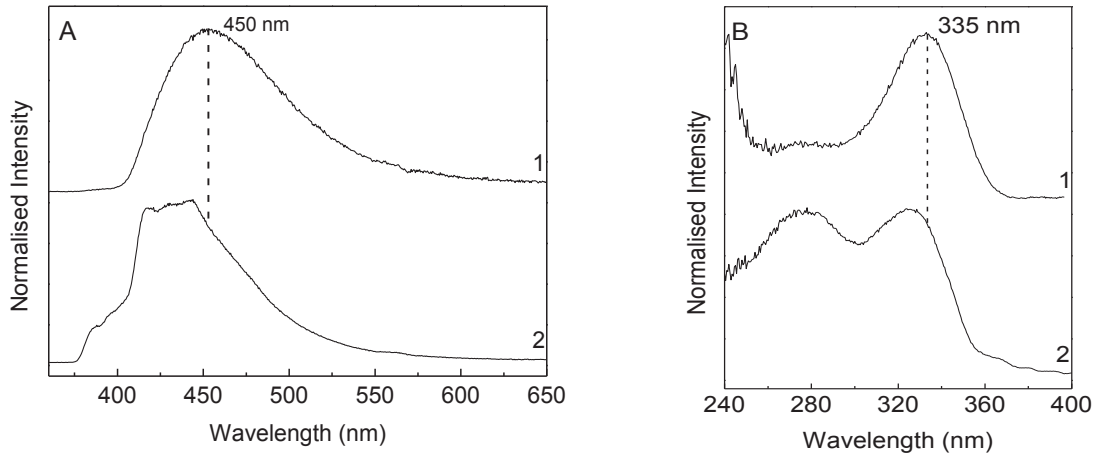

Figure 4.53. A) Emission spectra excited at 280 nm and B) Excitation spectra monitored at 440 nm of 1) **H(UT)** and 2) **M(UT).**

A similar behavior can be taken from the comparison of the emission and excitation spectra of bis-thiourea (**TT**) system, Figure 4.54.

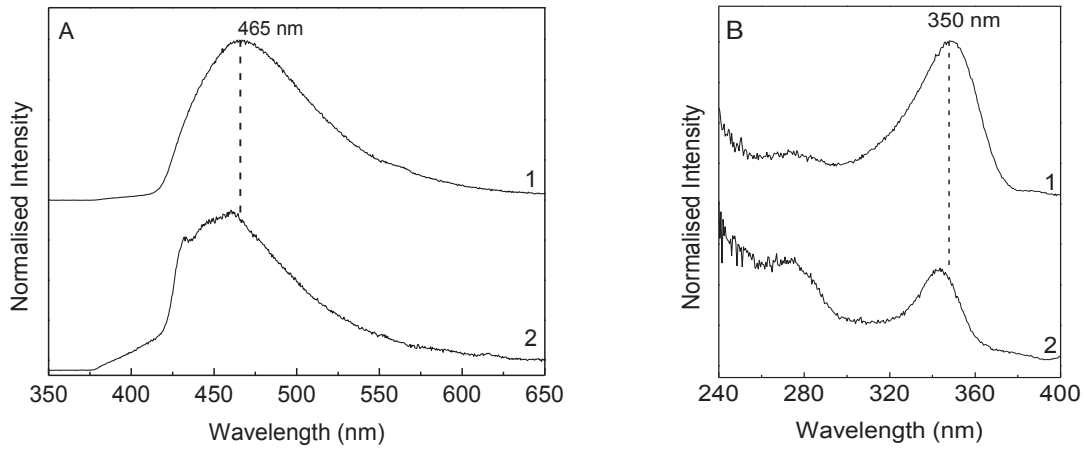

Figure 4.54. A) Emission spectra excited at 280 nm and B) excitation spectra monitored at 440 nm of 1) **H(TT)** and 2) **M(TT).**

In addition, an evident similarity between emission and excitation spectra of **H(UT)** and **H(TT)** can be observed. The changes in the photoluminescence properties for the hybrids **H(UT)** and **H(TT)** relatively to those of the organic model compounds **M(UT)** and **M(TT)** could be related with the decrease of H–bond interaction observed in case of hybrids and possible different arrangement relatively to the organic model compound.

In order to quantify the emission properties of the hybrid materials **H(UU)**, **H(TT)** and **H(UT)**, ϕ was measured, Table 4.14. The maximum ϕ value was obtained for **H(UU)** with a maximum of 0.06 excited at 300 nm. The incorporation of thiourea induces a decrease of the ϕ values.

Table 4.14. ϕ values obtained for different excitation wavelengths (λ_{exc}, nm) of **H(UT)** and **H(TT)**.

Reference	λ_{exc}	ϕ
H(UU)	280	0.05
	300	0.06
H(TT)	280	<0.01
	340	
	440	0.03
H(UT)	400	<0.01
	440	

To summarize, we have shown that the substitution of urea by thiourea group strongly affects the absolute emission quantum yield and emission spectral region. Moreover, the comparison of the emission of hybrids and correspondent organic model compounds has shown that a systematic blue shift is observed for the emission hybrids. The potential relation of this shift with a weaker H–bonded network has to be futher investigated and understood.

4.7 Conclusions

In this chapter, we study the influence of H–bond strength on the structuration of BS hybrids materials and associated organic models. In a second time, the optical properties of the different systems (hybrids and models) are studied.

In a first part, we presented organic model compounds respectively with bis-urea (**UU**), urea/thiourea (**UT**), and bis-thiourea (**TT**) potential linkers. These molecules have shown to be self-assembled into crystals through different H–bond interactions. The **UU** system is well known to self-assemble through bifurcated H–bonds. In **UT** and **TT** models, thanks to introduction of thiourea new types of H–bonds are found: bifurcated bonds involving in the same time urea and thiourea, inter thiourea cyclic bonds and inter thiourea linear H-bonds. We show that intradimer bifurcated H–bonds are weaker in **UT** than in **UU** as a consequence of introduction of thiourea. For interthiourea bonds (cyclic and linear), in **M(TT)**, smaller lengths are found indicating stronger H–bonds, despite expectation from literature. Different structural organizations result from these bonds. Bifurcated bonds favor lamellar structures in **M(UU)** but are limited to the scale of a dimer in **M(UT).** Moreover, complex entangled 3 D structures (see Appendix B) are shown for both thiourea based models **M(UT)** and **M(TT)** as a consequence of thiourea bond introduction.

This variety of bonds and structural arrangements results in specific mechanical and optical properties. Under pressure, all models exhibit a reversible compression mechanism involving a strengthening of H–bond up to a critical pressure above which H–bond distorsion and progressive appearance of disorder are observed.

The strengthening of H–bond occurs through a least two steps: a first regime with a very strong strengthening up to a limiting pressure P_1. A second regime is observed with a softer strengthening up to a critical pressure. Over that pressure the competition between a much smaller HBS and PE gives rise to a plateau or an upshift of intramolecular "Amide I" and "Amide A" vibrations.

- For birfucated urea-urea bonds, $P_1 \sim 2$ GPa and Pc ~6 GPa;
- For bifurcated urea thiourea dimer bond, $P_1 = 2$ GPa and Pc=6 GPa;
- For cyclic thiourea-thiourea H–bond, P_1 and Pc are similar and equal to 1 GPa;
- For linear thiourea-thiourea H-bond P_1=4 GPa and Pc ~ 6-8 GPa.

Our results indicate that a correlation appears between the frequency of "Amide I" and H–bond length. Based on this correlation we compare the total pressure shift between 0 GPa and Pc for the different type of bonds as a function of initial bond length assuming that this bond length is reflecting the bond strength, see Figure 4.55. A correlation is found for linear and bifurcated bonds, showing a pressure shift decreases for weaker H–bonds.

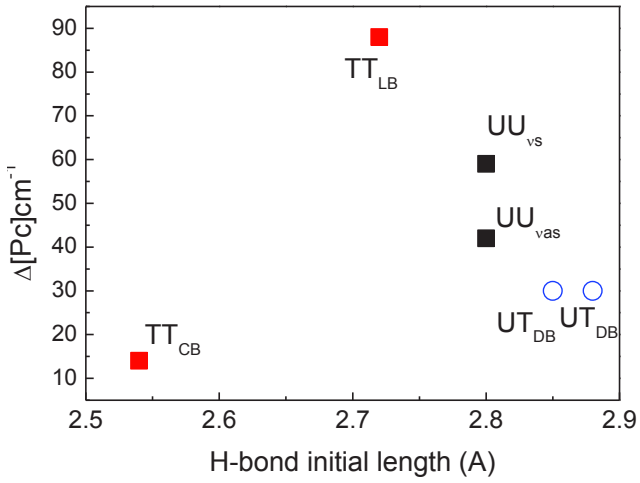

Figure 4.55. Pressure shift from 0 GPa to Pc for the different types of bond as a function of initial bond length (0 GPa).

In the pressure domain where H–bonding strengthening is the dominant effect; the elastic properties of organic models are well correlated to H–bond strengths except for cyclic H–bond involving thiourea moities. This could be related to the original geometry of this type of H–bonds.

Substitution of urea by thiourea also has a strong impact on luminescence properties, when **M(UU)** shows a rather sharp emission around 330 nm, **M(UT)** and **M(TT)** show a broad emission centered around 470 nm at 10 K. We can note that for **M(UT)**, thiourea component seems to dominate the luminescence properties. In a second time, 3 freeze dried hybrid materials with organic moieties corresponding to that of **UU**, **UT** and **TT** models have been synthesized and studied. Their properties are compared to the organic models. In hybrid **H(UU),** the transcription of the self assembled organic substructure organization from the model to the hybrid is found for urea-urea H–bonds with a resulting lamellar structure. In **UT** systems, the transcription is evidenced from **M(UT)** to **H(UT)** concerning the intra-dimer

H–bond (bifurcated bond). The resulting hybrid is amorphous. For **TT**, no obvious sign of transcription appears and the resulting structure is also amorphous. In all hybrids, H–bonds are involved in the compression mechanism with a strong HBS up to critical pressures found around 1-2 GPa. These critical pressures are much smaller than those observed for models. This behavior suggests that the inorganic polymerization limits the HBS under pressure. Over 6 GPa, the covalent siloxane network begins to be modified, leading to increasing disorder in the structure and irreversible structural modification is exhibited for inorganic moieties. At the opposite, organic substructure structural organization is recovered after pressure cycle. Finally, the emission properties of the hybrid materials seem to follow the trend shown by their respective organic models, despite the poor structural transcription from models to hybrids in the case of thiourea based hybrids. We can suggest that the presence of a thiourea group has a dominant effect on the energy of the emitted light, even in urea thiourea systems. From the model organic substructure and organic inorganic hybrid nanomaterial elaborations and vibrational study, we show that we can offer original thiourea and urea environments and modulate their local structure. Furthermore, we have seen that it is possible to modulate in situ local H–bond arrangement thanks to pressure. As a perspective, it could be interesting to study photoluminescence properties of pristine and future Ln^{3+} doped hybrids, *in situ*, as a function of pressure while modulating local arrangement around thiourea and urea.

5. Tri-ureasil bridged silsesquioxanes

5.1 Introduction

During the last decades, the sol-gel method has been extensively used to produce efficient white light-emitters based on organic-inorganic hybrids lacking metal activator centers [65,66,68,97,102,106-108,115,117,120,125-131], with particular emphasis to siloxane-based hybrids functionalized by amine/amide groups due to their high ϕ values.

The pioneering work of Green *et al.* [106] reported organic-inorganic hybrids based on APTES and a variety of organic carboxylic acids with a maximum ϕ value of 0.35±0.1. Following this work, the effect of the acidic catalysis was evaluated from the analysis of the interaction of APTES with acetic acid yielding organic-inorganic hybrids with tuned emission from the green to red spectral regions [97,112,125] with a maximum ϕ values of 0.21 [112]. In parallel, organic-inorganic hybrid materials composed of short poly(oxyethylene) (POE) chains with different lengths (8.5 to 40.5 oxyethylene repeat units) covalently bonded at both ends to a siliceous backbone by means of urea (di-ureasils) [64,107,115,129] and urethane (di-urethanesils) [68,126] crosslinks were developed using the conventional sol-gel method (in the absence of catalyst) [64,68,107,115,129] with a maximum ϕ values of 0.20±0.1 [68].

Another family of hybrid materials investigated in the last few years is the series of di-urea cross-linked alkyl-based silsesquioxanes [119,172], for which the synthesis conditions have also been tuned aiming to enhance these optical features. When prepared in the presence of the NH_4F catalyst the hybrids are essentially amorphous. In contrast, those prepared using acidic catalysis display a crystalline lamellar structure [119]. To increase the ϕ values, amorphous BS incorporating light harvesting chromophores, such as bipyridine groups present in the host hybrid framework, were produced [61,102]. These materials show an

efficient and tuneable blue-to-green emission, easily excited by commercial long-UV/blue LEDs [61,102].

More recently in the framework of my master thesis [198] a new family of tripodal poly(oxypropylene) (POP)/siloxane hybrid, termed as tri-ureasils and identified as **t-U(5000)**, were *t* stands for tripodal, *U* indicates the presence of urea cross linkages and 5000 is related with the average molecular weight of the organic precursor, was prepared by the sol-gel process under acidic catalysis (pH=2). In addition, **t-U(5000)** was also modified by the addition of two chromophores: phenyltriethoxysilane (PTES) and diphenyldimethoxysilane (DMDPS). All the hybrids show efficient emission at room temperature in the blue spectral region. Although there is no evidence of the chromophore intrinsic emission, the tripodal hybrids reveal a significant increase in the α value (80%), from 1.4×10^{3} cm^{-1} to 8.6×10^{3} cm^{-1} at 200 nm, and an enlargement of the absorption spectral region from 200–220 to 200–280 nm, compared with the hybrid performance in the absence of the chromophore groups. Moreover, the incorporation of PTES and DPDMS induces an increase in the ϕ values from 0.01 $\pm$0.001 to 0.07 $\pm$0.01 and 0.10 $\pm$0.01, respectively.

In order to improve the optical properties of the **t-U(5000)**, lacking addition of chromophores (PTES and DMDPS), two distinct synthesis strategies are presented in this chapter: (1) variation of the HCl concentration and water content and (2) use of controlled atmosphere conditions during the sol-gel reactions. At the end of the chapter, a detailed description of the chemical/physical nature of the **t-U(5000)** emission will be shown.

5.2 Variation of HCl concentration and water content

In this section, the role of the catalyst (HCl) concentration and water content in the tri-ureasil materials, on the local structure and photoluminescence features will be discussed. The tri-ureasil materials were processed as transparent monoliths by the sol-gel method using variable concentrations of HCl ($1.0\times10^{-3}\leq$[HCl]$\leq$2.0 M) and water content of 2.22 mmol or 22.2 mmol under laboratory conditions. Whereas at higher concentrations, ($1.0\times10^{-2}\leq$[HCl]$\leq$ 2.0 M), gelation occurred for all the samples (maximum gelation time of 288 h) at the lowest concentration ([HCl]=1.0×10^{-3} M) the tri-ureasils did not gel within 720 h. In order to control the gelation time and promote a faster sol-gel transition, the amounts of water and HCl

incorporated were varied. The hybrids will be hereafter designated as **t-U(5000)$_{[HCl]}$**, where [HCl] represent the HCl concentration used.

5.2.1 Synthesis

The first step is related to the synthesis of the non-hybrolised hybrid precursor, **t-UPTES(5000)**, based on the cross-links between the organic and the inorganic components formed by reacting the NH_2 groups of a triamine (***Jeffamine-T5000***®, Huntsman, average molecular weight 5000 gmol^{-1}) with the –N=C=O group of 3-isocyanatopropyltrietoxisilane (ICPTES, 95 % Sigma-Aldrich) in tetraidrofurano (THF), under magnetic stirring and reflux at 80 °C for 18 h. The **t-UPTES(5000)** was isolated after THF complete evaporation at 45 °C in rotary bench evaporator, see Scheme 5.1.

In the second step (EtOH, Sigma-Aldrich) was added to **t-UPTES(5000)** with ratio of 1:3 (v/w), (0.5 mL/1.5 g) under magnetic stirring at room temperature for 15 minutes. Then, a ethanolic solution of HCl (37%, Sigma-Aldrich) with different concentration values, see Table 5.1, was added to the **t-UPTES(5000)**, under magnetic stirring at room temperature for 0.5 h.

Table 5.1 Synthesis details of the tri-ureasils prepared under acidic catalysis.

Designation	[HCl] (M)	v_{sol} (mL)#	Amount HCl (mmol)	Amount H_2O (mmol)	Gelation time(h)
t-U(5000)$_{2.0}$ [198]	2.000	0.04	8.0×10^{-2}	2.2	0.08
t-U(5000)$_{0.25}$	0.250	0.04	1.0×10^{-2}	2.2	0.17
t-U(5000)$_{0.1}$	0.100	0.04	4.0×10^{-3}	2.2	0.25
		0.4	4.0×10^{-2}	22.2	0.17
t-U(5000)$_{0.05}$	0.050	0.04	2.0×10^{-3}	2.2	0.50
		0.4	2.0×10^{-2}	22.2	0.25
t-U(5000)$_{0.01}$	0.010	-	4.0×10^{-4}	2.2	*
		0.4	4.0×10^{-3}	22.2	12.00
t-U(5000)$_{0.001}$	0.001	-	4.0×10^{-5}	2.2	*
		0.4	4.0×10^{-4}	22.2	168.00
t-U(5000)$_{0.025}$	0.025	0.04	1.0×10^{-3}	2.2	288.00

* The monolith did not gel for a time period of 720 hours. # $V_{sol}=V_{H2O}+V_{HCl}$

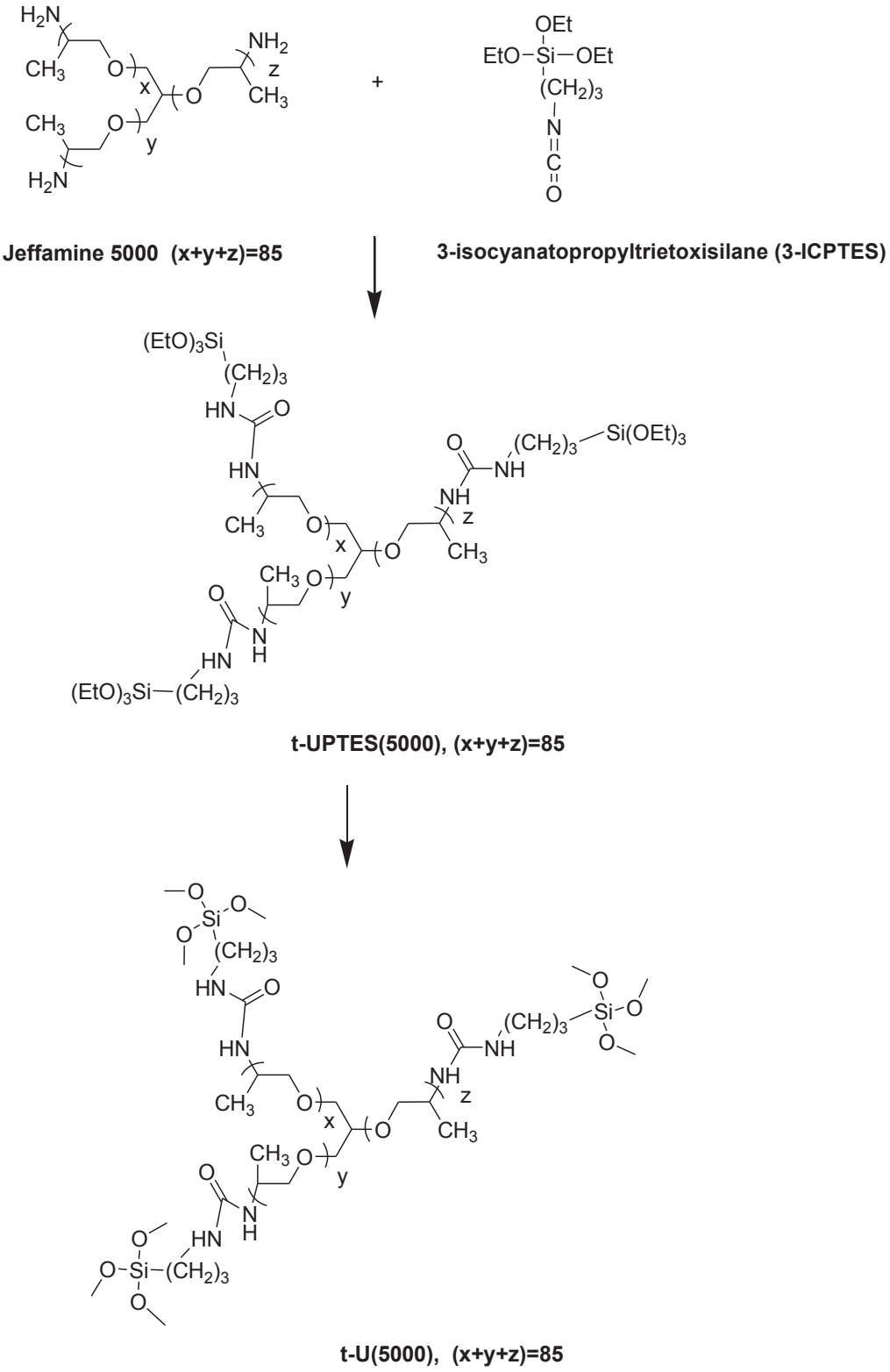

Scheme 5.1. Schematic representation of the synthesis of **t-UPTES(5000)** and **t-U(5000)**.

The sol was then cast onto a polystyrene mold (2×2×7 cm^3) and left to gel. The gelation time depended on the amount of HCl, Table 5.1. After gelation, the mold was covered with Parafilm® and kept at room temperature for 24 h. Finally the cover was removed and the mold was transferred to an oven at 45 °C for 7 days yielding transparent monoliths. The hybrids will be identified as **t-U(5000)$_{[HCl]}$** where [HCl] ranges from 1.0×10^{-3} and 2.0 M.

5.2.2 Local Structure

The X-ray diffraction patterns of selected hybrids are shown in Figure 5.1. The diffractogram of **t-U(5000)$_{2.0}$**, (prepared under acidic conditions, pH=2) previously reported in [198] is also shown for comparison purposes. The X-ray diffraction patterns of **t-U(5000)$_{[HCl]}$** are dominated by a large band with *fwhm* of ~ 12 ° centred at ~ 20 ° ascribed to the presence of amorphous siliceous domains [68,113]. The second-order diffraction of this peak appears as a broad weak hump around 40 °–44 ° [68]. In addition, a shoulder is clearly discerned in all patterns between 12 ° and 14 °. This feature was previously ascribed to other intra-siloxane domains in-plane ordering with a characteristic distance of ~7.0 Å, estimated using the Bragg Law, see equation 5.1 [68].

$$2d\ sin\theta = n\lambda \qquad 5.1$$

where d is the structural unit distance, θ is the scattering angle, n the diffraction order and λ is the wavelength of the CuKα radiation (1.54 Å). Concerning the component at ~ 20 ° the d values were estimated yielding 4.40±0.02 Å, 4.41±0.02 Å and 4.36±0.02 Å for **t-U(5000)$_{0.25}$**, **t-U(5000)$_{0.05}$** and **t-U(5000)$_{0.01}$** respectively. As previously observed for analogous tri-ureasil hybrids [198], these values are similar to those reported for vitreous SiO_2 (4.2 Å) [199] and larger than the Si–O (1.62 Å), O–O (2.65 Å), and Si–Si (3.12 Å) distances, pointing out that for the **t-U(5000)** the basic period is well beyond the first few near-neighbour distances [68,113]. The coherence length (L_c), over which the structural unit survives, was estimated using the modified Sherrer, see equation 5.2 [68]:

$$L_c = \frac{0.94 \times I \times \lambda}{A \times cos\theta} \qquad 5.2$$

where *I* is the corresponding maximum intensity and *A*, in radians, is the integrated area of the peaks. In order to estimate the values of *I* and *A* the X-ray diffraction patterns of **-U(5000)$_{0.25}$**, **t-U(5000)$_{0.05}$** and **t-U(5000)$_{0.01}$** were fitted using pseudo-Voigt functions, yielding similar L_c values of 10.5±0.2 Å, 10.9±0.2 Å and 10.0±0.2 Å, respectively. The peak appearing at lower angles (~ 2-3 °, see inset in Figure 5.1) is due to siliceous interparticle scattering interference [68,113,129]. From the peak maximum position we estimated an average interparticle distance (d_{ip}) of 44.7±2.3 Å, for all selected **t-U(5000)$_{[HCl]}$**. The *d*, L_c and d_{ip} values found are similar to analogous amide-functionalized hybrids [198] being practically independent of [HCl].

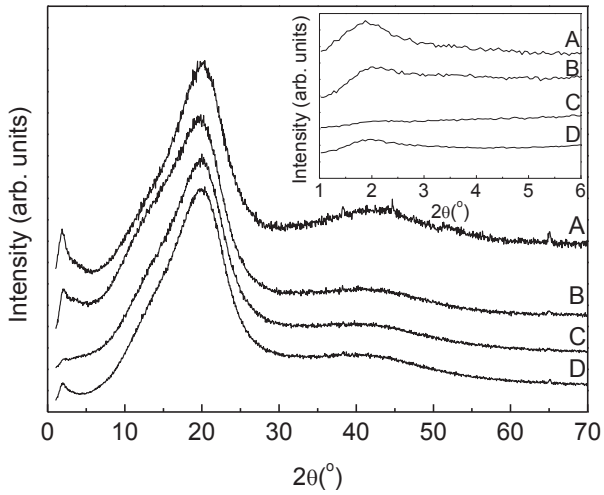

Figure 5.1. X-ray diffraction patterns of A) **t-U(5000)$_{2.0}$** [198], B) **t-U(5000)$_{0.25}$**, C) **t-U(5000)$_{0.05}$** and D) **t-U(5000)$_{0.01}$**. The inset shows the X-ray diffraction patterns in the low 2θ region (1.0-6 º). The hybrids were prepared with (A, B) 2.2 mmol and (C, D) 22.2 mmol of water.

The siliceous domains were further caractherized by nuclear magnectic resonance (NMR). A similar conclusion was derived from the analysis of the ^{29}Si MAS NMR and ^{13}C CP/MAS NMR spectra for selected hybrids (**t-U(50000)$_{0.25}$** and **t-U(5000)$_{0.05}$**). The ^{29}Si MAS NMR spectra, Figure 5.2, exhibit broad signals characteristic of T_2 and T_3 sites.

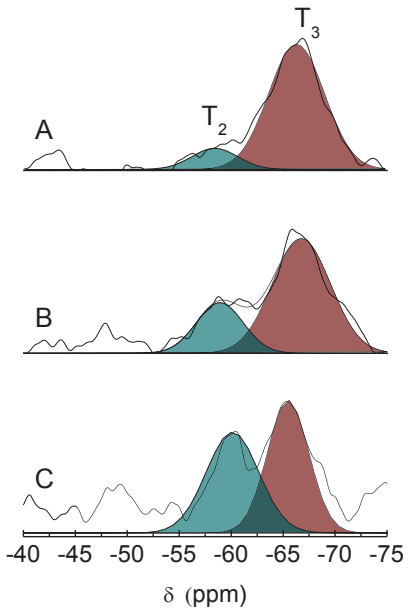

Figure 5.2 ^{29}Si MAS NMR spectra of A) **t-U(5000)$_{2.0}$**, B) **t-U(50000)$_{0.25}$** and C) **t-U(5000)$_{0.05}$** prepared with 2.2 mmol, 2.2 mmol and 22.2 mmol of water, respectively. The shadowed areas (dark cyan and pink) represent the T_2 and T_3 environments, respectively.

Table 5.2 show the position (δ) and assignment [111,200] of the resonance peaks of the ^{29}Si MAS NMR and ^{13}C CP/MAS NMR spectra.

The *c* values (calculated using the expression 3.1 detailed in Chapter 3), yield 91% and 92% for **t-U(50000)$_{0.25}$** and **t-U(5000)$_{0.05}$**, respectively, slightly smaller than for **t-U(5000)$_{2.0}$**.

The ^{13}C CP/MAS NMR spectra, Figure 5.3, are dominated by a pair of peaks located at 75.3 ppm and 73.5 ppm ascribed to the methane and methylene groups of the polyoxypropylene (POP) polymer chains, respectively. The intense peak at 17.4 ppm is due to the methyl groups of the oxypropylene repeat units. The broad, ill-defined signal at ~159 ppm is associated to the urea carbonyl groups [68].

Table 5.2 ^{29}Si MAS NMR and ^{13}C CP/MAS NMR spectroscopic data of **t-U(5000)$_{2.0}$** [198], **t-U(5000)$_{0.25}$** and **t-U(5000)$_{0.05}$**, δ (ppm), integrated area (A, %) and c (%) values.

^{29}Si MAS NMR (A)			**Assignment**
t-U(5000)$_{2.0}$	**t-U(5000)$_{0.25}$**	**t-U(5000)$_{0.05}$**	[111,200-202]
−58.4 (13.8)	−58.91 (26.1)	−60.13 (25.1)	T_2
−66.3 (86.2)	−66.74 (73.9)	−65.48 (74.9)	T_3
95	91	92	c
	^{13}C CP/MAS		
159.6	159.2	158.8	-N(C=O)N-
75.4	75.4	75.4	CH(CH$_3$)CH$_2$
73.5	73.46	73.5	CH(CH$_3$)CH$_2$
45.7	45.7	45.7	NCH$_2$CH$_2$CH$_2$Si
23.3	23.3	24.0	NCH$_2$CH$_2$CH$_2$Si-
17.4	17.71	17.70	CH(CH$_3$)CH$_2$

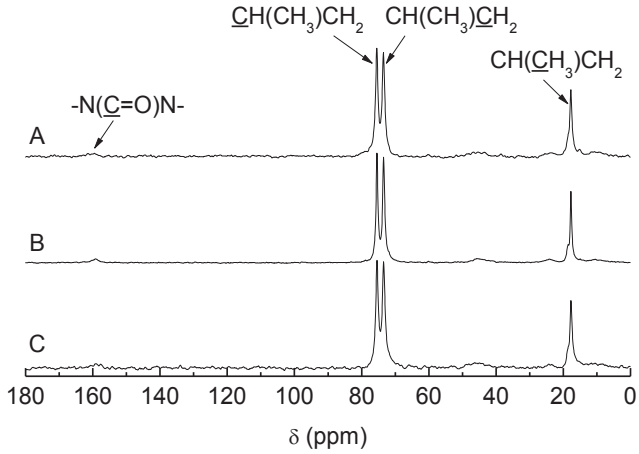

Figure 5.3. ^{13}C CP/MAS NMR spectra of A) **t-U(5000)$_{2.0}$** [198], B) **t-U(5000)$_{0.25}$** and C) **t-U(5000)$_{0.05}$** prepared with 2.2 mmol, 2.2 mmol and 22.2 mmol of water, respectively.

The FT-IR spectra of the **t-U(5000)$_{[HCl]}$** hybrids are depicted in Figure 5.4.

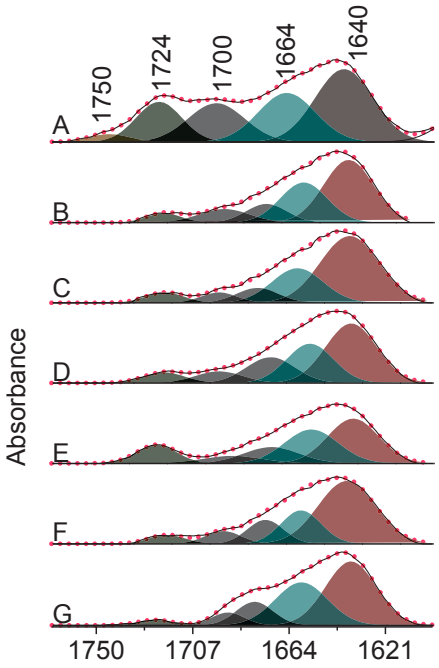

Figure 5.4. FT-IR spectra (*solid line*), simulated spectrum (*closed circles*) and deconvoluted bands (shadowed areas) of the hybrids A) **t-U(5000)$_{2.0}$** [198], B) **t-U(5000)$_{0.25}$**, C) **t-U(5000)$_{0.10}$**, D) **t-U(5000)$_{0.05}$**, E) **t-U(5000)$_{0.025}$**, F) **t-U(5000)$_{0.01}$** and G) **t-U(5000)$_{0.001}$** in the "Amide I" region. The hybrids were prepared with (A-C, E) 2.2 mmol and (D, F, G) 22.2 mmol of water.

The "Amide I" envelope band was resolved into components at 1750 cm^{-1}, 1724 cm^{-1}, 1700 cm^{-1}, 1664 cm^{-1} and 1640 cm^{-1}, using Gaussian band shapes. The band at ~ 1750 cm^{-1} is produced by urea groups which do not participate in any H–bonding interactions [64,113,115], being only detected for the hybrid prepared with [HCl]=2.0 M. The bands around 1724 cm^{-1}, 1700 cm^{-1}, 1664 cm^{-1} are ascribed to C=O groups belonging to disordered H–bonded POP/urea aggregates of increasing strength [64,113,115]. The 1640 cm^{-1} feature is assigned to C=O groups included in significantly more ordered H–bonded urea/urea aggregates [64,113,115]. The profile of the "Amide I" band of the hybrid materials suggest that globally the H–bonded array of the tripodal host material is not significantly affected by the presence of HCl, since neither the aggregates of **t-U(5000)** are entirely destroyed nor new ones are formed. Changes in [HCl] seem to affect the proportion of POP/urea aggregates slightly. This effect is manifested by band redistribution of the corresponding components. This is particularly evident in the case of **t-U(5000)$_{2.0}$** [198] where the fraction of POP/urea

aggregates responsible for the bands emerging at about 1724 cm^{-1} and 1700 cm^{-1} is higher than in all the other samples. In all the cases the amount of non-bonded carbonyl groups is negligible, an indication that all the urea groups are involved in the establishment of H–bonding interactions.

5.2.3 Photoluminescence

The UV-Visible absorption spectra of the selected tri-ureasil were recorded; see Figure 5.5, enabling the study of the absorption coefficient (α) with HCl concentration. The determination of the α was estimated using the Lambert–Beer equation:

$$\alpha = \frac{A}{t} \qquad 5.3$$

where t is the sample thickness (varying between 0.53 mm and 1.1 mm) and A is the absorbance defined as $A=-\log\frac{I_0}{I}$ where I_0 is the intensity of the incident light beam and I is the intensity of the light coming out of the samples.

All the spectra reveal a broad absorption region (250-500 nm) with a main component at ~ 278 nm and a low-relative intensity tail (330-500 nm). The inset in Figure 5.5 shows α values at the high absorption wavelength component (278 nm, α_{278}) and within the low-intensity tail (360 nm, α_{360}). The higher α_{278} value is observed for the hybrid prepared with [HCl]=0.05 M (α_{278}=6.78 cm^{-1}). For [HCl]= 0.025 M and [HCl]= 0.1 M, α_{278} display minor variations (3.11 cm^{-1} and 3.99 cm^{-1}, respectively), decreasing for [HCl]=0.25 M (α_{278}=1.45 cm^{-1}). At 360 nm, α displays minor variations, with a maximum value for the hybrid prepared with [HCl]=0.1 M of (α_{360}=0.69 cm^{-1}).

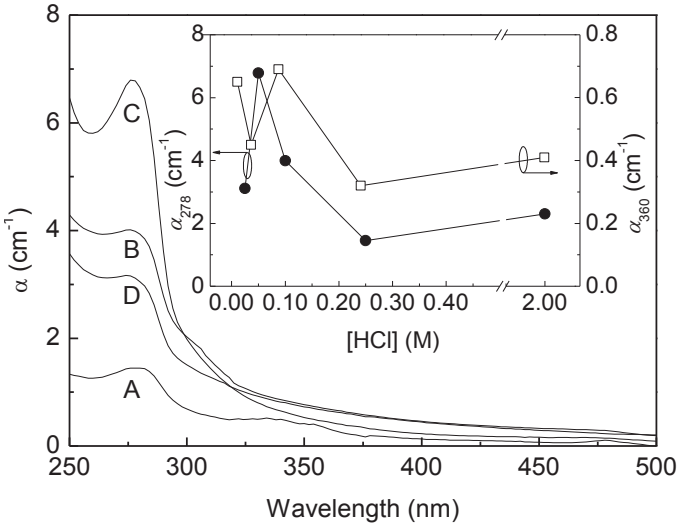

Figure 5.5. UV-Visible absorption spectra of A) **t-U(5000)$_{0.25}$**, B) **t-U(5000)$_{0.1}$**, C) **t-U(5000)$_{0.05}$** and D) **t-U(5000)$_{0.001}$**. The inset shows the absorption coefficient at 278 nm (α_{278}) and 360 nm (α_{360}), and the lines are visual guides. The hybrids were prepared with (A, B) 2.2 mmol and (C, D) 22.2 mmol of water. The α value for [HCl]=2 was reported in [198].

Under UV-Visible excitation, all hybrids display a similar emission at room temperature, a representative emission is illustrated in Figure 5.6 for **t-U(5000)$_{0.05}$**. The emission spectra are composed of a broad band (290-590 nm), which peak position deviates towards the red as the excitation wavelength increases from 270 nm to 360 nm, for **t-U(5000)$_{0.05}$** prepared with 22.2 mmol of water. These emission features (energy and *fwhm*) are independent of HCl concentration, resembling those previously reported for amine-functionalised hybrids being, therefore, ascribed to electron-hole recombinations mediated by a mechanism typical of D-A pairs occurring in the urea linkages and in the siliceous nanodomains [107,115], as we will detailed in the section 5.4 of this chapter. The inset in Figure 5.6 shows the excitation spectra for **t-U(5000)$_{0.05}$** monitored along the emission band, revealing a broad band (240-420 nm) with two main components at ~ 280 nm and 360 nm. The higher (360 nm) and lower (280 nm) wavelength components can be ascribed to the preferential excitation of NH/C=O and siliceous-related emissions, respectively [107,115]. The origin of the emission will be discussed in detailed in section 5.4 of this Chapter.

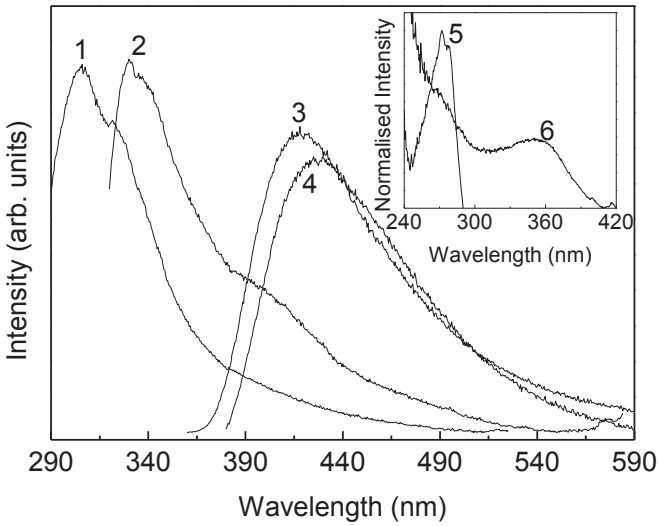

Figure 5.6. Emission spectra (300 K) excited at 1) 270 nm, 2) 300 nm, 3) 340 nm and 4) 360 nm of **t-U(5000)$_{0.05}$** prepared with 22.2 mmol of water. The inset shows the excitation spectra monitored at 5) 310 and 6) 440 nm.

The ϕ values were studied at different excitation wavelengths, at the maximum absorption peak position (278 nm, Figure 5.5) and within the absorption tail (330-400 nm). Under excitation at 278 nm, the ϕ values are very similar, increasing from 0.03±0.01 to 0.06±0.01 as the [HCl] decreases from 2.0 M to 0.025 M, respectively. Higher values are found for excitation wavelengths between 330-400 nm. In particular, the maximum ϕ values (0.13±0.01) were found to be constant within the excitation wavelength range of 360-380 nm for the hybrids prepared with [HCl]=0.01 M, [HCl]=0.05 M and [HCl]=0.1 M, Table 5.3.

Table 5.3. ϕ_{278} and ϕ_{360} excited at 278 and 360 nm, respectively, of the urea cross-linked tripodal siloxane-based hybrids.

Designation	ϕ_{278} (±0.01)	ϕ_{360} (±0.01)
t-U(5000)$_{2.0}$ [a] [198]	0.03	0.01
t-U(5000)$_{0.25}$ [a]	0.04	0.05
t-U(5000)$_{0.1}$ [a]	0.05	0.13
t-U(5000)$_{0.05}$ [a]	0.06	0.12
t-U(5000)$_{0.01}$ [b]	0.05	0.12
t-U(5000)$_{0.025}$ [a]	0.06	< 0.01
t-U(5000)$_{0.001}$ [b]	0.02	0.02

[a,b] The hybrids were prepared with 2.2 and 22.2 mmol of water, respectively.

At higher concentrations ([HCl]=0.25 M), the ϕ values decrease to 0.05±0.01. The higher reduction in the ϕ values was observed for the lowest [HCl]. It should be noted that a substantial decrease in the ϕ values was also found at high [HCl]=2.0 M. Therefore, we may establish the [HCl] range that contributes to boost the ϕ values of the urea cross-linked tripodal siloxane-based hybrids, namely 0.01≤[HCl]≤0.1 M. This values are higher than those previously reported for amine-functionalised hybrids (di-ureasils) derived from carboxylic acid solvolysis (0.096-0.104±0.01) [68] and those previously achieved for **t–U(5000)PTES** and **t–U(5000)DMDPS** (0.07±0.01 and 0.10±0.01, respectively) [198].

Time-resolved emission spectroscopy was used to further study the influence of [HCl] in the photoluminescence features of the urea cross-linked tripodal siloxane-based hybrids. The room temperature time resolved emission spectra display a large broad band (350-550 nm) peaking at 383 nm, for SD values within 0.4-18.0 ns, as illustrated for **t-U(5000)$_{0.05}$** in Figure 5.7.

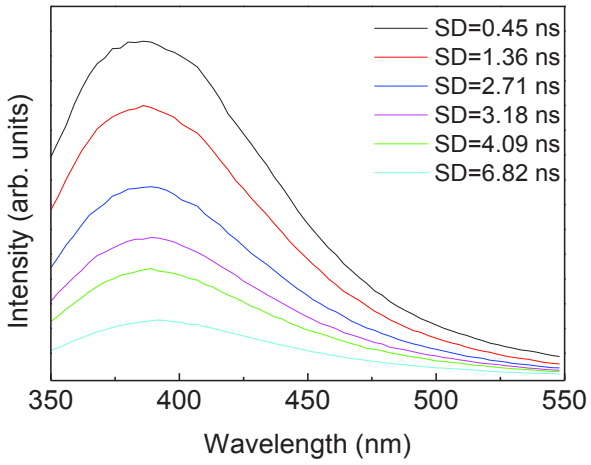

Figure 5.7. Time-resolved emission spectra (300K) excited at 330 nm and acquired at different SD values for **t-U(5000)$_{0.05}$** prepared with 22.2 mmol of water.

The emission decay curve illustrated in Figure 5.8, under excitation at 330 nm and monitored at the maximum emission peak position 383 nm is well described by a single exponential behavior. The lifetime value (τ) was obtained from the following expression:

$$I(t) = I_0 \times \exp^{\left(-\frac{t-t_0}{\tau}\right)} \qquad 5.4$$

where I_0 is the intensity at $t = t_0$=18.40 ns.

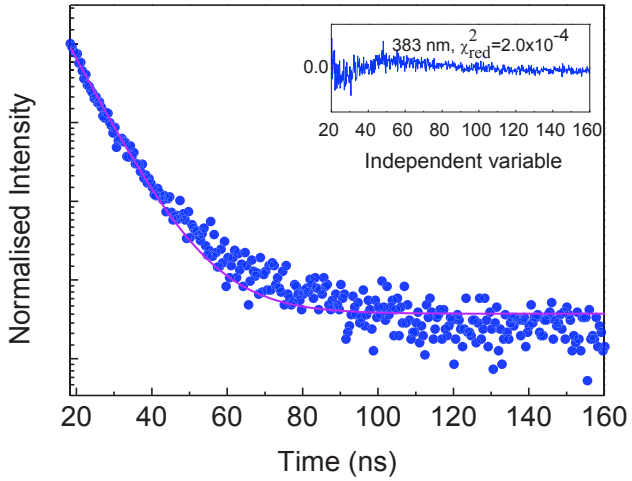

Figure 5.8. Room temperature (300 K) emission decay curve excited at 330 nm and monitored at 383 nm for **t-U(5000)$_{0.05}$** prepared with 22.2 mmol of water. The solid line represents the data best fit. The inset shows the respective regular residual plot also shown for a better judgment of the fit quality.

Decreasing the temperature to 12 K induces marked changes in the recombination mechanism time scale. Figure 5.9 illustrates the emission features obtained at 12 K for SD values between 0.05 ms and 5.00 ms for **t-U(5000)$_{0.05}$** excited at 360 nm, revealing four main components at 425 nm, 450 nm, 488 nm and 520 nm.

At longer SD values (SD≥ 10.00 ms), only the high-wavelength band (520 nm) ascribed to electron-hole recombinations within the N-H/C=O groups of the cross-linkages can be observed [68,198]. Similarly to that previously reported for analogous materials, the low-wavelength (425 nm, 450 nm and 488 nm) components are due to the presence of electron-hole recombinations within the siliceous nanocluster [68,198].

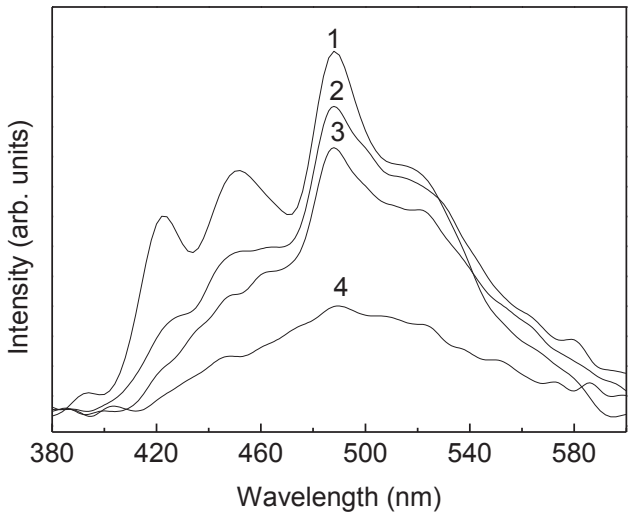

Figure 5.9. Time-resolved emission spectra (12 K) of **t-U(5000)$_{0.05}$** prepared with 22.2 mmol of water excited at 360 nm and acquired at SD values of 1) 0.05 ms, 2) 5.00 ms, 3) 10.00 ms, and 4) 50.00 ms.

The lifetime values of the siliceous and NH/C=O-related emission were estimated by monitoring the emission decay curves at 425 nm and 520 nm, illustrated in Figure 5.10.

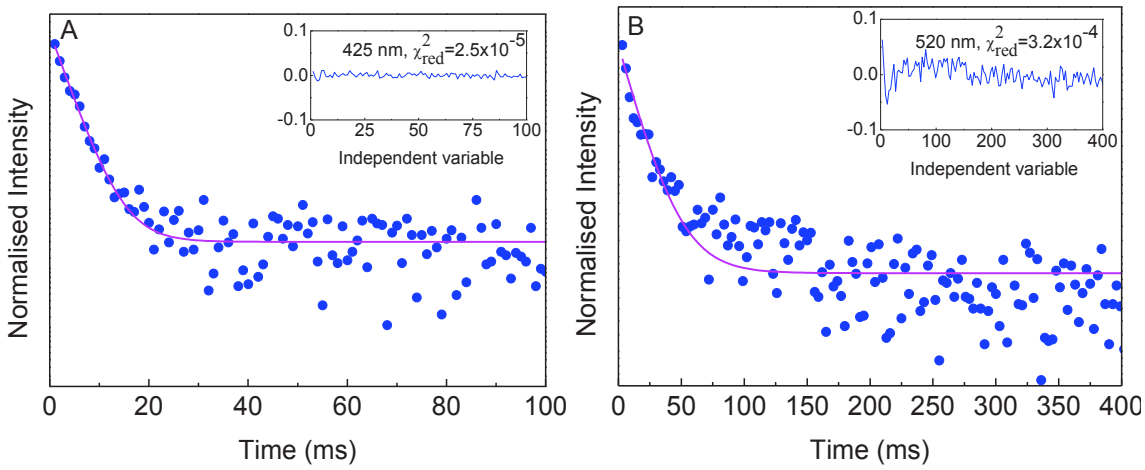

Figure 5.10. Low temperature (12 K) emission decay curve excited at 360 nm and monitored at A) 425 nm and B) 520nm of **t-U(5000)$_{0.05}$** prepared with 22.2 mmol of water. The solid lines represent the data best fit, using a single exponential function. The inset shows the respective regular residual plot also shown for a better judgment of the fit quality.

The emission decay curves monitored at 450 nm and 488 nm resemble that acquired at 425 nm. The emission decay curves are well modeled by a single exponential function yielding

lifetime values of 4.1±0.1 ms and 19.2±1.1 ms for the siliceous and N-H/C=O related components, respectively. The lifetime at 425 nm for **t-U(5000)$_{0.05}$** is greater than that found for the **t-U(5000)$_{2.0}$** (3.5±0.2 ms), however, the NH/C=O-related lifetime value is smaller (38.5±2.8 ms) [198], demonstrating that the synthesis conditions have impact on the time scale of the recombination mechanisms.

5.3 Role of the reactive atmosphere during the sol-gel synthesis

In this section we pursue the study of the **t-U(5000)** through the assessment of the role of the reactive atmosphere during the hydrolysis and condensation reactions on its optical properties. In particular, the local structure and optical features (α, emission spectral range and ϕ values) of **t-U(5000)** hybrids produced under controlled atmospheric conditions (inside a glove box with low oxygen and water concentrations) will be compared with previous results for the same materials synthesized under usual laboratory atmospheric conditions.

5.3.1 Synthesis

The synthesis of the **t-UPTES(5000)** follows the route above described (section 5.2). Next, inside the glove box, EtOH (J.T. Baker, ≥ 99.9 %) was added to **t-UPTES(5000)** (v/w ratio=1:3=0.5 mL/1.5 g) under magnetic stirring at room temperature. Then, an ethanolic solution of HCl with different concentration values, [HCl]=0.05 M, [HCl]=0.25 and [HCl]=1.00 M, and a volume of 0.06 μL, 0.31 μL and 1.24 μL, respectively and (2.2 mmol) of water, see Table 5.4, were added to **t-UPTES(5000)**, under magnetic stirring at room temperature for 0.5 h. Part of the solution was cast into a polystyrene mold (1×1×3 cm^3) and left to gel at room temperature for 24 h. Finally, the mold was transferred to an oven (Microtube, single tray) at 45 °C for 2 days yielding transparent monoliths.

Table 5.4. Synthesis and processing details of the urea cross-linked tripodal siloxane-based hybrids (monoliths and thin films) prepared inside the glove box.

Designation	[HCl] (M)	Amount of HCl (mmol)	Processing
t-U(5000)$_{0.05}$GB	0.05	0.002	monolith
t-U(5000)$_{0.25}$GB	0.25	0.01	
t-U(5000)$_{1.00}$GB	1.00	0.04	
F-t-U(5000)$_{0.05}$GB	0.05	0.002	film
F-t-U(5000)$_{0.25}$GB	0.25	0.01	

The remaining part of the solution with [HCl]=0.05 M and [HCl]=0.25 M was used to process thin films deposited on quartz substrates (Helma 6030, 25×25×1 mm^3) by a one-step dip-coating process at controlled velocity (Microquimica, MQCTL2000-MP), see Figure 5.11.

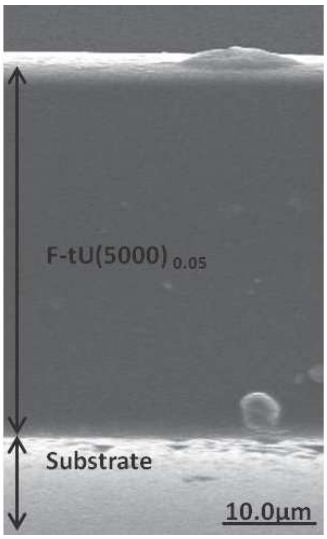

Figure 5.11. SEM images of the cross section of **F-t-U(5000)$_{0.05}$GB**.

The films were transferred to the oven at 45 °C for 2 days to remove residual solvents. The solution with [HCl]=1.00 M was not used to produce films because the gelation time occurred within a few seconds after HCl addition, preventing the deposition by dip-coating. The tri-ureasil layer was dense, smooth and crack-free with thickness of 38.7 µm, as illustrated in Figure 5.11 for the hybrid prepared with [HCl]=0.05 M.

After the heat treatment, the monoliths and films were sealed in plastics and transferred to the glove box where they were kept for 4 months. After this period their morphology, local

structure and optical features were characterized under ambient conditions at room temperature. The monoliths and films will be hereafter identified as **t-U(5000)$_{[HCl]}$GB** and **F-t-U(5000)$_{[HCl]}$GB**, respectively.

5.3.2 Local Structure

Figure 5.12 compares the X-ray diffraction patterns of the **t-U(5000)** hybrids prepared inside the glove box with variable HCl concentration and water content.

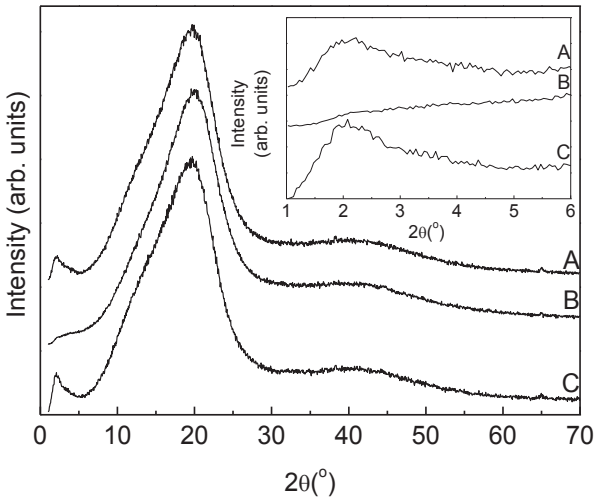

Figure 5.12. X-ray diffraction patterns of A) **t-U(5000)$_{0.05}$GB**, B) **t-U(5000)$_{0.25}$GB** and C) **t-U(5000)$_{1.00}$GB.** The inset shows a magnification of the low diffraction angle region (1.0 ≤2θ ≤6.0°).

All the X-ray diffraction patterns of tri-ureasils prepared inside glove box are composed of a large band (*fwhm* of ~ 10°) centered at ~ 20°, ascribed to the presence of amorphous siliceous domains with d=4.51±0.02 Å, independently of [HCl]. The L_c over which the structural unit survives was estimated yielding a value of 10.5±0.2 Å for all the hybrids. The values found for d and L_c are similar to those previously reported for analogous tri-ureasils prepared under usual laboratory atmospheric conditions.

The ^{29}Si MAS NMR spectra of **t-U(5000)$_{0.05}$GB**, **t-U(5000)$_{0.25}$GB** and **t-U(5000)$_{1.00}$GB** exhibit broad signals characteristic of T_2 and T_3 environments, see Figure 5.13. Table 5.5 show the position (δ) and assignment [111,200] of the resonance peaks of the ^{29}Si MAS NMR and ^{13}C CP/MAS NMR spectra.

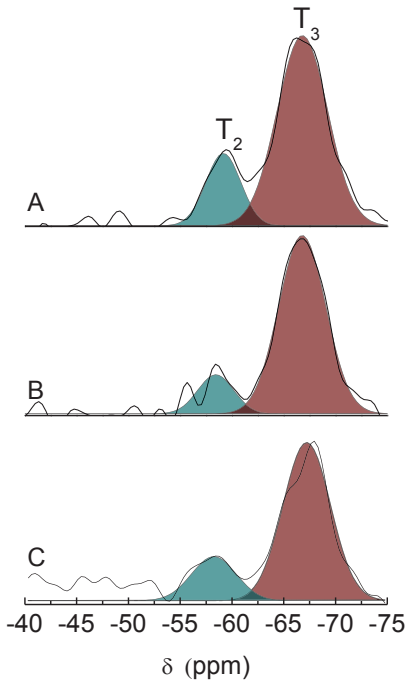

Figure 5.13. ^{29}Si MAS NMR spectra of A) **t-U(5000)$_{0.05}$GB**, B) **t-U(5000)$_{0.25}$GB**, C) **t-U(5000)$_{1.00}$GB**. The shadowed areas (dark cyan and pink) represent the T_2 and T_3 environments, respectively.

The *c* values were estimated yielding ~97 %, independently of [HCl]. We should note that these values are substantially higher than those previously reported for the same materials prepared under usual laboratory atmospheric conditions, for the same [HCl] and amount of water. Moreover, for the hybrids prepared under usual laboratory atmospheric conditions the *c* values depend on [HCl]. An increase of [HCl] from 0.05 M to 0.25 M resulted in an increase of the *c* values from 84 % to 91 %.

Table 5.5. ^{29}Si MAS NMR and ^{13}C CP/MAS NMR spectroscopic data of **t-U(5000)$_{0.05}$GB**, **t-U(5000)$_{0.25}$GB** and **t-U(5000)$_{1.00}$GB**, δ (ppm), integrated area (A, %) and c (%) values

^{29}Si MAS (A)			Assignment
t-U(5000)$_{0.05}$	**t-U(5000)$_{0.25}$**	**t-U(5000)$_{1.00}$**	[111,200-202]
-59.13 (12.81)	-58.49 (5.07)	-58.34 (9.48)	T_2
-66.82 (87.19)	-66.76 (94.93)	-67.72 (94.93)	T_3
96	98	97	c
	^{13}C CP/MAS		
159.3	159.5	159.5	-N(C=O)N-
75.5	75.4	75.4	CH(CH$_3$)CH$_2$
73.5	73.5	73.5	CH(CH$_3$)CH$_2$
45.8	46.0	45.9	NCH$_2$CH$_2$CH$_2$Si
23.3	23.3	23.3	NCH$_2$CH$_2$CH$_2$Si-
17.8	17.8	17.8	CH(CH$_3$)CH$_2$

The ^{13}C MAS NMR spectra, Figure 5.14, are dominated by a pair of peaks located at 75.3 ppm and 73.5 ppm ascribed to the methane and methylene groups of the POP polymer chains, respectively. The intense peak at 17.7 ppm is due to the methyl groups of the POP repeat units. The broad, ill-defined signal at ~159 ppm is associated to the urea carbonyl groups. In contrast to the situation found in the ^{29}Si MAS NMR spectra that point out changes in the Si local environment at variable [HCl], the ^{13}C MAS NMR spectra are independent of the synthesis atmosphere revealing that no changes occurred in the POP chains. Nevertheless, the processing of the materials inside the glove box induced major alterations in the urea-cross-links, when compared with the **t-U(5000)** hybrids prepared under usual laboratory atmosphere conditions, as detailed next.

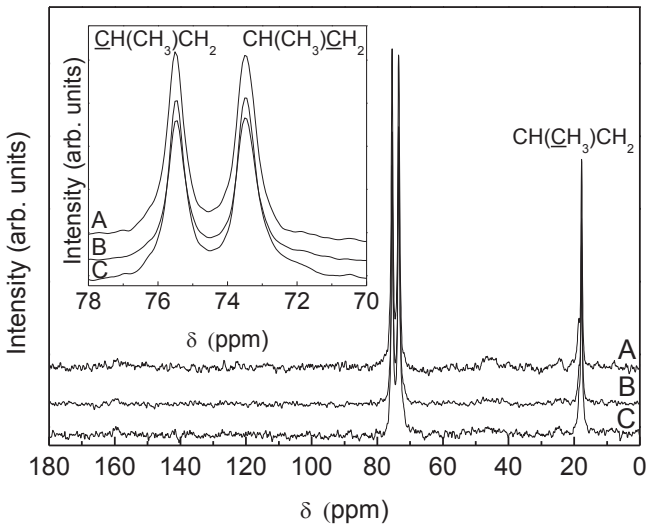

Figure 5.14. ^{13}C CP/MAS NMR spectra of A) **t-U(5000)$_{0.05}$GB**, B) **t-U(5000)$_{0.25}$GB**, C) **t-U(5000)$_{1.00}$GB**.

Figure 5.15 shows the FT-IR spectra in the "Amide I" and "Amide II" regions of **t-U(5000)$_{0.05}$GB**, **t-U(5000)$_{0.25}$GB** and **t-U(5000)$_{1.00}$GB**. The "Amide I" region mode is associated essentially with the C=O stretching vibration [115,203]. For the **t-U(5000)$_{0.05}$GB**, **t-U(5000)$_{0.25}$GB** and **t-U(5000)$_{1.00}$GB**, the "Amide I" envelope band was resolved into 6 components at 1745 cm^{-1}, 1718 cm^{-1}, 1700 cm^{-1}, 1674 cm^{-1}, 1664 cm^{-1} and 1640 cm^{-1}. The band at ~1745 cm^{-1} (Curve 1 in Figure 5.15) was ascribed to urea groups which do not participate in any H–bonding interaction [115,203].

We should note that the relative integral area of that component is higher for the **t-U(5000)$_{0.25}$GB** and has similar contributions for **t-U(5000)$_{0.05}$GB** and **t-U(5000)$_{1.00}$GB**. The bands at ~1718 cm^{-1} (Curve 2 in Figure 5.15), 1700 cm^{-1}, 1674 cm^{-1} and 1664 cm^{-1} are ascribed to C=O groups belonging to less engaged H–bonded POP/urea aggregates of increasing strength [115,203]. The 1640 cm^{-1} feature (Curve 3, Figure 5.15) is assigned to C=O groups included in significantly more engaged H–bonded urea/urea aggregates [115,203]. Globally, we note that, for the hybrids prepared under usual laboratory atmospheric conditions, the component at ~ 1745 cm^{-1} is only present for high [HCl]=2.0 M being absent for the hybrids prepared for $1.0\times10^{-3}\leq$[HCl]$\leq$0.25 M. Therefore, we are led to conclude that the proportion of free urea groups depends on the synthetic conditions, such as [HCl] and the atmospheric composition.

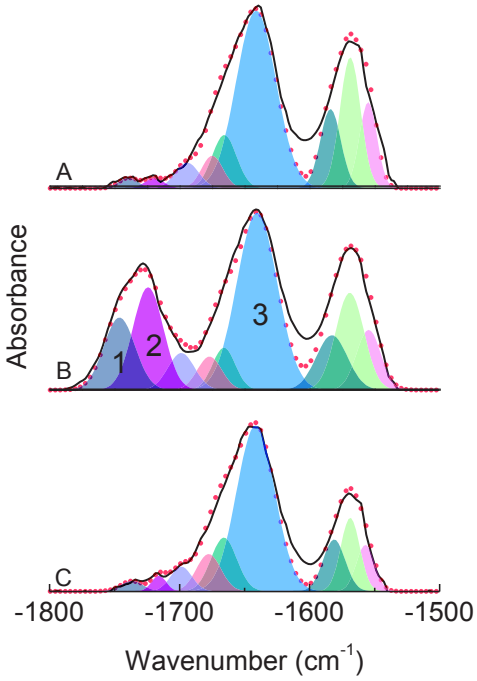

Figure 5.15. FT-IR spectra (solid lines) and curve-fitting results (red circles) of A) **t-U(5000)$_{0.05}$GB**, B) **t-U(5000)$_{0.25}$GB**, C) **t-U(5000)$_{1.00}$GB** in the 1800-1500 cm^{-1} spectral range, (1), (2) and (3) identify the C=O stretching vibration at 1745 cm^{-1}, 1718 cm^{-1} and 1640 cm^{-1}, respectively.

5.3.3 Photoluminescence

The optical features of all the hybrids prepared inside of the glove box were studied by UV-Visible absorption and photoluminescence. Figure 5.16 shows the α as a function of [HCl] for **t-U(5000)$_{0.05}$GB**, **t-U(5000)$_{0.25}$GB** and **t-U(5000)$_{1.00}$GB**.

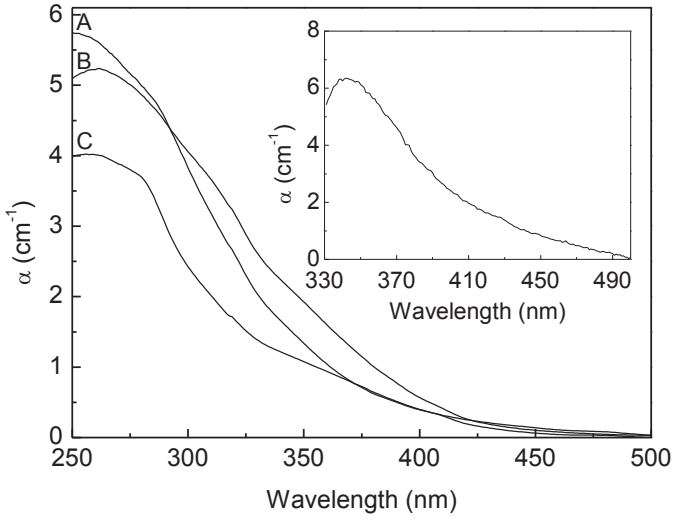

Figure 5.16. UV-Visible absorption coefficient (α) spectral dependence of A) **t-U(5000)$_{0.05}$**, B) **t-U(5000)$_{0.25}$**, and C) **t-U(5000)$_{1.00}$**. The inset shows the α variation for **F-t-U(5000)$_{0.05}$**.

The *a* has a maximum value at ~ 260 nm, ascribed to the preferential absorption of the siliceous rich domains [204], increasing from 4.01 cm^{-1} to 5.63 cm^{-1} as [HCl] decreases from 1.00 M to 0.05 M. The α values display another feature at ~335 nm, associated with the preferential absorption of the urea groups [204], with a maximum value for **t-U(5000)$_{0.25}$GB** (2.41 cm^{-1}).

The inset in Figure 5.16, shows the spectral variation of α for the **F-t-U(5000)$_{0.05}$GB**. The region below to 330 nm was not assessed due to the presence of the glass substrate that displays a very high absorbance. In the same wavelength range, the values of α for the film increase by a factor of 3, when compared with those measured for the hybrid processed as a monolith. Table 5.6 lists the values of α measured as function of [HCl] at selected wavelengths for the hybrids processed as monoliths and films. For the same materials processed under usual laboratory atmospheric conditions a deviation towards the red of the maximum value of α to ~278 nm was observed. Such deviation may be ascribed to the different *c* values of the hybrids prepared under different atmospheres that induce changes in the Si-local environment. When comparing the synthetic methodologies, the most interesting feature is the significant enhancement and enlargement of the absorption region associated with the urea groups. For instance, around 335 nm, the α of the hybrids prepared inside the glove box

Figure 5.16, are 60-80 % higher than the values measured for the same materials prepared under usual laboratory atmosphere conditions Figure 5.5.

Table 5.6. α at selected wavelengths of **t-U(5000)$_{0.05}$GB**, **t-U(5000)$_{0.25}$GB** and **t-U(5000)$_{1.00}$GB** processed as monoliths and films.

λ (nm)	t-U(5000)$_{0.05}$GB		t-U(5000)$_{0.25}$GB	t-U(5000)$_{1.00}$GB
	Monolith	Film	Monolith	Monolith
260	5.63	-	5.22	4.01
280	4.99	-	4.86	3.69
300	3.83	-	4.06	2.43
335	1.83	6.05	2.41	1.28
360	1.04	5.43	1.60	0.94
380	0.62	3.63	1.01	0.64
400	0.39	2.41	0.57	0.40
420	0.20	1.63	0.27	0.26
440	0.09	1.04	0.14	0.17

Under UV-Visible excitation all the hybrids display an efficient light emission visible at the naked eye, Figure 5.17 .

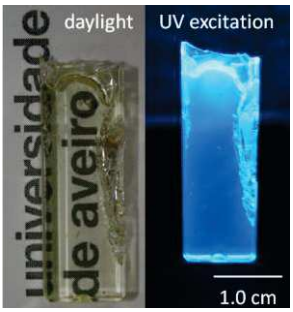

Figure 5.17. Photographs of **t-U(5000)$_{0.05}$GB** under daylight illumination and excited at 365 nm.

The emission spectra, Figure 5.18 are composed of a broad band (290-590 nm), whose peak position deviates towards the red in the excitation wavelength range between 300 nm and 340 nm.

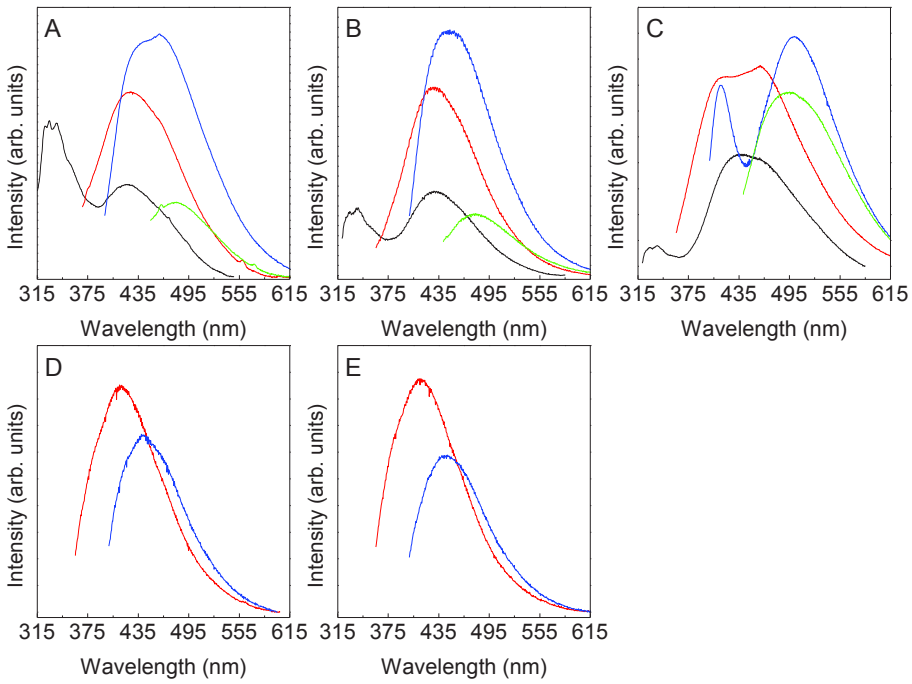

Figure 5.18. Emission spectra of A) **t-U(5000)$_{0.05}$GB**, B) **t-U(5000)$_{0.25}$GB**, C) **t-U(5000)$_{1.00}$GB**, D) **F-t-U(5000)$_{0.05}$GB** and E) **F-t-U(5000)$_{0.25}$GB** excited at (black line) 300 nm, (red line) 340 nm, (blue line) 380 nm and (green line) 420 nm.

The emission spectra are independent of [HCl], in the 0.05-0.25 M range. The emission features resemble those previously reported for amine-functionalized hybrids being, therefore, ascribed to electron-hole recombinations mediated by a mechanism typical of D-A pairs occurring in the urea linkages and in the siliceous nanodomains [107,115]. Analyzing the effect of the glove box synthesis conditions, we notice a relative enhancement of the high-wavelength component attributed to the urea groups in the emission spectra of **t-U(5000)$_{0.25}$GB**, Figure 5.18 B. The emission spectra of the hybrid prepared with higher [HCl]=1.00 M is deviated towards the red relatively to that found for **t-U(5000)$_{0.05}$GB** and **t-U(5000)$_{0.25}$GB**, and for an excitation wavelength of 380 nm it is clearly resolved into two components peaking at ~414 nm and 500 nm, Figure 5.18 C.

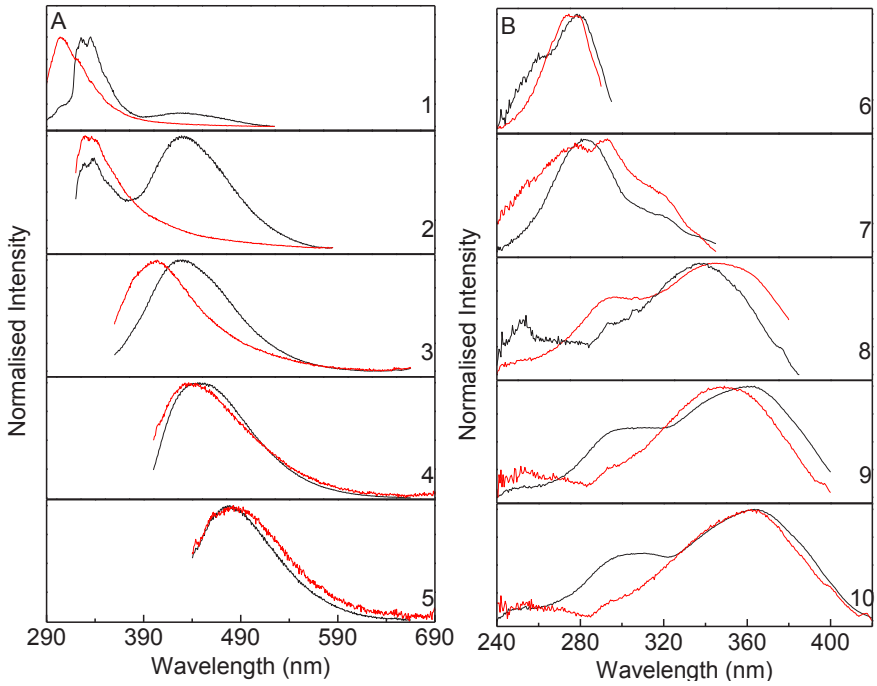

Figure 5.19. A) Emission spectra excited at (1) 270 nm, (2) 300 nm, (3) 340 nm, (4) 380 nm and (5) 420 nm and B) Excitation spectra monitored at (6) 310 nm, (7) 360 nm, (8) 400 nm, (9) 420 nm and (10) 440 nm of **t-U(5000)**$_{0.25}$ (black line) and **t-U(5000)**$_{0.25}$**GB** (red line).

The excitation spectra were monitored along the emission band (310-540 nm) being similar for the hybrids prepared with [HCl]=0.05 M and [HCl]=0.25 M. Under preferential monitoring of the siliceous-based component (monitoring wavelengths below 400 nm) the spectra reveal a broad band with two main components at ~280 nm and 320 nm. Increasing the monitoring wavelength (favoring the detection of the urea-related emission) another component at longer wavelength appears, whose peak position shifts from 335 nm to 360 nm as the monitoring wavelength increases from 400 nm to 540 nm. We should note that this high-wavelength component displays a larger relative intensity and *fwhm* compared with that found in the materials previously prepared under usual laboratory atmospheric conditions, Figure 5.19. The excitation spectra of **t-U(5000)**$_{1.00}$**GB** is similar to that of the hybrid prepared with lower [HCl] but is deviated to the red similarly to the situation found for the emission spectra. We should note that all the hybrids are excited in a wide spectral region from the UV to the blue (240-480 nm).

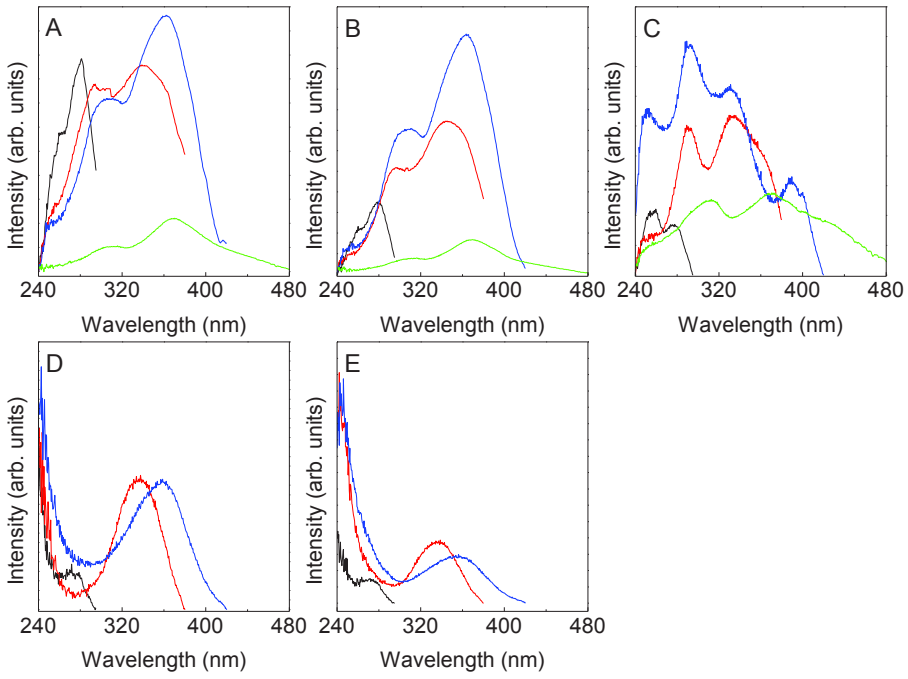

Figure 5.20. Excitation spectra of A) **t-U(5000)$_{0.05}$GB**, B) **t-U(5000)$_{0.25}$GB**, C) **t-U(5000)$_{1.00}$GB**, D) **F-t-U(5000)$_{0.05}$GB** and E) **F-t-U(5000)$_{0.25}$GB** monitored at (black line) 310 nm, (red line) 400 nm, (blue line) 440 nm and (green line) 540 nm.

For the hybrids processed as films, the emission peak position deviates to the blue (15 nm), relatively to the monoliths, as shown in Figure 5.18. The excitation spectra reveal essentially the same components detected in the spectra of the monolithic samples (also deviated to the blue), in which the relative high-wavelength component at ~ 280 nm is the most intense component, independent of the monitoring wavelength, Figure 5.20. The emission and excitation blue-shift effect observed for the samples prepared as films, relatively to those prepared as monoliths, was previously reported for other organic–inorganic hybrids, which can be explained based on the different kinetic behind the sol-gel process occurring in the solvent cast method to produce monoliths and in the deposition procedures via spin-coating to process films [204]. In the former case, the solvent is removed during and after the polycondensation reactions, mostly over the shrinkage step that takes hours, days or even months. In the case of thin films, the fast and compelled solvent extraction is much faster (seconds), and may result in a structure with lower degree of organization, compared with that of bulk hybrids [204].

The photoluminescence features were quantified through the measurement of the ϕ values as a function of the excitation wavelength, Table 5.7. The maximum ϕ values is 0.27±0.03, being constant (within the experimental error) for excitation wavelengths of 360 nm and 380 nm and independent of [HCl]. Under identical excitation conditions (UV spectral range between 360-400 nm), the values obtained here are higher than those previously reported for the previously tri-ureasils prepared under usual laboratory atmospheric conditions.

Table 5.7. ϕ excited at different wavelengths (λ_{exc}, nm) for **t-U(5000)$_{0.05}$GB**, **t-U(5000)$_{0.25}$GB** and **t-U(5000)$_{1.00}$GB**, **F-t-U(5000)$_{0.05}$GB** and **F-t-U(5000)$_{0.25}$GB** processed as monoliths and films.

λ_{exc}	ϕ				
	t-U(5000)$_{0.05}$	**F-t-U(5000)$_{0.05}$**	**t-U(5000)$_{0.25}$**	**F-t-U(5000)$_{0.25}$**	**t-U(5000)$_{1.00}$**
250	0.02	-	0.03	-	0.06
275	0.05	-	0.05	-	0.07
280	-	<0.01	-	<0.01	-
300	0.09	-	0.08	-	0.14
320	0.13	0.03	0.10	0.03	0.16
330	0.14	-	0.11	0.09	0.14
340	-	0.09	-	-	-
360	0.27	0.20	0.25	0.16	0.25
380	0.23	0.18	0.27	0.14	0.26
400	0.11	0.02	0.19	0.02	0.22
420	0.08	0.02	0.16	0.02	0.19
440	<0.01	-	0.18	-	0.18
453	-	-	0.13	-	0.13

Moreover, comparing the values measured for **t-U(5000)$_{0.05}$GB** and **t-U(5000)$_{0.25}$GB** with those measured for identical materials prepared under usual laboratory atmospheric conditions (0.12±0.01), we find out that the ϕ value are twice higher for the materials prepared inside a glove box. Moreover, the most interesting result is the fact that the materials prepared inside the glove box are also excited in visible spectral range (400-453 nm) with high ϕ values (0.18-0.22±0.01), in particular, for **t-U(5000)$_{0.25}$GB** and **t-U(5000)$_{1.00}$GB**. At excitation wavelengths of 453 nm, these two hybrids display a ϕ values of 0.13±0.01. The processing of **t-U(5000)** hybrids as thin films induces a small reduction in the maximum ϕ values to (0.14-0.20±0.02) excited within 360-380 nm. At higher wavelengths (400-453 nm) a significant

decrease was observed, as expected by the low relative intensity of the excitation spectra in that region.

The stability of the photoluminescence features was monitored by measuring the ϕ after the samples being kept under usual laboratory atmospheric conditions for 5 months. A small decrease was observed in the maximum ϕ values excited at 360 nm to 0.21±0.02. These above results (increased ϕ values under UV/blue excitation) point out the active role of the reaction atmospheric conditions (reduced amount of water and oxygen) during the hydrolysis and condensation reactions of sol-gel derived organic-inorganic hybrids in boosting the optical performance of the tri-ureasils.

5.4 Origin of the emission in amine- functionalized bridged silsesquioxanes

In an attempt to gain more insight into the origin and mechanisms responsible for the photonic properties of these triamine-functionalized hybrids, this section examines selectively the two emissions associated with the organic and inorganic counterparts. One model compound emulating the siliceous inorganic skeleton was synthesized and characterized. The organic counterpart is modeled using triamine (***Jeffamine T5000***®).

5.4.1 Synthesis

Inorganic model compound

A typical synthesis of the inorganic model compound involves the mixture of 2.0 mL (8.78 mmol) of tetraethoxysilan (TEOS, 99 %, ABCR) with 5.5 mL (30.4 mmol) of propyltrimethoxysilane (PTMOS, 97 %, ABCR), with a molar ratio TEOS/PTMOS=1:3.4 in a volume of 10.4 mL of EtOH. Then, 2.56 mL of 0.01 M HCl (pH=2) was added to this solution. The pH was measured yielding 2.5. The resulting sol was stirred in nitrogen at room temperature for 24 h. The sol was poured into a mold for gelation. Finally, the TEOS/PTMOS gel was obtained and dried at 50 °C for around one week. The reaction is shown in Scheme 5.2. The inorganic model compound will be designed as **1**.

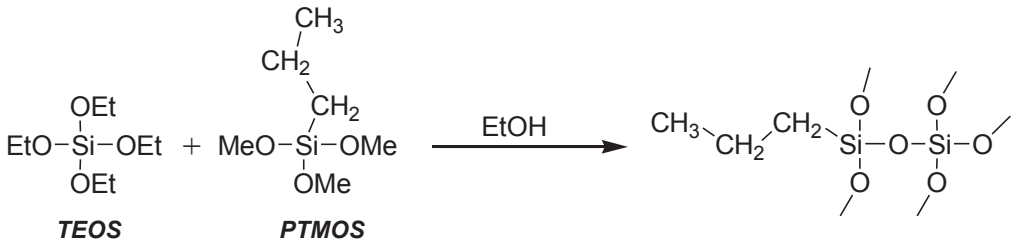

Scheme 5.2. Schematic representation of the synthesis of **1**.

The local structure of **1** will be study next by X-ray diffraction, ^{29}Si MAS NMR, ^{13}C CP/MAS NMR and FT-IR in order to confirme the structure of the material.

5.4.2 Local structure

The X-ray diffraction patterns of **1**, represented in Figure 5.21, are dominated by two main components at ~20.7 and at ~6.7 , ascribed to the presence of amorphous siliceous domains and due to interference effect between siliceous domains spatially correlated, respectively [128].

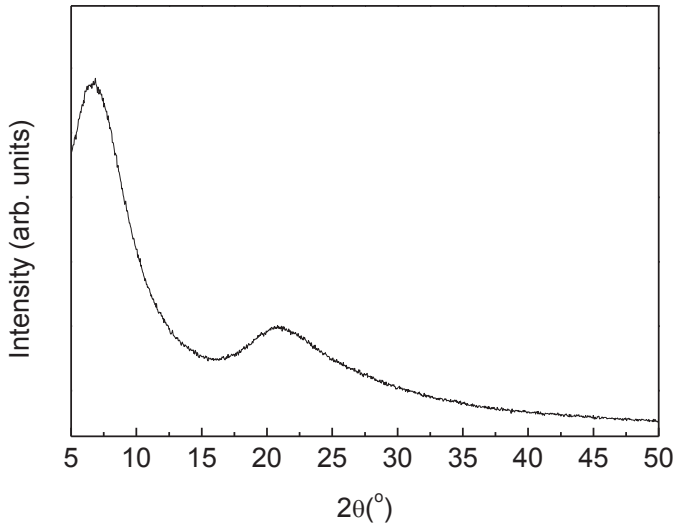

Figure 5.21. X-ray diffraction patterns of **1**.

For the component at higher angles a structural unit distance was estimated to be d_1=4.26±0.02 Å. These values are similar to those reported for vitreous SiO_2 (4.2 Å) [199,205,206], **t-U(5000)** (~4.4 Å) and larger than that previously calculated (3.67 Å) [128] for

an analogous compound prepared using a distinct molar ratio TEOS/PTMOS=1:4, indicating that the synthesis conditions induce changes in the conformation of the siliceous skeleton. The component at lower angles (~6.7) give us characteristic spacing of d_2=12.9±0.13 Å. We note that the siliceous domains are linked to an alkyl-chain comprising one bonds with average lengths [207] of 0.98 Å, 1.54 Å and 1.80 Å, respectively, thus, a chain length of 5.87 Å may be estimated. This suggests that **1** is composed of siliceous domains separated by two alkyl-chains chains. The difference between the estimated and experimental inter siliceous domains distance (11.74 Å and 12.9±0.13 Å, respectively) suggests ~1 Å of separation between alkyl-chains.

In order to verify the silicon environment, ^{29}Si MAS NMR was used. Figure 5.22 shows the ^{29}Si MAS NMR spectra of **1**, which exhibit T_1, T_2, T_3, Q^3 and Q^4 silicon environments. The T^n and Q_n sites result from hydrolysis and condensation of PTMOS and TEOS, respectively.

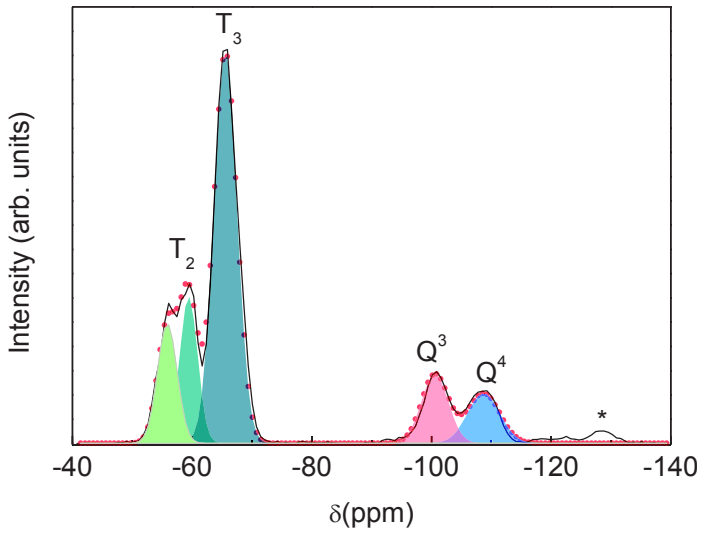

Figure 5.22. ^{29}Si MAS NMR spectra of **1**. The symbol (*) corresponds to a spinning side band.

The chemical shift and integrated area for each silicon environment were calculated through deconvolution of both envelopes using Voigt functions, (Figure 5.22 and Table 5.8). Condensation degrees (*CD*) of ~ 88 % was determined for **1** using the following expression:

$$CD = {}^{1}/_{3} \times (1 \times \%T_1 + 2 \times \%T_2 + 3 \times \%T_3) + 1/4 \times (1 \times \%Q^1 + 2 \times \%Q^2 + 3 \times \%Q^3 + +4 \times \%Q^4) \quad 5.5$$

Table 5.8. ^{29}Si CP/MAS NMR data (δ, ppm), integrated area (A, %) and assignment of **1**.

^{29}Si CP/MAS NMR (A)	Assignment
−56.5 (13.4)	T_2
−59.8 (14.9)	
−65.7 (51.9)	T_3
−101.5 (10.6)	Q^3
−109.0 (9.1)	Q^4
88 %	c

In addition the ^{13}C CP/MAS NMR was recorded with proposed to verify the organic part of **1**, see Figure 5.23.

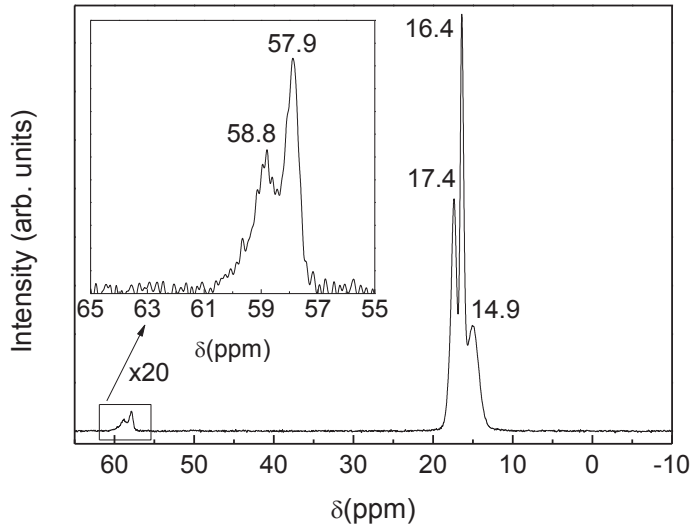

Figure 5.23. ^{13}C CP/MAS NMR spectra of **1**.

The position (δ) and assignment of the resonance peaks are given in Table 5.9. The ^{13}C CP/MAS NMR spectra display signals originating from the carbon atoms of the pendant alkyl chains and of the Si-bonded propyl chains which confirm the integrity of the latter organic functional groups of the organosilane precursor PTMOS. The ^{13}C CP/MAS NMR data also demonstrate that the hydrolysis reaction did not go to completion, as indicated by the presence of the peak at ~58 ppm, associated with the resonance of the ethoxyl carbon atoms.

Table 5.9. ^{13}C CP/MAS NMR spectra of **1**.

δ, ppm	**Attribution**
57.8	$O\underline{C}H_2CH_3$
17.4	$OCH_2\underline{C}H_3$
16.4	$OCH_2\underline{C}H_3$
14.9	$Si\underline{C}H_2CH_2$

The local structure of **1**, characterized by X-ray diffraction, ^{29}Si MAS NMR and ^{13}C CP/MAS NMR, support their use as inorganic structural model for the inorganic counterpart of tri-ureasil, being able to compare the emission features of **1** and with selected tri-ureasil (**t-U(5000)$_{0.05}$**, previously described. A comparison between the emission properties of ***Jeffamine T5000®*** and **1** with the emission features of **t-U(5000)$_{0.05}$** will be performed.

5.4.3 Photoluminescence

Figure 5.24 A shows the emission spectra of **t-U(5000)$_{0.05}$** excited at 260 nm. A broad band between 290 nm and 450 nm with a maximum at ~ 300 nm can be identified. A similar emission was observed for **1**. Increasing the excitation wavelength (330 nm and 360 nm), a broad band between 340 nm and 590 nm was observed, whose peak position deviates towards the red as the excitation wavelength increases, see Figure 5.24 B and C. A similar behavior was observed for ***Jeffamine T5000®*** and **1**, see Figure 5.25 A and B, respectively. The dependence of the emission with the excitation wavelength is characteristic of amine- amide functionalized hybrids materials and hybrid precursors [65,68,106-109], suggesting evidence of disordered-related processes generally associated with transitions occurring within localized states in noncrystalline structures [107].

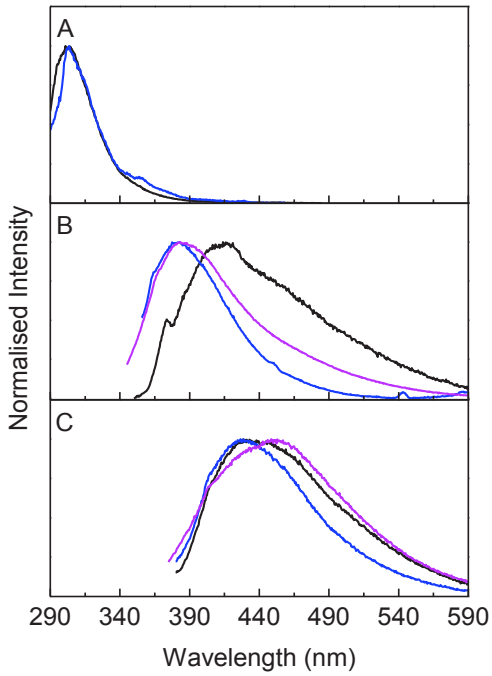

Figure 5.24. Room temperature emission spectra excited at A) 260 nm, B) 330 nm and C) 360 nm, of (black line) **t-U(5000)**$_{0.05}$, (blue line) **1** and (magenta line) ***Jeffamine T5000®***.

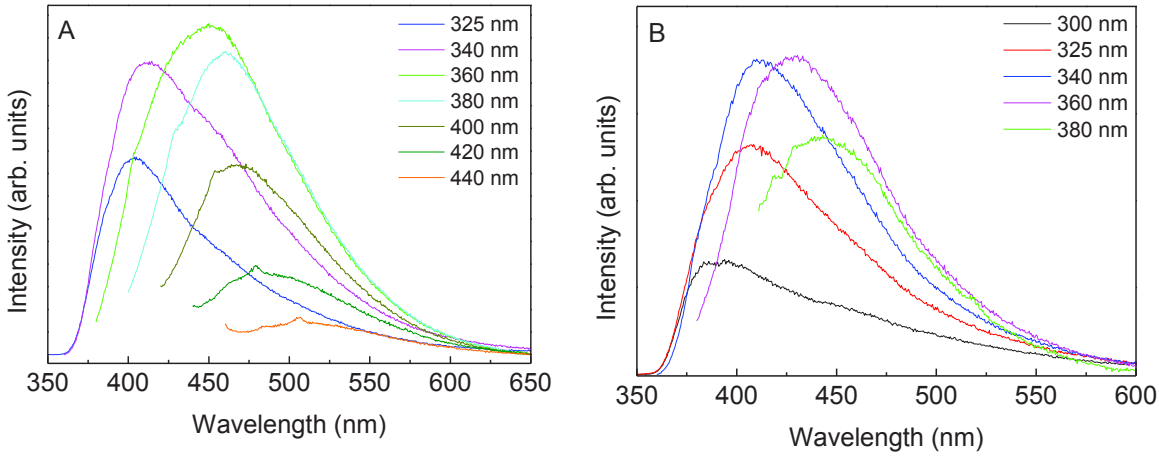

Figure 5.25. Room temperature emission spectra of A) ***Jeffamine T5000®*** and B) **1**.

Figure 5.26 shows the excitation spectra of **t-U(5000)**$_{0.05}$, **1** and ***Jeffamine T5000®***. The excitation spectra were monitored at the maximum emission peak position obtained at lower excitation wavelength (260 nm) for **1** and **t-U(5000)**$_{0.05}$ and in the high wavelength range (360 nm) for **t-U(5000)**$_{0.05}$ and ***Jeffamine T5000®***. The excitation spectrum monitored at 330 nm

of **t-U(5000)$_{0.05}$** shows a broad band peaking at 270 nm, similarly to that found for **1**. The excitation spectrum monitored at 440 nm reveals a broad band (240-420 nm) with three main components at (260 nm, 320 nm and 360 nm). The lower (260 and 320 nm) wavelength components, were also identify for **1.**

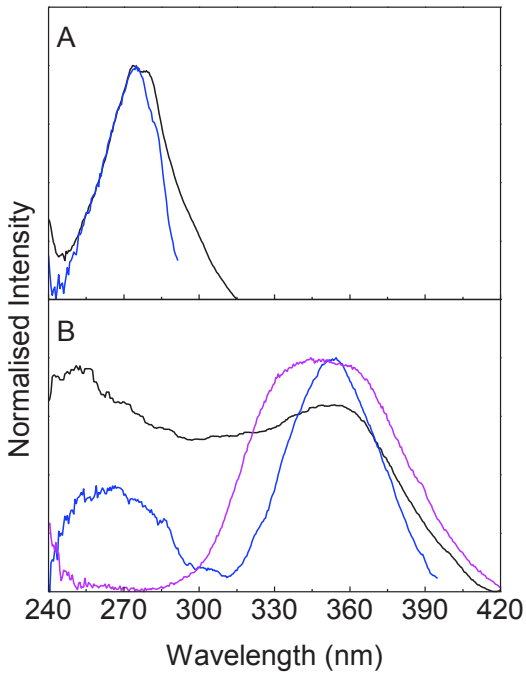

Figure 5.26. Room temperature excitation spectra monitored at A) 330 nm and B) 440 nm of (black line) **t-U(5000)$_{0.05}$**, (blue line) **1** and (magenta line) ***Jeffamine T5000***.

While the origin of the emission of the broad band between 340 nm and 590 nm has been discussed in previous works based on amine- and amide- hybrid materials [65,68,106,107,113,115-117,175,208], which was associated to radiative recombinations involving thermal relaxation within localized states in the framework of the extended multiple trapping approach [209]. The origin of the emission component that appears at low wavelength (290-390 nm) is unknown. In order to further study this emission component, that appears in hybrid and inorganic model compound, time resolved emission spectroscopy was used.

Figure 5.27 shows the time resolved emission spectra (acquired at 12 K with SD of 0.05 ms) of **t-U(5000)$_{0.05}$** and **1**. Two main components can be identified under 260 nm of excitation: a fast component (see inset of the Figure 5.27) constituted by a broad band

between 290 nm and 340 nm with maximum ~ 300 nm, with lifetime values of 1.1±0.1×10^{-5} s for **t-U(5000)$_{0.05}$** and **1** and a slow component based on a broad band between 350 nm and 540 nm with lifetime values of 0.1128±0.0044 s for **t-U(5000)$_{0.05}$** and 0.068±0.0075 s for **1**, see Table 5.10.

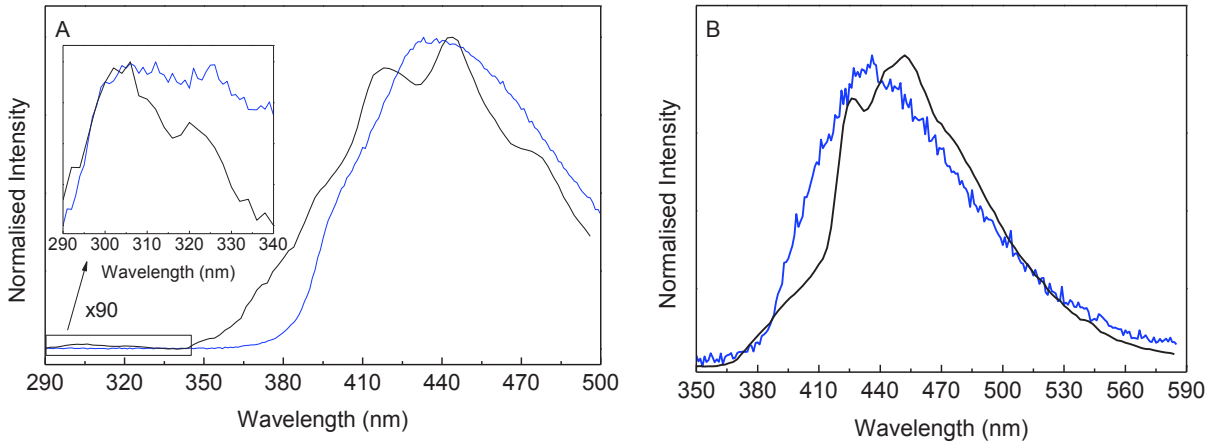

Figure 5.27. Time resolved emission spectra (12 K) A) excited at 260 nm and B) 300 nm of (black line) **t-U(5000)$_{0.05}$** and (blue line) **1** acquired at SD of 0.05 ms.

Table 5.10. Lifetime values (τ, s) obtained at 12 K of **t-U(5000)$_{0.05}$** and **1**.

	Temperature (K)	**12**	
	λ_{exc} (nm)	**260**	**300**
	λ_{em} (nm)	**300**	**435**
t-U(5000)	***τ (s)***	1.1±0.1×10^{-5}	0.1128±0.0044
1		1.1±0.1×10^{-5}	0.068±0.0075

Comparing the lifetime values measured at 12 K of **t-U(5000)$_{0.05}$** and **1** we note that monitoring exited at 260 nm and monitoring at 300 nm the lifetimes of hybrid and inorganic model compound are the same. However, excited at 300 nm and monitoring at higher wavelength (400 nm) the lifetime values of tri-ureasil are much higher than in case of inorganic model compound.

In addition, in order to evaluate the recombination mechanisms responsible for the emission of tripodal organic-inorganic hybrid, additional emission measurements with He-Cd

laser under 325 nm of excitation and as function of the power excitation were carried out. A comparison of the physical nature behind the emission features of the organic and inorganic model compounds with those of the hybrid **t-U(5000)$_{0.05}$**, in particular the presence of radiative emission mediated by D-A pairs was verified.

The existence of D-A pairs can be inferred from the analysis of the behavior of the emission intensity, *I*, as the excitation power, *L*, is varied. The emission intensity depends on the excitation power according to the power-law $I \propto L^{k}$. Whereas $k \leq 1$ is characteristic of D-A pairs, $1 < k < 2$ is typical of exciton-like transitions [107,128,210].

Figure 5.28 A shows the emission integrated intensity depends linearly with the power excitation for **1** and ***Jeffamine T5000®***, revealing a slope *k* of 0.67 and 0.90, respectively.

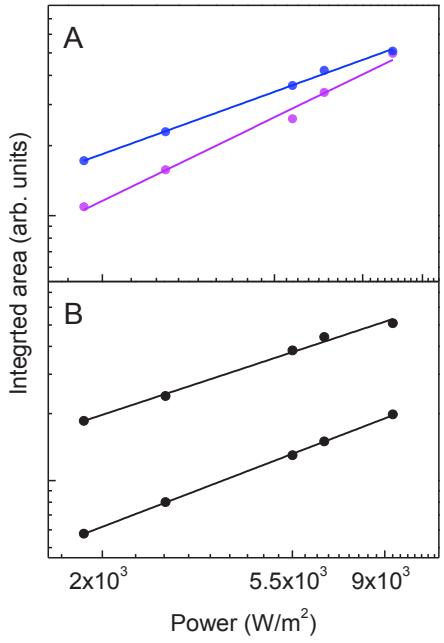

Figure 5.28. Emission integrated intensity of (blue circles) **1** (magenta circles) ***Jeffamine T5000®*** and (black circles) **t-U(5000)$_{0.05}$** at different power excitations. The solid lines correspond to linear fits to the data ($r^2 > 0.99$).

Concerning the **t-U(5000)$_{0.05}$** the emission spectra was fitted in two components keeping constant the peak position and *fwhm*. Figure 5.28 B shows the dependence of the emission integrated intensity of the two components (assigned to **1** and ***Jeffamine T5000®***) with power excitation, revealing a *k* of 0.64 and 0.75, respectively. These values are similar to those found in isolated **1** and ***Jeffamine T5000®*** and those reported for different organic-inorganic hybrids

[128], indicating that the hybrids and those model compounds emission is mediated by D-A pairs.

5.5 Conclusions

In this chapter transparent monoliths of urea cross-linked tripodal siloxane based hybrids, named tri-ureasils, were prepared by the sol–gel process, using a wide concentration range of HCl ($1.0\times10^{-3}\leq$ [HCl] $\leq$ 2.0 M) and water content (2.2 mmol and 22.2 mmol) under usual laboratory and controlled atmosphere conditions.

Their local structure was characterized by X-ray diffraction, ^{29}Si MAS and ^{13}C CP/MAS NMR, infrared, UV-visible absorption and photoluminescence spectroscopies.

X-ray diffraction point out that all the hybrids are amorphous with characteristic distances of ~4.40±0.02 Å and coherence lengths of ~10.5±0.2 Å. The ^{29}Si MAS NMR results indicate that all the exhibit a high condensation degree (varying between 91 % and 98 %).

In addition, the photoluminescence study show that all the hybrids display UV and blue emission at room temperature. For the materials prepared inside the glove box it was observed an enlargement of the UV/blue absorption regions (350–500 nm) comparatively those materials prepared under usually laboratory conditions. The origin of the emission UV/blue emission results from a convolution of the emission originated from electron-hole recombinations occurring in the siliceous nanodomains and within the NH/C=O groups, respectively. These two components reveal a radiative recombination mechanism typical of donor-acceptor pairs, mediated by some localized centers.

The effect of [HCl] and athmosphere conditions was quantified in the enhancement of the emission quantum yield. Varying the HCl concentration and water content it was possible achieve a maximum quantum yield of 0.13±0.01. For the same HCl concentration and water content, the materials prepared inside of glove box present a maximum emission quantum yield of 0.27±0.03.

The enhancement of the optical features demonstrated by the increase of the ϕ values points out that the usage of controlled atmosphere has a great potential to be generalized in the development of organic–inorganic hybrid materials, boosting the optical performance

6. Eu^{3+}-based malonamide and di-malonamide bridged silsesquioxanes

6.1 Introduction

In this chapter the incorporation of Ln^{3+} into the malonamide BS organic-inorganic hybrid host was performed in order to develop materials with monochromatic emission for the development of LSCs. Ln^{3+} are used extensively in luminescent materials due to their characteristics, arising from the particular *4f* electronic energy level configuration such as photostability, long lifetimes (>10^{-4} s), large ligand-induced Stokes shift (>200 nm), narrow bandwidth emissions (*fwhm* ~ 1×10^{7} cm^{-1}) lying from the UV to the near-infrared (NIR) spectral regions, high ϕ values (up to 90 %) and ligand-dependent sensitization [211-213]. All of these features offer excellent prospects for designing new Ln^{3+}-based luminescent materials with a wide range of applications as agriculture and horticulture [214], lighting [43], integrated optics and optical telecommunications, solar cells [212], nanomedicine [215] and LSCs [216-220].

Furthermore, Ln^{3+} ions can be complexed by a wide variety of organic molecules, which harvest light and transfer energy efficiently onto the metal ions. The formation of complexes between Ln^{3+}–ions and certain organic ligands has an extra beneficial effect, protecting metal ions from vibrational coupling and increasing the light absorption cross-section by ligand sensitization [160]. However, these Ln^{3+}–complexes show a rather low thermal and photochemical stability, that together with the poor mechanical properties and photodegradation upon UV exposure are important disadvantages concerning its technological applicability [163,221].

One solution to improve the mechanical and optical properties of Ln^{3+}–based complexes is introduce them in a stable rigid matrix, for example, silica-based hybrid material. In this context, Ln^{3+}–containing organic-inorganic hybrids are good candidates, combining the physical properties and functionalities of the inorganic network and/or the organic fragments with the Ln^{3+}luminescence [54,75,211,212,214,222,223].

Ln^{3+}-containing BS [224,225] obtained by hydrolysis–condensation of organo-bridged polytrialkoxysilanes, are able to incorporate a high loading of Ln^{3+} complexes (up to 11.2 wt%) [60] covalently bonded to the siloxane network being easily processed as thin films with excellent homogeneity and transparency [60,130,226-231]. These films are luminescent active coatings, whose applicability as LSCs was recently highlighted [60,130]. The concept of LSCs reappeared as a promising way to improve solar cells efficiency [232], despite the first reports date from 1976 [233]. LSCs are composed of films bearing optically active centers that collect the incident sunlight and reemit it partially at a specific wavelength. Part of this emitted light is trapped inside the layer and concentrated at the edge of the film, where it can be collected by a PV cell. The main requirements for efficient LSCs are: 1) broad spectral absorption; 2) high absorption efficiency over the whole absorption spectrum; 3) large Stokes shifts; 4) high luminescence efficiency; and 5) emission energy resonant with the PV cell responsivity [220].

During last decades, different organic-inorganic hybrids containing optically active centers have been tested as LSCs such as: organic dyes [233-235], quantum dots (QDs) [236-238] and Ln^{3+} [60,130,213,219,239,240].

Promising results have been obtained for dye-based LSCs with an optical conversion efficiency (η_{opt}) of 18.8 % [90]. The intrinsic small Stokes-shift of the dye molecules, however, induced high self-absorptions, which is a significant drawback. The Ln^{3+}-based materials, are good candidates for application in LSCs due to an appropriate balance between relatively high emission quantum yield values and negligible self-absorption [220].

Despite this potential, few works were published on Ln^{3+}-based LSCs providing quantitative evidence of the improvement of PV cells performance, *e.g.*, Eu^{3+}–based LSCs pointing out an increase of 15 % [216] and 12.5 % [241] on the PV cell photocurrent and an enhancement of the power conversion efficiency of 0.28 % [219], 0.007 % [220], and 0.0441 % [242]. In addition η_{opt} values of Ln^{3+}–based LSCs were calculated for selected excitation wavelengths, namely 8.8 %, for Tb^{3+}–based poly(vinylalcohol) incorporating salicylic acid

[243], 9 %, for $Eu(tta)_3$.ephen (ephen=5,6–epoxy–5,6–dihydro[1,10] phenanthroline) embedded into the hybrid host **t-U(5000)** [213] and 4.3 % and 1.7 %, for Eu^{3+}-[60] and Tb^{3+}-doped [130] BS, respectively.

In this chapter two distinct multifunctional materials based on malonamide BS (**P2-m**, Scheme 3.1) and di-malonamide BS (**P4-m,** Scheme 3.2) precursors, were modified by the incorporation of $EuCl_3 \cdot 6H_2$ and $Eu(tta)_3(H_2O)_2$. The hybrids were prepared as powders, free standing films and also as thin films. Their local structure and optical properties were investigated by SEM, TGA, X-ray diffaction, ^{29}Si MAS NMR, ^{13}C CP/MAS NMR, FT-IR spectroscopy, UV-visible absorption and photoluminescence spectroscopies. These materials exhibit high ϕ values that make them interesting materials to be tested as LSCs. Thus, featuring applications in the field of LSCs, the synthesis conditions used to prepare **M4-m-2**, were selected to be used to prepare thin films (by spin-coating). Once, **M4-m-2** and **M4-m-3** hybrids present similar ϕ values and **M4-m-3** contain free tta–H, the synthesis conditions used to prepare **M4-m-2** were selected to be used to prepare thin films. The role of the **P4-m** precursor concentration, the ageing time of the solution to be deposited, the spinning conditions and the solvent were varied aiming at optimizing the optical properties of the films. The performance of the LSCs was also evaluated throught the quantification of $\eta_{opt.}$

6.2 Synthesis

Eu^{3+}–based di-malonamide BS

In the first stage, a solution of $EuCl_3 \cdot 6H_2O$ (35.5 mg, 0.097 mmol) in a mixture of DMF (0.74 mL) and MeOH (2.2 mL) (ratio of DMF/MeOH = 1/3 v/v, 1.0:5.7 molar ratio) was added to the precursor **P4-m** (300 mg, 0.294 mmol). The mixture was heated at 60 °C until a clear solution was obtained. Then, distilled H_2O (129.4 μL, 7.16 mmol) was added and the solution was stirred for 20 min at 60 °C. Finally, 0.1 M of NH_4F (29.4 μL, 0.00294 mmol) was added. The final molar ratio was P4-m:H_2O:NH_4F:$EuCl_3 \cdot 6H_2O$ = 1:30:0.01:0.33. A white powder was obtained and identified as **M4-m-1**. Aiming at enhancing the light harvesting ability of the Eu^{3+}-doped hybrids, the chromophore tta–H was also incorporated. $EuCl_3 \cdot 6H_2O$ (35.5 mg) and tta–H (43.1 mg for **M4-m-2** or 64.7 mg for **M4-m-3**) were added

to the precursor **P4-m**, with a ratio P4-m:H_2O:NH_4F:$EuCl_3 \cdot 6H_2O$:tta-H = 1:30:0.01:0.33:0.66 for (**M4-m-2**) and P4-m:H_2O:NH_4F:$EuCl_3 \cdot 6H_2O$:tta-H = 1:30:0.01:0.33:0.99 for (**M4-m-3**), following a similar procedure as used to prepare **M4-m-1**. A schematic representation of the synthesis is shown in Scheme 6.1.

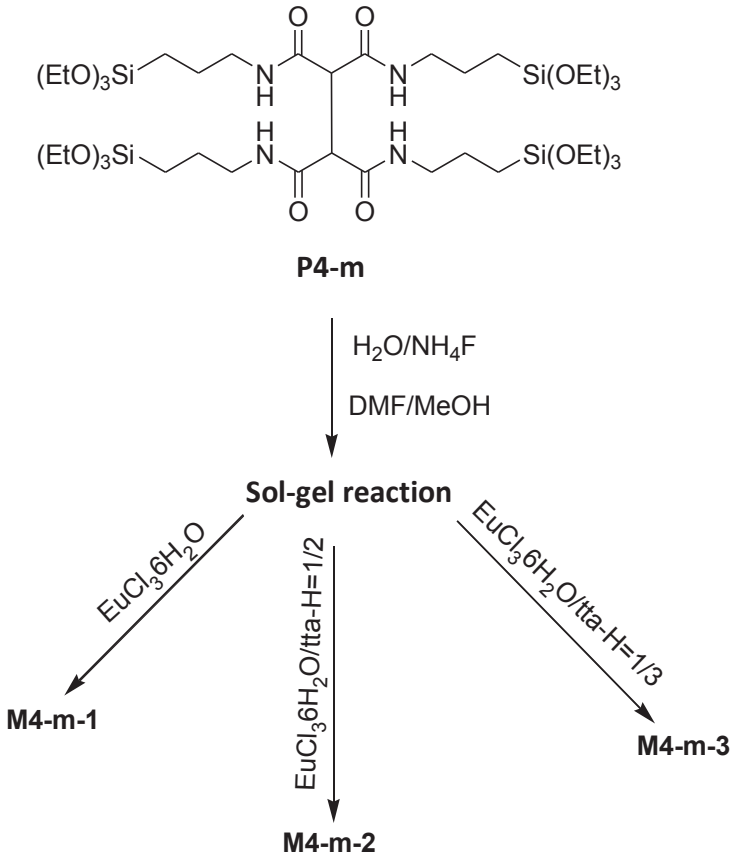

Scheme 6.1. Schematic representation of the synthesis of the hybrids **M4-m-1**, **M4-m-2** and **M4-m-3**.

The suspensions were cast into a polystyrene mold and left to gel covered with Parafilm® and kept at room temperature for 2 days. Gelation occurred within 20 min yielding free-standing films with thickness (*l*) value of 440±10 μm, obtained by SEM. The samples were dried at 50 °C for 1 week. The photographs of **M4-m-1** and **M4-m-2** are depicted in Figure 6.1. Due to photographic similarities between the hybrids **M4-m-2** and **M4-m-3** the last one is not shown.

Elemental analyses for Si and Eu^{3+} were performed for **M4-m-2** and **M4-m-3** hybrids and the obtained values % (w/w), were: **M4-m-2** (Si, 10.6; Eu^{3+}, 4.4) and **M4-m-3** (Si, 10.6; Eu^{3+}, 3.0).

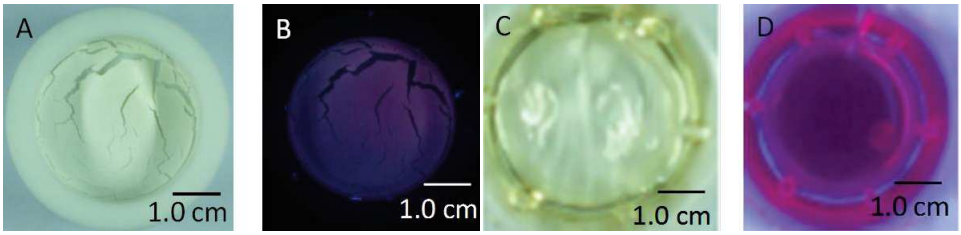

Figure 6.1. Photographs of **M4-m-1** under A) daylight illumination and B) excited at 365 nm and of **M4-m-2** under C) daylight illumination and D) excited at 365 nm.

Eu^{3+}−based malonamide BS

In the first stage, a solution of $EuCl_3 \cdot 6H_2O$ (35.5 mg, 0.097 mmol) and tta−H (43.1 mg for **M2-m-1** or 64.7 mg for **M2-m-2**) in a mixture of DMF (0.74 mL) and MeOH (2.2 mL) (ratio of DMF/MeOH=1/3, v/v, 1.0:5.7 molar ratio) was added to **P2-m** (300 mg, 0.59 mmol). The mixture was heated at 50 °C until a clear solution was obtained. Then, distilled H_2O (129 μL, 7.16 mmol) was added and the solution was stirred for 20 min at 50 °C. Finally, 0.1 M NH_4F (29 μL, 0.0029 mmol) was added. The final molar ratio was P2-m:H_2O:NH_4F:$EuCl_3 \cdot 6H_2O$:tta-H=1:15:0.005:0.165:0.33 for **M2-m-1** and P2-m:H_2O:NH_4F:$EuCl_3 \cdot 6H_2O$:tta-H=1:15:0.005:0.165:0.50 for **M2-m-2**. A schematic representation of the synthesis is shown in Scheme 6.2. The suspensions were cast into a polystyrene mould and left to gel covered with Parafilm® and kept at room temperature for two days. The samples were dried at 50 °C for about one week. The photographs of **M2-m-1** are depicted in Figure 6.2. Due to photographic similarities between the hybrid **M2-m-1** and **M2-m-2** the last one is not shown.

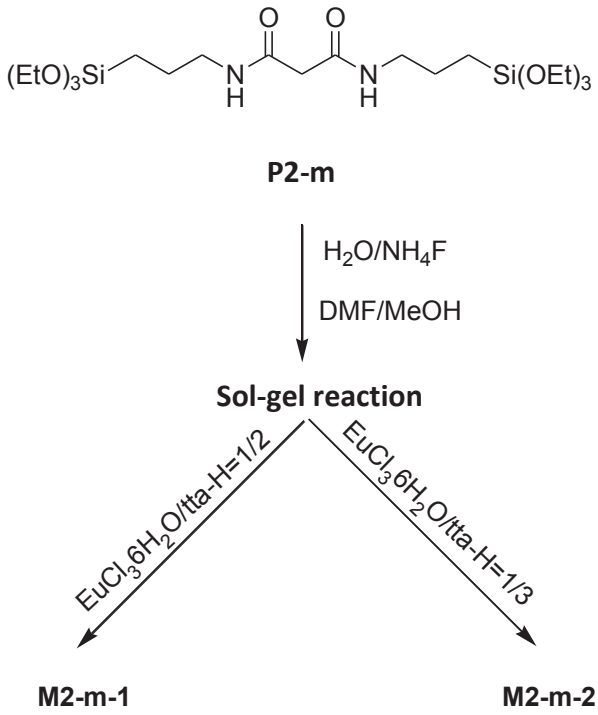

Scheme 6.2. Schematic representation of the synthesis of the hybrids **M2-m-1** and **M2-m-2**.

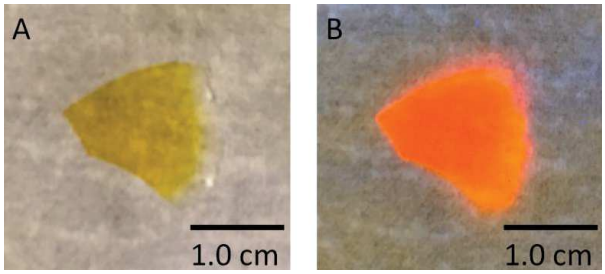

Figure 6.2. Photographs of **M2-m-1** under A) daylight illumination and B) excited at 365 nm.

Thin films based on Eu^{3+}−based di-malonamide BS

Borosilicate substrates (Normax microslides 25 × 25 mm^2) were cleaned with acetone, immersed in a mixture of hydrogen peroxide and sulfuric acid (piranha solution), and then rinsed and stored in distilled H_2O. Prior to coating, they were dried by spin-coating (5000 rpm, 50 s), treated with MeOH, and dried again by spin-coating immediately prior to use. The thin films, sequentially designed from **F1** to **F25**, were prepared based on different conditions,

such as amount of the precursor, spinning speed, aging time prior to coating, and solvent type, Table 6.1.

Table 6.1. Amount of precursor (wt%), spinning speed rotation (rpm), ageing time prior to coating (min) and solvent type for the thin films Eu^{3+}–based di-malonamide BS.

Films	Amount of precursor (mg)	Spinning speed (rpm)	Ageing time (min)	Solvent
F1	3	1000	1	DMF+MeOH
F2			4	
F3			8	
F4			14	
F5	9	2000	1	
F6		5000	11	
F7	12	1000	1	
F8	3	2000	1	MeOH
F9				EtOH
F10				1-PrOH
F11				DMF+MeOH
F12		1000		EtOH
F13	6	2000	1	DMF+MeOH
F14	9	1000	1	EtOH
F15			5	
F16			1	DMF+MeOH
F17			4	
F18			10	
F19		2000	4	
F20			8	
F21		5000	1	
F22			4	
F23	12	1000	4	
F24			8	
F25			12	

$EuCl_3 \cdot 6H_2O$ (3.55 mg), tta−H (4.3 mg), and H_2O (5 μL) were incorporated into a suspension of **P4-m** (30 mg or 90 mg or 120 mg) dissolved in 1.30 mL, 1.26 mL, 1.25 mL, and 1.25 mL of EtOH, MeOH, 1-PrOH, and DMF:MeOH = 1:5.5 molar ratio, respectively. The mixture was stirred for 20 min at room temperature, leading to a clear solution, then 0.1 M NH_4F (0.5 μL) was added. The final weight concentrations of **P4-m** were 3.0 wt %, 9.0 wt %, and 12.0 wt %. The substrates were held by suction on a chuck, which was placed on the

axis of the spin coater (SCS Specialty Coating Systems, spin-coat G3−8). The thin films were prepared by spin-coating using two drops of the sol (with variable aging time prior to coating: 1 min, 4 min, 8 min, 11 min, and 14 min) on the glass substrates, with an acceleration time of 10 s and a spin time of 50 s, and at a spin rate of 1000 rpm, 2000 rpm, or 5000 rpm. They were finally dried at 70 °C overnight. The representative photograph of thin film designated by **F6** is depicted in Figure 6.3.

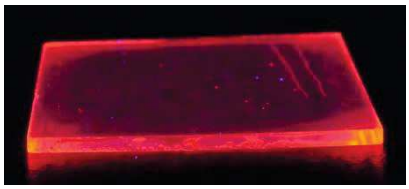

Figure 6.3. Photograph of **F6** excited at 365 nm.

6.3 Local structure

Eu^{3+}−based di-malonamide BS

Figure 6.4 shows the comparison between the SEM image of **M4-m** (undoped hybrid study in Chapter 3) and **M4-m-1** (doped with $EuCl_3 \cdot 6H_2O$).

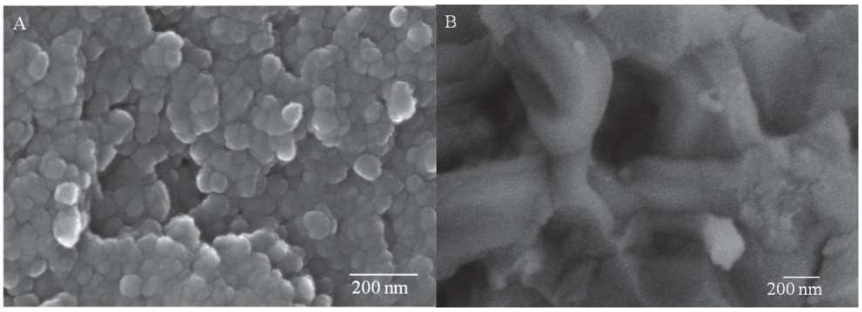

Figure 6.4. SEM images of A) **M4-m** and B) **M4-m-1**.

The addition of $EuCl_3 \cdot 6H_2O$ into the hybrid host induce modifications in the morphology of the materials. The nanospheres present in **M4-m**, Figure 6.4 A, are destroyed when $EuCl_3 \cdot 6H_2O$ is incorporated into the hybrid host, originating plates randomly

distributed, Figure 6.4 B. The incorporation of $Eu(tta)_3(H_2O)_2$ (**M4-m-2** and **M4-m-3**) induces dense structures, difficult to be detailed through by SEM.

Figure 6.5 show the comparison of the thermal behaviour of the undoped (**M4-m**) and doped (**M4-m-1**, **M4-m-2** and **M4-m-3**) materials.

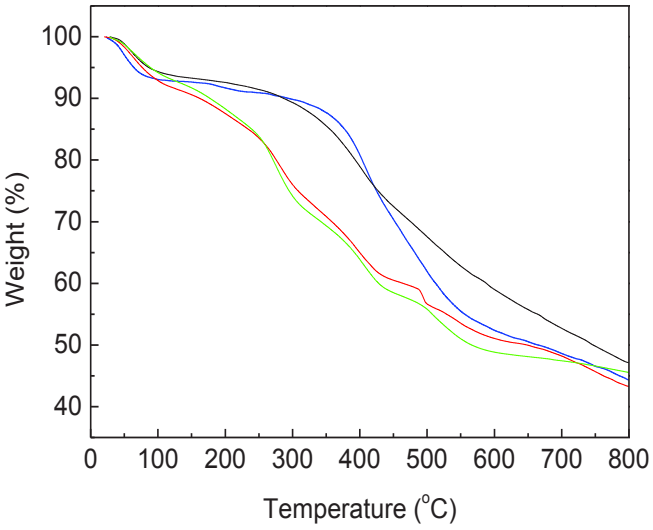

Figure 6.5. TGA curves of **M4-m** (blue line) **M4-m-1** (black line), **M4-m-2** (red line) and **M4-m-3** (geen line).

Four main decomposition steps can be observed in the TGA curves for the di-malonamide BS hybrid materials. In the first decomposition step, for temperatures below to 100 °C, all the hybrids show a weight loss of ~7 % ascribed to desorption of physically absorbed water and residual solvents on the surface [170,171]. As discussed in Chapter 3, for **M4-m**, the weight loss of ~5 % observed between ~100 °C and ~350 °C was related to the removal of entrapped water and solvents. The incorporation of additional water into the hybrid host, present in $EuCl_3 \cdot 6H_2O$ (**M4-m-1**) and $Eu(tta)_3(H_2O)_2$ (**M4-m-2** and **M4-m-3**) induced an increase of the weight loss of ~5 % for **M4-m-1** and ~10 % for **M4-m-2** and **M4-m-3** between ~100 °C and ~250 °C. Between 350 °C and 550 °C the TGA curves of **M4-m-1**, **M4-m-2** and **M4-m-3** show a weight loss of ~30 %, related with the decomposition of the organic part. The weight loss above 550 °C of ~8 % and 3 % for **M4-m-2** and **M4-m-3** respectively, was ascribed to the release of water formed from the further self-condensation of silanol groups [170,171].

The ^{29}Si MAS NMR spectra of **M4-m-2** and **M4-m-3** are depicted in Figure 6.6 A and B, respectively.

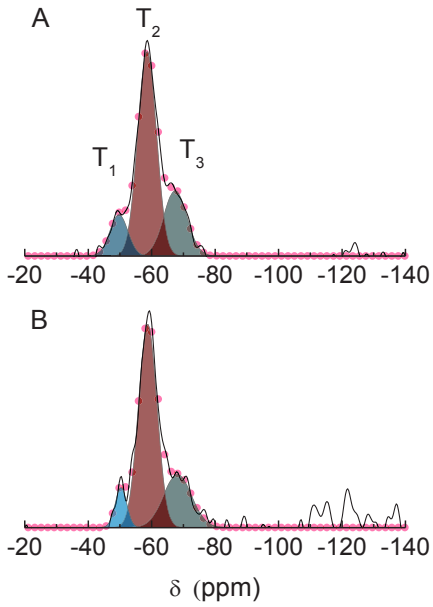

Figure 6.6. ^{29}Si MAS NMR spectra of A) **M4-m-2** and B) **M4-m-3**. The fit using a sum of Gaussian functions (shadowed areas) ascribed to T_1, T_2 and T_3 silicon environments, and the overall fit (r^2 >0.99) (red circles) are also shown.

The ^{29}Si MAS NMR spectra exhibits three peaks at ~−49.7 ppm, ~−58.6 ppm and ~−67.5 ppm, characteristic of T_1, T_2 and T_3 silicon environments, respectively. A *c* value of 54 % and 52 % (calculated using the equation 3.1, detailed in Chapter 3) were obtained for **M4-m-2** and **M4-m-3**, respectively.

The ^{13}C CP/MAS NMR spectra of **M4-m-2** and **M4-m-3** are shown in Figure 6.7 B and C, respectively. The covalent bonding of the organic fragment with the siloxane network is proved by the presence of the resonances peaks corresponding to C^1, C^2 and C^3, respectively. The resonances corresponding to C^5 and C^4 are related to HC-$(C=O)_2$ and C=O, respectively. Overall, these ^{13}C NMR spectra are very similar to those of **P4-m** with the exception of the two signals peaking at 18.0 ppm and 58.0 ppm assignable to $(EtO)_3$-Si groups that disappear after the sol-gel reaction in the case of **M4-m-2** and **M4-m-3**. No signal corresponding to the tta−H ligand (expected in the 130-140 ppm range and around 180 ppm) is detected. This might be due to the chelation of tta−H to the paramagnetic Eu^{3+} ions.

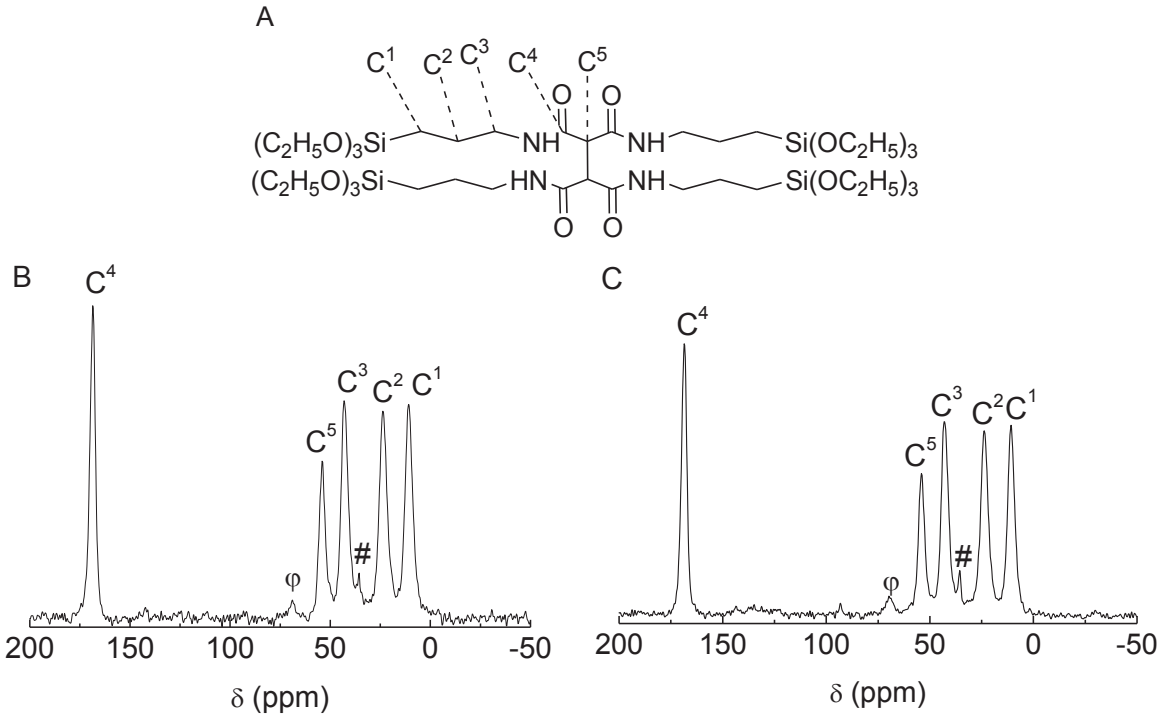

Figure 6.7. A) Schematic representation of the structure of **P4-m**. The C^1, C^2, C^3, C^5 and C^4 resonances appear at 10.8 ppm, 23.7 ppm, 42.9 ppm, 54.0 ppm and 168.6 ppm, respectively. ^{13}C CP/MAS NMR spectra of B) **M4-m-2** and C) **M4-m-3**. The symbols (φ and #) correspond to spinning side band and DMF solvent, respectively.

A comparison of the X-ray diffraction pattern of the undoped hybrid (**M4-m**) and doped hybrids (**M4-m-1**, **M4-m-2** and **M4-m-3**) are depicted in Figure 6.8. The diffractograms of all the hybrids evidence amorphous structures. The sharp peak observed at 3.72 nm^{-1} for **M4-m,** related with the distance between siliceous domains (detailed in Chapter 3), disappears after incorporation of $EuCl_3 \cdot 6H_2O$ (**M4-m-1**) and $Eu(tta)_3(H_2O)_2$ (**M4-m-2** and **M4-m-3**), giving us indication of the loss of the structural unit after $EuCl_3 \cdot 6H_2O$ and $Eu(tta)_3(H_2O)_2$ incorporation. The component at ~8.5 nm^{-1} observed for **M4-m** appears at lower *q* values for **M4-m-1** (~8.0 nm^{-1}) and **M4-m-2** and **M4-m-3** (~7.0 nm^{-1}). The shift could be related with an increase of the NH-NH distance (d=0.79± 0.01 nm for **M4-m-1** and d=0.87± 0.01 nm for **M4-m-2**/**M4-m-3**), due to the link between the urea group and $EuCl_3 \cdot 6H_2O$/$Eu(tta)_3(H_2O)_2$. The component at ~15 nm^{-1} associated with the presence of amorphous siliceous domains it is not affected with the incorporation of $EuCl_3 \cdot 6H_2O$/$Eu(tta)_3(H_2O)_2$.

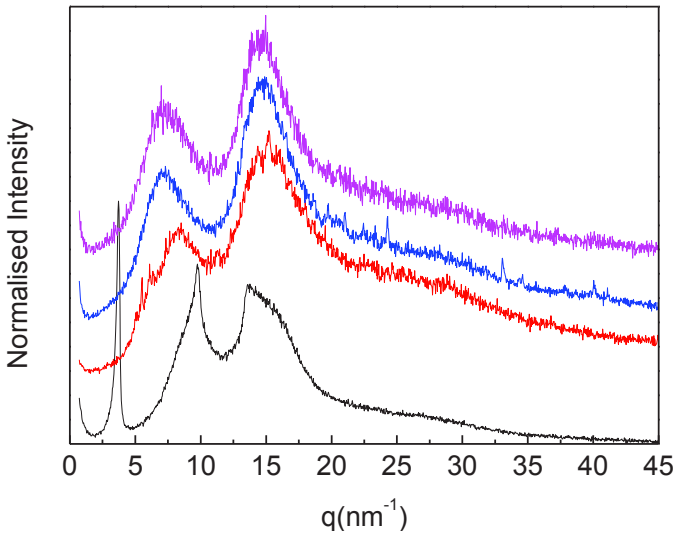

Figure 6.8. X-ray diffraction patterns of **M4-m** (black line), **M4-m-1** (red line), **M4-m-2** (blue line) and **M4-m-3** (magenta line).

With the objective to study the local coordination of the Eu^{3+} into the hybrid **M4-m-2** and **M4-m-3** MIR and FIR [187,244] spectroscopy is used. Figure 6.9 show the FT-IR comparison in the "Amide I" and "Amide II" regions of **M4-m** (undoped material) and **M4-m-1**. The "Amide I" band profile, is significantly modified after $EuCl_3 \cdot 6H_2O$ incorporation. As expected [213], a new contribution appears for **M4-m-1** at lower frequency around 1650 cm^{-1} featuring the ligand interaction between Eu^{3+} ions and carbonyl groups. As the "Amide I" band is splitted between unengaged (1673 cm^{-1}) and engaged C=O (1650 cm^{-1}) in the ligand interaction, complexation seems to involve mainly one part of the carbonyl pairs. "Amide II" vibration, appear to be insensitive to the $EuCl_3 \cdot 6H_2O$ incorporation.

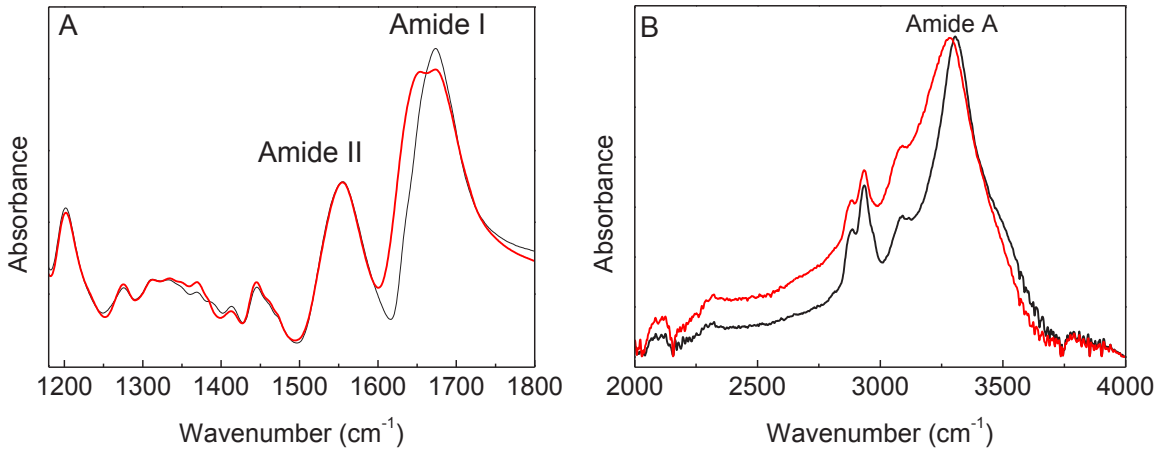

Figure 6.9. FT-IR spectra in the region of A) "Amide I" and "Amide II" regions, B) "Amide A" region of **M4-m** (black line) and **M4-m-1** (red line).

Figure 6.10 shows the deconvolution of the "Amide I" and "Amide II" bands that evidences a broader dispersion of "Amide I" vibrations in **M4-m-1**, as compared to **M4-m-2**.

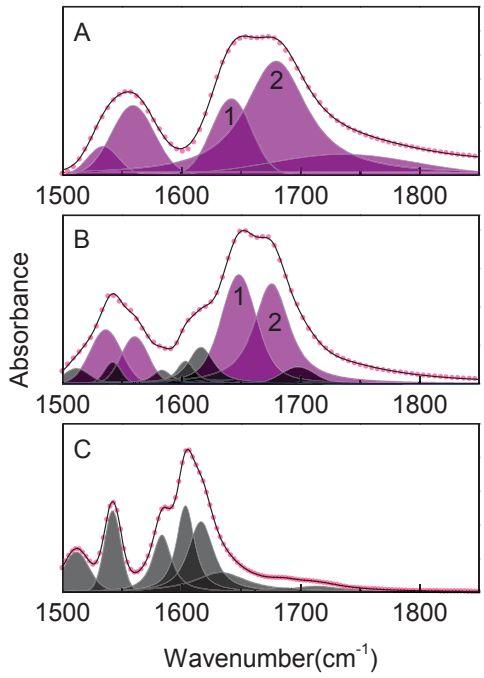

Figure 6.10. FT-IR spectra in the region of "Amide I" and "Amide II" vibrations of A) **M4-m-1**, B) **M4-m-2** and C) $Eu(tta)_3$ $(H_2O)_2$. The fit using a sum of Gaussian functions (shadowed areas) and the overall fit (r^2 >0.99) (red circles) are also shown.

The relative intensity and positions between the most engaged ν(CO) (component 1) and the less engaged ν(CO) (component 2) are deeply modified after tta–H incorporation. The main "Amide I" (component 2) appears more intense, broader and blue-shifted for **M4-m-1**, indicating that supramolecular interactions around carbonyl due to the complexation with Eu^{3+} are increased for **M4-m-2**. Therefore, this trend indicates a deep modification of the ligand environment due to the presence of tta–H around Eu^{3+}. **M4-m-2** and **M4-m-3** cannot be considered as a simple physical mixture between **M4-m-1** and $Eu(tta)_3(H_2O)_2$.

Figure 6.11 shows the superimposition of the vibrational results obtained for **M4-m-1**, **M4-m-2**, **M4-m-3**, $Eu(tta)_3(H_2O)_2$ and tta–H. The spectra of the hybrids **M4-m-2** and **M4-m-3** appear to be dominated by the combination of the spectra of $Eu(tta)_3(H_2O)_2$ and **M4-m**. The FT-IR results show that some tta–H ligand molecules remain uncomplexed as tta–H vibrational feature at 1110 cm^{-1} is observed in **M4-m-2** and **M4-m-3** (see arrow on Figure 6.11).

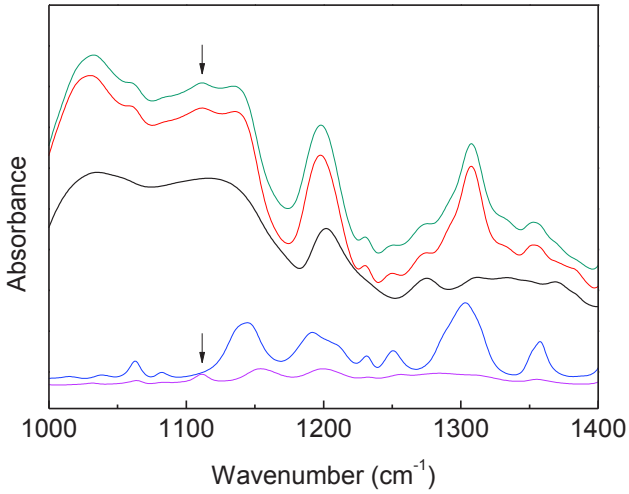

Figure 6.11. FT-IR spectra of **M4-m-1** (black line), **M4-m-2** (red line), **M4-m-3** (green line), $Eu(tta)_3(H_2O)_2$ (blue line) and tta-H (magenta line). The spectra of **M4-m-1**, $Eu(tta)_3(H_2O)_2$ and tta-H have been multiplied respectively by 0.73, 0.13 and 0.1.

Specific Eu^{3+}-ligand vibrational features can be probed in the FIR domain below 300 cm^{-1} [245,246]. Figure 6.12 shows the FIR absorption spectra comparing **M4-m**, **M4-m-1**, **M4-m-2**, $Eu(tta)_3(H_2O)_2$ and tta–H.

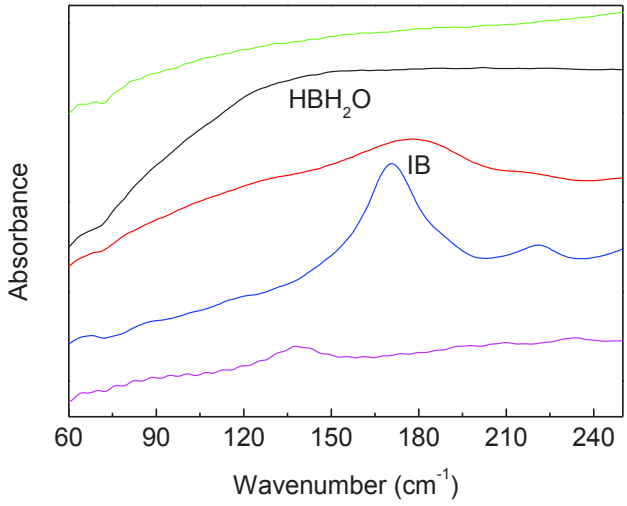

Figure 6.12. FIR spectra of **M4-m** (green line), **M4-m-1** (black line), **M4-m-2** (red line), $Eu(tta)_3(H_2O)_2$ (blue line) and tta–H (magenta line).

The FAR-infrared spectrum of **M4-m** is dominated by a broad band assigned to intermolecular H–bonding between H_2O molecules (HBH_2O). **M4-m-1** (compared to **M4-m**) gives rise to a very broad vibrational contribution centred around 140 cm^{-1} typical from HBH_2O confined in nanomaterials. This behaviour is in agreement with significant H–bonded H_2O fingerprint exhibited in the MIR (Figure 6.9 B). For **M4-m-1**, a broad band is overlapped to ν(NH) feature; this contribution is deported to lower wavenumbers relative to the maximum intensity of "Amide A" band. This trend is classically interpreted as the presence of H–bonded water molecules.

The FIR spectrum of **M4-m-2** is dominated by a significant features around 177 cm^{-1} (labelled IB), superimposed with a broad continuum of HBH_2O contribution, in accord with the vibrational contribution exhibited on **M4-m-1** spectrum. The infrared spectrum of $Eu(tta)_3(H_2O)_2$ gives insight concerning the origin of this IB band. Indeed, an intense sharp feature around 170 cm^{-1} is seen for $Eu(tta)_3(H_2O)_2$ relative to tta–H ligand. We assume therefore that IB signs the interaction of Eu^{3+} with complexed tta–H and H_2O molecules. Furthermore, the decrease in intensity of the HBH_2O contribution for **M4-m-2** suggests that the number of Eu^{3+}-coordinated water molecules decreases, compared to **M4-m-1**.

In agreement with this assumption, Figure 6.13 shows the temperature dependence of this band is anharmonic (around +5 cm^{-1}), as expected for an external mode [247], whereas

internal features are *quasi* harmonic. Besides, for **M4-m-2**, IB band is up-shifted (+7 cm^{-1}), compared to $Eu(tta)_3(H_2O)_2$. A strengthening of the complexation efficiency is therefore suggested for **M4-m-2**, compared to **M4-m-1**, in agreement with the results in the MIR. Thus, our results suggest a cooperative effect of malonamide and tta–H to complex Eu^{3+} ions.

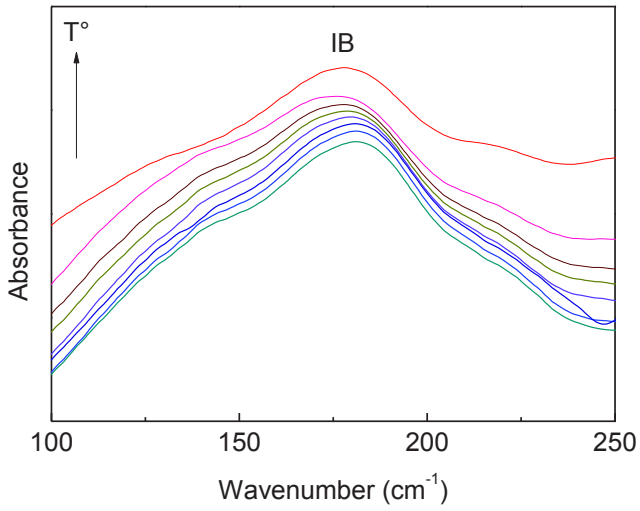

Figure 6.13. FIR spectra of **M4-m-2** between 10 K and 300 K, showing the thermal dependence of IB feature.

Eu^{3+}−based malonamide BS

The SEM images of **M2-m-1** and **M2-m-2** hybrids, depicted in Figure 6.14, show the presence of amorphous and anisotropic particles with micrometer size randomly distributed, similar to observed for undoped material (**M2-m**, study in Chapter 3).

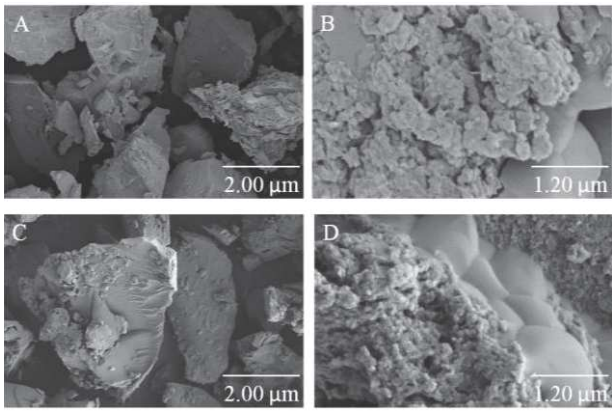

Figure 6.14. SEM images of A, B) **M2-m-1** and C, D) **M2-m-2**.

Figure 6.15 shows the comparision between the TGA curves of the undoped (**M2-m**) and doped (**M2-m-1** and **M2-m-2**) materials. For temperatures below to 100 °C, all the hybrids show a weight loss of ~7 % ascribed to desorption of physically absorbed water and residual solvents, similar to observed for **M4-m**, **M4-m-1**, **M4-m-2** and **M4-m-3**. The weight loss of ~15 % observed between 100 °C and 350 °C for **M2-m-1** and **M2-m-2** was related with entrapped water and solvents, induced by the additional incorporation of water present in $Eu(tta)_3(H_2O)_2$. Between 350 °C and 550 °C the TGA curves of **M2-m-1** and **M2-m-2** shows a weight loss of ~30 % s related with the decomposition of the organic part of the hybrids, a similar weight loss was observed for **M4-m-2** and **M4-m-3**. Above 550 °C a weight loss of ~5% and 4 % observed in **M2-m-1** and **M2-m-2**, respectively, was ascribed to the release of water formed from the further self-condensation of silanol [170,171].

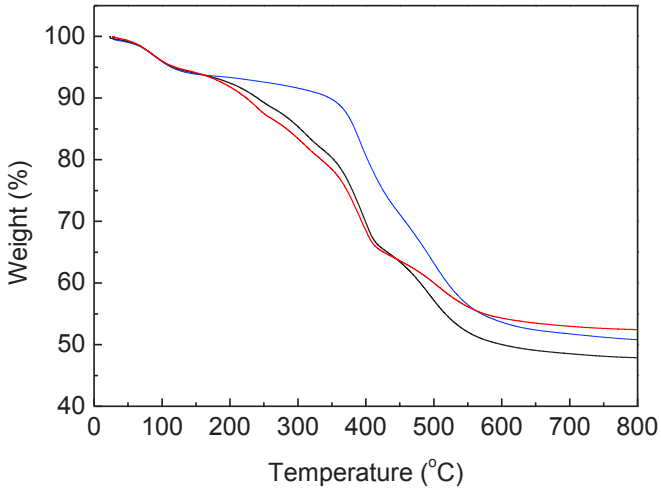

Figure 6.15. TGA curves of **M2-m** (blue line), **M2-m-1** (black line) and **M2-m-2** (red line).

The ^{29}Si MAS NMR spectra of **M2-m-1** and **M2-m-2** hybrids are depicted in Figure 6.16.

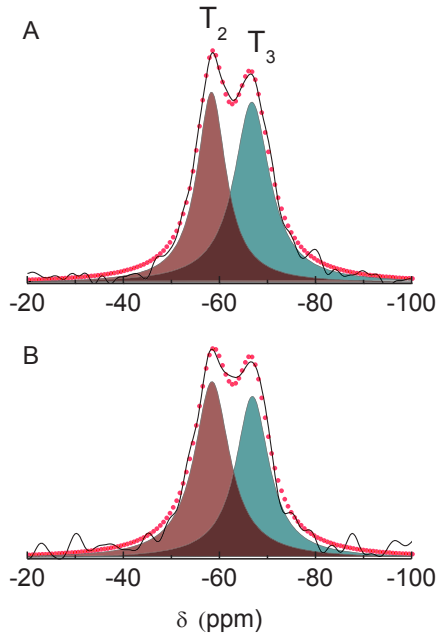

Figure 6.16. ^{29}Si MAS NMR of A) **M2-m-1** and B) **M2-m-2**. The fit using a sum of Gaussian functions (shadowed areas) ascribed to T_2 and T_3 silicon environments, and the overall fit (r^2 >0.99) (closed circles) are also shown.

The ^{29}Si MAS NMR spectra present two peaks at −58.4 ppm and −66.8 ppm for **M2-m-1** and −58.5 ppm and −66.9 ppm for **M2-m-2** characteristic of T_2 and T_3 silicon environments,

respectively. The *c* values calculated (using the Equation 3.1, detailed in Chapter 3) of 85 % and 79 % was obtained for **M2-m-1** and **M2-m-2**, respectively. The *c* values observed in **M2-m-1** and **M2-m-2** are higher than the values calculated for **M4-m-2** and **M4-m-3**, which mean that the polycondensation is higher in case of Eu^{3+}-based di-malonamide materials.

The ^{13}C CP/MAS NMR spectra of **M2-m-1** and **M2-m-2**, are shown in Figure 6.17 B

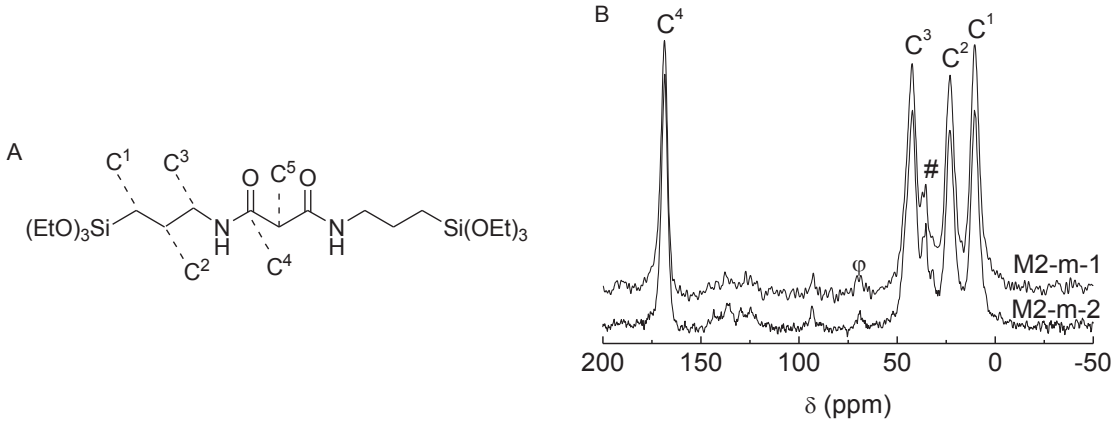

Figure 6.17. A) Schematic representation of **P2-m** precursor and B) ^{13}C CP/MAS NMR spectra of **M2-m-1** and **M2-m-2**. The dashed lines assign the C^1, C^2, C^3 and C^4 resonances at 10.6, 23.1, 42.4 and 168.6 ppm, respectively. The symbols (#,φ) correspond to spinning sidebands and DMF solvent, respectively.

The covalent bonding of the organic fragment with the siloxane network is proved by the presence of the resonances peaks corresponding to C^1, C^2 and C^3, respectively. The resonance corresponding to C^4 was ascribed to C=O. The signal at ~124 ppm and 137 ppm could be ascribed to the resonance of carbons in tta–H ligand. The C^5 resonance that usually appears between 40-45 ppm is probably hidden by C^3 resonance.

Figure 6.18 shows the comparison between the deconvolution infrared spectra in the "Amide I" and "Amide II" regions for **M2-m**, **M2-m-1** and $Eu(tta)_3(H_2O)_2$.

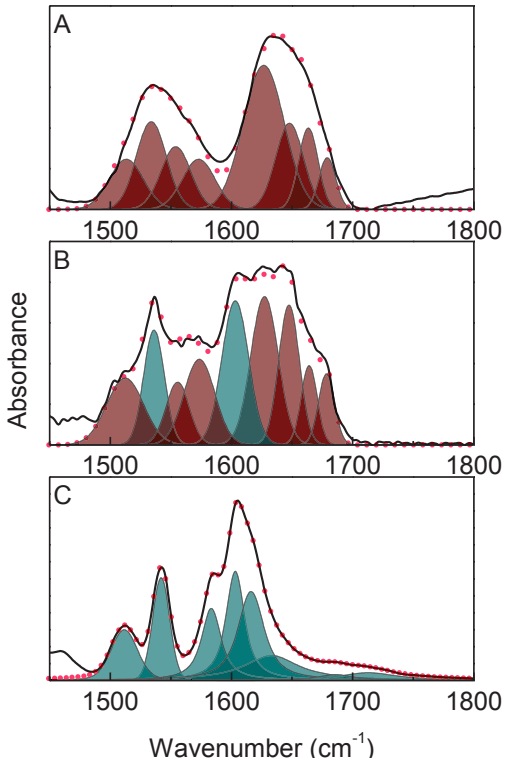

Figure 6.18. FT-IR spectra in the region of the "Amide I" and "Amide II" regions of A) **M2-m-3**, B) **M2-m-1** and C) $Eu(tta)_3(H_2O)_2$. The fit using a sum of Gaussian functions (shadowed areas) and the overall fit (r^2 >0.99) (open circles) are also shown.

The vibrational distribution and relative intensity that appears after $Eu(tta)_3(H_2O)_2$ incorporation in "Amide I" are indicative of an interaction between C=O group and complex. Also **M2-m-1** cannot be considered as a simple physical mixture between the hybrid host (**M2-m**) and $Eu(tta)_3(H_2O)_2$. The same conclusion can be obtained for **M2-m-2**.

In addition, the vibrational dispersion and the relatively intensity in the "Amide I" and "Amide II" regions for **M2-m-1**, as compared to **M4-m-2**, evidence better coordination between $Eu(tta)_3(H_2O)_2$ and the hybrid host. This conclusion are in good agreement with the higher *c* values obtained for Eu^{3+}−based malonamide BS.

6.4 Photoluminescence

Eu^{3+}−based di-malonamide BS

Figure 6.19 A compares the room-temperature emission spectra of **M4-m-1**, **M4-m-2** and **M4-m-3** excited at the wavelength that maximized the emission intensity of each sample.

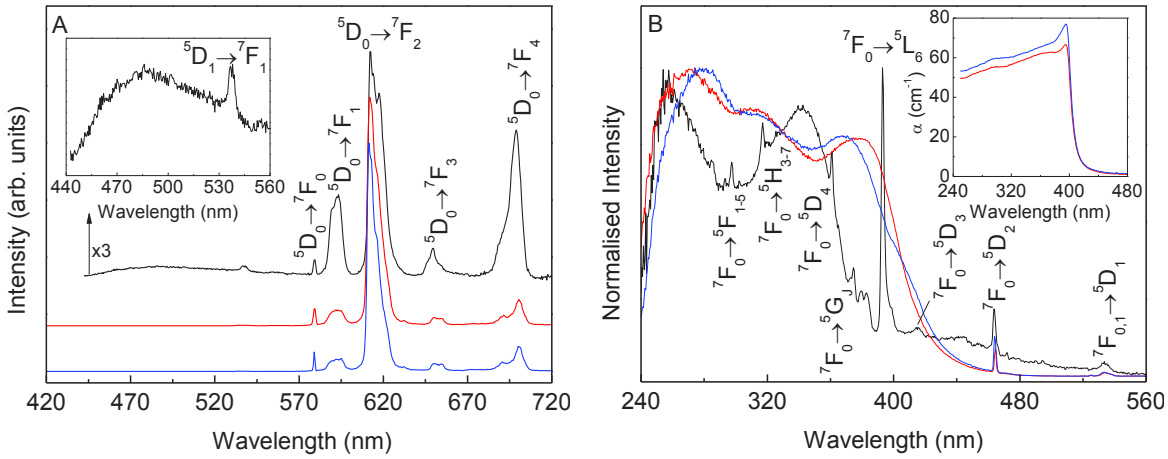

Figure 6.19. A) Emission spectra of **M4-m-1** (black line) excited at 393 nm and of **M4-m-2** (red line) and **M4-m-3** (blue line) excited at 380 nm and B) excitation spectra monitored at 612 nm. The insets in A) show a magnification of the emission spectrum (×3) of **M4-m-1** and in B) the UV-Visible absorption coefficients of **M4-m-2** and **M4-m-3**.

The emission spectra of **M4-m-2** and **M4-m-3** are formed by a series of straight lines ascribed to the Eu^{3+} $^5D_0 \rightarrow ^7F_{0\text{-}4}$ transitions. Independently of the selected excitation wavelengths (270-464 nm), no sign of the **M4-m** (hybrid host) intrinsic emission was observed, which readily suggest efficient hybrid-to-ligand and/or hybrid-to-Eu^{3+} energy transfer [127]. The emission spectrum of **M4-m-1** displays the intra-$4f^6$ lines overlapped with a broad emission (350-550 nm) assigned to the hybrid host (inset in Figure 6.19 A). Changes in the Eu^{3+} coordination sphere resulting from the addition of the tta−H can be inferred from the analysis of the relative intensity of the intra-$4f^6$ transitions for **M4-m-1**, **M4-m-2** and **M4-m-3**. It is clear that the relative intensity of the $^5D_0 \rightarrow ^7F_{1,4}$ transitions significantly decreases after the tta−H incorporation. In fact, the integrated intensity ratios I_{02}/I_{04} and I_{02}/I_{01} (I_{0J}, J=1, 2 and 4, represents the integrated intensity of the $^5D_0 \rightarrow ^7F_{1,2,4}$ transitions) strongly depend

on the presence of tta–H, in particular I_{02}/I_{04} and I_{02}/I_{01} increases from 1.6 and 3.4 (**M4-m-1**) to 6.6/6.5 and 11.7/13.5 (**M4-m-2**/**M4-m-3**). Moreover, the similarity between the intensity ratios for **M4-m-2** and **M4-m-3** suggests an analogous Eu^{3+} local coordination. Therefore, the larger concentration of tta–H in **M4-m-3**, compared to that in **M4-m-2**, leads to the presence of free (non-coordinated) tta–H, as detected in the FT-IR and Raman studies.

The excitation spectra of **M4-m-2** and **M4-m-3** were monitored in the $^5D_0 \rightarrow {}^7F_2$ transition, Figure 6.19 B, showing three main components peaking at 270 nm/280 nm, 320 nm and 380 nm and two low-relative intensity intra-$4f^6$ transitions. The relatively low intensity of the intra-$4f^6$ lines indicates that the Eu^{3+} excited states in **M4-m-2** and **M4-m-3** are mainly populated via ligand-sensitization. The high-wavelength components at 320 nm and 380 nm resemble those already observed for isolated $Eu(tta)_3(H_2O)_2$ [248] and for organic-inorganic hybrids incorporating $Eu(tta)_3(H_2O)_2$ and $Eu(tta)_3$phen (phen=1,10-phenantroline), being ascribed to the π-π* electronic transition of the organic ligands [249]. We should note that the hybrid intrinsic excited states also contribute for the excitation spectra. This conclusion is derived from the analysis of the excitation spectra of **M4-m** monitored along the hybrid host emission (Figure 3.10, Chapter 3) that reveal a broad band with two components at 280 and 320 nm. Moreover, these two components are also present in the excitation spectrum of **M4-m-1** monitored at 612 nm. For this hybrid the relative intensity of the intra-$4f^6$ lines is higher than that of the hybrid-related components indicating that the Eu^{3+} sensitization occurs essentially through direct intra-$4f^6$ excitation. Apart from changes in the relative intensity, the UV–visible absorption spectra (inset in Figure 6.19 B) reveal the same components already detected in the excitation spectra. Moreover, an increase in the α at 395 nm from 67 cm^{-1} to 77 cm^{-1} is observed as the tta–H amount increases from **M4-m-2** to **M4-m-3**.

Figure 6.20 shows the $^5D_0$ emission decay curves monitored under direct intra-$4f^6$ excitation (393 nm, $^5L_6$, and 465 nm, $^5D_2$) revealing a single exponential behaviour. From the data best fit, $^5D_0$ lifetime values of 0.266±0.002 ms (**M4-m-1**), 0.395±0.002 ms (**M4-m-2**) and 0.392±0.002 ms (**M4-m-3**) were found. The higher values found in the presence of tta–H are in good agreement with the ligand coordination to the Eu^{3+} ions in **M4-m-2** and **M4-m-3**. Moreover, the identical values measured for **M4-m-2** and **M4-m-3** reinforces that the Eu^{3+} local coordination is similar in both hybrids, being, therefore independent of the tta–H concentration (as suggested above).

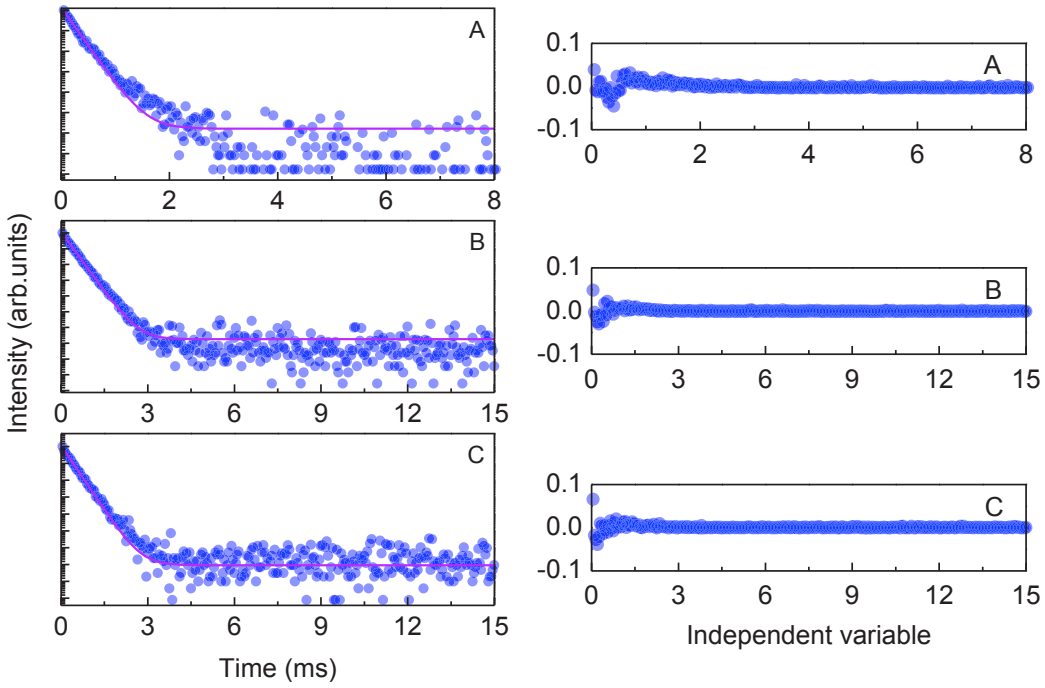

Figure 6.20. Emission decay curves of A) **M4-m-1**, B) **M4-m-2** and C) **M4-m-3** monitored at 612 nm and excited at 393 nm for **M4-m-1** and 464 nm for **M4-m-2** and **M4-m-3**. The solid lines represent the data best fit (r^2 >0.93), using a single exponential function. The respective residual plots are shown on the right side.

The $^5D_0$ lifetime values of **M4-m-2** (0.47±0.01 ms) and **M4-m-3** (0.52±0.01 ms) excited at 380 nm are larger than the value reported for $Eu(tta)_3(H_2O)_2$ (0.190 ms) excited at 389 nm [250], which clearly points to minimization of radiationless deactivation in a coordination environment devoid of water molecules [171]. To further confirm it, the $^5D_0$ A_r and A_{nr} transition probabilities, the $^5D_0$ η and n_w, were determined following the methodology described in Chapter 2. For **M4-m-2**/**M4-m-3** analogous values of η (32/31 %), A_r (0.846/0.802 ms^{-1}), A_{nr} (1.686/1.749 ms^{-1}) and identical n_w (1.5±0.1) were calculated, reinforcing the similarity of the Eu^{3+} local coordination sites in both hybrids.

Table 6.2 shows the maximum ϕ values of 0.22±0.02 and 0.34±0.03 (excited at 320 nm) measured for **M4-m-2** and **M4-m-3**, respectively. Lower ϕ values (0.12±0.01) were measured at higher excitation wavelengths (400 nm). Independently of the selected excitation wavelength, ϕ values of 0.020±0.002 were measured in the absence of the tta−H (**M4-m-1**), excited within 260-393 nm.

Table 6.2. ϕ values obtained under distinct excitation wavelengths (λ_{exc}, nm) for the Eu^{3+}-based di-malonamide BS.

Designation	λ_{exc}	ϕ
M4-m-1	260	0.010±0.001
	280	
	340	0.020±0.002
	393	
M4-m-2	270	0.19±0.02
	320	0.22±0.02
	360	0.17±0.02
	380	0.16±0.02
	400	0.12±0.01
	464	0.05±0.01
M4-m-3	270	0.29±0.03
	320	0.34±0.03
	360	0.29±0.03
	380	0.23±0.02
	400	0.12±0.01
	464	0.03±0.01

Next sub-section will be focused on the photoluminescence properties of the Eu^{3+}-based malonamide BS.

Eu^{3+}−based malonamide BS

Figure 6.21 compares the room temperature emission spectra of **M2-m-1** and **M2-m-2** excited at 360 nm. The emission spectra are formed by a series of straight lines ascribed to the Eu^{3+} $^5D_0 \rightarrow {}^7F_{0-4}$ transitions, similar to the previously observed for **M4-m-2** and **M4-m-3**, previously described. No sign of the **M2-m** intrinsic emission (Figure 3.10, Chapter 3) was observed, which suggest efficient hybrid-to-ligand and/or hybrid-to- Eu^{3+} energy transfer, similar to observed for **M4-m** [127].

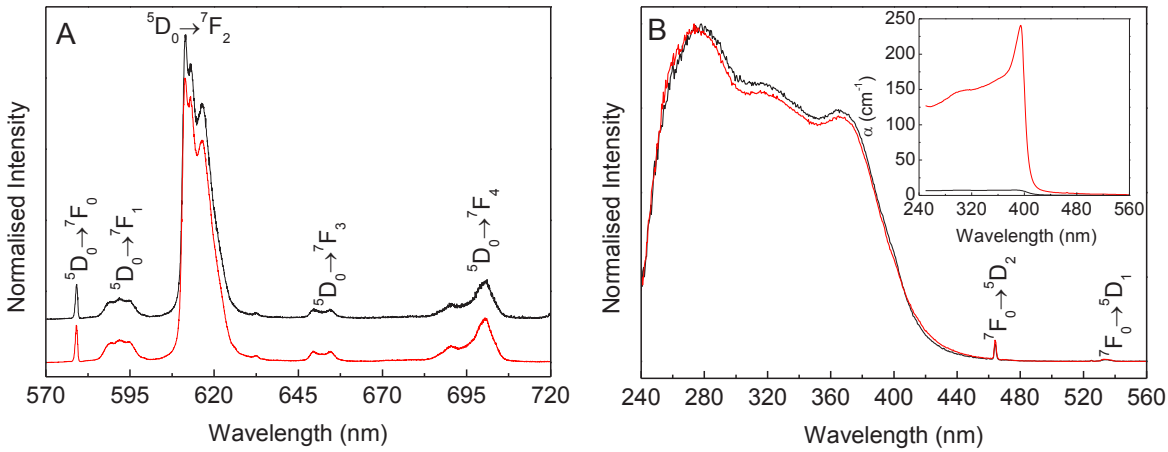

Figure 6.21. A) Emission spectra of **M2-m-1** (black line) and **M2-m-2** (red line) excited at 360 nm and B) excitation spectra monitored at 612 nm. The inset shows the UV-Visible absorption coefficients of **M2-m-1** (black line) and **M2-m-2** (red line).

The excitation spectra, Figure 6.21 B, of **M2-m-1** and **M2-m-2** were monitored around the $^5D_0 \rightarrow ^7F_2$ transition and are composed of three main components peaking at 275 nm, 320 nm and 365 nm and of two low-relative intensity intra-$4f^6$ transitions. The contribution at 275 nm is ascribed to the hybrid intrinsic excited states. The high-wavelength components at 320 nm and 380 nm resemble those already observed for the isolated $Eu(tta)_3(H_2O)_2$ [248] and for the organic-inorganic hybrids incorporating the $Eu(tta)_3(H_2O)_2$ and $Eu(tta)_3$phen (phen=1,10-phenantroline) being ascribed to the π-π* electron transition of the organic ligands [249] also identified for **M4-m-2** and **M4-m-3**. The UV-visible absorption spectra reveal the same components already detected in the excitation spectra, and an increase in the α at 395 nm from 7 cm^{-1} to 240 cm^{-1} was observed as the tta–H amount increase from **M2-m-1** to **M2-m-2** (inset on the Figure 6.21 B). Moreover, an increase of 3 times in the α value was observed for **M2-m-2** comparatively to the hybrid materials **M4-m-2** prepared with the same ratio of Eu^{3+} and tta–H ligand based di-malonamide, previously described.

The $^5D_0$ emission decay curves were monitored under direct intra-$4f^6$ excitation (380 nm) revealing a single exponential behavior, see Figure 6.22. From the data best fit, $^5D_0$ lifetime values of 0.685±0.003 ms (**M2-m-1**) and 0.676±0.003 ms (**M2-m-2**) were found. These values are higher than the values previously reported for the same ratio of Eu^{3+} and tta–H based hybrid (**M4-m-2**).

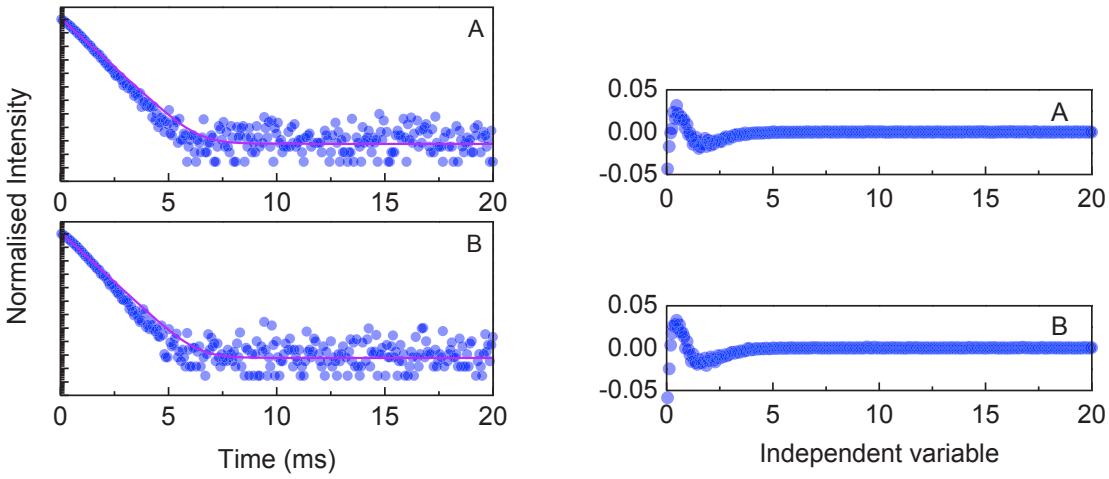

Figure 6.22. Emission decay curves of A) **M2-m-1** and B) **M2-m-2** excited at 380 nm and monitored at 612 nm. The solid lines represent the data best fit (r^2 >0.93), using a single exponential function. The respective residual plots are shown on the right side.

Table 6.3 presents the maximum ϕ values of 0.48±0.04 and 0.47±0.04 excited at 320 nm for **M2-m-1** and **M2-m-2,** respectively. These ϕ values are higher that the values reported for the same ratio of Eu^{3+} and tta–H based on di-malonamide hybrids (**M4-m-2** and **M4-m-3**).

Table 6.3. ϕ values obtained under distinct excitation wavelengths (λ_{exc}, nm) for the Eu^{3+}-based malonamide BS.

Hybrids	λ_{exc}	ϕ
M2-m-1	270	0.42±0.04
	320	0.48±0.05
	360	0.40±0.04
	380	0.30±0.03
	400	0.13±0.01
	464	0.09±0.01
M2-m-2	270	0.42±0.04
	320	0.47±0.05
	360	0.40±0.04
	380	0.28±0.03
	400	0.11±0.01
	464	0.07±0.01

6.5 Optical properties of thin films

Apart from minor differences in the energy and relative intensity, the emission and excitation spectra of thin films based on **M4-m-2** are independent of the processing conditions, see Figure 6.23 A and B, respectively.

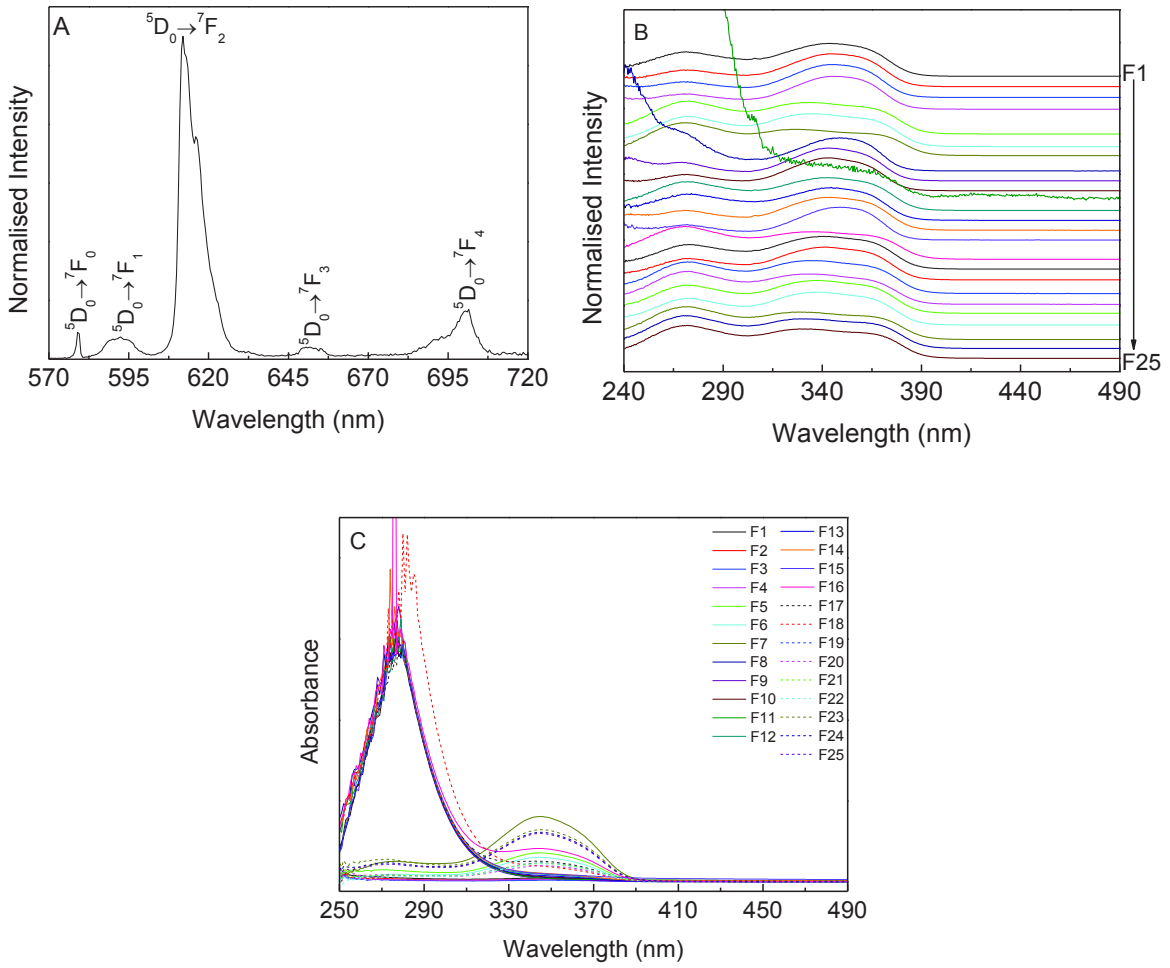

Figure 6.23. A) Emission spectrum of **F6** excited at 380 nm, B) excitation spectra of **F1-F25** monitored at 612 nm and C) UV-visible absorption of **F1-F25**.

The emission spectra of the films **F1-F25** are formed by a series of straight lines ascribed to the Eu^{3+} $^5D_0 \rightarrow {}^7F_{0\text{-}4}$ transitions. Due to similarities between the emission spectra of all films, Figure 6.23 A shows a representative emission spectrum of the **F6**, whose energy and relative intensity (I_{02}/I_{01} and I_{02}/I_{04} of 11.9 and 4.4, respectively) are closer to those of **M4-m-2** (I_{02}/I_{04} and I_{02}/I_{01} of 11.7 and 6.6, respectively).

The excitation spectra of **F1-F25** shown in Figure 6.23 B, monitored within the $^5D_0 \rightarrow {}^7F_2$ transition, denote the presence of the hybrid intrinsic excited states (270 nm) and the organic ligands-related states (320 and 380 nm) that are blue shifted when compared with that found **M4-m-2**. This blue shift, also detected in the UV-Visible absorption spectrum, Figure 6.23 C, was already reported for analogous hybrids, being ascribed to the distinct gelification and condensation rates of the spin-coated thin films [60].

Figure 6.24 and Table 6.4 depicted the $^5D_0$ emission decay curves excited at 360 nm and monitored at 612 nm for **F1**-**F25**. The $^5D_0$ lifetime varies between 0.306±0.03 ms for **F8** and 0.476±0.05 ms for **F1**.

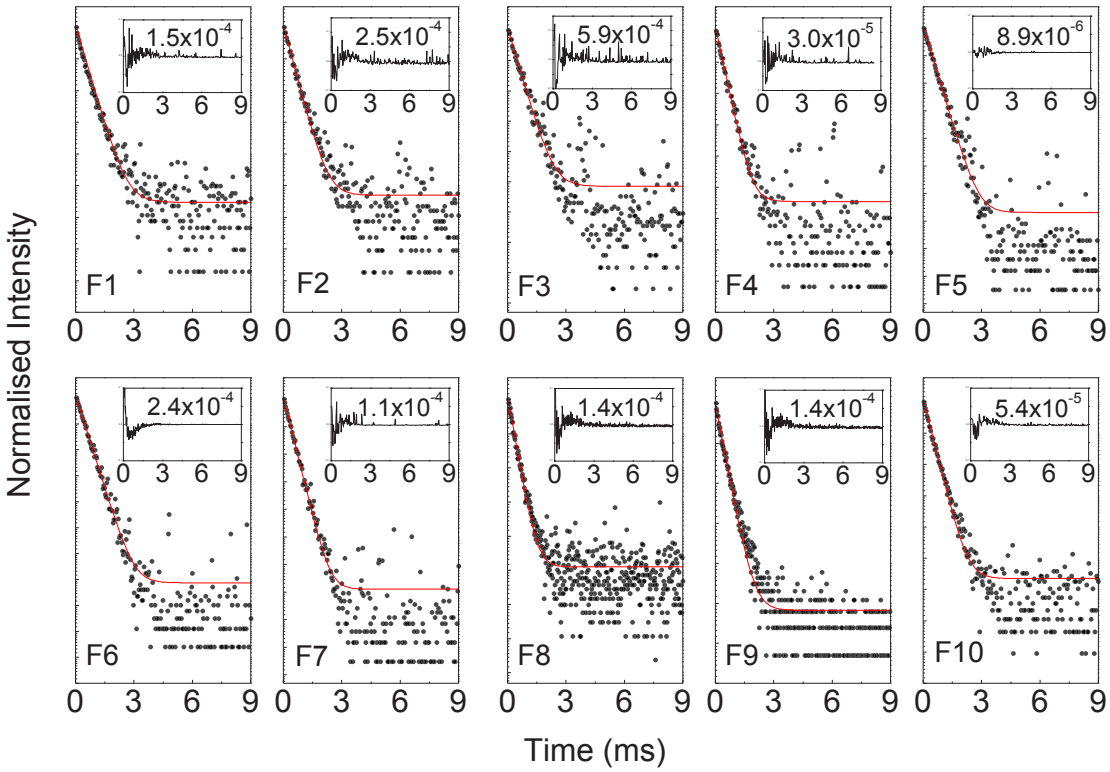

Figure 6.24. Emission decay curves of **F1**-**F25** excited at 360 nm and monitored at 612 nm. The solid lines represent the data best fit (r^2 >0.93), using a single exponential function. The inset show the residual plots.

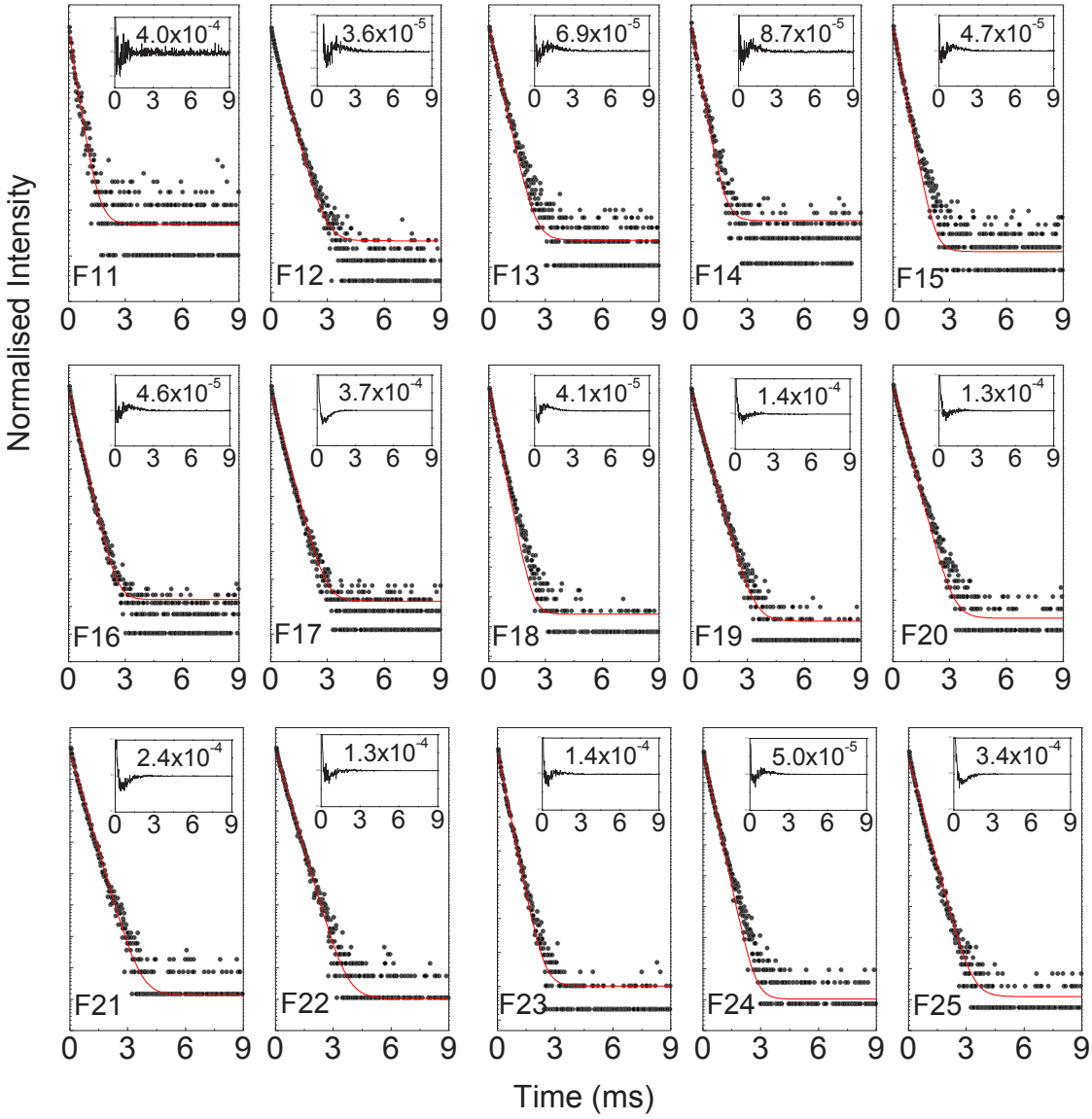

Figure 6.24 (continued)

Table 6.4. $^5D_0$ Lifetime values (τ, ms) excited at 360 nm and monitored at 612 nm of **F1-F25**.

Film reference	τ (ms)
F1	0.476±0.005
F2	0.429±0.004
F3	0.454±0.006
F4	0.342±0.004
F5	0.423±0.003
F6	0.418±0.002
F7	0.345±0.002
F8	0.306±0.003
F9	0.387±0.003
F10	0.399±0.003
F11	0.365±0.006
F12	0.416±0.002
F13	0.392±0.002
F14	0.333±0.002
F15	0.322±0.002
F16	0.338±0.005
F17	0.387±0.006
F18	0.302±0.001
F19	0.439±0.004
F20	0.422±0.002
F21	0.472±0.005
F22	0.471±0.004
F23	0.350±0.002
F24	0.341±0.002
F25	0.425±0.006

The photoluminescence features were quantified through the measurement of ϕ as function of the excitation wavelength, see Table 6.5. The ϕ values are strongly affected by the preparation conditions. The highest value (0.60±0.06) was measured for **F1** under 345 nm of excitation.

Table 6.5. Maximum ϕ value obtained under distinct excitation wavelengths (λ_{exc}, nm) for **F1–F25**.

Reference	λ_{exc} (nm)	ϕ
F1	345	0.60
F2	345	0.39
F3	365	0.31
F4	365	0.30
F5	345	0.23
F6	365	0.21
F7	365	0.36
F8	365	0.20
F9	365	0.17
F10	365	0.30
F11	270-365	0.01
F12	365	0.12
F13	365	0.09
F14	365	0.08
F15	365	0.13
F16	365	0.09
F17	365	0.07
F18	365	0.07
F19	345	0.15
F20	345	0.13
F21	345-365	0.16
F22	345-365	0.15
F23	365	0.11
F24	345	0.10
F25	345	0.10

Based on the ϕ values, seven films with highest ϕ values were selected to be tested as LSCs. The photograph depicted in Figure 6.25 A illustrates the potential of the films to be used as LSCs. Under AM1.5 illumination, the light emitted at the surface is guided and concentrated at the substrate edges, where it can be collected by a photodiode.

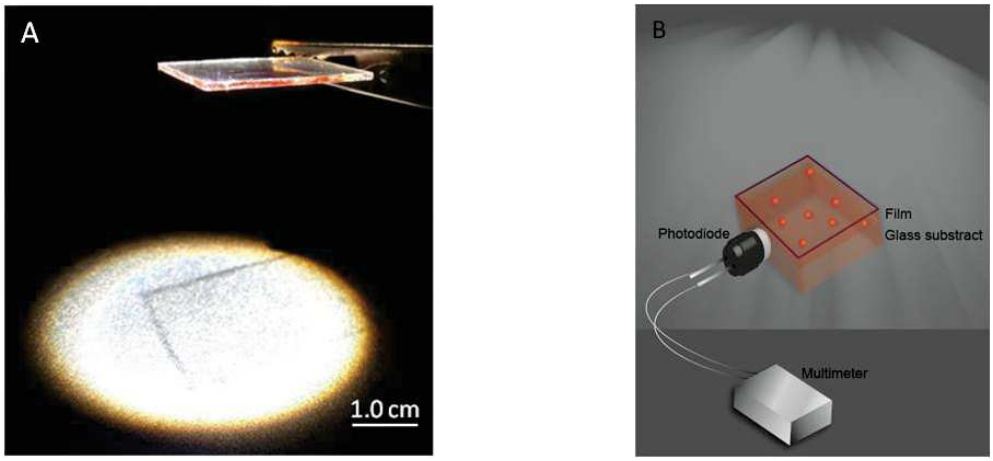

Figure 6.25. A) Photograph of **F6** under AM1.5G illumination, B) schematic representation of the procedure used to measure the n_{opt} of LSCs.

The performance of the LSCs was quantified through the measurement of η_{opt} under AM1.5G illumination. Figure 6.25 B show a schematic representation of the procedure used to measure the η_{opt} which is given by the ratio between the power of the photodiode attached to the LSC (P_{out}) and the power of the photodiode exposed directly to the solar radiation (P_{in}) [90]:

$$\eta_{opt} = \frac{P_{out}}{P_{in}} = \frac{I_{sc}^{L} V_{0}^{L}}{I_{sc} V_{0}} \frac{1}{G} \frac{\eta_{solar}}{\eta_{PV}} \frac{\int_{\lambda_2} I_{AM1.5G}(\lambda) d\lambda}{\int_{\lambda_1} I_{AM1.5G}(\lambda) d\lambda} \qquad 6.1$$

where I^{L}_{SC} and V^{L}_{0} represent the short-circuit current and the open voltage when the photodiode is coupled to the LSC (I_{sc} and V_0 are the corresponding values of the photodiode), $G=A_s/A_e$ is the ratio between the surface area (A_s) and the area of the plate edges (A_e), η_{solar} is the efficiency of the photodiode relatively to the total solar spectrum and η_{PV} is the efficiency of the photodiode at the LSC emission wavelengths. The ratio:

$$\frac{\eta_{solar}}{\eta_{PV}} = \frac{\int EQE_{Device}(\lambda) I_{AM1.5G}(\lambda) d\lambda}{\int EQE_{PD}(\lambda) I_{AM1.5G}(\lambda) d\lambda} = 1.15 \qquad 6.2$$

where EQE_{Device} and EQE_{PD} are the external quantum efficiencies of the LSC coupled to photodiode and of the photodiode, respectively. We note that despite the photodiode is coupled to a single edge, G is calculated considering A_e as the area of the extremities, as the same light concentration is expected at each LSC end. The η_{opt} values were calculated considering the fraction of absorbed photons (53 $W \cdot m^{-2}$) and the total solar spectral irradiance (1000 $W \cdot m^{-2}$). Concerning the mismatch in the UV spectral region between the AM1.5G solar irradiance and that of the Xe lamp of the solar simulator used Figure 6.26, $I_{AM1.5G}$ in equation 6.1 is replaced by the emission spectrum of the solar simulator, $\frac{\eta_{solar}}{\eta_{PV}} = 0.9$.

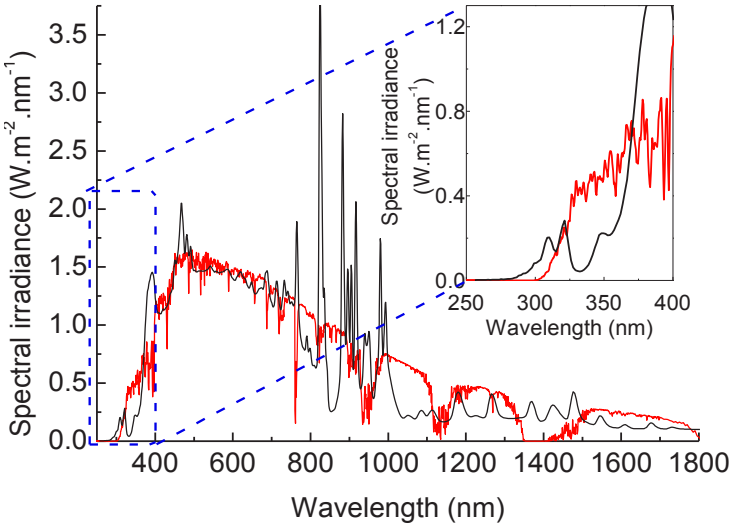

Figure 6.26. Spectral irradiance of the Abet Technologies model 10500 solar simulator (black line) and of standard AM1.5 (red line) spectra. The inset shows a magnification in the UV region (250-400 nm).

Thus, the performance of the **F5**, **F6** and **F7**-based LSCs is compared with the figures of merit known for planar single-layer LSCs, whose optically active centres are QDs [236,251,252], dyes [236,253-255] and Ln^{3+}–based LSCs [60,130,213,243]. We note that as distinct definitions and experimental conditions may be employed to estimate η_{opt}, the comparison will be performed using the figure of merit calculated using Equation 6.1, or an identical definition, under AM1.5G solar illumination. Examples involving illumination using

other standard conditions (*e.g.*, diffuse cloudy day indoor illumination [256]) are not consider for the comparison.

The maximum η_{opt} value here reported calculated using the fraction of absorbed photons (12.3 % for **F5**) is of the same order of magnitude of LSCs based on CdSe/CdS QDs incorporated in poly(methyl methacrylate) (PMMA) (10.2 %) [252] and LSCs using red305-doped PMMA (16.3 %) [254]. In the case of η_{opt} values calculated considering the total number of incident photons, the highest value measured for **F5** (0.43 %) is similar to that found for CdSe and ZnS QDs in toluene (0.3 %) [236] being, however, one order of magnitude smaller than the η_{opt} of LSCs containing PbS QDs (1.4 %) [251], Rhodamine B (2.6 %) [236] and RedF (3.4 %) [236] in toluene and PMMA co-doped with LumogenF and Red305 (2.8 %) [255]. The η_{opt} values of Ln^{3+}–based LSCs were calculated for selected excitation wavelengths, namely 8.8%, for Tb^{3+}–based poly(vinylalcohol) incorporating salicylic acid [243], 9%, for $Eu(tta)_3$.ephen (ephen=5,6–epoxy–5,6–dihydro[1,10] phenanthroline) embedded into **t-U(5000)** hybrid material [213] and 4.3% and 1.7%, for Eu^{3+}-[60] and Tb^{3+}-doped [130] BS, respectively.

We note that **F5** and **F6** reveal similar η_{opt} values, whereas for **F7** a lower value was found. Aiming at further interpret the differences in the measured η_{opt} values, spectroscopic ellipsometry was used to characterize the dispersion curves for **F6** and **F7**, see Figure 6.27, enabling the determination of the trapping efficiency, $\eta_{trap}=(1-1/n_p^2)^{1/2}$, where n_p is the refractive index of the emitting medium at the emission wavelength (612 nm). The η_{trap} defines the fraction of photons confined within the substrate. The refractive index values of **F6** are higher than those of **F7** reinforcing the role of the deposition conditions on this optical parameter, as recently highlighted for analogous hybrid materials [130]. The thickness measured by profilometry of the films **F1**, **F4**, **F5**, **F6** and **F7** is 430 (5.8) nm, 100 (19.2) nm, 90 (9.3) nm 201 (2.6) nm and 375 (25) nm, respectively, the value in brackets represent the standard deviation. The calculated thicknesses are t=205.0±4.8 nm (**F6**) and t=407.0±3.3 nm (**F7**), which are in good agreement with the complementary profilometry studies, suggesting that the modelling of the ellipsometric data yielded realistic parameters. Despite the larger refractive index of **F6** (1.525) at the Eu^{3+} maximum emitting wavelength (612 nm) compared with that of **F7** (1.489) an analogous η_{trap}=75 % is calculated for the LSCs based on **F6** and **F7**. Therefore, we suggest that the larger t of the optical active layer in **F7** may induce larger

transport losses due to the scattering of the emitted light in the film [60] explaining the lower η_{opt} value relatively to **F6** and **F7**.

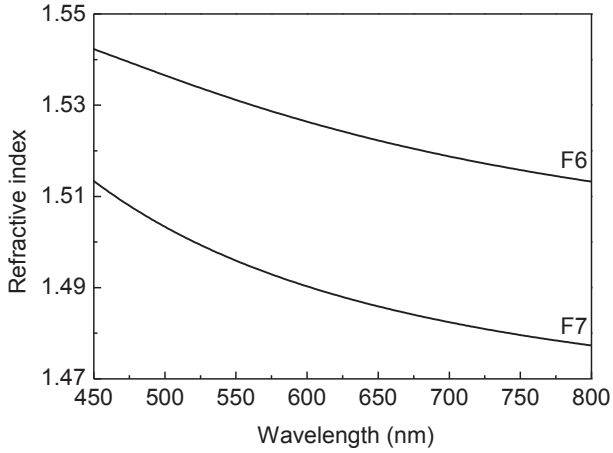

Figure 6.27. Refractive index dispersion curves of **F6** and **F7**.

6.6 Conclusions

The synthesis of the malonamide and di-malonamide hybrid materials prepared under nucleophilic catalysis in the presence of Eu^{3+} with and without tta–H has been achieved. Specific Eu^{3+} local coordination in **M4-m-2** (with tta–H) compared to **M4-m-1** (tta–H free) is suggested from vibrational and photoluminescence results. A Eu^{3+} cooperative complexation by tta–H and hybrids lead to a very significant increase of the ϕ.

Aiming an improvement of the optical properties of the Eu^{3+}-based hybrids a new system based on malonamide (**P2-m**) were projected. An increase of the *c* values was observed for the $Eu(tta)_3(H_2O)_2$ based on malonamide BS. Also the FT-IR data show better interaction between the hybrid host and the $(Eu(tta)_3(H_2O)_2)$ complex. The higher complexation observed in the case of Eu^{3+}-based malonamide BS are well presented in photoluminescence study observed for the increase of 3 times in the α, τ and ϕ values, observed for **M2-m-2/M2-m-3** comparatively to **M4-m-2/M4-m-3**.

In order to develop LSCs, Eu^{3+}-based di-malonamide BS in particular **M4-m-2** was processed as thin films by spin-coating on glass substrates. The **P4-m** concentration, aging time, spinning speed conditions and solvent type were varied to optimize the optical

properties of the LSCs. Films with ϕ of 0.60±0.06 excited at 345 nm and η_{opt} of 12.3 % in the absorbing spectral region of the active layer (300-380 nm) were produced.

7. General conclusions and perspectives

In the domain of green photonics, in particular SSL applications, it is required the development of new materials featuring: 1) high absolute emission quantum yield, 2) high brightness, 3) stability in time and under irradiation and 4) ability to be excited with cheap light sources *e.g.* long-wavelength UV excitation (360-400 nm) and blue commercial light emitting diodes (LEDs).

In this thesis new BS organic-inorganic hybrids functionalized by amide and thioamide groups were obtained from linear or branched structure precursors by sol-gel process: The local structure of the BS organic-inorganic hybrids was studied by X-ray diffraction, ^{29}Si MAS NMR, ^{13}C CP/MAS NMR and FT-IR spectroscopy. In addition, the relationship between the local structure and the optical properties was discussed. The main conclusions derived by structural and photoluminescence characterization of the BS organic-inorganic hybrid here presented are listed bellow.

- *Malonamide and di-malonamide BS*

The hybrid materials (**M2-m** and **M4-m**) were obtained from linear precursors (**P2-m** and **P4-m**) based on the malonamide group. The presence of one (**M2-m**) or two (**M4-m**) malonamide groups induces differences in terms of morphology, local structure and optical properties. The **M2-m** processed as free standing film presents a condensation degree of 91 % and an absolute emission quantum yield of 0.22±0.02. The **M4-m** is a white powder with condensation degree of 80 % and an absolute emission quantum yield of 0.10±0.01.

- *Amide- Thioamide BS*

M(UU), **M(UT)** and **M(TT)** organic models self-assembled through H–bonds involving urea and/or thiourea groups have new opportunities for the chemical engineering of H–bonded material. Substitution of urea by thiourea leads to different H–bond conformations allowing a modulation of H–bond strength. The transcription of the local sub-structures from the model to the hybrid was found in **H(UU)** with bifurcated urea-urea H–bond leading to a lamellar structure. In **H(UT)** the partial transcription limited to inter-dimer urea-thiourea bifurcated bond leads to an amorphous structure. For thiourea-thiourea H-bond, a poor transcription was found leading to a material with a strong dispersion in H–bond strength. Therefore, beyond the potential modulation of H–bond strength associated to the substitution, some geometrical factors associated to urea or thiourea H–bonds also participate to the structuration during the sol-gel process. For optical properties, it was shown that the substitution or urea by thiourea in **UT** and **TT** leads to a redshift of the emission from UV toward blue for models and hybrids. Despite the low absolute emission quantum yield, these materials offer original thiourea and urea environments that could present some interest for the incorporation of Ln^{3+}.

- *Tri-ureasil BS*

The hybrid materials, (**t-U(5000)**), derived from the branched hybrid precursor (**t-UPTES (5000)**) based on amide group, have been prepared under different synthetic conditions, varying the HCl concentration ($1.0\times10^{-3}\leq[HCl]\leq2.0$ M) and water content (2.2 mmol and 22.2 mmol) under usual laboratory and controlled atmosphere conditions. All the **t-U(5000)** present a UV/blue emission under UV excitation, which origin was ascribed to electron-hole recombination occurring in the siliceous nanodomains and within the NH/C=O groups, respectively. The radiative recombination mechanisms responsible for the emission in **t-U(5000)** were identified as donor-acceptor pairs. Under laboratory atmosphere conditions the variation of [HCl] enabled an increase of the absolute emission quantum yield to 0.13 ± 0.01 for $1.0\times10^{-2}\leq[HCl]\leq 1.0\times10^{-1}$ M. For these optimized [HCl] values, the synthesis was performed under controlled atmosphere conditions ($[O_2]<0.5$ ppm, $[H_2O]=350$ ppm), yielding an enlargement of the UV/blue/green absorption regions (350–500 nm) and an increase of the absolute emission quantum yield from 0.13 ± 0.01 to 0.27 ± 0.03.

- *Eu^{3+}-based Malonamide BS*

Chosen for their structural simplicity, the **P2-m** and **P4-m** precursors were doped with $EuCl_3$•$6H_2O$ and $Eu(tta)_3(H_2O)_2$ yielding BS organic-inorganics hybrids (**M2-m-2**, **M2-m-3**, **M4-m-1**, **M4-m-2**, **M4-m-3**). Specific Eu^{3+} local coordination in **M2-m-1**, **M2-m-3**, **M4-m-2** and **M4-m-3** (with $Eu(tta)_3(H_2O)_2$) compared with **M2-m** and **M4-m** (free $Eu(tta)_3(H_2O)_2$) is suggested from vibrational and photoluminescence results. While for Eu^{3+}-based di-malonamide BS the incorporation of the different ratios of Eu^{3+}:tta–H (1:2 or 1:3) seems to have no influence in the coordination between $Eu(tta)_3(H_2O)_2$ and hybrid host due to the presence of the some free tta-H. In the case of Eu^{3+}-based malonamide BS the molar ratio of 1:3 of Eu:tta-H induces better coordination with the hybrid host, observed by the increase of the absolute emission quantum yield and absorption coefficient. The development of Eu^{3+}-based di-malonamide BS thin films show a maximum absolute emission quantum yield of 0.60±0.06 (excited at 345 nm) and η_{opt} of 12.3 % in the absorbing spectral region of the active layer (300-380 nm).

Our contribution in the development of different hybrid materials achieved from different precursors using different synthesis strategies will certainly help to improve the performance of future developing materials in order to be used as white light emitters. Knowing the origin of the defects responsible for the emission in amide- thioamide-functionalized hybrids could be an important advance in this sense.

Appendix A

Experimental techniques

Elemental Analysis. Elemental analysis for Eu and Si were performed by inductively coupled plasma optical emission spectroscopy (ICP-OES) analysis on a Jobin Yvon Activa-M instrument with a glass concentric nebulizer. For the Eu analysis the samples were digested under microwaves with 0.5 mL of HCl and 1 mL of nitric acid (HNO_3). For the Si analysis the samples were digested under microwaves with 1 mL of HNO_3 and 0.5 mL of hydrofluoric acid. After being digested under microwaves the samples were recovered in a 50 mL of ultrapure water. The method is accurate within 10 %. The measurements were performed by Dra. Lina Carvalho (University of Aveiro/CICECO, Portugal).

Scanning electronic microscopy-(SEM). The SEM images were obtained with a Hitachi Model SU-70 microscope after carbon metallization. The measurements were performed by Dra. Marta Ferro in University of Aveiro/CICECO, Portugal.

Thermogravimetric analysis-TGA. The TGA was performed using a Shimadzu TGA-50 system from 0 °C to 800 °C at a heating rate of 10 °C min^{-1}, under a static atmosphere of air. The measurements were performed by Dra. Celeste Azevedo in University of Aveiro, Portugal.

^{29}Si magic-angle spinning (MAS) nuclear magnetic resonance (NMR)- ^{29}Si MAS NMR. The ^{29}Si MAS NMR spectra were recorded with a Bruker III Avance 400 and Bruker III Avance 500 (9.4 T) spectrometer at 79.49 MHz and 100.62 MHz, respectively. ^{29}Si MAS NMR spectra were recorded with 2 μs (*ca.* 30) rf pulses, a recycle delay of 60 s and at a 5.0 kHz spinning rate. Chemical shifts (δ) are quoted in ppm from TMS. The measurements were performed by Dra. Paula Santos in University of Aveiro/CICECO, Portugal.

^{13}C cross-polarization (CP) MAS NMR spectra- ^{13}C CP/MAS NMR. The ^{13}C CP/MAS NMR spectra were recorded with 4 μs ^{1}H 90º pulses, 2 ms contact time, a recycle delay of 4 s and at a spinning rate of 8 kHz. Chemical shifts (δ) are quoted in ppm from TMS. The measurements were performed by Dra. Paula Santos in University of Aveiro/CICECO, Portugal.

Powder X-ray Diffraction- XRD: The X-ray diffraction patterns were collected using a Philips X'Pert MPD powder X-ray diffractometer. The samples were exposed to the CuK_α radiation (1.54 Å) over a *q* ($q=4\pi \sin\theta/\lambda$, 2θ being the scattering angle) in a 2θ range between 1º and 60º with a step of 0.05 and resolution of 40 s per step. The measurements were performed by Dra. Rosário Soares in University of Aveiro/CICECO, Portugal.

Fourier transform infrared (FT-IR) spectroscopy. Middle-infrared experiments (400–5000 cm^{-1}) were recorded both in the transmission and attenuated total reflectance (ATR) mode. The measurements were carried out on a Bruker IFS 113V spectrometer under vacuum equipped with a N_2-cooled mercury (Hg) cadmium telluride (MCT) detector, a Globar source, and potassium bromide (KBr) beam splitter. The spectral resolution was 4 cm^{-1}, and 64 scans were co-added for each spectrum. In transmission, KBr pellets (0.8 mg sample / 300 mg KBr) were prepared under 8 tons pressure. Prior to recording the spectra, the pellets were dried at 100 ºC for about 20 h, in order to reduce the levels of adsorbed water. FAR-infrared (30–400 cm^{-1}) experiments were recorded in the transmission mode using a He-cooled bolometer, Hg arc discharge source and mylar 6μm beam splitter coated with germanium. Polyethylene pellets (3 mg sample / 70 mg polyethylene) were prepared. The tta–H concentration was increased up to 5.5 mg to be able to discriminate its vibrational signatures.

FT-IR under pressure: Concerning the FT-IR done under pressure, the control system is based on diamond anvils coupled to a FT-IR operating system under vacuum primary. The study was performed in the mid-infrared (4000-400 cm^{-1}) with Globar source, a separation in KBr and an MCT detector cooled with nitrogen whose domain detecting extends between 7500-750 cm^{-1}.

Raman. The micro-Raman diffusion spectra were recorded with a Jobin Yvon T64000, Raman (excitation with argon or krypton lasers) and Bruker RFS100 Raman spectrometer (excitation at 1064 nm).

UV-Vis absorption. UV-Vis absorption spectra were measured using a dual-beam spectrometer Lambda 950, (Perkin-Elmer) with a 150 mm diameter Spectralon integrating sphere, over the scan range 250–800 nm and a resolution of 1.0 nm. For the spin-coating films the region below 300 nm was not assessed due to the glass substrate high absorbance. The absorption coefficient (α, cm^{-1}) was estimated using the Lambert–Beer equation ($\alpha = A_{bs}/t$, where A_{bs} is the absorbance).

Photoluminescence. The photoluminescence spectra were recorded at low (12 K) and room (300 K) temperature with a modular double grating excitation spectrofluorimeter with a TRIAX 320 emission monochromator (Fluorolog-3, Horiba Scientific) coupled to a R928 Hamamatsu photomultiplier, using a front face acquisition mode. The excitation source was a 450 W Xenon (Xe) arc lamp. The emission spectra were corrected for detection and optical spectral response of the spectrofluorimeter and the excitation spectra were corrected for the spectral distribution of the lamp intensity using a photodiode reference detector. The emission decay curves were measured with the setup described for the luminescence spectra using a pulsed Xe–Hg lamp (6 μs pulse at half width and 20–30 μs tail).

Absolute emission quantum yields (ϕ). The ϕ were measured at room temperature using a quantum yield measurement system C9920-02 from Hamamatsu with a 150 W Xenon lamp coupled to a monochromator for wavelength discrimination, an integrating sphere as sample chamber and a multi-channel analyzer for signal detection. Three measurements were made for each sample so that the average value is reported. The method is accurate to within 10 %.

Profilometry. A TENCOR Alpha-Step IQ profilometer was used to measure the thickness t of the films. The method is accurate to within 0.1 %.

Ellipsometry. The spectroscopic ellipsometry measurements were made using an AutoSE ellipsometer (Horiba Scientific) with a total of 250 points in the wavelength interval of 440–800 nm, an incidence angle of 70°, an acquisition time of 22 ms per point, and an average of 10 measurements per point. The refractive index dispersion curve was calculated using the Lorentz model detailed elsewhere [61,257]. The measurements were performed by Sandra Correia in University of Aveiro/CICECO, Portugal.

Optical conversion efficiency. The optical power at the LSC output was estimated using a commercial photodiode (IF D91, Industrial Fiber Optics, Inc.) with wall-plug

efficiency to the AM1.5G solar spectrum distribution of 4 %. All measurements were performed under AM1.5G illumination (at 1000 W/m^2) using a 150 W xenon arc lamp class A solar simulator (Abet Technologies model 10500).

Refractive index: The refractive index dispersion curves were measured considering three-layered structural model: glass substrate, organic-inorganic hybrid layer and air as an ambient medium with refractive index value of 1.0. The thickness of the glass substrate was considered infinite and the refractive index was obtained by direct inversion of the ellipsometric data (not shown). The experimental ellipsometric parameters (*Is* and *Ic*) and the respective fit using the Lorentz model.

Computational detail

DFT calculation: The DFT based calculations were performed using the VASP package [258] and the generalized gradient approximation to the exchange correlation functional as proposed by Perdew, Burke and Ernzerhof [259]. Interactions between ions and electrons were described by the projector augmented wave method in the real space representation. The electronic wave functions were expanded in plane-waves up to a kinetic energy cutoff of 460 eV and integrals over the Brillouin zone were approximated by sums over a 6x4x2 mesh of special k-points following the Monkhorst-Pack scheme [260]. For the structural relaxation, experimental lattice parameters were fixed and only the atomic positions were relaxed by using a fine integration grid until the maximum residual atomic force was less than 6x10-3 eV/Å. The zone-center dynamical matrix were calculated within the harmonic approximation by finite difference of the Hellmann-Feynman forces using an atomic displacement of 0.03 Å. Positive and negative displacements are used to minimize the anharmonic effects. Born effective charges were computed using the linear response. The infrared absorption spectra were calculated following the methodology described in [261].

Following the DFT calculation, a assignment of the main vibrational modes will be achieved for **M(UT)** and **M(TT)**. We will focus our attention on some vibrational features and their link to well identified short range structure. As the local range structure of the hybrid materials through self-assembly involves H–bond interactions between "Amide" and "Thioamide" groups, we will especially focus on the frequencies that involve these groups as presented below.

Appendix B

Supplementary data of Chapter 4

Synthesis

BS organic-inorganic hybrid materials

The synthesis of the amide- thioamide BS organic-inorganic precursors and hybrid materials (**P(UU)** and **H(UU)**, **P(UT)** and **H(UT)**, **P(UT)** and **H(TT)**) are described below.

P(UU): to a solution of 1,4–diaminobenzene (560 mg, 5.18 mmol) in anhydrous dichloromethane (40 mL) placed under argon in a Schlenk tube was added (3–isocyanatopropyl)triethoxysilane (ICPTES, 2.69 g, 10.9 mmol). The solution was stirred at room temperature for 24 h. The solvent was evaporated under vacuum and then the solid was washed with pentane (3 × 10 mL), filtered and then dried under vacuum. The NMR data are in agreement with the previously published results [186].

H(UU): In a Shlenk tube, **P(UU)** (0.41 g, 0.68 mmol) was mixed with THF (3.6 mL) under vigorous stirring at 50 °C. Upon cooling, distilled water was added (7.2 mL) forming a white precipitate. Then HCl 1 M (0.136 mL) was added to the solution, which was kept under stirring at 60 °C for 2 days. After this period of time the hybrid material was recovered by filtration and was successively washed with water, ethanol and acetone. Finally, the hybrid was dried under vacuum during 1 day. The molar ratio of the reactants is the following: P(UU):THF: H_2O: HCl=1:65:600:0.2. Finally the hybrid material **H(UU)** was freeze dry. A schematic representation of the synthesis of **P(UU)** and **H(UU)** is shown in Scheme B.1.

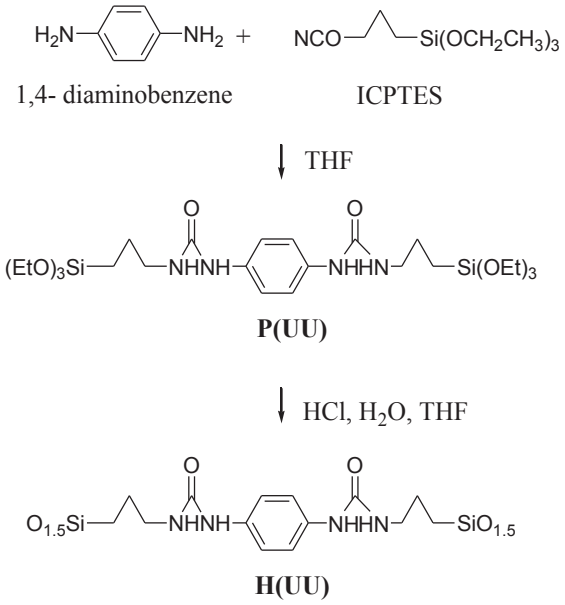

Scheme B.1. Schematic representation of the synthesis of **P(UU)** and **H(UU)**.

P(UT): to a solution of 1,4– diaminobenzene (1.0 g, 9.3 mmol) in anhydrous THF (50 mL) placed under Ar in a Schlenk tube was added (3– isothiocyanatopropyl)triethoxysilane (ITCPTES, 2.47 g, 9.4 mmol). The solution was stirred at room temperature for 18 h under argon. The THF was then removed under vacuum, and the white residue was washed with pentane. The thiourea intermediate was isolated in quantative yield after drying and used without further purification in the next step. ^{1}H NMR ($CDCl_3$, 400 MHz): 7.38 (br, 1H); 6.95 (d, J = 8.6 Hz, 2H); 6.61 (d, J = 8.6 Hz, 2H); 5.88 (br, 1H); 3.74 (q, J = 7.0 Hz, 6H); 3.36 (m, 2H); 1.59 (m, 2H); 1.14 (t, 9H); 0.53 (m, 2H). ^{13}C NMR ($CDCl_3$, 100 MHz): 181.5; 146.6; 128.2; 116.1; 58.6; 47.7; 22.6; 18.4; 7.7.

This amino-thiourea intermediate (3.45 g, 9.3 mmol) was suspended in dry THF (50 mL) then ICPTES (2.9 g, 11.7 mmol) was added and the mixture was stirred for an additional 18 h at room temperature. The solvent was evaporated undr vacuum and the mixture was washed repeatedly with pentane (3 × 10 mL), filtered and dried under vacuum. A white powder was obtained. ^{1}H NMR ($CDCl_3$, 400 MHz): 8.03 (br, 1H); 7.38 (br, 1H); 7.12 (d, J = 6.8 Hz, 2H); 6.92 (d, J = 6.8 Hz, 2H); 6.82 (br, 1H); 6.64 (br, 1H); 3.76 (m, 12H); 3.56 (m, 2H); 3.16 (m, 2H); 1.67 (m, 2H); 1.59 (m, 2H) 1.20 (m, 18H); 0.61 (m, 4H). HRMS (ESI^+) Calc. for $C_{26}H_{51}N_4O_7Si_2S$: 372.1750; exp. 372.1765.

H(UT): In a Shlenk **P(UT)** (0.58 g, 0.94 mmol) was dissolved in anhydrous ethanol (1 mL) under vigorous stirring at 80 °C. Then distilled water (0.216 mL) was added forming a white precipitate. Then 1 M of HCl (0.01 mL) was added to the solution and was kept under stirring at 80 °C for 2 days. After this period of time the hybrid material was recovered by filtration and was successively washed with water, ethanol and acetone. Then, the hybrid was dried under vacuum during 1 day. The molar ratio of the reactants is the following: P(UT):H_2O:HCl=1:600:0.2. Finally the hybrid material **H(UT)** was freeze dry. A schematic representation of the synthesis of **P(UT)** and **H(UT)** is shown in Scheme B.2.

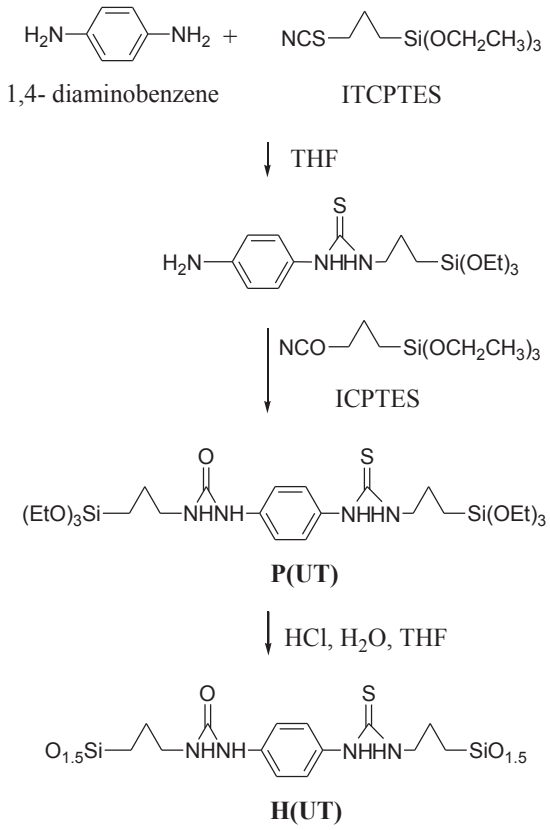

Scheme B.2. Schematic representation of the synthesis of **P(UT)** and **H(UT)**.

P(TT): to a solution of 1,4-isothiocyanate (0.76 mg, 0.004 mmol) in anhydrous THF (30 mL) placed in a Schlenk tube under Ar was added (3-aminopropyl)triethoxysilane (APTES, 2.2 mL, 9.4 mmol). The solution was heated at 50 °C for 24 h under vigorous stirring. The solvent was evaporated under vacuum and then the solid was washed with pentane (3 × 10 mL), filtered and then dried under vacuum. ^{1}H NMR ($CDCl_3$, 400 MHz): 9.40

(br, 2H, NH); 7.69 (br, 2H, NH); 7.33 (s, 4H, CH_{Ar}); 3.76 (q, J = 7.0 Hz, 12H, OCH_2); 3.44 (br, 4H, NCH_2); 1.59 (br, 4H, NCH_2CH_2) 1.16 (t, J = 7.0 Hz, 18H, CH_3); 0.57 (m, 4H, CH_2Si). ^{13}C NMR ($CDCl_3$, 100 MHz): 180.2 (C=S); 135.3 (Cq_{Ar}); 123.3 (CH_{Ar}); 57.7 (OCH_2); 46.3 (NCH_2); 22.0 (NCH_2CH_2); 18.2(CH_3); 7.3 (CH_2Si).

H(TT): in a Shlenk **P(TT)** (0.30 g, 0.47 mmol) was mix with Acetonitrile (ACTN, 1.72 mL) and stirred vigorously at 80 °C. Then distilled water (5.4 mL) was added forming a white precipitate. Then HCl 1 M (0.004 mL) was added to the solution which was stirring at 80 °C for 4 days. After this period of time the hybrid material was recovered by filtration and was successively washed with water, ethanol and acetone. Then, the hybrid was dried under vacuum during 1 day. The molar ratio of the reactants is the following: P(TT):ACTN:H_2O:HCl=1:65:600:0.2. Finally the hybrid material **H(TT)** was freeze dry. A schematic representation of the synthesis of **P(TT)** and **H(TT)** is shown in Scheme B.3.

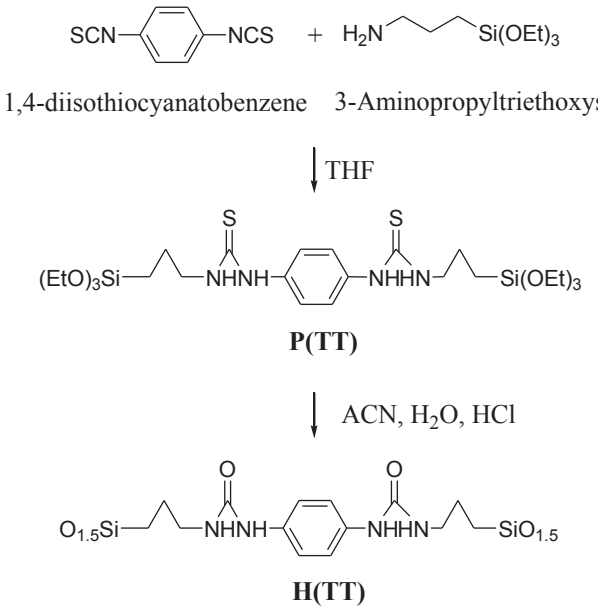

Scheme B.3. Schematic representation of the synthesis of **P(TT)** and **H(TT)**.

Organic model compounds

The synthesis of the organic model compounds (**M(UU)**, **M(UT)** and **M(TT)**) are described below.

M(UU): to a solution of 1,4- diaminobenzene (0.45 g, 4.2 mmol) in dimethylformamida (DMF, 10 mL) was added butylisocyanate (1 mL, 8.9 mmol). A precipitate started to form rapidly. The solution was kept under vigorous stirring for 18 h. A solid powder was collected then washed with ethanol (3 × 10 mL), filtered and then dried under vacuum. ^{1}H NMR (dmso-d_6, 400 MHz): 9.39 (br, 2H, NH-Ar); 7.64 (br, 2H, N*H*-CH_2); 7.31 (s, 4H, Ar); 3.43 (br, 4H, CH_2-N); 1.52 (m, 4H, C*H*$_2$-CH_2-N); 1.31 (m, 4H, C*H*$_2$-CH_3); 0.89 (t, J = 7.3 Hz, 6H, CH_3). ^{13}C NMR (dmso-d_6, 101 MHz): 180.2 (C=S); 135.3 (Cq_{Ar}); 123.4 (CH_{Ar}); 43.5 (CH_2-N); 30.6 (*C*H_2-CH_2-N); 19.6 (*C*H_2-CH_3); 13.7 (CH_3). A schematic representation of the synthesis of **M(UU)** is shown in Scheme B.4.

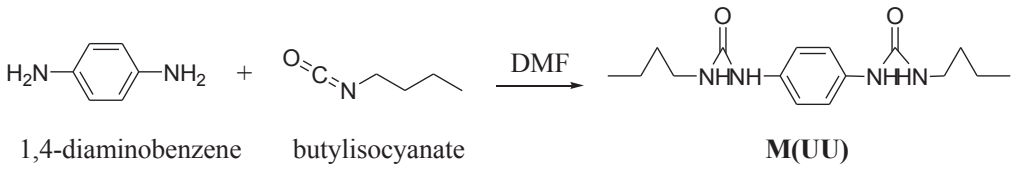

Scheme B.4. Schematic representation of the synthesis of **M(UU)**.

M(UT): To a solution of freshly sublimed 1,4-diaminobenzene (2.68 g, 24.8 mmol) in THF (50 mL) was added butylisothiocyanate (3.00 mL, 24.8 mmol). The mixture was stirred for 18 h at 50 °C. The THF was then removed by rotary evaporation, and the precipitate was washed with pentane. The thiourea intermediate was isolated after drying and used without further purification in the next step. ^{1}H NMR ($CDCl_3$, 400 MHz): 7.43 (br, 1H); 6.97 (d, J = 8.6 Hz, 2H); 6.69 (d, J = 8.6 Hz, 2H); 5.74 (br, 1H); 3.84 (br, 2H); 3.59 (m, 2H); 1.50 (m, 2H); 1.28 (m, 2H); 0.89 (t, J = 7.3 Hz, 3H). ^{13}C NMR ($CDCl_3$, 100 MHz): 181.3; 146.4; 128.0; 125.9; 116.0; 45.2 ; 31.1; 20.0; 13.8.

This amino-thiourea intermediate (1.95 g, 8.74 mmol) was suspended in dry THF (20 mL) then butylisocyanate (1.08 mL, 9.62 mmol) was added. The mixture was stirred at 50 °C for 16 h under argon then the solvent was evaporated and the mixture was washed repeatedly with pentane. A white powder was obtained. Single crystals were obtained after cooling a hot acetone solution. ^{1}H NMR (dmso-d_6, 400 MHz): 9.23 (br, 1H, (C=S)NH-Ar); 8.38 (s, 1H,

(C=O)NH-Ar); 7.45 (br, 1H, (C=S)N*H*-CH_2); 7.32 (d, J = 8.6 Hz, 2H, Ar); 7.13 (d, J = 8.6 Hz, 2H, Ar); 6.07 (t, J = 5.4 Hz, 1H, (C=O)N*H*-CH_2); 3.42 (br, 2H, C*H*$_2$-NH-CS); 3.06 (m, 2H, C*H*$_2$-NH-CO); 1.54-1.22 (m, 8H,CH_2); 0.88 (t, J = 7.3 Hz, 6H, CH_3). ^{13}C NMR (dmso-d_6, 101 MHz): 180.2 (C=S); 155.2 (C=O); 137.5 (*C*q$_{Ar}$-NH-CS); 132.0 (Cq$_{Ar}$-NHCO); 124.6 (CH_{Ar}); 117.7 (CH_{Ar}); 43.6 (C*H*$_2$-NH-CS); 38.6 (C*H*$_2$-NH-CO); 31.9 (*C*H_2-CH_2-N); 30.7 (*C*H_2-CH_2-N); 19.6 (*C*H_2-CH_3); 19.5 (*C*H_2-CH_3); 13.74 (CH_3); 13.68 (CH_3). MP: 179 °C. A schematic representation of the synthesis of **M(UT)** is shown in Scheme B.5.

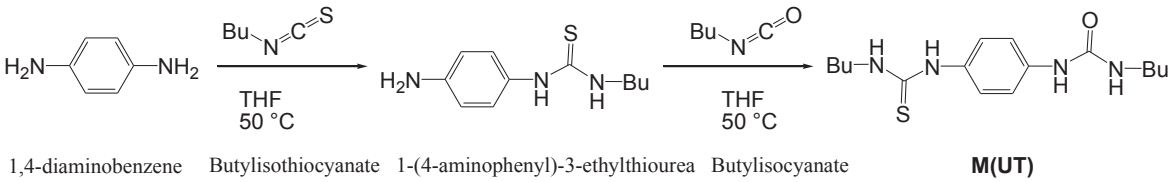

1,4-diaminobenzene Butylisothiocyanate 1-(4-aminophenyl)-3-ethylthiourea Butylisocyanate **M(UT)**

Scheme B.5. Schematic representation of the synthesis of **M(UT)**.

M(TT): to a solution of 1,4-isothiocyanatobenzene (0.48 g, 2.5 mmol) in DCM (30 mL) was added butylamine (0.59 mL, 9.7 mmol). The solution was kept under vigorous stirring for 18 h. A solid powder was formed that was collected by filtration and washed 3 times with pentane (3 × 10 mL) then dried under vacuum. **M(TT)** single crystals were grown from ACNT. ^{1}H NMR (dmso-d_6, 400 MHz): 9.39 (br, 2H, NH-Ar); 7.64 (br, 2H, N*H*-CH_2); 7.31 (s, 4H, Ar); 3.43 (br, 4H, CH_2-N); 1.52 (m, 4H, C*H*$_2$-CH_2-N); 1.31 (m, 4H, C*H*$_2$-CH_3); 0.89 (t, J = 7.3 Hz, 6H, CH_3). ^{13}C NMR (dmso-d_6, 101 MHz): 180.2 (C=S); 135.3 (Cq$_{Ar}$); 123.4 (CH_{Ar}); 43.5 (CH_2-N); 30.6 (*C*H_2-CH_2-N); 19.6 (*C*H_2-CH_3); 13.7 (CH_3). A schematic representation of the synthesis of **M(TT)** is shown in Scheme B.6.

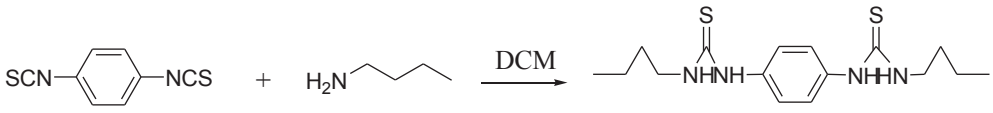

1,4-isothiocyanatobenzene butylamine **M(TT)**

Scheme B.6. Schematic representation of the synthesis of **M(TT)**.

The SEM images of organic model compounds **M(UU)**, **M(UT)** and **M(TT)**, depicted in Figure B.1 shows the presence of highly packed platelets of nanometer thickness and micrometer lateral dimensions reminds lamellar stacking of thin plates. Whereas the SEM

image of **M(UU)** exhibited regular size and well-defined packing thin plates, the SEM images of **M(UT)** and **M(T′T)** shows an assembly of thin plates with irregular size distribution.

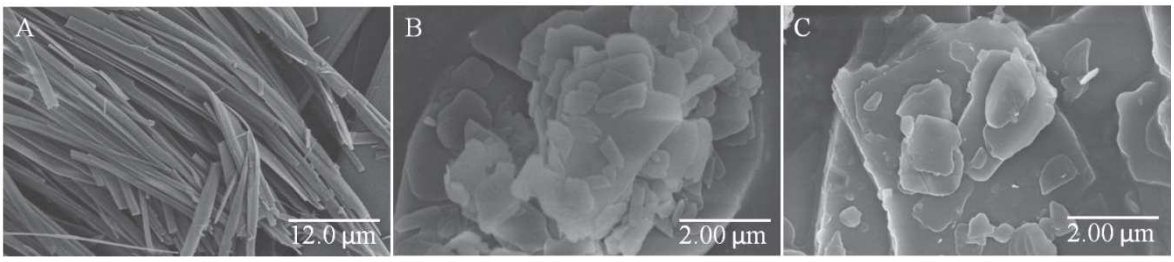

Figure B.1. SEM images of A) **M(UU)**, B) **M(T′T)** and C) **M(UT)**.

Local structure of organic model compounds

The local structure of organic model compounds was verified by ^{13}C CP/MAS NMR in order to check if the structure of the materials is as expected. The X-ray diffraction of organic model compound and hybrid materials are also represented.

The ^{13}C CP/MAS NMR spectra of organic model compounds **M(UU)**, **M(T′T)** and **M(UT)** are reproduced in Figure B.2 (Left), the corresponding assignment is indicated in schematic representation of the structure in Figure B.2 (Right). The presence of C=O or C=S groups is evidenced by the low field signal at ~ 158 ppm and ~ 179 ppm, respectively. The butyl group can be assigned by the presence of the carbons resonances at (14.8 ppm, 22.9 ppm, 32.1 ppm, 42.9 ppm) for **M(UU)**, (16.2 ppm, 23.9 ppm, 31.3 ppm, 49.2 ppm) for **M(T′T)**) and (14.6 ppm, 15.4 ppm, 20.2 ppm, 21.2 ppm, 32.7 ppm, 33.8 ppm, 38.5 ppm, 42.3 ppm) for **M(UT)**. The carbon resonance (C and CH) from the phenyl group was identified at (132.8 ppm and 123.7 ppm) for **M(UU)** and **M(T′T)**, and 117.3 ppm, 119.6 ppm, 126.0 ppm, 128.2 ppm, 132.8 ppm and 135.1 ppm for **M(UT)**.

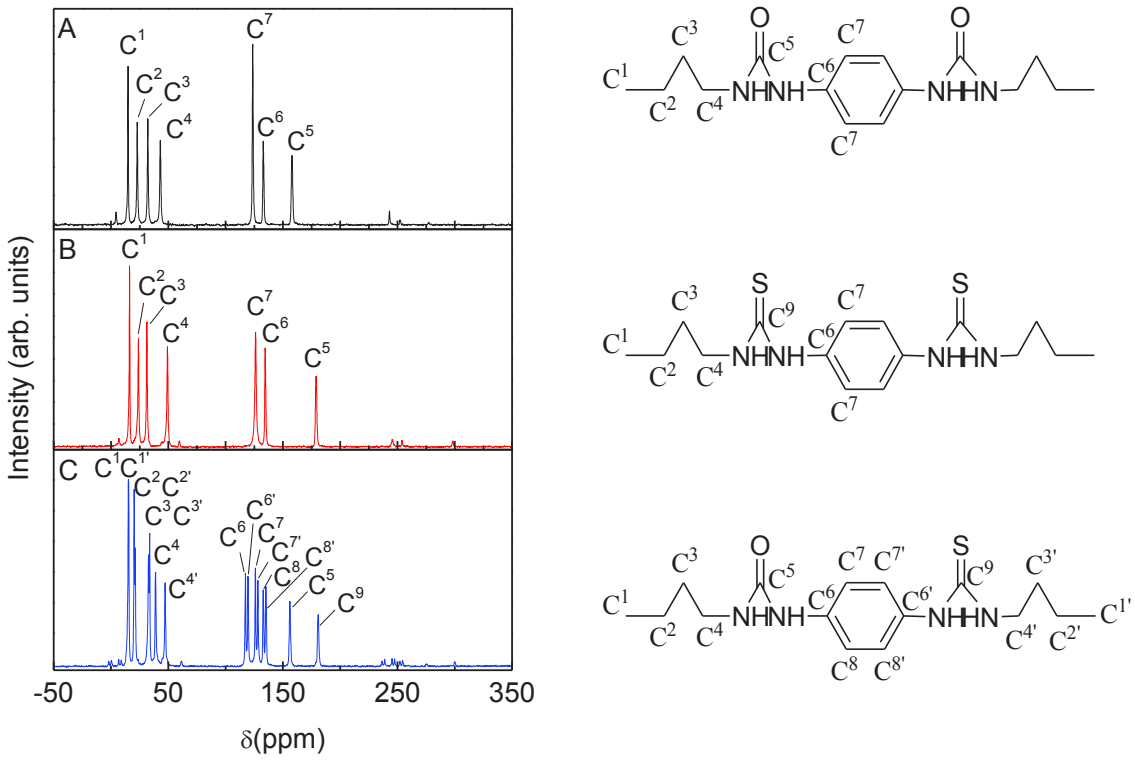

Figure B.2. (Left) ^{13}C CP/MAS NMR spectra of A) **M(UU)**, B) **M(TT)** and **M(UT)** and (Right) Schematic representation of the structure of organic model compounds and correspondent assignment of the ^{13}C CP/MAS NMR.

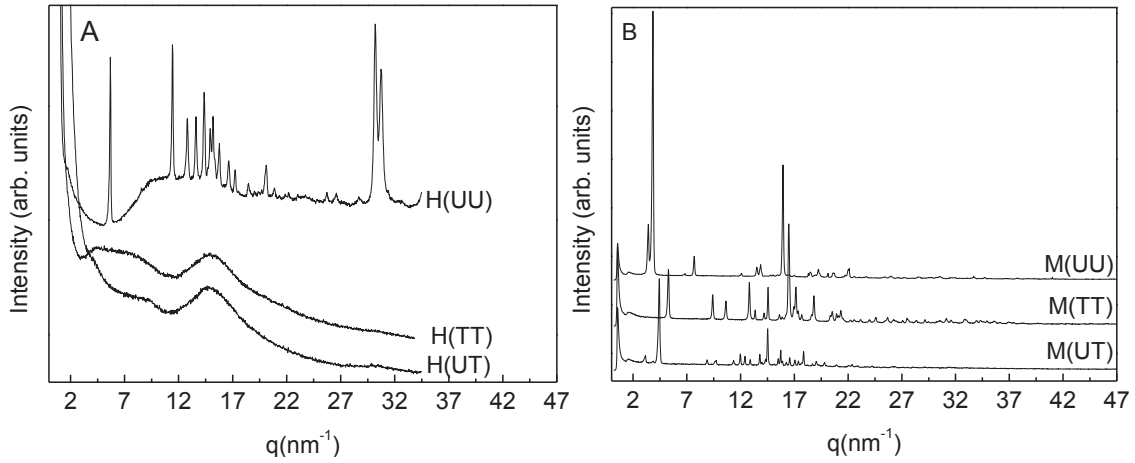

Figure B. 3. X-ray diffraction pattern of A) hybrids and B) organic model compounds.

Concerning the structure of **M(UT)** single crystal, Figure B. 4 shows the arrangement of **M(UT)** that crystallize in the orthorhombic *Pbca* space group, Table B. 1.

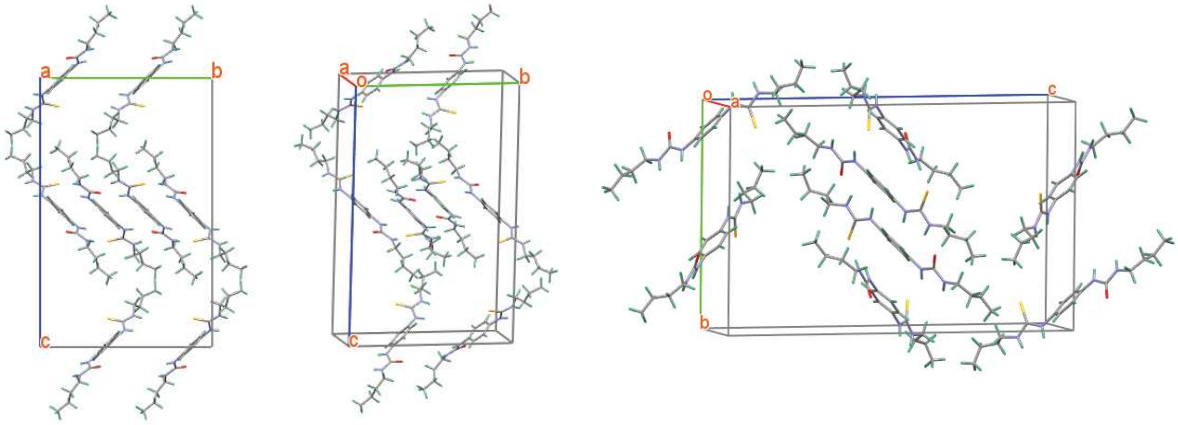

Figure B. 4. Crystal cell of **M(UT)** relaxed from simulation.

Table B. 1. Crystal data and structure refinement of **M(UT)**.

Chemical formula	$C_{16}H_{26}N_4OS$
Formula mass	322.47
Melting point (°C)	179 MPL
Crystal system	Orthorhombic
Space group	*P*bca
T (K)	120
a (Å)	7.11172(11)
b (Å)	17.6688(3)
c (Å)	27.6680(5)
V (Å^3)	3476.64(10)
Z/Z'	Z = 8
Reflns collected	92650
Indep reflns	3345
R_{int}	0.0654
Final R_1 values (I>2σ (I))	0.0761
Final wR (F^2) values (I>2σ (I))	0.2134
Goodness of fit on F^2	1.047

Figure B. 5 and Table B.2 show the structure and crystal cell parameters, respectively of **M(TT)** that crystallize in the monoclinic $P2_1/c$ space group.

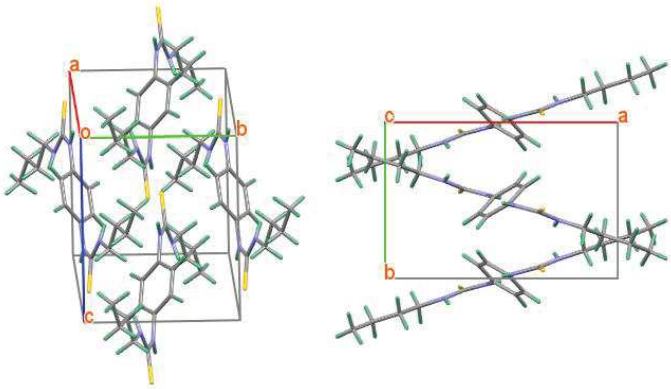

Figure B. 5. Crystal cell of **M(TT)** relaxed from simulation.

Table B.2. Crystal data and structure refinement of **M(TT)**.

Chemical formula	$C_{32}H_{52}N_8S_4$
Formula mass	677.06
Crystal system	monoclinic
Space group	$P2_1/c$
T (K)	120
a (Å)	12.5229 (2)
b (Å)	7.88321(15)
c (Å)	9.35299(16)
V (Å^3)	868.782
Z/Z'	Z = 2
Reflns collected	79293
Indep reflns	3702
R_{int}	0.0594
Final R_1 values (I>2σ (I))	0.0498
Final wR (F^2) values (I>2σ (I))	0.1053
Goodness of fit on F^2	1.314

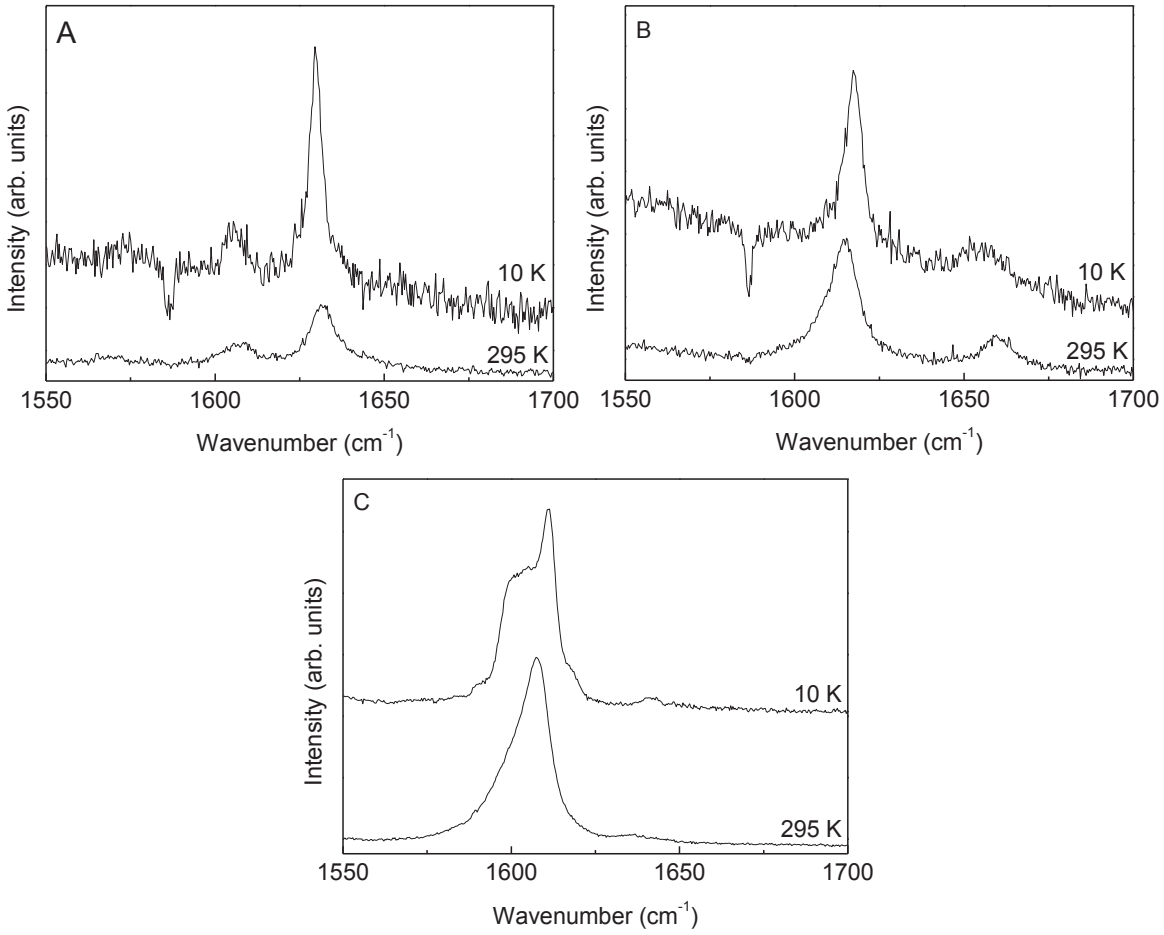

Figure B. 6. Raman spectra in "Amide I", "Amide II" regions at 10 K and 295 K of A) **M(UU)**, B) **M(UT)** and C) **M(TT)**.

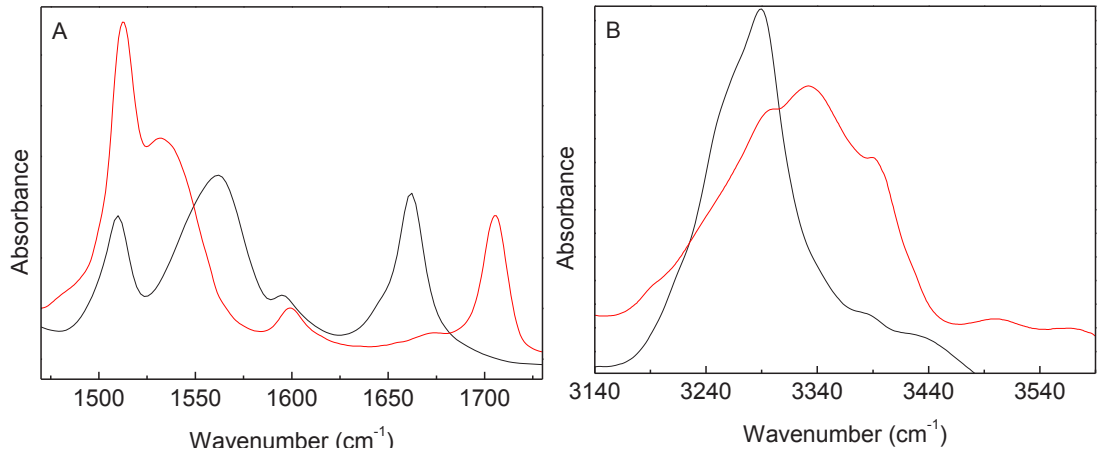

Figure B. 7. FTIR spectra in A) "Amide I" and "Amide/Thioamide II" regions and B) "Amide/Thioamide A" region of (black line) **M(UT)** in bulk and (red line) **M(UT)** in THF.

Appendix C

Resumé en Français

Dans la cadre de la recherche de solutions durables dans les domaines de l'éclairage et du photovoltaïque, ce travail de thèse est centré sur la synthèse, la caractérisation structurale et l'étude des propriétés de luminescence de matériaux hybrides organiques-inorganiques. Ces matériaux combinent les propriétés respectives des sous-unités organiques et inorganiques. Les sous-structures organiques sont choisies pour les fonctionnalités qu'elles apportent au matériau. Des propriétés telles qu'un comportement hydrophile ou hydrophobe, la stabilité chimique, la biocompatibilité ou des propriétés optiques peuvent diriger ce choix. Par contraste, la partie inorganique permet une meilleure mise en forme du matériau en apportant stabilité mécanique et thermique.

Dans les matériaux hybrides l'interaction entre la partie organique et la partie inorganique peut être assurée par des liaisons faibles types van der Waals (Classe I) ou par des liaisons fortes comme les liaisons covalentes (Classe II). Les matériaux que nous étudions dans le cadre de ce travail sont de Classe II et sont générés par synthèse sol-gel à partir d'un précurseur hybride.

Le procédé sol-gel qui se déroule à température peu élevée est compatible avec l'incorporation de sous-structures organiques, avantage considérable pour l'élaboration de matériaux hybrides. Ce procédé repose principalement sur deux réactions distinctes: l'hydrolyse et la condensation. Dans la réaction d'hydrolyse, les groupements hydroxyles (OH) remplacent les groupes alcoxyles (OR). Selon le type de catalyseur et la proportion d'eau ajoutée, l'hydrolyse peut être complète (tous les groupes alcoxy sont remplacés par des hydroxy) ou incomplète. Dans la réaction de condensation, des molécules partiellement

hydrolysées ($(RO)_3Si$-OH) réagissent pour former un lien Si-O-Si en produisant de l'eau ou de l'alcool. Suite à ce processus, un groupement ($(RO)_3Si$-OX, X=H, R ou Si) peut présenter plusieurs degrés de polymérisation de 1 à 3. L'hydrolyse et la condensation peuvent être obtenues en conditions acides ou basiques, en fonction du pH de la réaction et de la nature des catalyseurs, la structure et la morphologie du matériau résultant seront différentes. En particulier, la nano-structuration et le contrôle de la morphologie à travers les conditions de synthèse de ces matériaux ont fait l'objet de nombreux travaux pendant ces dernières décennies. Deux voies principales ont été explorées pour obtenir pour parvenir à la nanostructuration de ces matériaux :

i) des méthodes passant par l'intervention d'un surfactant;

ii) de l'auto-organisation à travers l'incorporation de groupements favorisant l'auto-assemblage de sous-structures organiques.

Dans le premier cas (i) l'utilisation de surfactants permet la formation mésostructures [262-265] dont la morphologie macroscopique peut être contrôlée [266,267]. Dans le cas de l'auto-organisation (ii), des groupements tels que de longues chaines alkyles [119] des groupements urées [69,268] ou amides [54] et éventuellement des interactions de type "π-stacking" [186] peuvent favoriser l'auto-assemblage non covalent au cours de la réaction sol-gel.

Dans les matériaux présentés dans ce travail, l'auto-assemblage des sous-structures organiques est favorisé par la présence de groupements amide, urée…qui peuvent former des liaisons hydrogène intermoléculaires. Ces dernières années, des hybrides organiques-inorganiques silsesquioxane fonctionnalisés avec des groupements amines ou amides ainsi auto-assemblés ont été reportés comme stables et présentant de bonnes propriétés d'émission blanche sans qu'il soit nécessaire d'y incorporer des centres optiquement actifs. Des matériaux basés sur le APTES et l'acide acétique avec des émissions dans les régions spectrales bleues et jaunes présentent des rendements ϕ intéressants, 0.21 and 0.12, respectivement. La combinaison avec l'acide formique a permis d'obtenir des rendements d'émission blanche encore supérieurs (ϕ=0.35±0.10), Green *et al.* [106]. On reporte aussi de très bons rendements obtenus pour des matériaux di-ureasil, di-urethanesils et di-amidosil [68,98,107,113,115-117]. L'origine de l'émission dans ces matériaux résulte d'une convolution entre l'émission des groupements C=O/NH de l'urée, uréthane ou amide et l'émission associée aux recombinaisons électrons-trous dans les nanodomaines silylés.

Dans la lignée de ces travaux, nous cherchons d'une part à développer de nouveaux matériaux avec des rendements de luminescence blanche significatifs. D'autre part, un travail plus fondamental est mené, visant à comprendre les mécanismes qui sont à l'origine des propriétés d'émission et comment ces propriétés d'émission peuvent être modulées via la relation structure propriétés. Ainsi nous nous intéressons aux mécanismes gouvernant la structuration de tels matériaux en explorant d'une part l'influence de la modulation de liaison hydrogène (Chapitre 4), d'autre part l'impact des conditions de synthèse sur le degré de condensation de la partie silylée (Chapitre 5).

Enfin, la complexation de matériaux hybrides organiques-inorganiques avec des lanthanides dans l'optique de générer des matériaux d'émission monochromatique suffisante pour des applications de type concentrateur solaire sera présentée dans le Chapitre 6.

Ainsi, dans le cadre de cette thèse, trois familles distinctes de matériaux sont synthétisées, basées sur six précurseurs pouvant s'auto-assembler à travers des liaisons hydrogène et dont les parties silylées peuvent être poly-condensées lors de la réaction sol-gel. Ces précurseurs diffèrent par leur sous-structure organique *i.e.* i) structure linéaire où la partie organique est basée sur le groupement malonamide (**P2-m** et **P4-m**), ii) structure linéaire dans laquelle un aromatique sépare deux groupements amide et/ou thioamide (**P(UU)**, **P(UT)** and **P(TT)**) et iii) structure à trois embranchements dont la partie organique est basée sur des groupements amides (**t-UPTES(5000)**). Les précurseurs sont schématiquement représentés sur la Figure C. 1.

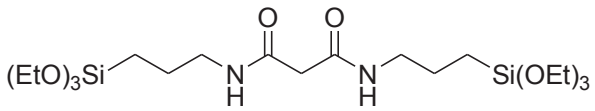

P2-m

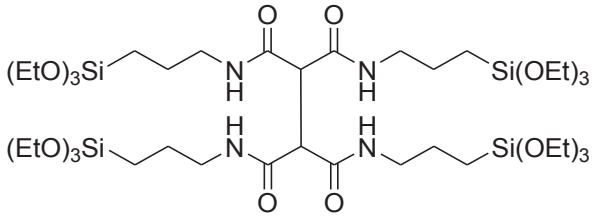

P4-m

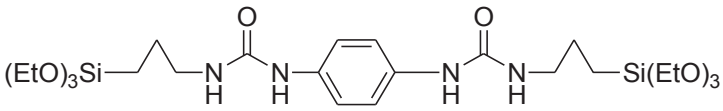

P(UU)

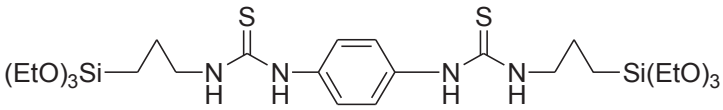

P(TT)

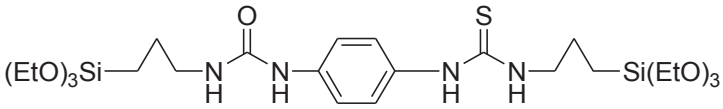

P(UT)

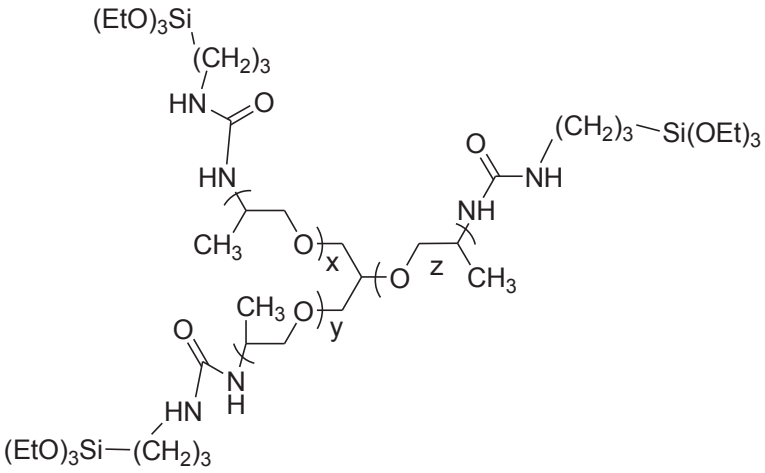

t-UPTES (5000), (x+y+z)~85

Figure C. 1. Structure moléculaire de précurseurs pour les matériaux hybrides synthétisés.

La première phase de ce travail concerne les deux hybrides organiques inorganiques (**M2-m** et **M4-m**) résultant de l'hydrolyse condensation des précurseurs **P2-m** et **P4-m** synthétisés en l'absence de lanthanides. Ces systèmes présentent une géométrie linéaire basée sur le groupement malonamide (NH-C=O-CH_2-C=O-NH) relié a à la sous-structure silylée par un groupement propylène. Tandis qu'un seul groupe malonamide est présent dans le composé nommé malonamide BS (**M2-m**), dans le composé di-malonamide BS (**M4-m**) on trouve deux groupements malonamides. La présence d'un seul ou de deux groupements malonamides entraine des différences de morphologie, de structure locale et de propriétés optiques pour les matériaux hybrides résultants. L'hybride **M2-m** a pu être obtenu sous forme d'un film autosupporté démontrant un degré de condensation très élevé (91 %) et un rendement quantique maximum ϕ de 0.22±0.02 sous une excitation à 360 nm. En ce qui concerne le matériau **M4-m,** obtenu sous forme de poudre blanche, un degré de condensation de 80 % est mesuré, il présente un rendement quantique inférieur **(**ϕ =0.10±0.01) pour une excitation à 360 nm également.

Le deuxième système étudié dans cette thèse est basé sur une sous-structure organique comportant un cycle aromatique séparant des groupements amides et/ou thioamides favorisant l'auto-assemblage par liaison hydrogène. L'objectif de ce travail étant 1) de suivre la modulation de la liaison hydrogène induite par la substitution de groupements urées par des groupements thio-urées, 2) de comprendre l'impact de cette modulation sur la structure locale des hybrides résultants et 3) de mesurer l'impact de cette substitution en relation avec la structure locale sur les propriétés optiques des hybrides. Les matériaux hybrides amorphes (**H(UU)**, **H(UT)** and **H(TT)**) où (**U**) représente un groupement urée et (**T**) un groupement thio-urée sont synthétisés par hydrolyse et condensation à partir des précurseurs hybrides de sous-structures organiques correspondantes (**P(UU)**, **P(UT)** and **P(TT)**). Dans un premier temps, des composés organiques modélisant la sous-structure organique sont étudiés en couplant l'étude structural de monocristaux, des simulations DFT et des mesures par spectroscopie infrarouge. La formation de différents types de liaisons hydrogène urée/urée bifurquées, urée/thio-urée bifurquées, thio-urée/thio-urée linéaires et cycliques est mise en évidence, accompagnée ou entrainant une structuration très différente dans les 3 modèles (**M(UU)**, **M(UT)** et **M(TT)**). La modulation de la force de ces liaisons H est mise en relation avec les différentes signatures spectroscopiques des vibrations amides. Dans un second temps,

les mesures de spectroscopie vibrationnelle dans les régions des vibrations amides sur les composés hybrides, parfois amorphes, en lien avec le travail effectué sur les modèles correspondants permet de mettre en évidence si le processus d'auto-assemblage pendant la réaction sol-gel est similaire ou différent de celui du modèle, selon qu'il s'agit de liaisons impliquant des groupements urées ou thio-urées.

Pour le système **UU** dont la structure locale repose sur des liaisons hydrogène bifurquées entre groupements urées, la transcription de la structure locale entre le modèle **M(UU)** et l'hybride **H(UU)**.est proposée sur la base des résultats de spectroscopie IR. Tandis que le modèle organique **M(UT)** présente deux types de liaisons bifurquées urée/thiourée, la transcription de la structure locale du modèle à l'hybride **H(UT)** semble être partielle et limitée à la liaison bifurquée urée/thiourée reliant deux molécules pour former un dimère. Cette population de liaisons hydrogène disperses mais plutôt fortement engagées est accompagnée par une deuxième population de liaisons faiblement engagées, et la structure macroscopique de l'hybride est amorphe. Les deux liaisons hydrogène fortes cyclique (***CB***) et linéaire (***LB***) identifiées dans le modèle **M(TT)** ne semblent pas être directement retrouvées dans l'hybride **H(TT)** présentant une grande dispersion de liaisons hydrogènes modérées et une structure amorphe. Ainsi, l'auto-assemblage par liaison hydrogène au cours du processus sol-gel n'est pas gouverné seulement par la capacité des sous-structures à former des liaisons fortes. La conformation potentielle des liaisons, des molécules et du groupement silylé condensé semblent également jouer un rôle important dans la structure issue du processus sol-gel.

Les propriétés optiques des matériaux sont ensuite analysés à la lumière des différents types de liaisons hydrogène (urée/urée, urée/thio-urée et thio-urée/thio-urée). Nous montrons que la substitution de l'urée par la thio-urée dans entraine un déplacement de l'émission de l' UV pour le système **UU** vers le bleu pour les systèmes **UT** et **TT**. En dépit d'un rendement quantique faible, les matériaux contenant des groupements thio-urées offrent des environnements nouveaux qui pourraient être propices à l'incorporation de centres émetteurs actifs.

Par ailleurs, l'étude des matériaux modèles et hybrides par spectroscopie infrarouge à haute pression montre qu'une modulation de la force de liaison hydrogène peut également être obtenue sous pression. Pour tous les matériaux, un renforcement de la liaison hydrogène en plusieurs étapes, dépendant du type de liaison (urée/urée, urée/thio-urée ou thio-urée/thio-

urée), est observé quand la pression augmente. Une prochaine étape de ce travail serait d'étudier l'impact de cette modulation sur les propriétés optiques par des mesures de photoluminescence sous pression.

Un troisième système hybride synthétisé selon différentes stratégies à partir de précurseurs **t-UPTES(5000)** est étudié. Il s'agit de molécules silylées à trois branches inter-reliées par les ponts urée/urée qui sont obtenus pour une large gamme de concentrations en HCl et pour des teneurs en eau variables, à la fois sous conditions atmosphériques et sous atmosphère contrôlée. Les hybrides résultants se présentent sous la forme de monolithes transparents. La structure locale de ces hybrides est caractérisée par diffraction X, RMN du ^{29}Si et du ^{13}C et par spectroscopie vibrationnelle. La diffraction X montre que tous ces hybrides sont amorphes. La RMN confirme l'existence de liaisons covalentes entre la partie organique et inorganique et démontre également le fort degré de condensation (entre 91 % et 98 %).

L'étude de la photoluminescence démontre que tous les hybrides présentent des émissions UV et bleues à température ambiante. Les hybrides préparés en boite à gants montrent un accroissement de l'absorption UV/bleue/verte dans la région (350–500 nm) due à une multiplication par trois du coefficient d'absorption, par rapport aux valeurs mesurées pour les hybrides préparés sous conditions ambiantes. Afin de quantifier les propriétés d'émission des matériaux tri-ureasils, les rendements quantiques ϕ sont mesurés. La variation de la concentration en HCl et en eau permet de trouver une augmentation de la valeur ϕ à 0.13 ± 0.01 pour [HCl] entre 0.01 M et 0.1 M. Pour ces valeurs de concentrations [HCl] optimisées, la synthèse a été reproduite sous atmosphère contrôlée ($[O_2]<0.5$ ppm, $[H_2O]=350$ ppm) en boite à gants. Les valeurs maximales de ϕ présentent une amélioration significative d'un facteur deux jusqu'à 0.27 ± 0.03. L'explication de ce phénomène reste encore une question ouverte, cependant la RMN MAS du ^{29}Si a démontré un degré de condensation exceptionnel de (97%) pour ces hybrides préparés sous atmosphère contrôlée comparés à ceux qui sont obtenus en conditions atmosphériques (0.84–0.91%). Ces forts rendements quantiques mettent en évidence l'intérêt de synthèses sol-gel en atmosphère contrôlée dans le développement de matériaux hybrides organiques-inorganiques, débouchant sur une amélioration de leurs performances optiques.

L'amélioration des propriétés optiques des matériaux passe par la compréhension des mécanismes physico-chimiques responsables de l'émission blanche des silsesquioxanes pontés

présentés ici. Ces dernières années, l'origine de l'émission dans les hybrides organiques inorganiques silylés fonctionnalisés par des groupements urées a fait l'objet de plusieurs études [65,68,102,107,114,115,128]. Dans nos précédentes études l'émission dans les hybrides basés sur des amides a été associée à des défauts. Ces défauts sont générés par la rupture de liaisons hydrogène intermoléculaires urée/urée (N-H•••O=C). Dans le cas des cristaux d'urée, on reporte que sous irradiation, un transfert de proton est induit engendrant la création de deux défauts de charges opposées, NH^{2+} and N^{-}. Ces deux défauts peuvent agir comme pièges pour les électrons et les trous qui peuvent se recombiner de façon radiative et ainsi générer une émission [68,107,128]. Ces mécanismes peuvent être généralisés à d'autres hybrides fonctionnalisés par des amines et basés sur les APTES [68,106,117]. Concernant l'émission bleue violette, les études par RPE ont permis de détecter la présence de défauts intrinsèques à l'oxygène, provenant de liaisons non saturées dans le réseau silylé [107]. Tandis qu'il est difficile d'établir de façon non ambiguë la structure des défauts impliqués, les données de RPE convergent vers la présence de radicaux peroxy bien connus dans SiO_2, où le silicium est en coordinence avec un carbone et deux atomes d'oxygène $^{\bullet}$O-O-Si≡(CO_2) [107].

Afin d'appréhender les mécanismes de recombinaison responsables de l'émission dans les matériaux multi-branches (**t-U(5000)**), les propriétés optiques de ces composés organiques-inorganiques, celles d'un modèle inorganique et celles d'un modèle organique la jeffamine5000® ont été étudiées. Cette comparaison permet de démontrer que l'émission des hybrides et du modèle inorganique excités à 325nm est induite par des paires donneurs/accepteurs plutôt que par des transitions de type excitoniques.

Enfin dans la dernière partie de cette thèse, nous nous intéressons cette fois à des matériaux hybrides organiques-inorganiques présentant des propriétés d'émission monochromatique. Pour cela les ions lanthanides trivalents (Ln^{3+}) ont été incorporés dans des hybrides organiques inorganiques malonamides étudiés précédemment. Les ions Ln^{3+} sont utilisés de manière extensive dans les matériaux luminescents en raison de leurs propriétés d'émission caractéristiques reliées aux niveaux d'énergies électroniques 4*f*. Ces propriétés sont la photostabilité, des temps de vie élevés ($>10^{-4}$ s), des déplacements Stokes importants selon les ligands (>200 nm), des raies d' émission de largeur de bande étroite (largeur à mi-hauteur ~ 1×10^{7} cm^{-1}) allant du domaine spectral UV au proche infra-rouge, des valeurs de rendement quantiques ϕ qui peuvent être élevées (jusqu'à 90 %) selon le ligand [211-213]. En effet, les ions Ln^{3+} ions peuvent être complexés par une grande variété de molécules, qui absorbent la

lumière et transfèrent efficacement cette énergie à l'ion métallique. La formation de complexes Ln^{3+} par certains ligands organiques peut être doublement profitable car elle empêche les couplages vibrationnels et augmente la section efficace d'absorption. Cependant, ces complexes Ln^{3+}–ligands organiques présentent une faible stabilité thermique et photochimique, qui, ajouté à la photodégradation sous irradiation UV sont des désavantages pour les applications technologiques [163,221].

Afin de remédier à ces inconvénients, il est proposé est d'introduire les ions Ln^{3+} dans une matrice stable et rigide, comme des matériaux hybrides silylés, qui présentent de surcroit des propriétés mécaniques intéressantes. Dans ce contexte, les matériaux hybrides organiques inorganiques contenant des ions Ln^{3+} deviennent de bons candidats pour la photonique combinant les propriétés physiques de la partie inorganique, les propriétés de ligand de la partie organique et les propriétés d'émission du Ln^{3+}[54,75,211,212,214,222,223]. Ils ont la capacité d'incorporer et de complexer de fortes charges en Ln^{3+} (jusqu'à 11.2 masse%) [60]. Ils peuvent être facilement mis en forme comme films minces homogènes et transparents [60,130,226-231]. De tels films sont prometteurs pour élaborer des revêtements luminescents actifs, dont l'utilisation dans le domaine des concentrateurs solaires a récemment été mise en avant [60,130].

Ainsi, dans le cadre de ce dernier chapitre, des ions lanthanides ont été incorporés dans les malonamides présentés plus haut, choisis pour leur structure simple et leurs rendements quantiques ϕ intéressants. Les précurseurs malonamide (**P2-m**) and di-malonamide (**P4-m**) ont été modifiés par l'incorporation de $EuCl_3 \cdot 6H_2$ (**M4-m-1)** dans un premier temps et de $Eu(tta)_3(H_2O)_2$ (**M4-m2- et 3)** dans un second temps. Leurs propriétés optiques ont été étudiées par absorption UV et spectroscopie de photoluminescence. Compte tenu des rendements quantiques ϕ élevés mesurés pour ces matériaux, ils ont été testés pour des applications de type concentrateurs solaires. Ainsi des films minces ont été préparés par dépôt à la tournette selon les conditions de synthèses appliquées pour la préparation de **M4-m-2.** Les paramètres tels que la concentration en précurseur **P4-m**, le temps de vieillissement de la solution à déposer, les conditions de dépôt et le type de solvant ont été explorés afin d'optimiser les propriétés optiques des films. Les performances des concentrateurs solaires sont évaluées à travers la quantification du facteur $\eta_{opt.}$ Nous démontrons alors qu'il est possible de produire des films avec un rendement quantique maximum ϕ de 0.60±0.06 pour

une excitation à 345 nm et un facteur η_{opt} de12.3 % dans la région d'absorption de la couche active (300-380 nm).

En conclusion, nous avons montré que pour les hybrides de types malonamides, la présence d'un ou deux groupes malonamides impacte la structures et le rendement quantique (maximum 0.22 pour **M2-m**). Pour les matériaux urée/thio-urée, nous avons démontré qu'une modulation de la liaison hydrogène était possible, qu'elle impactait fortement les propriétés d'auto-assemblage des sous-structure organiques dans le cas des modèles et que pour les hybrides l'incorporation d'un ou deux groupements thio-urées donnait lieu à une grande dispersion de forces de liaisons hydrogène et une structure désordonnée à grande distance. Les résultats de photoluminescence donnent des rendements quantiques faibles (0.01 à 0.03) lorsque la thio-urée est incorporée, cependant la modulation du domaine d'émission ainsi que les nouveaux environnements structuraux obtenus méritent d'être considérés pour l'incorporation de centres optiques actifs. Les matériaux multibranches (**t-U(5000)**) présentent des rendements quantiques beaucoup plus élevés, nous montrons que ces rendements peuvent être optimisés par les conditions de synthèse et plus particulièrement la synthèse en environnement contrôlé permet de doubler le rendement jusqu'à une valeur de 0.27. Nous démontrons également que les propriétés de luminescence de ces composés sont associées à des paires donneurs/accepteurs.

Enfin, nous montrons que l'incorporation de lanthanides et de complexes lanthanides/tta lors de la synthèse de composés types malonamide étudiés précédemment permet d'obtenir des rendements quantiques significatifs (0.60) d'émission monochromatique. Ces matériaux déposés sous forme de films minces présentent un intérêt pour des applications de type concentrateur solaire avec un facteur η de 12.3%.

Appendix D

List of publications that resulted from the work presented in this thesis

- **V.T. Freitas**, P.P. Lima, V. de Zea Bermudez, R.A.S. Ferreira, L.D. Carlos, "Boosting the Emission Quantum Yield of Urea Cross-Linked Tripodal Poly(oxypropylene)/Siloxane Hybrids Through the Variation of Catalyst Concentration", *Eur. J. Inorg. Chem*, 5390-5395, 2012.
- **V. T. Freitas**, P. P. Lima, E. Pecoraro, S. J. L. Ribeiro, V. de Zea Bermudez, L. D. Carlos, R. A. S. Ferreira, "Role of the reactive atmosphere during the sol–gel synthesis on the enhancing of the emission quantum yield of urea cross-linked tripodal siloxane-based hybrids", *J. Sol-Gel Sci. Technol.*, 70, 227-235, 2014.
- **V. T. Freitas**, R.A.S Ferreira, L.D. Carlos, "Organic–Inorganic Hybrids for Lighting", edited by G. Kickelbick, WILEY-VCH, Verlag GmbH, Weinheim, Germany, 2015.
- **V. T. Freitas**, L. Fu, A. M. Cojocariu, X. Cattoën, J. R. Bartlett, R. Le Parc, J.-L. Bantignies,M. Wong Chi Man, P. S. André, R. A. S. Ferreira, L. D. Carlos, *"Eu^{3+}-Based Bridged Silsesquioxanes for Transparent Luminescent Solar Concentrators", ACS Appl. Mater. Interfaces*, 7, 8770 –8778, 2015.

- **V. T. Freitas**, A. M. Cojocariu, X. Cattoën, R. Le Parc, J.-L. Bantignies, Wong Chi Man, J. R. Bartlett, H. Wadepohl, R. A. S. Ferreira, L. D. Carlos, *"H–bonding in mixed urea-thiourea structures: investigations through crystallography, Infrared and Raman spectroscopies",* to be submitted.
- **V. T. Freitas**, A. M. Cojocariu, X. Cattoën, R. Le Parc, J.-L. Bantignies, M. Wong Chi Man, J. R. Bartlett, H. Wadepohl, R. A. S. Ferreira, L. D. Carlos, *"Spectroscopic studies of supramolecular organization via Self-Assembly through thiourea group."* to be submitted.
- **V. T. Freitas,** A. M. Cojocariu, R. Le Parc, J.-L. Bantignies, R. A. S. Ferreira, L. D. Carlos, J. R. Bartlett, I. Gautier-Luneau, H. Wadepohl, X. Cattoën, M. Wong Chi Man*,"Hydrogen bonding networks in phenylene-bridged bis(urea), bis(thiourea) and mixed urea-thiourea systems",* to be submitted.
- **V. T. Freitas**, L. Fu, A. M. Cojocariu, X. Cattoën, J. R. Bartlett, R. Le Parc, J.-L. Bantignies,M. Wong Chi Man, R. A. S. Ferreira, L. D. Carlos,*" Eu^{3+}-malonamide organosilicas for luminescent solar concentrators",* to be submitted.

8. References

[1] J. Q. Grim, L. Mannaab, I. Moreels, *Chem. Soc. Rev.*, 44, 5897, (2015).

[2] V. L. Kalyani, C. Charan, *JMEIT*, 1, 9, (2014).

[3] M. S. Lebby, *Electron. Lett.*, 45, 1007, (2009).

[4] B. Wessler, U. Tober, presented at the SPIE Eco-Photonics 2011, (2011).

[5] F. Quan, *J. Optics*, 14, 024001, (2012).

[6] R. A. S. Ferreira, C. D. S. Brites, C. M. S. Vicente, P. P. Lima, A. R. N. Bastos, P. G. Marques, M. Hiltunen, L. D. Carlos, P. S. André, *Laser Photonics Rev.*, 7, 1027, (2013).

[7] S. Reineke, M. Thomschke, B. Lussem, K. Leo, *Rev. Mod. Phys.*, 85, 1245, (2013).

[8] C. J. Humphreys, *MRS Bull.*, 33, 459, (2008).

[9] S. Pimputkar, J. S. Speck, S. P. DenBaars, S. Nakamura, *Nat. Photonics*, 3, 179, (2009).

[10] R. Haitz, J. Y. Tsao, *Phys. Status Solidi A*, 208, 17, (2011).

[11] M. M. Shang, C. X. Li, J. Lin, *Chem. Soc. Rev.*, 43, 1372, (2014).

[12] E. F. Schubert, J. K. Kim, *Science*, 308, 1274, (2005).

[13] C. Czeisler, *Nature*, 497, S13, (2013).

[14] F. Quan, *J. Optics*, 14, 024001, (2012).

[15] International energy agency, Light's labour's lost: Policies for energy-efficient lighting, (2006).

[16] Philips, Lighting the clean revolution, https://www.theclimategroup.org/sites/default/files/archive/files/LED_report_web1.pdf (2012)

[17] J. R. Brodrick, Energy Savings Forecast of Solid-State Lighting in General Illumination Applications, (2015).

[18] Green Photonics Market OIDA, http://www.oida.org/news/oida-news/2009/377 (2009)

[19] R. Le Toquin, A. K. Cheetham, *Chem. Phys. Lett.*, 423, 352, (2006).

[20] CREE, Cree breaks 300lm/W efficacy barrier for white LEDs, http://www.semiconductor-today.com/news_items/2014/MAR/CREE_260314.shtml (2014)

[21] H. Wu, L. Ying, W. Yang, Y. Cao, *White-emitting polymers and devices*, Berlin, (2011).

[22] LUMEC, LEDs for outdoor lighting applications, http://www.lumec.com/

[23] Y. Narukawa, M. Ichikawa, D. Sanga, M. Sano, T. Mukai, *J. Phys. D Appl. Phys.*, 43, 354002, (2010).

[24] N. Holonyak, S. F. Bevacqua, *Appl. Phys. Lett.*, 1, 82, (1962).

[25] J. R. Sheats, H. Antoniadis, M. Hueschen, W. Leonard, J. Miller, R. Moon, D. Roitman, A. Stocking, *Science*, 273, 884, (1996).

[26] J. M. Shaw, P. F. Seidler, *IBM J. Res. Dev.*, 45, 3, (2001).

[27] S. Nakamura, M. Senoh, T. Mukai, *Jpn. J. Appl. Phys. 2*, 32, L8, (1993).

[28] N. Bardsley, S. Bland, L. Pattison, M. Pattison, K. Stober, F. Welsh, M. Yamada, Solid-state lighting research and development. Multi-year program plan, (2012).

[29] G. M. Farinola, R. Ragni, *Chem. Soc. Rev.*, 40, 3467, (2011).

[30] J. Kovac, L. Peternai, O. Lengyel, *Thin Solid Films*, 433, 22, (2003).

[31] Y. L. Chang, Z. H. Lu, *J. Disp. Technol.*, 9, 459, (2013).

[32] NEC Lighting, NEC Lighting developed the world's most efficient OLED device at 156 lm/W, http://www.oled-info.com/nec-lighting-developed-worlds-most-efficient-oled-device-156-lmw (2011)

[33] C. Tang, X. D. Liu, F. Liu, X. L. Wang, H. Xu, W. Huang, *Macromol. Chem. Phys.*, 214, 314, (2013).

[34] L. Li, J. J. Liang, S. Y. Chou, X. D. Zhu, X. F. Niu, Z. B. Yu, Q. B. Pei, *Sci. Rep.-UK*, 4, 4307, (2014).

[35] Solid-state lighting research and development. Multi-year program plan, (2013).

[36] S. Nakamura, G. Fasol, *The blue laser diode: GaN based light emitters and lasers* Berlin, (1996).

[37] R. Mueller-Mach, G. Mueller, M. R. Krames, H. A. Hoppe, F. Stadler, W. Schnick, T. Juestel, P. Schmidt, *Phys. Status Solidi A*, 202, 1727, (2005).

[38] T. Taguchi, *LED materials and devices*, Chichester, (2008).

[39] J. Silver, R. Withnall, *Color conversion phosphors for LEDs* Chichester, (2008).

[40] N. C. George, K. A. Denault, R. Seshadri, *Annu. Rev. Mater. Res.*, 43, 481, (2013).

[41] H. Daicho, T. Iwasaki, K. Enomoto, Y. Sasaki, Y. Maeno, Y. Shinomiya, S. Aoyagi, E. Nishibori, M. Sakata, H. Sawa, S. Matsuishi, H. Hosono, *Nat. Commun.*, 3, 1132, (2012).

[42] Y. Kajiwara, A. Nagai, K. Tanaka, Y. Chujo, *J. Mater. Chem. C*, 1, 4437, (2013).

[43] S. Y. Kwak, S. Yang, N. R. Kim, J. H. Kim, B. S. Bae, *Adv. Mater.*, 23, 5767, (2011).

[44] E. R. Dohner, E. T. Hoke, H. I. Karunadasa, *J. Am. Chem. Soc.*, 136, 1718, (2014).

[45] J. D. Furman, A. Y. Warner, S. J. Teat, A. A. Mikhailovsky, A. K. Cheetham, *Chem. Mater.*, 22, 2255, (2010).

[46] P. F. Gu, Y. Zhang, Y. Feng, T. Q. Zhang, H. R. Chu, T. Cui, Y. D. Wang, J. Zhao, W. W. Yu, *Nanoscale*, 5, 10481, (2013).

[47] K. Binnemans, P. T. Jones, B. Blanpain, T. Van Gerven, Y. X. Yang, A. Walton, M. Buchert, *J. Clean. Prod.*, 51, 1, (2013).

[48] S. V. Eliseeva, J. C. G. Bunzli, *New J. Chem.*, 35, 1165, (2011).

[49] D. Kang, H. S. Yoo, S. H. Jung, H. Kim, D. Y. Jeon, *J. Phys. Chem. C*, 115, 24334, (2011).

[50] M. Zeuner, S. Pagano, W. Schnick, *Angew. Chem. Int. Edit.*, 50, 7754, (2011).

[51] P. F. Smet, I. Moreels, Z. Hens, D. Poelman, *Materials*, 3, 2834, (2010).

[52] T. W. Kuo, W. R. Liu, T. M. Chen, *Opt. Express*, 18, 1888, (2010).

[53] B. Z. Wang, X. P. Zhang, H. M. Liu, *AIP Adv.*, 3, 052125, (2013).

[54] L. D. Carlos, R. A. S. Ferreira, V. de Zea Bermudez, S. J. L. Ribeiro, *Adv. Mater.*, 21, 509, (2009).

[55] L. Nicole, L. Rozes, C. Sanchez, *Adv. Mater.*, 22, 3208, (2010).

[56] L. D. Carlos, R. A. S. Ferreira, V. de Zea Bermudez, *Organic–Inorganic Hybrids for Light-Emitting Devices and Integrated Optics*, New York, (2009).

[57] K. J. Shea, D. A. Loy, O.W. Webster, *Chem. Mater.*, 6, 572, (1989).

[58] R. J. P. Corriu, D. Leclercq, *Angew. Chem., Int. Ed.*, 35, 1420, (1996).

[59] L.-C Hu, K. J. Shea, *Chem. Soc. Rev.*, 40, 688, (2011).

[60] J. Graffion, X. Cattoën, M. Wong Chi Man, V. R. Fernandes, P. S. André, R. A. S. Ferreira, L. D. Carlos, *Chem. Mater.*, 23, 4773, (2011).

[61] J. Graffion, X. Cattoën, V. T. Freitas, R. A. S. Ferreira, M. Wong Chi Man, L. D. Carlos, *J. Mater. Chem.*, 22, 671, (2012).

[62] L. S. Fu, R. A. S. Ferreira, S. S. Nobre, L. D. Carlos, J. Rocha, *Organically modified silica-based xerogels derived from 3-aminopropyltrimethoxysilane and 3-isocyanatepropyltriethoxysilane through carboxylic acid solvolysis*,(2006).

[63] M. Fernandes, S. S. Nobre, Q. Xu, C. Carcel, J. N. Cachia, X. Cattoën, J. M. Sousa, R. A. S. Ferreira, L. D. Carlos, C. V. Santilli, M. Wong Chi Man, V. de Zea Bermudez, 115, 10877, (2011).

[64] V. de Zea Bermudez, L. D. Carlos, M. C. Duarte, M. M. Silva, C. J. R. Silva, M. J. Smith, M. Assunção, L. Alcácer, *J. Alloy. Compd.*, 277, 21, (1998).

[65] S. C. Nunes, V. de Zea Bermudez, J. Cybinska, R. A. S. Ferreira, J. Legendziewicz, L. D. Carlos, M. M. Silva, M. J. Smith, D. Ostrovskii, J. Rocha, *J. Mater. Chem.*, 15, 3876, (2005).

[66] S. C. Nunes, V. de Zea Bermudez, J. Cybinska, R. A. S. Ferreira, L. D. Carlos, J. Legendziewicz, M. M. Silva, M. J. Smith, D. Ostrovskii, *J. Alloy. Comp.*, 451, (2008).

[67] S. C. Nunes, C. B. Ferreira, J. Hümmer, R. A. S. Ferreira, L. D. Carlos, P. Almeida, V. de Zea Bermudez, *J. Mater. Chem. C*, 1, 2290, (2013).

[68] L. S. Fu, R. A. S. Ferreira, N. J. O. Silva, L. D. Carlos, V. de Zea Bermudez, J. Rocha, *Chem. Mater.*, 16, 1507, (2004).

[69] J. J. E. Moreau, L. Vellutini, M. Wong Chi Man, C. Bied, P. Dieudonne, J. L. Bantignies, J. L. Sauvajol, *Chem. Eur. J.*, 11, 1527, (2005).

[70] C. Sanchez, F. Ribot, *New. J. Chem.*, 18, 1007, (1994).

[71] P. Gomez-Romero, C. Sanchez, *Functional Hybrid Materials*, Weinheim, (2004).

[72] C. Sanchez, B. Julián-López, P. Belleville, M. Popall, *J. Mater. Chem.*, 15, 3559, (2005).

[73] O. J. Dautel, G. Wantz, R. Almairac, D. Flot, L. Hirsch, J. P. Lere-Porte, J. P. Parneix, F. Serein-Spirau, L. Vignau, J. J. E. Moreau, *J. Am. Chem. Soc.*, 128, 4892, (2006).

[74] L. Wu, Q. Chen, Z. Lv, W. Sun, L. Chen, J. Wu, *J. Sol-Gel Sci. Technol.*, 60, 214, (2011).

[75] J. Feng, H. Zhang, *Chem. Soc. Rev.*, 42, 387, (2013).

[76] F. Dong, C.-S. Ha, *Macromol. Res.*, 20, 335, (2012).

[77] A. Dabrowski, M. Barczak, *Croat. Chem. Acta*, 80, 367, (2007).

[78] H. E. Romeo, M. A. Fanovich, R. J. J. Williams, L. Matejka, J. Plestil, J. Brus, *Macromol Chem Physic*, 208, 1202, (2007).

[79] H. S. Jung, Y. J. Kim, S. W. Ha, J. K. Lee, *J. Mater. Chem. C*, 1, 5879, (2013).

[80] Y. Kajiwara, A. Nagai, Y. Chujo, *J. Mater. Chem.*, 20, 2985, (2010).

[81] Y. Yang, M. Q. Wang, G. D. Qian, Z. Y. Wang, X. P. Fan, *Opt. Mater.*, 24, 621, (2004).

[82] J. S. Kim, S. C. Yang, S. Y. Kwak, Y. Choi, K. W. Paik, B. S. Bae, *J. Mater. Chem.*, 22, 7954, (2012).

[83] I. A. Lei, D. F. Lai, T. M. Don, W. C. Chen, Y. Y. Yu, W. Y. Chiu, *Mater. Chem. Phys.*, 144, 41, (2014).

[84] H. Kim, J. Y. Bae, Y. H. Kim, Y. B. Kim, B. S. Bae, *J. Appl. Polym. Sci.*, 131, 39968, (2014).

[85] X. Bai, G. Caputo, Z. Hao, V. T. Freitas, J. Zhang, R. A. S. Ferreira, N. Pinna, *Nature Comm.*, 5, 5702, (2014).

[86] D. B. Mitzi, K. Chondroudis, C. R. Kagan, *IBM J. Res. Dev.*, 45, 29, (2001).

[87] E. Fred Schubert, *Light-emitting diodes*, United States of America, (2003).

[88] H. Cho, S.-H. Jeong, M.-H. Park, Y.-H. Kim, C. Wolf, C.-L. Lee, J. H. Heo, A. Sadhanala, N. Myoung, S. Yoo, S. H Im, R. H. Friend, T.-W. Lee, *Science*, 350, 1222, (2015).

[89] C. W. Tang, S. A. Vanslyke, *Appl. Phys. Lett.*, 51, 913, (1987).

[90] R. Reisfeld, D. Shamrakov, C. Jorgensen, *Sol. Energ. Mat. Sol. C*, 33, 417, (1994).

[91] E. Pecoraro, S. Garcia-Revilla, R. A. S. Ferreira, R. Balda, L. D. Carlos, J. Fernandez, *Opt. Express*, 18, 7470, (2010).

[92] E. Carregal-Romero, A. Llobera, V. J. Cadarso, M. Darder, P. Aranda, C. Dominguez, E. Ruiz-Hitzky, C. Fernandez-Sanchez, *ACS Appl. Mater. Inter.*, 4, 5029, (2012).

[93] T. Dantas de Morais, F. Chaput, K. Lahlil, J. P. Boilot, *Adv. Mater.*, 11, 107, (1999).

[94] T. Dantas de Morais, F. Chaput, J. P. Boilot, K. Lahlil, B. Darracq, Y. Levy, *C.R.. Acad. Sci. IV-Phys.*, 1, 479, (2000).

[95] N. Mizoshita, Y. Goto, Y. Maegawa, T. Tani, S. Inagaki, *Chem. Mater.*, 22, 2548, (2010).

[96] D. P. Fasce, R. J. J. Williams, L. Matějka, J. Pleštil, J. Brus, B. Serrano, J. C. Cabanelas, J. Baselga, *Macromolecules*, 39, 3794, (2006).

[97] M. L. Gómez, D. P. Fasce, R. J. J. Williams, C. M. Previtali, L. Matějka, J. Pleštil, J. Brus, *Macromol. Chem. Phys.* , 209, 634, (2008).

[98] M. L. Gómez, D. P. Fasce, R. J. J. Williams, C. M. Previtali, H. A. Montejano, *Macromol. Mater. Eng.*, 295, 1042, (2010).

[99] M. L. Gómez, D. P. Fasce, R. J. J. Williams, H. A. Montejano, C. M. Previtali, *J. Polym. Sci. Pol. Phys.*, 46, 289, (2008).

[100] F. Olivero, F. Carniato, C. Bisio, L. Marchese, *J. Mater. Chem.*, 22, 25254, (2012).

[101] X. H. Yang, T. Giovenzana, B. Feild, G. E. Jabbour, A. Sellinger, *J. Mater. Chem.*, 22, 12689, (2012).

[102] S. S. Nobre, X. Cattoën, R. A. S. Ferreira, M. Wong Chi Man, L. D. Carlos, *Phys. Status Solidi-RRL*, 4, 55, (2010).

[103] K. V. Rao, K. K. R. Datta, M. Eswaramoorthy, S. J. George, *Adv. Mater.*, 25, 1713, (2013).

[104] D. R. Lin, L. J. Hu, H. You, R. J. J. Williams, *Eur. Polym. J.*, 47, 1526, (2011).

[105] K. V. Rao, A. Jain, S. J. George, *J. Mater. Chem. C*, 2, 3055, (2014).

[106] W. H. Green, K.P. Le, J. Grey, T. T. Au, M. J. Sailor, *Science*, 276, 1826, (1997).

[107] L. D. Carlos, R. A. S. Ferreira, R. N. Pereira, M. Assunção, V. de Zea Bermudez, *J. Phys. Chem. B*, 108, 14924, (2004).

[108] C. D. S. Brites, V. T. Freitas, R. A. S. Ferreira, A. Millan, F. Palacio, L. D. Carlos, *Langmuir*, 28, 8190, (2012).

[109] M. L. Gómez, I. E. Dell'Erba, C. A. Chesta, C. E. Hoppe, R. J. J. Williams, *J. Mater. Sci.*, 48, 8559, (2013).

[110] S. C. Nunes, N. J. O. Silva, J. Hümmer, R. A. S. Ferreira, P. Almeida, L. D. Carlos, V. de Zea Bermudez, *RSC Adv.*, 2, 2087, (2012).

[111] L. D. Carlos, V. de Zea Bermudez, V. S. Amaral, S. C. Nunes, N. J. O. Silva, R. A. S. Ferreira, J. Rocha, C. V. Santilli, D. Ostrovskii, *Adv. Mater.*, 19, 341, (2007).

[112] V. Bekiari, P. Lianos, *Langmuir*, 14, 3459, (1998).

[113] L. D. Carlos, V. de Zea Bermudez, R.A.S. Ferreira, L. Marques, M. Assunção, *Chem. Mater.*, 11, 581, (1999).

[114] R. A. S. Ferreira, L. D. Carlos, V. de Zea Bermudez, *Thin Solid Films*, 343, 476, (1999).

[115] L. D. Carlos, R. A. S. Ferreira, V. de Zea Bermudez, S. J. Ribeiro, *Adv. Funct. Mater.*, 11, 111, (2001).

[116] V. Bekiari, P. Lianos, U. L. Stangar, B. Orel, P. Judeinstein, *Chem. Mater.*, 12, 3095, (2000).

[117] T. Brankova, V. Bekiari, P. Lianos, *Chem. Mater.*, 15, 1855, (2003).

[118] M. C. Gonçalves, V. de Zea Bermudez, R. A. S. Ferreira, L. D. Carlos, D. Ostrovskii, J. Rocha, *Chem Mater*, 16, 2530, (2004).

[119] S. S. Nobre, X. Cattoën, R. A. S. Ferreira, C. Carcel, V. de Zea Bermudez, M. Wong Chi Man, L. D. Carlos, *Chem. Mater.*, 22, 3599, (2010).

[120] A. M. Jakob, T. A. Schmedake, *Chem. Mater.*, 18, 3173, (2006).

[121] L. Wang, M. C. Estevez, M. O'Donoghue, W. H. Tan, *Langmuir*, 24, 1635, (2008).

[122] D. Y. Kong, C. M. Zhang, Z. H. Xu, G. G. Li, Z. Y. Hou, J. Lin, *J. Colloid Interface Sci.*, 352, 278, (2010).

[123] V. V. Annenkov, E. N. Danilovtseva, V. A. Pal'shin, S. N. Zelinskiy, E. P. Chebykin, V. Yu Gak, R. Yu Shendrik, (2016).

[124] L. D. Carlos, Y. Messaddeq, H. F. Brito, R. A. S. Ferreira, V. de Zea Bermudez, S. J. L. Ribeiro, *Adv. Mater.*, 12, 594, (2000).

[125] V. Bekiari, P. Lianos, *Adv. Mater.*, 10, 1455, (1998).

[126] L. D. Carlos, R. A. S. Ferreira, I. Orion, V. de zea Bermudez, J. Rocha, *J. Lumin.*, 87-9, 702, (2000).

[127] P. P. Lima, S. S. Nobre, R. O. Freire, S. Alves Junior, R. A. S. Ferreira, U. Pischel, O. L. Malta, L. D. Carlos, *J. Phys. Chem. C*, 111, 17627, (2007).

[128] S. S. Nobre, P. P. Lima, L. Mafra, R. A. S. Ferreira, R. O. Freire, L. S. Fu, U. Pischel, V. de Zea Bermudez, O. L. Malta, L. D. Carlos, *J. Phys. Chem. C*, 111, 3275, (2007).

[129] L. S. Fu, R. A. S. Ferreira, M. Fernandes, S. C. Nunes, V. de Zea Bermudez, G. Hungerford, J. Rocha, L. D. Carlos, *Opt. Mater.*, 30, 1058, (2008).

[130] J. Graffion, A. M. Cojocariu, X. Cattoën, R. A. S. Ferreira, V. R. Fernandes, P. S. André, L. D. Carlos, M. Wong Chi Man, J. R. Bartlett, *J. Mater. Chem.*, 22, 13279, (2012).

[131] E. F. Molina, L. Marcal, H. W. P. de Carvalho, E. J. Nassar, K. J. Ciuffi, *Polym. Chem-UK*, 4, 5819, (2013).

[132] C. Sanchez, P. Belleville, M. Popall, L. Nicole, *Chem. Soc. Rev.*, 40, 696, (2011).

[133] L. Nicole, C. Laberty-Robert, L. Rozes, C. Sanchez, *Nanoscale*, 6, 6267, (2014).

[134] P. Judeinstein, C. Sanchez, *J. Mater. Chem.*, 6, (1996).

[135] C. Sanchez, B. Lebeau, *Mrs Bull*, 26, 377, (2001).

[136] C. Sanchez, B. Lebeau, F. Chaput, J. P. Boilot, *Adv. Mater.*, 15, 1969, (2003).

[137] C. Sanchez, H. Arribart, M. M. G. Guille, *Nat Mater*, 4, 277, (2005).

[138] C. Sanchez, D. E. Diab, V. Connord, P. Clerc, E. Meunier, B. Pipy, B. Payre, R. P. Tan, M. Gougeon, J. Carrey, V. Gigoux, D. Fourmy, *ACS Nano*, 8, 1350, (2014).

[139] C. J. Brinker, G. W. Scherrer, *Sol-Gel Science: The Physics and Chemistry of Sol-Gel Processing*, San Diego, (1990).

[140] L. D. Carlos, R. A. S. Ferreira, V. de Zea Bermudez, *Hybrid Materials for Optical Applications*, Weinheim, (2007).

[141] R. A. S. Ferreira, L. D. Carlos, V. de Zea Bermudez, *Luminescent Organic–Inorganic Nanohybrids*,(2004).

[142] D. Avnir, D. Levy, R. Reisfeld, *J. Phys. Chem.*, 88, 5956, (1984).

[143] A. E. Danks, S. R. Hall, Z. Schnepp, *Mater. Horiz.*, 3, 91, (2016).

[144] B. L. Cushing, V. L. Kolesnichenko, C. J. O'Connor, *Chem. Rev.*, 104, 3893, (2004).

[145] B. Boury, R.J.P. Corriu, *Chem. Commun.*, 8, 795, (2002).

[146] J. J. E. Moreau, L. Vellutini, P. Dieudonné, M. Wong Chi Man, J. L. Bantignies, J. L. Sauvajol, C. Bied, *J. Mater. Chem.*, 15, 4943, (2005).

[147] G. Férey, *Chem. Soc. Rev.*, 37, 191, (2008).

[148] G. Férey, C. Serre, T. Devic, G. Maurin, H. Jobic, P. L. Llewellyn, G. D. Weireld, A. Vimont, M. Daturi, J.-S. Chang, *Chem. Soc. Rev.*, 40, 550, (2011).

[149] J. Rocha, L. D. Carlos, F. A. Paz, D. Ananias, *Chem. Soc. Rev.*, 40, 926, (2011).

[150] A. C. McKinlay, R. E. Morris, P. Horcajada, G. Férey, R. Gref, P. Couvreur, C. Serre, *Angew. Chem. Int. Ed.*, 49, 6260, (2010).

[151] U. Schubert, *Chem. Soc. Rev.*, 40, 575, (2011).

[152] C. Sanchez, L. Rozes, F. Ribot, C. Laberty-Robert, D. Grosso, C. Sassoye, C. Boissiere, L. Nicole, *C. R. Chimie*, 13, 3, (2010).

[153] Lighting Research Cente, Light sources and color http://www.lrc.rpi.edu/programs/nlpip/lightinganswers/lightsources/appendixb.asp (2004)

[154] C. S. McCamy, *Correlated Color Temperature as an Explicit Function of Chromaticity Coordinates*, New York, (1992).

[155] J.-C. G. Bünzli, *Lanthanide Probes in Life, Chemical and Earth Sciences, Theory and Practice*, Amsterdam, (1989).

[156] J. Becquerel, *Phys. Z*, 8, 632, (1908).

[157] C. K. Jørgensen, *J. Iborg. Nuclear Chem.*, 1, (1955).

[158] O. L. Malta, L. D. Carlos, *Quim. Nova*, 26, 889, (2003).

[159] M. H. V. Werts, R. T. F. Jukesa, J. W. Verhoeven, *Phys. Chem. Chem. Phys*, 4, 1542, (2002).

[160] N. Sabbatini, M. Guardigli, J. M. Lehn, *Coordin. Chem. Rev.*, 123, 201, (1993).

[161] G. F. de Sá, O. L. Malta, C. de Mello Donegá, A. M. Simas, R. L. Longo, P. A. Santa-Cruz, E. F. da Silva, *Coord. Chem. Rev.*, 196, 165, (2000).

[162] P. Gawryszewska, J. Sokolnicki, J. Legendziewicz, *Coordin Chem Rev*, 249, 2489, (2005).

[163] K. Binnemans, *Rare Earth Beta-Diketonates*, Amsterdam, (2005).

[164] R. M.; Supkowski, W. D. Horrocks, *Inorg. Chim. Acta*, 340, 44, (2002).

[165] C. Musikas, *Inorg. Chim. Acta*, 140, 197, (1987).

[166] S. P. Macciotta, A. Rucci, A. Serpi, *J. Lumin.*, 9, 488, (1975).

[167] R. A. Sá Ferreira, L. D. Carlos, V. de Zea Bermudez, *Hybrid Materials: synthesis, characterization, and applications*, Weinheim, (2007).

[168] C. Huang, *Rare Earth Coordination Chemistry: Fundamentals and Applications*, Singapore, (2010).

[169] A. P. Pavia, M. C. Costa, *Hydrometallurgy*, 7, 103, (2005).

[170] Y. Wang, Y. Feng, H. Zhao, Q. Gan, X. Yu, *J. Sol-Gel Sci. Technol.*, 58, 711, (2011).

[171] S. Biju, Y. K. Eom, J.-C. G. Bunzli, H. K. Kim, *J. Mater. Chem C* 1, 3454, (2013).

[172] J. J. E. Moreau, L. Vellutini, M. Wong Chi Man, C. Bied, J. L. Bantignies, P. Dieudonne, J. L. Sauvajol, *J Am Chem Soc*, 123, 7957, (2001).

[173] S. S. Nobre, C. D. S. Brites, R. A. S. Ferreira, V. de zea Bermudez, C. Carcel, J. J. E. Moreau, J. Rocha, M. Wong Chi Man, L. D. Carlos, 18, 4172, (2008).

[174] P. Dieudonne, M. Wong Chi Man, B. P. Pichon, L. Vellutini, J. L. Bantignies, C. Blanc, G. Creff, S. Finet, J. L. Sauvajol, C. Bied, J. J. E. Moreau, *Small*, 5, 503, (2009).

[175] E. Stathatos, P. Lianos, B. Orel, A.S. Vuk, R. Jese, *Langmuir*, 19, 7587, (2003).

[176] F. H. Allen, C. M. Bird, R. S. Rowland, P. R. Raithby, *Acta Cryst.*, B53, 680, (1997).

[177] Gautam R. Desiraju, *Acconts Chem. Res.*, 35, 565, (2002).

[178] Gaëlle Creff, *Mécanismes de structuration de silices hybrides auto-assemblées*, Université Montpellier II, (2009).

[179] J. E. Stewart, *J. Chem. Phys.*, 26, 248, (1957).

[180] Srinivasan K., Gunasekaran S, Krishnan S., *Spectrochim Acta A Mol Biomol Spectrosc.*, 75, 1171, (2010).

[181] V. Z. Vassilevaa, P. P. Petrovab, *Croat. Chem. Acta*, 78, 295, (2005).

[182] H. Takahashi, B. Schrader, W. Meier, K. Gottlieb, *J. Chem. Phys.*, 47, 3842, (1967).

[183] N.B. Colthup, L.H. Daly, *Introduction to Infrared and Raman Spectroscopy*, New York, (1975).

[184] G. Creff, G. Arrachart, P. Hermet, H. Wadepohl, R. Almairac, D. Maurin, J.-L. Sauvajol, C. Carcel, J. J. E. Moreau, P. Dieudonné, M. Wong Chi Man, J.-L. Bantignies, *Phys. Chem. Chem. Phys*, 14, 5672, (2012).

[185] D. J. Skrovanek, S. E. Howe, P. C. Painter, M. M. Coleman, *Macromolecules*, 18, 1676, (1985).

[186] J. J. E. Moreau, B. P. Pichon, M. Wong Chi Man, C. Bied, H. Pritzkow, J. L. Bantignies, P. Dieudonné, J. L. Sauvajol, *Angew. Chem. Int. Ed.*, 43, 203, (2004).

[187] G. Creff, B. P. Pichon, C. Blanc, D. Maurin, J. L. Sauvajol, C. Carcel, J. J. E. Moreau, P. Roy, J. R. Bartlett, M. Wong Chi Man, J. L. Bantignies, *Langmuir*, 29, 5581, (2013).

[188] V. B. Bregovic, N. Basaric, K. Mlinaric-Majerski, *Coordin. Chem. Rev.*, 295, 80, (2015).

[189] R. Custelcean, Gorbunova M. G., Bonnesen P. V., *Chem. Eur. J.*, 11, 1459, (2005).

[190] A. Madarász, Z. Dósa, S. Varga, T. Soós, A. Csámpai, I. Pápai, *ACS Catal.*, 6, 4379, (2016).

[191] R. Custelcean, *Chem. Commun.*, 295, (2008).

[192] Dan Lehnherr, David D. Ford, Andrew J. Bendelsmith, C. Rose Kennedy, Eric N. Jacobsen, *Org. Lett.*, 18, 3214, (2016).

[193] J. Klimowskwi, W. Wanarskla, D. Ozqo, *Phys. Stat. Sol.*, 34, 697, (1976).

[194] A. Banerji, S. K. Deb, *J. Phys. Chem. B*, 111, 10915, (2007).

[195] E. V. Boldyreva, *J. Mol. Struct.*, 700, 151, (2004).

[196] Q. Wang, T. Yan, K. Wang, H. Zhu, Q. Cui, B. Zou, *J. Chem. Phys.*, 142, 244701, (2015).

[197] L. D. Carlos, R. A. S. Ferreira, S. S. Nobre, M. Wong Chi Man, J. J. E. Moreau, C. Bied, B. Pichon, *Photolurninescence changes induced by self-organisation in bridged silsesquioxanes*,(2006).

[198] V. T. Freitas, *Materiais Híbridos Orgânicos-Inorgânicos nanoestruturados para aplicação em fotónica.*, Universidade do Minho, (2011).

[199] S. C. Moss, D. Adler, H. Fritzche, S. Ovshinsky, *Physics of Disorder Materials*, New York, (1985).

[200] C. Arenz, A. Giannis, *Eur. J. Org. Chem.*, 137, (2001).

[201] E. J. Nassar, L. R. Avila, P. F. S. Pereira, E. C. O. Nassor, *Quim. Nova*, 30, (2007).

[202] Y. J. Fan, M. Kobayashi, H. Kise, *J. Polym. Sci. Pol. Chem.*, 39, 1318, (2001).

[203] V. de Zea Bermudez, L. D. Carlos, L. Alcácer, *Chem. Mater.*, 11, 569, (1999).

[204] E. Pecoraro, R. A. Sá Ferreira, C. Molina, S. J. L. Ribeiro, Y. Messsaddeq, L. D. Carlos, *J. Alloy. Compd.*, 451, 136, (2008).

[205] A. Guinier, *X-ray Diffraction in Crystals, Imperfect Crystals and Amorphous Bodies*, New York, (1994).

[206] B. E. Warren, *X-ray Diffraction*, New York, (1969).

[207] The Cambridge Crystallographic Data Centre, (2015).

[208] M. C. Gonçalves, V. de Zea Bermudez, R.A.S. Ferreira, D. Ostrovskii, J. Rocha, L. D. Carlos, *Chem. Mater.*, 16, 2530, (2004).

[209] R. A. S. Ferreira, A. L. Ferreira, L. D. Carlos, *Eur. Phys. J. B*, 50, (2006).

[210] T. Schmidt, K. Lischka, W. Zulehner, *Phys. ReV. B.*, 45, 8989, (1992).

[211] P. Escribano, B. Julián-López, J. Planelles-Aragó, E. Cordoncillo, B. Viana, C. Sanchez, *J. Mater. Chem.*, 18, 23, (2008).

[212] L. D. Carlos, R. A. S. Ferreira, V. de Zea Bermudez, B. Julián-López, P. Escribano, *Chem. Soc. Rev.*, 40, 536, (2011).

[213] M. M. Nolasco, P. M. Vaz, V. T. Freitas, P. P. Lima, P. S. André, R. A. S. Ferreira, P. D. Vaz, P. Ribeiro-Claro, L. D. Carlos, *J. Mater. Chem. A*, 1, 7339, (2013).

[214] K. Binnemans, *Chem. Rev.*, 109, 4283, (2009).

[215] Y. Zhang, W. Wei, G. K. Das, T. T. Y. Tan, *J. Photochem. Photobio. C*, 20, 71, (2014).

[216] K. Machida, H. Li, D. Ueda, S. Inoue, G. Adachi, *J. Lumin.*, 87-9, 1257, (2000).

[217] L. R. Wilson, B. S. Richards, *Appl. Optics*, 48, 212, (2009).

[218] O. Moudam, B. C. Rowan, M. Alamiry, P. Richardson, B. S. Richards, A. C. Jones, N. Robertson, *Chem. Commun.*, 6649, (2009).

[219] T. X. Wang, J. Zhang, W. Ma, Y. H. Luo, L. J. Wang, Z. J. Hu, W. X. Wu, X. Wang, G. Zou, Q. J. Zhang, *Sol. Energy*, 85, 2571, (2011).

[220] S. F. H. Correia, V. de Zea Bermudez, S. J. L. Ribeiro, P. S. André, R. A. S. Ferreira, L. D. Carlos, *J. Mater. Chem. A*, 2, 5580, (2014).

[221] P. P. Lima, M. M. Nolasco, F. A. A. Paz, R. A. S. Ferreira, R. L. Longo, O. L. Malta, L. D. Carlos, *Chem. Mater.*, 25, 586, (2013).

[222] Y. G. Wang, N. N. Lin, *Photoch. Photobio. Sci.*, 10, 42, (2011).

[223] B. Yan, *RSC Adv.*, 2, 9304, (2012).

[224] R. J. P. Corriu, J. J. E. Moreau, P. Thepot, M. Won Chi Man, *Chem. Mater.*, 4, 987, (1994).

[225] K. J. Shea, D. A. Loy, *Chem. Mater.*, 13, 3306, (2001).

[226] B. D. Hatton, K. Landskron, W. Whitnall, D. D. Perovic, G. A. Ozin, *Adv. Funct. Mater.*, 15, 823, (2005).

[227] I. Karatchevtseva, D. J. Cassidy, M. Won Chi Man, D. R. G. Mitchell, J. V. Hanna, C. Carcel, C. Bied, J. J. E. Moreau, J. R. Bartlett, *Adv. Funct. Mater.*, 17, 3926, (2007).

[228] H. Hu, L. Q. Xiong, J. Zhou, F. Y. Li, T. Y. Cao, C. H. Huang, *Chem-Eur. J.*, 15, 3577, (2009).

[229] Z. E. Chamas, X. M. Guo, J. L. Canet, A. Gautier, D. Boyer, R. Mahiou, *Dalton Trans.*, 39, 7091, (2010).

[230] Y. Wang, Y. Wang, Q. Gan, *J. Sol-Gel Sci. Techn.*, 56, 141, (2010).

[231] Y. Wang, Y. G. Wang, P. P. Cao, Y. N. Li, H. R. Li, *Crystengcomm*, 13, 177, (2011).

[232] J.-C. G Bünzli, A.-S. Chauvin, *Lanthanides in Solar Energy Conversion*, Amsterdam, (2014).

[233] W. H. Weber, J. Lambe, *Appl. Optics.*, 15, 2299, (1976).

[234] M. J. Currie, J. K. Mapel, T. D. Heidel, S. Goffri, M. A. Baldo, *Science*, 321, 226, (2008).

[235] G. Maggioni, A. Campagnaro, S. Carturan, A. Quaranta, *Sol. Energ. Mat. Sol. C.*, 108, 27, (2013).

[236] V. Sholin, J. D. Olson, S. A. Carter, *J. Appl. Phys.*, 101, 123114, (2007).

[237] R. H. Inman, G. V. Shcherbatyuk, D. Medvedko, A. Gopinathan, S. Ghosh, *Opt. Express*, 19, 24308, (2011).

[238] P.-M. Finn, Y. K. Gun'ko, *J. Mater. Chem.*, 22, 16687, (2012).

[239] W. Wu, T. Wang, X. Wang, S. Wu, Y. Luo, X. Tian, Q. Zhang, *Sol. Energy*, 84, 2140, (2010).

[240] D. K. Boer, Dirk J. Broer, M. G. Debije, W. Keur, A. Meijerink, C. R. Ronda, Paul P. C. Verbunt, *Opt. Express*, 20, A395, (2012).

[241] G. Katsagounos, E. Stathatos, N. B. Arabatzis, A. D. Keramidas, P. Lianos, *J. Lumin.*, 131, (2011).

[242] Xin Wang, Tongxin Wang, Xiujie Tian, Lijuan Wang, Wenxuan Wu, Yanhua Luo, Qijin Zhang, *Sol. Energy*, 85, 2179, (2011).

[243] V. Misra, H. Mishra, *J. Chem. Phys.*, 128, 244701, (2008).

[244] J. L. Bantignies, L. Vellutini, J. L. Sauvajol, D. Maurin, M. Wong Chi Man, P. Dieudonne, J. J. E. Moreau, *J. Non-Cryst. Solids*, 345, 605, (2004).

[245] R. J. H. Clark, C. S. Williams, *Inorg. Chem.*, 4, 350, (1965).

[246] V. F. Zolin, L. N. Puntus, V. I. Tsaryuk, V. A. Kudryashova, J. Legendziewicz, P. Gawryszewska, R. Szostak, *J. Alloys Compd.*, 380, 279, (2004).

[247] R. Le Parc, P. Hermet, S.Rols;, D. Maurin, L. Alvarez, A. Ivanov, J. M. Quimby, C. G. Hanley, L. T. Scott, J.-L. Bantignies, *J. Phys. Chem. C*, 116, 25089, (2012).

[248] J. A. Kai, M. C. F. C. Felinto, L. A. O. Nunes, O. L. Malta, H. F. Brito, *J. Mater. Chem.*, 21, 3796, (2011).

[249] M. Fernandes, V. de Zea Bermudez, R. A. S. Ferreira, L. D. Carlos, A. Charas, J. Morgado, M. M. Silva, M. J. Smith, *Chem. Mater.*, 19, 3892, (2007).

[250] K. Binnemans, P. Lenaerts, K. Driesen, C. Gorller-Walrand, *J. Mater. Chem.*, 14, 191, (2004).

[251] G. V. Shcherbatyuk, R. H. Inman, C. Wang, R. Winston, S. Ghosh, *Appl. Phys. Lett.*, 96, 191901, (2010).

[252] F. Meinardi, A. Colombo, K. A. Velizhanin, R. Simonutti, M. Lorenzon, L. Beverina, R. Viswanatha, V. I. Klimov, S. Brovelli, *Nature Photon.*, 8, 392, (2014).

[253] V. Wittwer, W. Stahl, A. Goetzberger, *Sol. Energ. Mater.*, 11, 187, (1984).

[254] P. T. M. Albers, C. W. M. Bastiaansen, M. G. Debije, *Sol. Energy*, 95, 216, (2013).

[255] G. Griffini, M. Levi, S. Turri, *Sol. Energ. Mat. Sol. C*, 118, 36, (2013).

[256] R. Reisfeld, D. Shamrakov, C. Jorgensen, *Sol. Energ. Mat. Sol. C.*, 33, 417, (1994).

[257] V. R. Fernandes, C. M. S. Vicente, N. Wada, P. S. André, R. A. S. Ferreira, *Opt. Express*, 18, 16580, (2010).

[258] G. Kresse, J. Furthmüller, *J. Phys. Rev. B*, 54, 11169, (1996).

[259] J.P. Perdew, K. Burke, M. Ernzerhof, *Phys. Rev. Lett.*, 77, 3865, (1996).

[260] H. J. Monkhorst, J. D. Pack, *Phys. Rev. B*, 13, 5188, (1976).

[261] P. Hermet, J.L. Bantignies, A. Rahmani, J.L. Sauvajol, M.R. Johnson, F.J. Serein, *Phys. Chem. A*, 109, 1684, (2005).

[262] S. Inagaki, S. Guan, Y. Fukushima, T. Ohsuna, O. Terasaki, *J. Am. Chem. Soc.*, 121, 9611, (1999).

[263] T. Asefa, M. J. MacLachlan, N. Coombs, G. A. Ozin, *Nature*, 402, 867, (1999).

[264] B. J. Melde, B. T. Holland, C. F. Blanford, A. Stein, *Chem. Mater.*, 11, 3302, (1999).

[265] Y. Li, L. F. Bi, S. B. Wang, Y. L. Chen, B. Z. Li, X. L. Zhu, Y. G. Yang, *Chem. Commun.*, 46, 2680, (2010).

[266] Ono Y. Jong Hwa Jung, S. Shinkai, *Angew. Chem., Int. Ed.*, 39, 1862, (2000).

[267] S. Guan, S. Inagaki, T. Ohsuna, O. Terasaki, *J. Am. Chem. Soc.*, 122, 5660, (2000).

[268] S. S. Nobre, C. D. S. Brites, R. A. S. Ferreira, V. de Zea Bermudez, C. Carcel, J. J. E. Moreau, J. Rocha, M. Wong Chi Man, L. D. Carlos, *J. Mater Chem*, 18, 4172, (2008).